FIELD ENHANCEMENT OF NEAR FIELD TRANSDUCER USING METAMATERIAL FOR HEAT ASSISTED MAGNETIC RECORDING
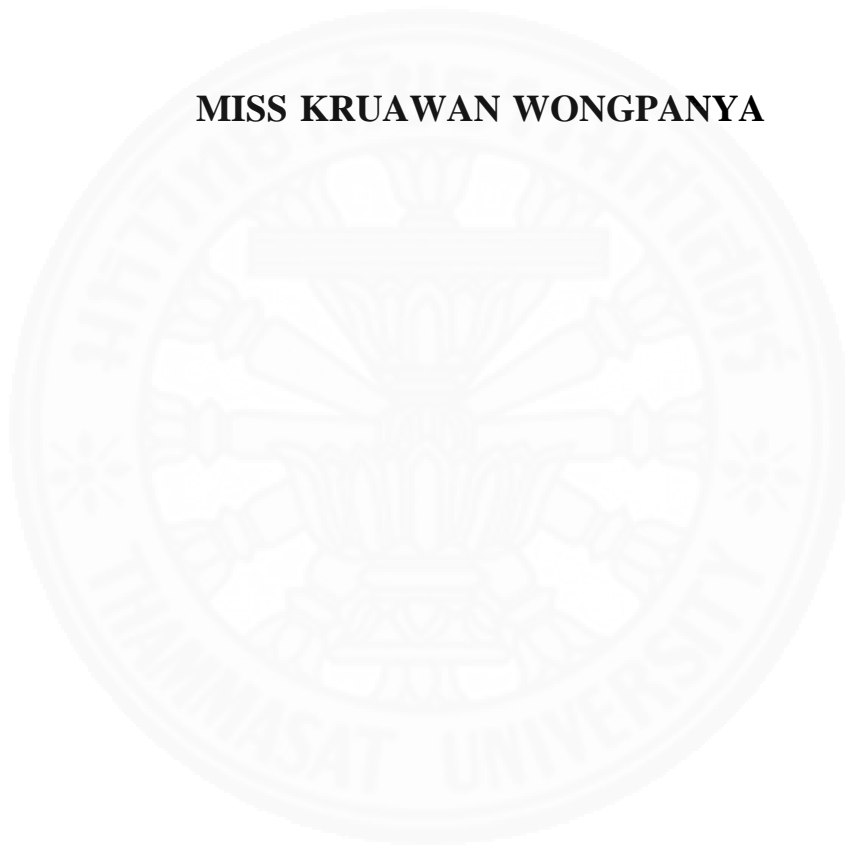
BY

MISS KRUAWAN WONGPANYA

A DISSERTATION SUBMITTED IN PARTIAL FULFILLMENT
OF THE REQUIREMENTS FOR THE DEGREE OF DOCTOR OF
PHILOSOPHY IN ENGINEERING
FACULTY OF ENGINEERING
THAMMASAT UNIVERSITY
ACADEMIC YEAR 2017
COPYRIGHT OF THAMMASAT UNIVERSITY

FIELD ENHANCEMENT OF NEAR FIELD TRANSDUCER USING METAMATERIAL FOR HEAT ASSISTED MAGNETIC RECORDING

BY

MISS KRUAWAN WONGPANYA

A DISSERTATION SUBMITTED IN PARTIAL FULFILLMENT
OF THE REQUIREMENTS FOR THE DEGREE OF DOCTOR OF
PHILOSOPHY IN ENGINEERING
FACULTY OF ENGINEERING
THAMMASAT UNIVERSITY
ACADEMIC YEAR 2017
COPYRIGHT OF THAMMASAT UNIVERSITY

THAMMASAT UNIVERSITY
FACULTY OF ENGINEERING

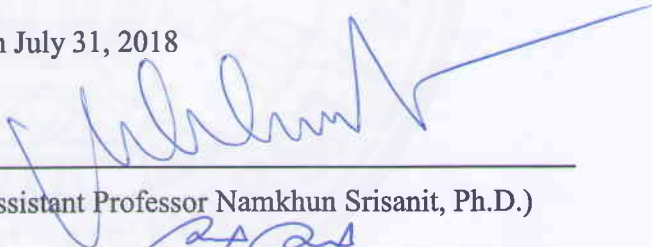DISSERTATION

BY

MISS KRUAWAN WONGPANYA

ENTITLED

FIELD ENHANCEMENT OF NEAR FIELD TRANSDUCER USING
METAMATERIAL FOR HEAT ASSISTED MAGNETIC RECORDING

was approved as partial fulfillment of the requirements for
the degree of Doctor of Philosophy in Engineering
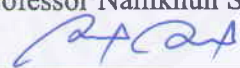
on July 31, 2018

Chairman _____
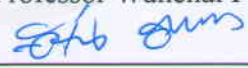(Assistant Professor Namkhun Srisanit, Ph.D.)

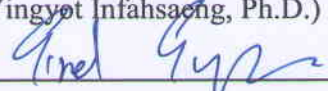Member and Advisor _____
(Associate Professor Wanchai Pijitrojana, Ph.D.)

Member _____
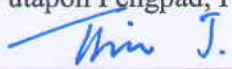(Yingyot Infahsaeng, Ph.D.)

Member _____
(Sirod Sirisup, Ph.D.)

Member _____
(Putapon Pengpad, Ph.D.)

Dean _____
(Associate Professor Thira Jearsiripongkul, Dr.-Ing.)

Dissertation Title	FIELD ENHANCEMENT OF NEAR FIELD TRANSDUCER USING METAMATERIAL FOR HEAT ASSISTED MAGNETIC RECORDING
Author	Miss Kruawan Wongpanya
Degree	Doctor of Philosophy (Engineering)
Major Field/Faculty/University	Electrical and Computer Engineering Faculty of Engineering Thammasat University
Dissertation Advisor	Associate Professor Wanchai Pijitrojana, Ph.D.
Dissertation Co-Advisor (If any)	-
Academic Years	2017

ABSTRACT

As an analyst from International Data Corp. and Western Digital Corp, the storage demands, hard disk drives (HDDs), is increasing. Unfortunately, the conventional magnetic recording technology is not able to increase storage capacity more than the superparamagnetism limit because the stability problem of the recording medium. The heat-assisted magnetic recording (HAMR) is a new technique which is introduced to overcome the data density limitation by increasing the areal density, expressed in bits per square inch by using a laser to temporary heat a recording medium to reduce the magnetic coercivity before writing process, which is then quickly cooled back to its high-anisotropy state at ambient temperature to stabilize it. The heart of HAMR is a light delivery system called the near field transducer (NFT), to focus light onto a nano-sub-diffraction-limit spot or nano-focusing, in the recording medium. The NFT is made from plasmonic devices which supports the Surface Plasmon Polaritons (SPPs), the main mechanism for overcoming the diffraction limit and helps to enhance the field and coupling efficiency of the NFT. Therefore, the smallest nano-focusing with the high efficiency are required. Therefore, in this dissertation, the investigation of the field enhancement of NFT using metamaterial is proposed, the NFT based on 3D MIM structure for confining light on the deep sub-wavelength scale with input and

output part made from metamaterial for optical experiment evaluating. The fabrication of NFT associated with the mass-productive manufacturing using the simple process capability are also demonstrated.

The fabrication of a metal-insulator-metal plasmon waveguide with a linear taper is reported. Highly efficient nano-focusing of light with a Au-SiO$_2$-Au waveguide with a three-dimensional taper had been demonstrated. However, conventional vertical taper structures were fabricated with a low-throughput process based on electron beam scanning. An efficient, mass-productive fabrication process using a standard dry etching technique is proposed. A key improvement is the employment of a mixed gas of CHF$_3$ and O$_2$. By optimizing the gas composition and the cooling process of the substrate, a SiO$_2$ vertical taper with an angle of 19 deg., which is very close to the optimum 20 deg. was successfully produced. At the tip section, an ultra-thin waveguide as thin as 5.6 nm, only one third of the conventional demonstration, is reproducibly realized by the employment of an atomic layer deposition of Al$_2$O$_3$. Coupling efficiency as high as 72% was numerically.

To practical applications, it very difficult to do alignment for the light source to directly incident light to the bottom of the MIM waveguide which is a nano scale. Therefore, the metamaterial was integrated to the MIM waveguide as the input part and output part. The new structure required the longer body part causing the coupling efficiency was extremely reduced from 79% to 3.65%. However, this output efficiency can be observed in characterization. Furthermore, it is found that the optimized taper angle is not 19 deg. as the feasibility study but it is 30 deg.

The characterization feasibility study was found that the propagating length of the 5 nm-Al$_2$O$_3$ is too short, so it is extended to 40 nm-Al$_2$O$_3$. For fabrication process and to remove the SPPs outer surface, both required Ti for adhesion and preventing the SPPs outer surface. But Ti's effect seriously reduced the efficiency. Another big problem is that the Gaussian beam from the light source is too large, the possible to observe the output light, the 4.22 μm-distance between the grating and slit long is required. Finally, the final specimen of structure which can be observed in the characterization is composed of 300nm-Au/3nm-Ti/200nm- SiO$_2$/40nm-Al$_2$O$_3$/80nm-Au/20nm-Ti. The optimum input structures are the 4 holes of grating, period 520 nm

and hole width 110 nm and the optimized taper angle is 30 deg. With all modifications above, the final specimen efficiency as reduces from 3.65% to 0.1% was calculated.

The fabrication results, The 8 typical taper angles (10 – 50 deg.) of final specimens are obtained as A-H specimens with good linearity and controllability of taper angles using the oxide dry etching machine which is the embedded cooling system. But it also produced the 20-30 nm-vertical step length in dry etching process. Fabrication yield is about 1.2%.

The characterization, the 830 nm-wavelength of Gaussian light source with 620 nm-beam waists was operated. As the characterization results, the efficiency of A-B and E-H specimens were slightly different from the simulation results. But C and D specimens were large different from the simulation results. The re-simulation with the actual structures shown that the presence or absence of the vertical step and the 3 nm-thickness of Ti at the tip area are the main factor for the discrepancy between the simulation results and the experiment results. Finally, the highest efficiency 0.045%-0.05% are obtained with the 512 nm x 853 nm spot size. The efficiency is dropped from the simulation forecasting because the vertical step appearing in the fabrication process and the Gaussian beam waist reducing to 620 nm. Lastly, the future work target is to improve the coupling efficiency by removing disadvantages above, other parameters which relate to the coupling efficiency will be investigated, and the new design of the input and output part should be also necessary to improve the coupling efficiency to 72% as closed as the ideal concept design.

ACKNOWLEDGEMENTS

Miss Kruawan Wongpanya

TABLE OF CONTENTS

LIST OF TABLES

LIST OF FIGURES

LIST OF ABBREVIATIONS

Symbols/Abbreviations	Terms
EB	Exabyte
ASTC	Advanced Storage Technology Consortium
V	Volume
K_u	The uniaxial anisotropy coefficient
E_p	The magnetic anisotropy energy
E_T	The environment thermal energy
K_B	Boltzmann's constant 1.38×10^{-23} J/K
T	The absolute temperature in Kelvin
HAMR	Heat-assisted magnetic recording
HDD	Hard disk drive
NFT	Near Field Transducer
PSIM	A planar solid immersion mirror
λ	Lambda, the wavelength
D	The full-width spot diameter
FWHM	Full width half maximum
SPPs	Surface Plasmon Polaritons
LSPR	Localized Surface Plasmon Resonance
FOM	Figure of merit
SIL	A solid immersion lens
P_{diss}	The dissipated power density
ε_0	The vacuum permittivity
μ_0	The vacuum permeability
ω	The angular frequency of the laser
ε	Permittivity
μ	Permeability
NPs	Nano-Particles
σ	The complex optical conductivity of the lossy material
k_0	The wave vector
β	The propagation constant
TM	The transverse magnetic
TE	The transverse electric
H	Magnetic field
E	Electric field

Symbols/Abbreviations	Terms
λ_{SPPs}	Surface Plasmon Polariton wavelength
l_{prop}, L_p	SPPs Propagated length
n	Refractive index
ω_p	Plasma frequency
ω_{sp}	The surface plasma frequency
MIM	Metal-Insulator-Metal
NPC	Nano-plasmonic photon compressor
Au	Gold
SiO_2	Silicon di oxide
Al_2O_3	Aluminum oxide
Ti	Titanium
O_2	Oxygen
CHF_3	Fluoroform
SEM	Scanning electron microscopy
TEM	Transmission electron microscopy
FEM	Frequency Element Method
υ_g	The group velocity
I	Intensity
η_0	The impedance of the free space
P_B	Power flow across the body part
P_T	Power flow across the tip part
P_{in}	Power flow at the input area
P_{out}	Power flow at the output area
S_{11}, S_{21}	S-parameters in terms of power flow in COMSOL
T	Transmittance
R	Reflectance
PR	Photoresist
w_0	The Gaussian beam waist
E-Beam lithography	The electron beam lithography
EBID	An electron-beam-induced deposition
ALD	Atomic layer deposition
HDMS	Hexamethyldisilazane
TMAH	Tetramethylammonium hydroxide
NMP	*N*-Methyl-2-pyrrolidone

Symbols/Abbreviations	Terms
M	Mirror
d	Distance between taper and slit
ND	Newtrual-density
Ix0	Intensity of horizontal cross section
Iy0	Intensity of vertical cross section
I0	Total Intensity
Wx0	Beam waist of horizontal direction
Wy0	Beam waist of vertical direction

CHAPTER 1

INTRODUCTION

1.1 Introduction

The data storage capacity demands are increasing as an analyst from International Data Corp. and Western Digital Corp. estimated that the industry by 2020 will be approximately total to 2,900 Exabytes (1 EB = 1 million TB), up from around 1,000 EB in 2015 as shown in figure 1.1 [1]. ASTC (Advanced Storage Technology Consortium) also disclosed the HDD technology roadmap that the capacity of hard drives will rise to 100 TB by 2025 as shown in figure 1.2 [2]. Demand for storage will be driven by various factors, including Big Data, Internet-of-Things, user-generated content, enterprise storage, personal storage and so on [1]. These needs are solved by an increase in the areal density, express in bits per square inch. Normally the data storage medium consists of many magnetic grains, which is collected into volume (V), the uniaxial anisotropy coefficient (K_u) is the constant to define how hard to change magnetization in order to record '1' and '0'into the medium. If K_u is high value, it is difficult to change the magnetization of data bit in the medium. The magnetic anisotropy energy is $E_p = K_u V$ which presents the stability of magnetic grain. As the volume of a magnetic grain is reduced, it reaches a point where the magnetic orientation of the grain becomes thermally unstable. The environment's thermal energy is $E_T = K_B T$, where K_B is Boltzmann's constant which is 1.38 x 10^{-23} J/K and T is the absolute temperature in Kelvin. The stability of thermal energy within the grain is shown in equation 1.1.

$$\frac{E_p}{E_T} = \frac{K_u V}{K_B T} \geq 60 \tag{1.1}$$

This equation describes the areal density or the "superparamagnetic limit" of magnetic storage density.

Due to $K_B T$ is the constant value, so to increase the areal density by reduce V must use a high anisotropy recording medium, with smaller grains that are thermally stable. Unfortunately, it is difficult with traditional recording technology to

achieve larger densities. As the storage density increases, the area of each bit decreases, but to maintain the same level of signal-to-noise ratio [3]. This is limited due to the superparamagnetism limit because when considering small enough particles, the magnetic polarization can flip randomly under the influence of temperature [4], [5]. One way to overcome this effect is by temporary heating the media because the media coercivity is indirect variable to the temperature. So, the magnetic anisotropy of the medium is momentarily reduced to enable recording by raising its temperature that is the Heat-assisted magnetic recording (HAMR), which is the new technology, to achieve areal densities in the in the range of 1–40 Tb/in^2 [6, 7].
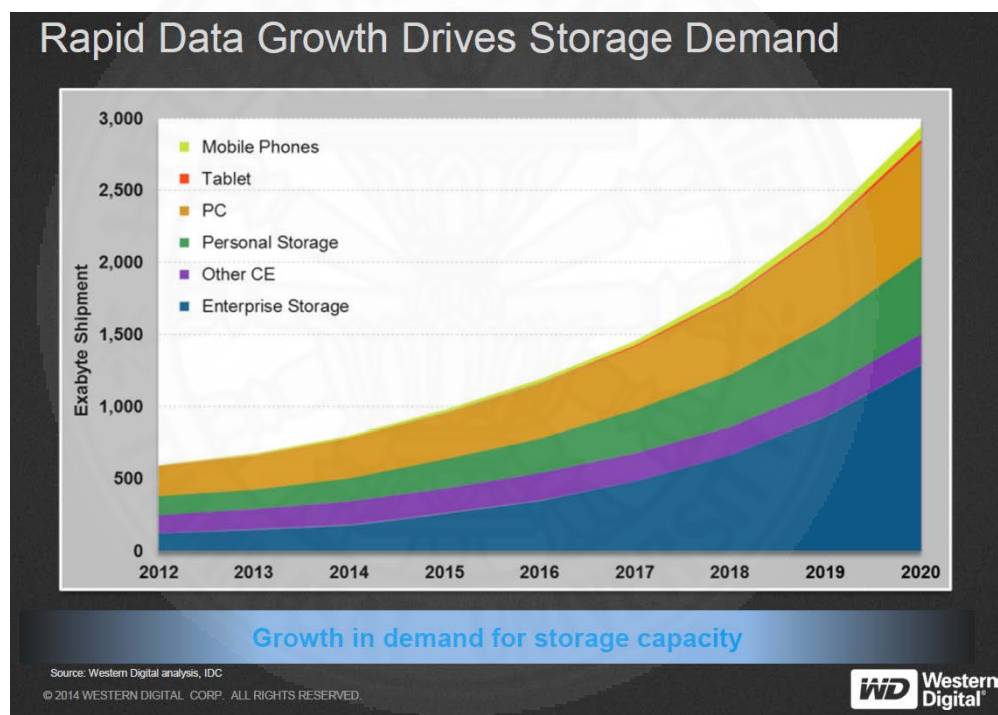
Figure 1.1 The growth in demand for data storage capacity [1].
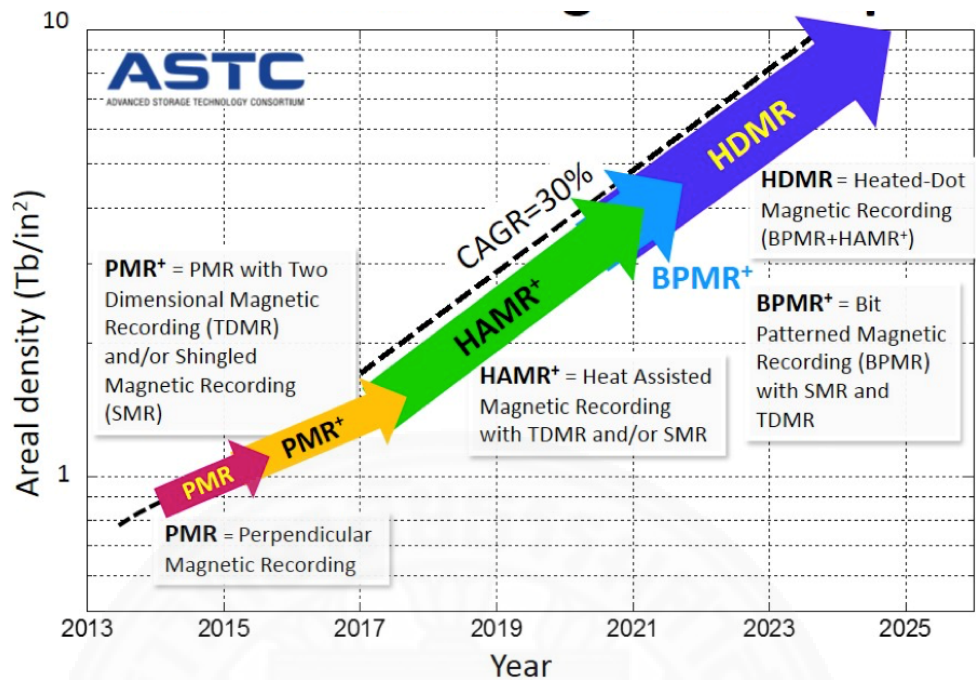
Figure 1.2 The HDD technology roadmap [2].

1.2 Heat-assisted magnetic recording (HAMR)

HDD industry invented a new technology, HAMR, to overcome the data density limitation by an increase in the areal density, express in bits per square inch. The HAMR uses a laser to temporary heat a recording medium above its Curie temperature to reduce the magnetic corecivity before writing process, then quickly cools back to its high-anisotropy state at ambient temperature to stabilize it. The writing process is shown in figure 1.3. At the general temperature, the media has a high coercivity. In the written process, the HAMR system applies the laser power to heat the media target region temporarily until the temperature exceeds the curie temperature (300-400°C) because of which the magnetic corecivity lowers below the available applied magnetic write field region, allowing higher media anisotropy and therefore reducing the thermally stable grains. The heated region is then rapidly cooled back to a stable state and completely recorded data in the media [8]. The sketch illustrating the HAMR recording head is shown in figure 1.4A.
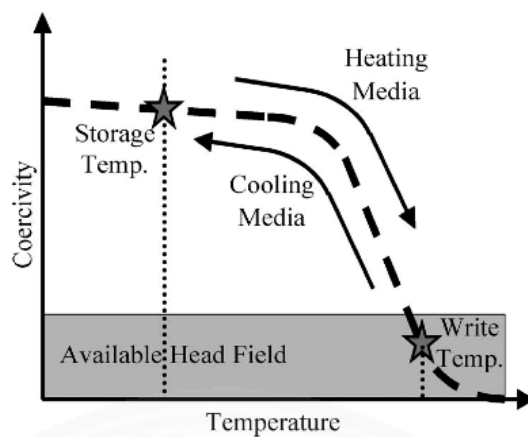
Figure 1.3 A schematic diagram of the HAMR write is shown [8].
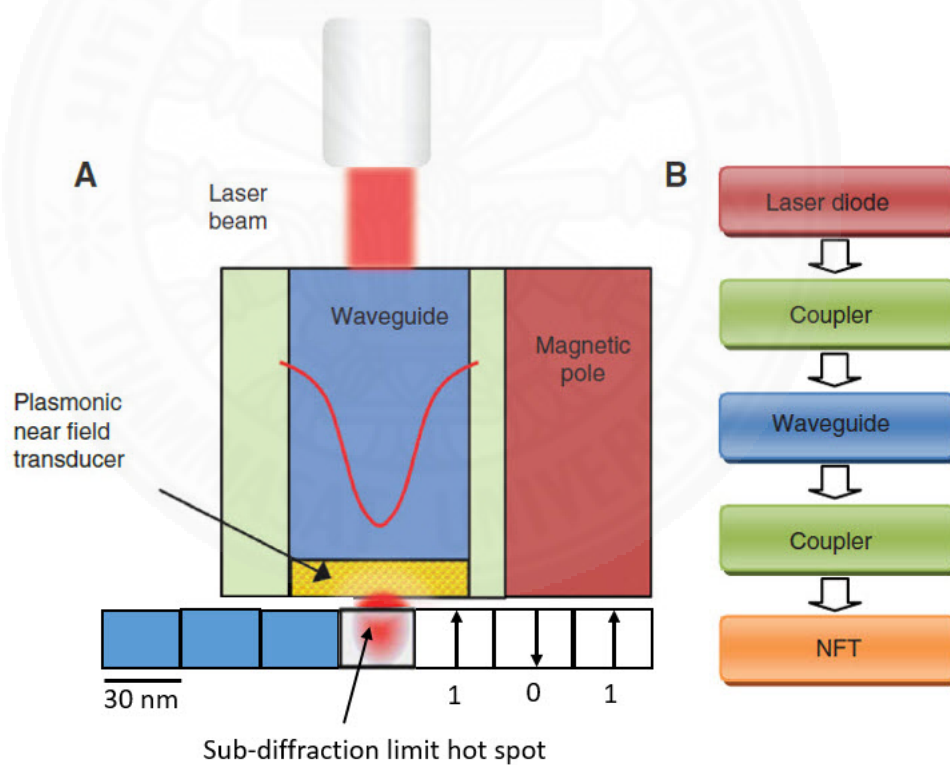
Figure 1.4 (A) HAMR head. (B) The light delivery system in a HAMR head [9].

1.3 HAMR system

The conventional recording for the applied magnetic field is very small (approximately 0.02 T) but, the applied field for HAMR is highly localized, very large in magnitude (up to 1 T or more) and generated by a miniature recording pole positioned within tens of nanometers of the optical spot as shown in figure 1.4A. Therefore, the next generation of recording head of HDD requires many technologies to support the HAMR system as shown in figure 1.5. The three major challenges for the HAMR head design and process will be addressed here: 1) magnetic field delivery; 2) optical delivery; and 3) integration of magnetic and optical field delivery components. Especially, the key component in HAMR is near field transducer (NFT) for applying heat through the use of a laser to the media. Such devices are possible by making use of the near field that is concentrated energy and generate a sub-diffraction limited optical spot, which is becoming useful in HAMR transducer. Thus, the HAMR NFT must have a power coupling efficiency into the recording medium. The light delivery system to NFT consists of the common elements which is shown in figure 1.4B. The light delivery system is started with a laser diode which is coupled to a waveguide using a coupler. Then the light propagates down by coupler into the NFT where it is converted into thermal energy with a sub-diffraction-limited light spot [9].
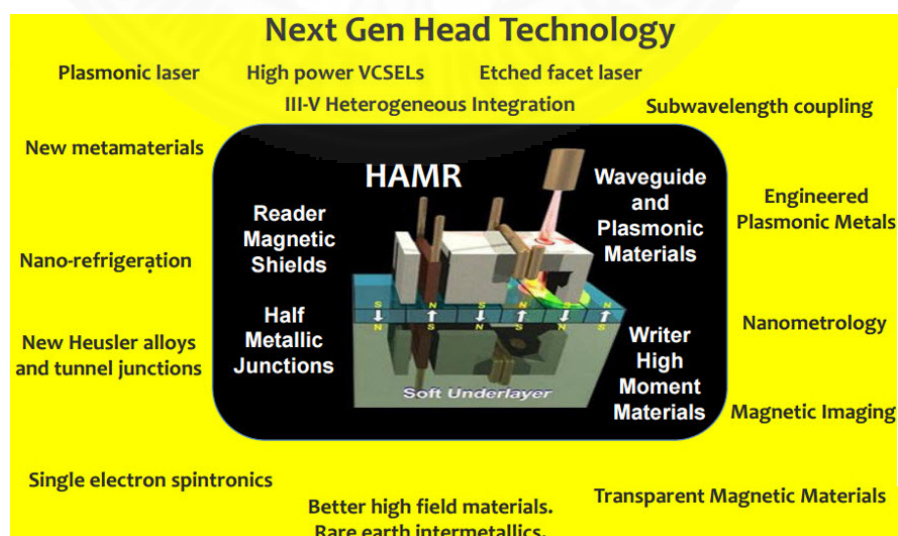
Figure 1.5 Recording Head Technology [10].

Details of the optical delivery part use a planar solid immersion mirror (PSIM) to confine light as show in figure 1.6. The PSIM consists of a planar waveguide, which is a high index of refraction layer sandwiched between two lower layers that are shown in Fig 1.6. (a) is a diagram of planar waveguide with a grating coupler and a planar solid immersion mirror (PSIM) focusing. (b) is the cross-sectional and (c) is the top down diagrams of a HAMR head that combines a PSIM with an input coupling grating and a magnetic recording ring head. (d) is a legend for (a), (b) and (c). A grating for coupling light into the waveguide can be formed in the core of the waveguide. The planar waveguide can be patterned into the shape of a parabola and a metal can be deposited onto the sidewalls of the parabolic waveguide to enhance the reflectivity. The PSIM sidewall needs to be nearly vertical and optically smooth so that it does not reflect the light out of the waveguide. When the light strikes the edge of the parabola, the light is reflected and focused at the focal point of the parabola. The width of the spot in the plane of the waveguide determines the data track width. The mode confinement in the waveguide will, in part, determine the down track thermal gradient [11].
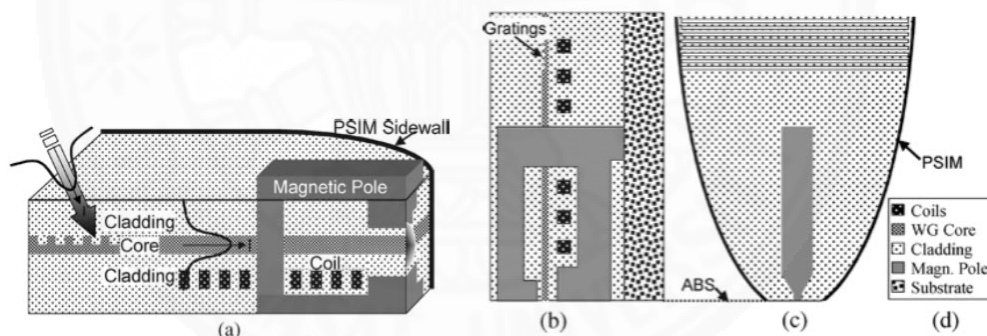
Figure 1.6 Diagram of the optical delivery of HAMR [12].

The HAMR is the one way to achieve areal densities in the in the range of $1–40 \, \text{Tb/in}^2$, as the areal density increases, the area of each bit decreases, but to maintain the same level of signal-to-noise ratio. Therefore, greater areal densities require smaller magnetic grains. The magnetic grain diameter is presently on the order of 10 nm. If areal density is more than 1 Tb/in. ^{2}, the track width is required to be about 25 x 25 nm^2 [13]. In order to, confine the heat for the recording area without having it interfere with the adjacent tracks, the optical spot used to heat the recording medium in HAMR must

be an order of magnitude smaller than the optical wavelength of high-power lasers. However, the ability of conventional devices is limited by the fundamental laws of diffraction. One cannot focus light smaller than a half wavelength of light (~λ/2) [11].

1.4 Diffraction limit

A conventional lens can only focus light to a spot size as shown is figure 1.7 which is defined by the diffraction of light or the diffraction limit,

$$D = \frac{0.5\lambda}{n \sin \theta} \tag{1.2}$$

where D is the full-width spot diameter at the half maximum point (FWHM), λ is the wavelength, n is the refractive index of the medium in which the light is focused, and θ is the half angle of the cone of the focused light.
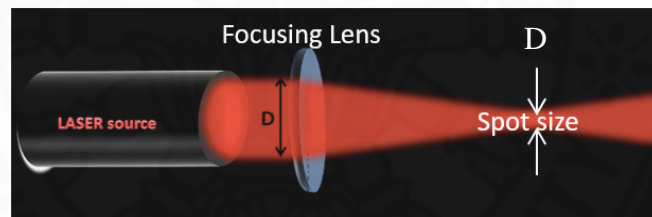
Figure 1.7 A conventional lens focus light to a spot size with the diffraction limit [14].

For example, the shortest-wavelength light source, a 400 nm Blu-ray laser diode, offers a 200 nm minimum diameter spot size in air. To reach a 25 x 25 nm² spot size, the nano-focusing device would need a medium with refractive index of 7, which does not exist in nature [13]. As previously discussed, the NFT HAMR must be located within a few nanometers of the media for the reader to have sufficient resolution at Tb/in² storage densities. As a result, it is necessary to employ near field optics to reach sub diffraction limit spot size. The plasmonic optic structure can support the Surface Plasmon Polaritons (SPPs), Localized Surface Plasmon Resonance (LSPR), and lightning rod that is the feasible mechanism to overcome the diffraction limit [8]. Details of these mechanisms will describe in chapter 2.

1.5 Problem statement

The utilization of plasmonic optical devices has been proposed as the mechanism for overcoming the diffraction limit and to help in enhancing the field and coupling efficiency of the NFT. They are based on various supported plasmonic modes such as SPP, Localized Surface Plasmon Resonance (LSPR), and lightning rod. The designs of plasmonic NFT have been proposed several time, but some structure is not useful for HAMR system. The NFTs make use of an antenna including aperture type antenna, and many designs are based on LSPR and SPPs. Some simple shapes include nanoscale spheres, holes, or rectangular apertures, but these shapes have some limitations and there dimensions must be reduced in order to obtain a small spot, resulting in transmission or coupling efficiency that is too low to be useful for HAMR[9]. For a single hole or small aperture, the energy of NFT cannot penetrate small aperture and the transmitted spot size is larger than the aperture because of the problem of low transmission of a single aperture [15]. An array of holes, grating structures, and groove around the aperture [16- 18] are of the order of several wavelengths [19, 20], which questionable make the NFT to be integrated into a recording head [9]. In order to improve the transmission or power output of a single nanostructure, many variants of simple circular and rectangular structures have been investigated, where sharp, nanoscale tips, pins, and notches are intentionally used to take advantage of the lightning rod effect. Common designs include triangle antenna [21, 22] and triangle aperture [23, 24], C aperture [32–36], bow-tie antenna [25-28] and bow-tie aperture [17, 29-33]. The bow-tie and C apertures are good examples for utilizing the combined effect of resonance and non-resonant amplification by nanostructures. For larger square apertures of bow-tie, its results are in a propagation mode, but without field confinement. In the same way, for C aperture, it is noted that if the gap region is very small and the aperture is very wide, there is a chance to produce unwanted elongated spot, because of the propagation of SP along the ridges. For other type of design, E-antenna, it is very similar to a C aperture antenna by adding the notch at the center, which concentrates the surface charges that is generated through a plasmonic resonance in the body. The bow-tie, C, half bow-tie aperture, and E-antenna, they are quite varied in the gap dimensions to generate elongated spots to match the bit

aspect ratio on the recording track [34]. Furthermore, another type of NFT design, the SPP and LSPR utilities are used for a lollipop and a nanobeak. The Lollipop is designed like a larger circular disk which acts as the LSPR and a small peg which localizes the optical energy to a recording medium via the lightning rod effect. For the nanobeak antenna, the field enhancement occurs at the tip of the beak which is also based on the lighting rod effect. Apart from the mechanisms used in the designs as previously discussed, the dual-dipole effect existing in two closed spaced nanoparticles [29, 35] and the Fabry-Perot effect in relatively thick films [29] can also be applied in NFT design. In addition, the shapes of NFT maniputlates the coupling efficiency and the spot size, which is localized into the record medium. The last NFT design is a 3D tapered MIM with a linear taper that is supporting the SPPs mode. This structure determines the cross-track spot size in the recording media. Ultimately, the spot size in the medium generates complex results, that is determined by the smallest structural dimension, which has a direct impact on the manufacturing requirements [9].

Therefore, in this dissertation, the investigation of the field enhancement of NFT using metamaterial is proposed, the NFT based on 3D MIM structure for confining light on the deep sub-wavelength scale with input and output part made from metamaterial for optical experiment evaluating. The fabrication of NFT associated with the mass-productive manufacturing using the simple process capability are also demonstrated.

1.6 Objectives

1. To introduce the artificial material, Metamaterials, for applications of NFT to enhance the incident field with the MIM plasmonic waveguide.

2. To design, simulation, and fabrication of the NFT based on the MIM plasmonic waveguide and improve the coupling efficiency using metamaterials.

3. To improve the fabrication of MIM plasmonic waveguide associated with the mass-productive manufacturing.

4. For the comparison of the NFT performance between the Conventional vs the new NFT.

CHAPTER 2
REVIEW OF LITERATURE

Within an optical nano-focusing system, that is used for the HAMR, energy is transferred at the nano-scale via electromagnetic and thermal physics. First, to study the different mechanisms of energy transfer with a small-sub-diffraction limit spot and HAMR requirements. The HAMR system requires the optical and thermal structure to implement a high power nano-focusing, As the literature review [13], the desired energy that must be deposited in the hotspot to achieve a 400 °C temperature rise in a ~30 nm diameter within 100 ps is 100 µW or 10^7 W/cm^2 of power density. In chapter 1, the discussion of the plasmonic optic devices which can be a feasible mechanism for breaking the diffraction limit and they can be applied to HAMR light delivery. The plasmonic NFT is based on various supported plasmonic modes, in order to get an understanding of all different mechanisms, in this chapter will present the NFT performance consideration, mechanisms for enhancement of the NFT performance or figure of merit (FOM), the literature review of plasmonic NFT structures and comparison of NFT, in the last chapter the literature review of metamaterials, and how to enhance the NFT coupling efficiency using metamaterails will be presented.

2.1 To consider the NFTs performance

A variety of NFT approaches have been proposed to deliver the light in the recording medium. For NFT performance evaluation, various criteria are used such as the power transmitted, the coupling efficiency, and the spot size in the recording area. One popular efficiency measure is the value of the enhancement of the electric field in the vicinity of the NFT relative to that of an incident plane wave. Another measurement, the percentage of the total focused power dissipated as heat in the recording medium within a confined spot, as has been reported by Seagate Technology [36] and HGST [37]. In a standard geometry, a solid immersion lens (SIL) measures the coupling efficiency, which is computed as the fraction of the incident optical power coupled into a 50 x 50 nm^2 area in the cobalt layer, at the resonant wavelength of each NFT [29].

This criteria is noted that the coupling efficiency depends strongly on the NFT-medium separation distance because of the evanescent nature of local fields [36,38].

Another measurement of NFTs, is the FOM [39], that is the amount of power transmitted through an NFT aperture relative to the incident power on the NFT integrated over the surface of the NFT aperture. This measurement is directly related to the near-field transducer coupling efficiency. This FOM includes peak field intensity in the neighboring medium, the ratio of the power dissipated within the optical hot spot of the recording medium to the total power in the incident beam or percent dissipated power in the medium, and temperature rise in the medium or the FWHM size of the thermal spot. The FOM details are as follows;

1. Percent Disspated Power in the recording medium will be evaluated on the percentage of the power in the incident beam that is dissipated within a circular area of 50 nm (for high-density HAMR storage, the bit cell will be smaller than 50 nm) in diameter in the recording medium. To get an understanding of the effects of the optical properties on NFT performance, the equation for computing dissipated power density in NFT is calculated [75].

$$P_{diss} = \frac{1}{2} Re(\sigma)|E|^2 = \frac{1}{2} \varepsilon_0 \omega Im(\varepsilon)|E|^2 \tag{2.1}$$

where ε_0 is the vacuum permittivity and ω is the angular frequency of the laser. The relationship between the relative permittivity ε and the complex optical conductivity of the lossy material, σ.

2. Peak field or Field intensity is the ratio of the peak electric field amplitude in the vicinity of the NFT to the electric field amplitude of an incident plane wave. The peak field intensity in a lossy medium is directly proportional to the dissipated power density. The peak field intensity in the incident beam is a function of the wavelength and polarization of the incident focused beam. So, if two NFTs couple light into a medium with the same peak, but at two different wavelengths, then the NFT which operates at the shorter wavelength will be generating a smaller spot size. The peak field intensity within the medium normalized by the incident field intensity is closely related to the total power dissipation within the medium. The peak field

intensity in the incident beam is a function of the wavelength and polarization of the incident focused beam that is proportional to $\frac{1}{\lambda^2}$.

3. Temperature rise in the recording medium is considered by the FWHM size of the thermal spot and its peak temperature for a given input power to the transducer that are directly related to the capability of the NFT.

2.2 Mechanisms for enhancement of the figure of merit (FOM)

At several different mechanisms that operate in a well-designed NFT for enhancing the FOM are described. These proposes the mechanisms of FOM enhancement either the peak $|E|^2$ intensity in the medium or the dissipated power in the medium. Three major mechanisms are proposed; localized surface plasmon resonance (LSPR), Surface Plasmon Polaritons (SPPs), and the lightning rod effect.

2.2.1 Localized Surface Plasmon Resonance

LSP is non-propagating excitations of the conduction electrons coupled to the electromagnetic field. For a spherical nanoparticle, the curved surface of the nanoparticle exerts a restoring force on the electrons to result in a resonance. This resonance is called a localized surface plasmon resonance (LSPR) or in short localized Plasmon resonance as shown in figure 2.1. It is concluded that these modes arise naturally from scattering problem of the small, subwavelength conductive nanoparticles in the oscillating EM field. This kind of resonance can be excited by direct light illumination, which is a consequence of the curved surface of the metal nanoparticles. As in surface plasmon resonance, the result can be a coherent localized plasmon oscillation with a resonant frequency that strongly depends on the composition, size, geometry, dielectric environment and separation distance of nano-particle (NPs) [40]. At resonance, the nanoparticles absorb the incident optical energy much more efficiently and generate enhanced electric fields at their surfaces from the oscillating surface charge. This resonance of gold and silver nanoparticles occurs in the visible region of the electromagnetic spectrum. As a consequence, the bright colors are

exhibited by the particles, both in transmitted and reflected light, due to resonantly enhanced absorption and scattering [41, 42].
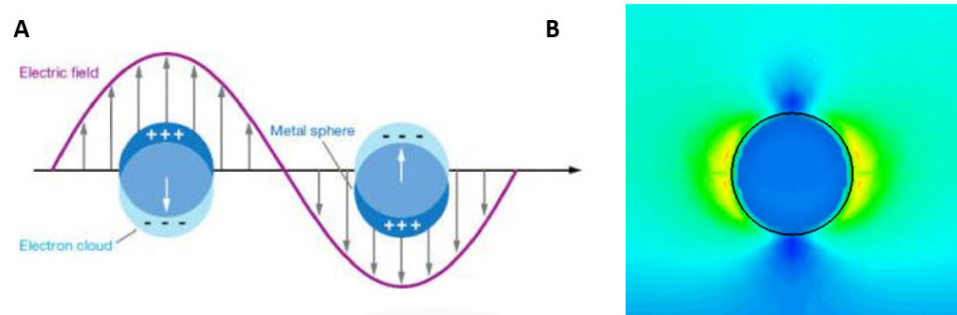
Figure 2.1 (A) Diagram of resonating of Localized Surface Plasmon

(B) Simulation of Localized Surface Plasmon Resonance by CST [41, 42].

2.2.2 Surface Plasmon Polaritons (SPPs)

SPPs is an excitation of a coupled state between photons and plasma oscillations at the interface between a metal and a dielectric or they are surface charge density wave which propagate along the interface between metal and dielectric media with confinement below the diffraction limit. They are excited by the coupling of the electromagnetic field of the light wave and the oscillations of free electrons in the metal [41-42]. SPPs are confined strongly to the surface of the metal and can be squeezed into very small volumes (d); $d \ll \lambda$.

To investigate the physical background properties of SPPs [44, 45], Maxwell's equation (2.2) are applied to the flat interface between a conductor and a dielectric by using the general of wave equation. The absence external charge and current densities which is represented by the curl equation can be combined to yield

$$\nabla \times \nabla \times E = -\mu_0 \frac{\partial^2 D}{\partial t^2} \tag{2.2}$$

Using the identities $\nabla \times \nabla \times E \equiv \nabla(\nabla \cdot E) - \nabla^2 E$ as well as $\nabla \cdot (\varepsilon E) \equiv E \cdot \nabla \varepsilon + \varepsilon \nabla \cdot E$, due to the absence of external stimuli $\nabla \cdot D = 0$, so equation (2.2) can be rewritten as

$$\nabla\left(-\frac{1}{\varepsilon}\mathrm{E}\cdot\nabla\varepsilon\right)-\nabla^2\mathrm{E}=\mu_0\varepsilon_0\varepsilon\frac{\partial^2\mathrm{E}}{\partial t^2} \qquad (2.3)$$

This simplifies to the central equation of the electromagnetic wave theory, it can be negligible the variation of the dielectric profile $\varepsilon = \varepsilon(r)$ over distances on the order of one optical wavelength in (2.3),

$$\nabla^2\mathrm{E}-\frac{\varepsilon}{c^2}\frac{\partial^2\mathrm{E}}{\partial t^2}=0. \qquad (2.4)$$

To descript the confined propagating waves, this equation has been solved separately and assume in all generality a harmonic time dependence $\mathrm{E}(r,t) = \mathrm{E}(r)e^{-i\omega t}$ of the electric field in (2.4), this yield

$$\nabla^2\mathrm{E}+k_0^2\varepsilon\mathrm{E}=0,. \qquad (2.5)$$

where $k_0 = \frac{\omega}{c}$ is the wave vector of the propagating wave in vcuum.

In this, the propagation geometry is defined as the waves propagate along the x-direction of a Cartesian coordinate system, and show no spatial variation in the perpendicular, in-plane y-direction (see in figure 2.2 A). Therefore $\varepsilon = \varepsilon(z)$. So the propagating waves, can be written as $\mathrm{E}(x,y,z) = \mathrm{E}(z)e^{i\beta x}$. The $\beta = k_x$ is called the propagation constant of the traveling wave. So (2.5) can be expressed in the desired form of the wave equation

$$\frac{\partial^2\mathrm{E}(z)}{\partial z^2}+(k_0^2\varepsilon-\beta^2)\mathrm{E}=0.. \qquad (2.6)$$

Next, in order to use the wave equation for determining the spatial field profile and dispersion of propagating waves, the explicit expression for the different field components of E and H are required. Further, the curl equations are used to express this. It is set in the transverse magnetic (TM or p) mode, where only the field component E_x, E_z, and H_y are nonzero. Then E_x, E_z are obtained and the wave equation for TM modes are

$$\frac{\partial^2 E(z)}{\partial z^2} + (k_0^2 \varepsilon - \beta^2)E = 0.. \tag{2.6}$$

$$E_x = -i\frac{1}{\omega\varepsilon_0\varepsilon}\frac{\partial H_y}{\partial z} \tag{2.7}$$

$$E_z = -i\frac{\beta}{\omega\varepsilon_0\varepsilon}H_y \tag{2.8}$$

$$\frac{\partial^2 H_y}{\partial z^2} + (k_0^2 \varepsilon - \beta^2)H_y = 0. \tag{2.9}$$

For the SPPs at a single interface, the simplest feature of sustaining SPPs is that of a single, flat interface between a dielectric, non-absorbing half space (z > 0) with positive real dielectric constant ε_2 and an adjacent conducting half space (z < 0) described via a dielectric function $\varepsilon_1(\omega)$ as shown in figure 2.2(Left) [44] that schematic representation of the semi-infinite single interface system showing the two material half spaces (*n1* & *n2*) and the chosen orientation of the Cartesian coordinate system. This section shows the propagating wave solutions confined to the interface with evanescent decay in the perpendicular *z*-direction as shown in figure 2.2 (Right) that a schematic of a continuous wave SPP excited at the interface between a metal and a dielectric. A snapshot of the surface charges, electric field lines and electric field intensity distribution perpendicular to the surface are depicted [45].
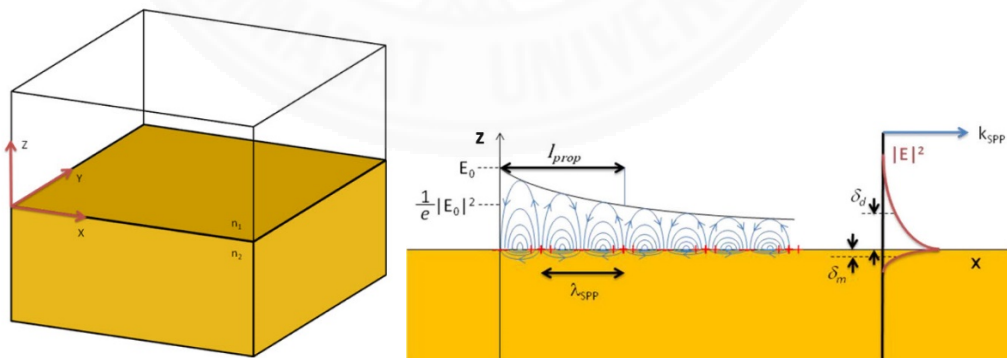
Figure 2.2 The schematic of the SPP excited at the interface between a metal and a dielectric [45].

For TM mode at *z* > 0, it can be expressed

$$H_y(z) = A_2 e^{i\beta x}e^{-k_2 z} \tag{2.10}$$

$$E_x(z) = iA_2 \frac{1}{\omega\varepsilon_0\varepsilon_2} k_2 e^{i\beta x} e^{-k_2 z} \tag{2.11}$$

$$E_z(z) = -A_1 \frac{\beta}{\omega\varepsilon_0\varepsilon_2} e^{i\beta x} e^{-k_2 z} \tag{2.12}$$

For $z < 0$,

$$H_y(z) = A_1 e^{i\beta x} e^{k_1 z} \tag{2.13}$$

$$E_x(z) = -iA_1 \frac{1}{\omega\varepsilon_0\varepsilon_1} k_1 e^{i\beta x} e^{k_1 z} \tag{2.14}$$

$$E_z(z) = -A_1 \frac{\beta}{\omega\varepsilon_0\varepsilon_1} e^{i\beta x} e^{k_1 z} \tag{2.15}$$

where $k_i \equiv k_{z,i} (i = 1, 2)$ is the component of the wave vector perpendicular to the interface in two media. If $A_1 = A_2$, then

$$\frac{k_2}{k_1} = -\frac{\varepsilon_2}{\varepsilon_1}. \tag{2.16}$$

The expression for H_y further has to fulfill the wave equation (2.9), yielding

$$k_1^2 = \beta^2 - k_0^2\varepsilon_1 \tag{2.17}$$
$$k_2^2 = \beta^2 - k_0^2\varepsilon_2. \tag{2.18}$$

Combining this and (2.16), the dispersion relation of SPPs propagating at the interface between the two half spaces as express

$$\beta = k_0 \sqrt{\frac{\varepsilon_1\varepsilon_2}{\varepsilon_1 + \varepsilon_2}} \tag{2.19}$$

The k_{spp} in x-direction is

$$k_{spp} = \frac{\omega}{c} \sqrt{\frac{\varepsilon_1\varepsilon_2}{\varepsilon_1+\varepsilon_2}} \tag{2.20}$$

and given the $\lambda_{spp} = \frac{2\pi}{k_{spp}}$ then, $\quad \lambda_{spp} = \lambda_0 \sqrt{\frac{\varepsilon_1+\varepsilon_2}{\varepsilon_1\varepsilon_2}}$. $\tag{2.21}$

For large wave vectors, the frequency of the SPP approaches the characteristic surface plasma frequency

$$\omega_{sp} = \frac{\omega_p}{\sqrt{1+\varepsilon_2}} \tag{2.22}$$

where ω_p is plasma frequency.

2.2.3 Lightning Rod Effect

The lightning rod effect refers to the well-known fact that sharp metallic objects tend to generate very large localized fields. Electric field lines must terminate normally to the surface of a perfect conductor. This effect tends to concentrate the field lines at any sharp points of highly conducting materials. This is a shaping effect, not a resonance effect, and therefore does not have any particular wavelength dependence. It may or may not be associated with a LSPR. The lightning rod effect can generate extremely large field enhancements [3].
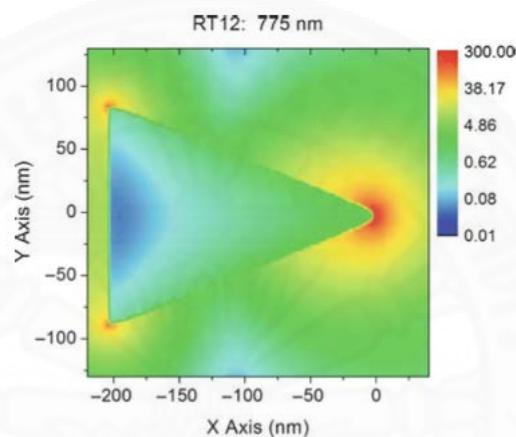
Figure 2.3 Local field intensity for a gold triangle antenna (lightning rod effect) [3].

2.3 Literature review of the near field transducer

A variety of approaching development of NFT that can efficiently deliver light into a recording medium in a region which is smaller than the diffraction limit has been proposed. Many plasmatic structures for supporting the LSPs, SPPs, and Lighting Rod are developed. The NFT usually makes use of the standard geometry of antennas or aperture antenna as shown figure 2.4 and 2.5.
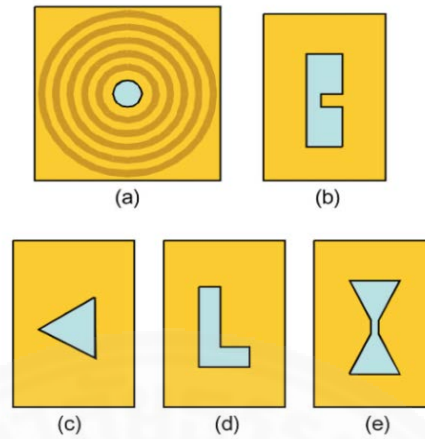
Figure 2.4 NFT aperture shapes: (a) circular hole surrounding by concentric grooves, (b) C aperture, (c) triangular aperture, (d) L aperture, and (e) bow-tie aperture [8].
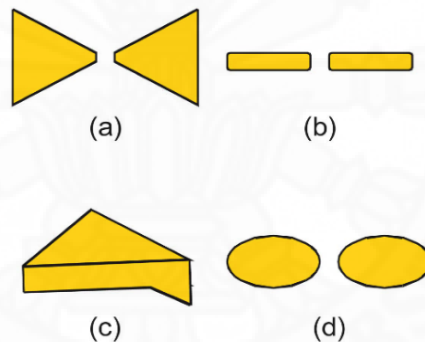
Figure 2.5 Antenna designs proposed for NFTs, including (a) the bow-tie, (b) dual nanowires, (c) the beaked triangle, and (d) dual ellipses [8].

To measure the NFT performance, The FOMs result is the field intensity, are shown in figure 2.6 and the summary of NFT performance, the peak intensity, the percent dissipated power, and the spot size are shown in table 2.1.
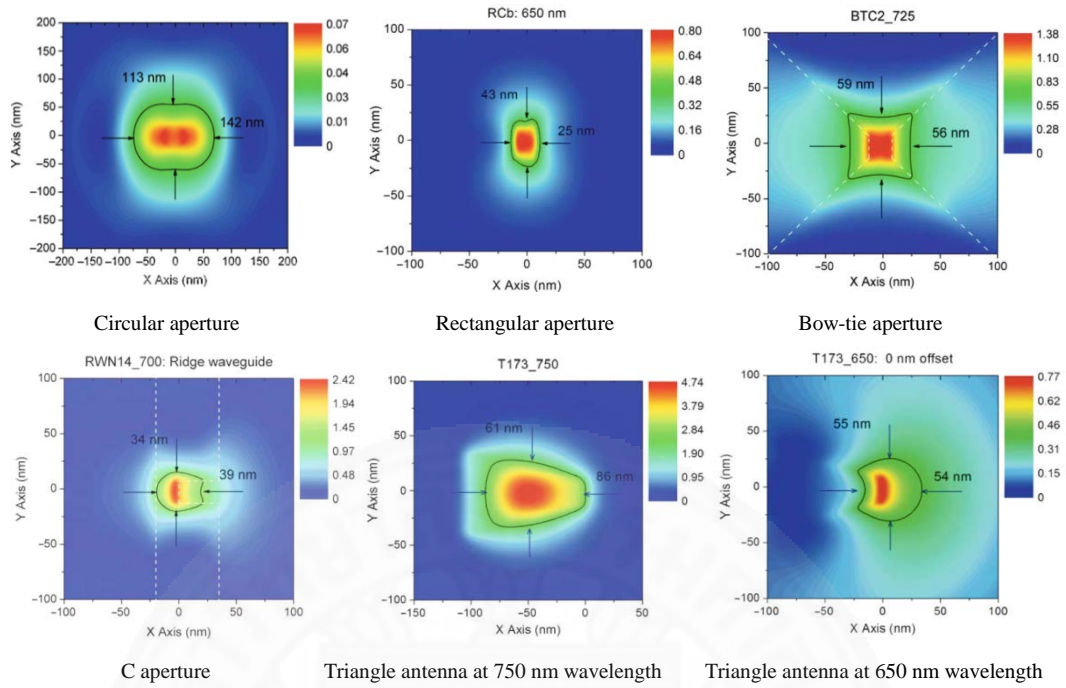
Figure 2.6 Field intensity within the recording medium of various NFT shapes [3].
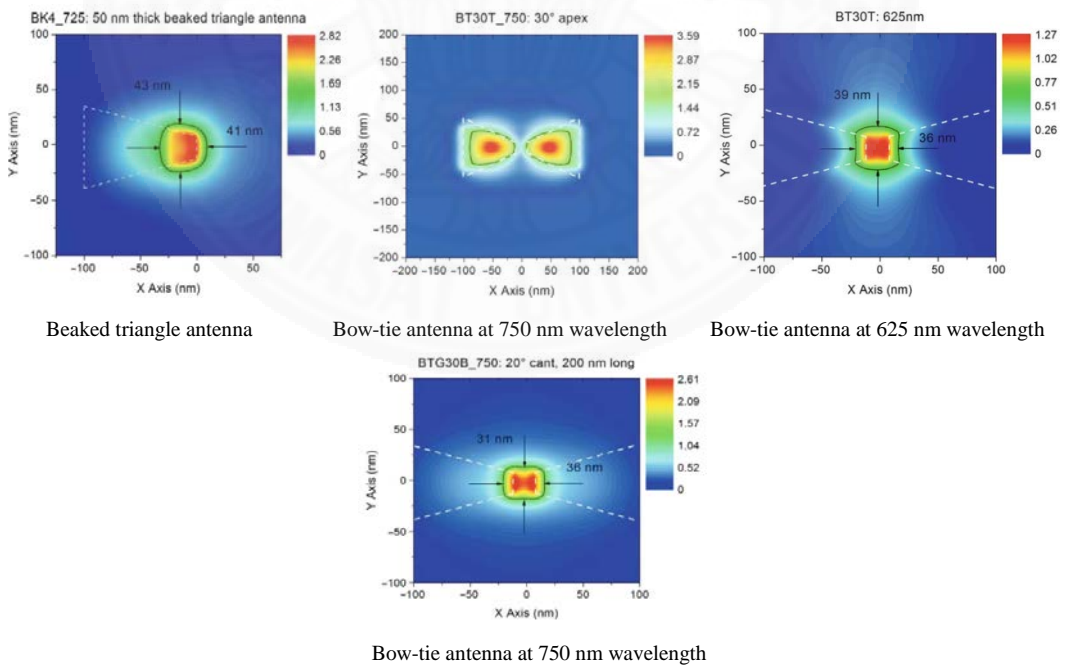
Figure 2.7 Field intensity within the recording medium of various NFT shapes [3].

Table 2.1 Summary of NFT performance. The peak intensity is normalized by that of the incident beam [3].

NFT design	λ_{res}	Peak $|E|^2$	Coupling efficiency	FWHM spot size (nm^2)
Circular aperture	650	0.07	0.14%	113 x 142
Rectangular aperture	650	0.80	0.92%	43 x 25
Bow-tie aperture	725	1.38	1.7	59 x 56
C aperture	700	2.42	2.1	34 x 39
Triangle antenna	650	0.77	1.1	55 x 54
Beaked triangle	725	2.82	2.9	43 x 41
Bow-tie antenna	650	1.41	1.4	39 x 36
Canted bow tie	750	2.61	2.1	31 x 36

FWHM full width at half maximum

For field enhancement of HAMR system, the high-power coupling efficiency with small dissipated power density and a sub diffraction limit spot of NFT are required. To achieve this target, an efficient NFT should make use of the SPPs effect. This effect requires a metallic surface that is highly conductive at optical frequencies such as gold, silver, and aluminum, etc. At present, gold is widely used as the NFT material because of its chemical stability, melting point that is much greater than the Curie point of popular recording medium, and high thermal conductivity [35]. However, it is high loss energy in metal medium due to the strong absorption of metal in the visible or near-infrared spectrum. Recently, there is a significant interest in searching for alternative low-loss plasmonic materials [46-51]. For optimization of the NFT design for the greatest field enhancement, several structures have been proposed for LSP and SPPs optimization including MIM waveguide that the papers are organized as followed;

2.3.1 Heat-assisted magnetic recording by near-field transducer with efficient optical energy transfer

In [36], the work was optimized near-field transducer design. An NFT has been designed, that can efficiently transfer optical energy into an absorptive medium in a much smaller region than the diffraction limit. Surface plasmon is collective oscillations of surface charge that is confined to an interface between a dielectric and a metal. It shows that optical energy can be transferred efficiently to metallic medium and yet remains confined in a spot that is much smaller than the diffraction limit. Such a transducer was integrated into a recording head and flown over a magnetic recording medium on a rotating disk. Optical power from a semiconductor laser at a wavelength of 830 nm was efficiently coupled by the transducer into the medium to heat a 70-nm track above the Curie point in nanoseconds and record data at an areal density of 375 Tb/in.[2].

2.3.2 Fluorescence enhancement by a two-dimensional dielectric annular Bragg resonant cavity

In this work [52], they showed that the photons can be efficiently extracted from fluorescent molecules, utilizing the strongly enhanced local field of a two- dimensional dielectric annular Bragg resonant cavity. Due to the diffraction and constructive interference together with the annular focusing, the periodic ring structure converts the normal incident light into planar guided modes and forms a hot spot at the center of the structure. Theoretically, the field can be enhanced more than 40 times, which leads to the averaged 20- fold enhancement of the fluorescence signal observed in experiments. Compared with fluorescence enhancement by plasmonic structures, this dielectric approach does not suffer from pronounced quenching that often occurs near metallic structures. These results not only can be applied as ultrasensitive sensors for various biological systems, but also have broad potential applications, such as optical trapping and fluorescent microscopy. Figure 2.7 (Left) shows the schematic of the annular Bragg resonator. The perpendicular incident waves are converted to in-plane resonant guided modes and focused at the center of the cavity. Consequently, fluorescence emission is enhanced. (Right) shows the distribution of the electric field in the cavity at the wavelength of 640 nm [52].
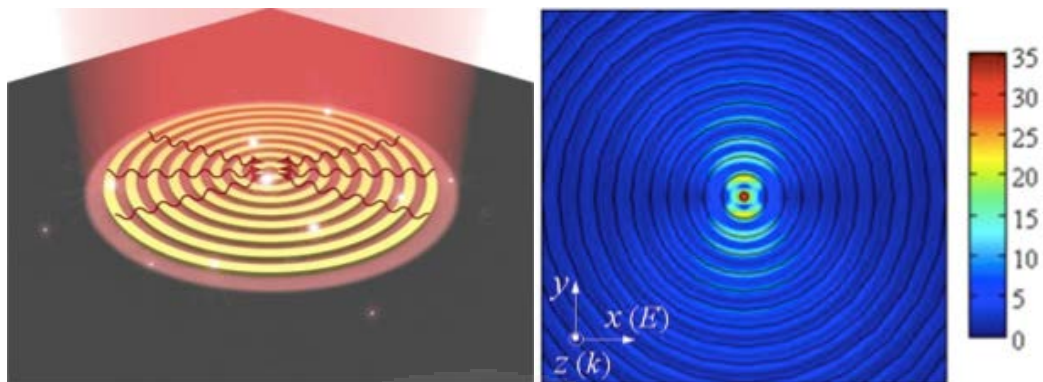
Figure 2.8 The schematic of the annular Bragg resonator and E-field in the cavity [52].

2.3.3 A smooth optical superlens

In this work [53], they demonstrate a smooth and low loss silver (Ag) optical superlens capable of resolving features at $1/12^{th}$ of the illumination wavelength with high fidelity. This is made possible by utilizing state-of-the-art nano imprint technology and intermediate wetting layer of germanium (Ge) for the growth of flat silver films with surface roughness at sub nanometer scales. The measurement of the resolved lines of 30 nm half-pitch shows a full-width at half-maximum better than 37 nm, in excellent agreement with theoretical predictions. The development of this unique optical superlens leads promise to parallel imaging and nanofabrication in a single snapshot.
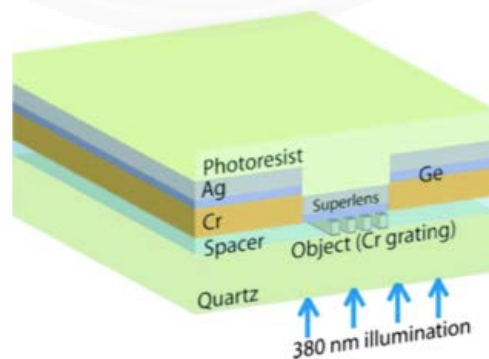
Figure 2.9 Schematic drawing of a smooth silver superlens [53].

2.3.4 Gold helix photonic metamaterials: A numerical parameter study

In [54], it describes metamaterials composed of three-dimensional gold helices periodically arranged on a square lattice can be used as compact "thin-film" circular polarizes with one octave bandwidth. The physics of the motif of these artificial crystals is closely related to that of microwave sub-wavelength helical antennas in end-fire geometry. Here, it systematically studies the dependence of the metamaterials with chiral optical properties on helix pitch, helix radius, two-dimensional lattice constant, wire radius, number of helix pitches, and angle of incidence. Their numerical calculations show that the optical properties are governed by resonances of the individual helices yet modified by interaction effects. Furthermore, their study shows the possibilities and limitations regarding performance optimization.

2.3.5 Relationship Between Near Field Optical Transducer Laser Absorption and Its Efficiency

In this study [55], a C-aperture is used as the transducer. Geometry simulation includes transducer dimension, Optical model, Granular medium geometry laser wavelength for evaluation. The temperature rise of the transducer is one of the reasons that lead to its failure. In this paper, the laser absorption of the transducer is investigated compared with the transducer efficiency (high efficiency is one of the main targets in the transducer design). The results show that with a fixed medium and fix transducer material high efficiency is always accompanied by high laser absorption that could be 10-25%. Optimizing the media properties and using transducer material with low refractive index can obtain high efficiency and low absorption. With the built HAMR head model, the transducer temperature rise is evaluated. The results show that the increasing temperature of the transducer depends on the absorbed power, its size, and the space between the transducer and magnetic pole. The space affects the transducer temperature rise more seriously in large transducer size.

2.3.6 The integration of Grating-Nano slot Probe Tip for Near-field Subwavelength Light Confinement and Fluorescent Sensing

In this work [56], they demonstrate a near-field sub-wavelength light confinement probe tip comprised of compact embedded metallic focus grating (CEMFG) coupler and photonic crystal (PhC) based λ/4 nano-slot tip, in terms of its far-field radiation directivity and near-field sub-wavelength light enhancement. The embedded metallic grating coupler increases the free space coupling at a tilted coupling angle of 25° with over 280 times light intensity enhancement for 10 μm coupler size. Further, 20 nm air slot embedded in single line defect PhC waveguide are designed, using the impedance matching concept of the λ/4 air rod, to form the TE mode light wave resonance right at the probe tip aperture opening. This leads to the light beam spot size reduction down to λ/20. The near-field center peak intensity is enhanced by 4.2 times from that of the rectangular waveguide input, with the total enhancement factor of 1,185 from free space laser source intensity. The near-field fluorescence excitation and detection also demonstrate its single molecular enhanced fluorescence measurement capability.
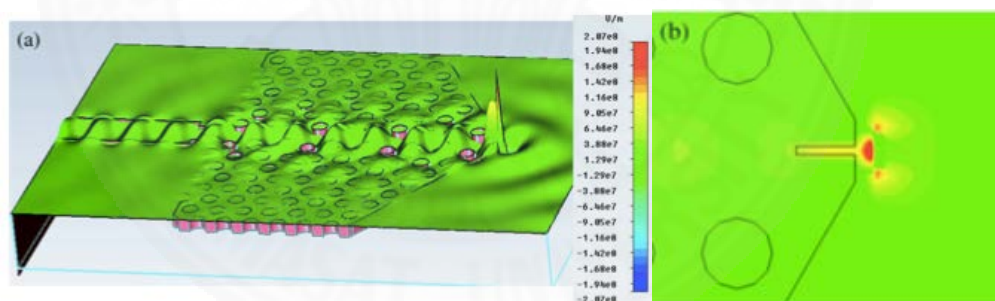
Figure 2.10 The distribution plots on the *xy* center (a) 3-D surface plot on center *xy* cross plane. (b) Close up plot of |*Ey*| amplitude around probe tip aperture on the *xy* cross plane [56].

2.3.7 A Highly Efficient On-chip 3D Plasmonic Nano-focusing Structure

In [57], Choo and et al. proposed a significant concept of on-chip 3D MIM NPC which realized highly efficient focusing of light into a deep sub-wavelength spatial scale [11]. They demonstrated experimentally the achievement of highly efficient nano-focusing in an Au– SiO$_2$ –Au gap plasmon waveguide using a carefully

engineered three-dimensional taper. The dimensions of the SiO_2 layer, perpendicular to the direction of wave propagation, linear taper below 100 nm. The simulations suggest that the three-dimensional with the linear-tapering approach could focus 830 nm light into a 2×5 nm^2 area with ≤3 dB loss and an intensity enhancement of 3.0×10^4. In a two-photon luminescence measurement, our device achieved an intensity enhancement of 400 within a 14×80 nm^2 areas, and a transmittance of 74%.
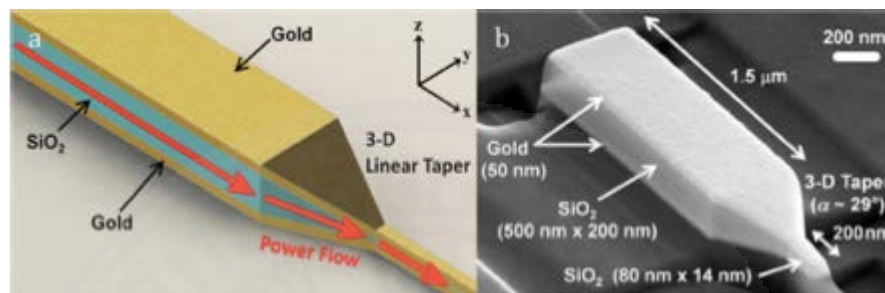
Figure 2.11 (a) Schematic illustration of a 3D NPC structure. (b) SEM image of a 3D NPC structure [57].

Figure 2.12 Cross-sectional side views of the E^2 profiles along the *y–z* plane for *h* = 200, 100, 50, and 10 nm, respectively [57].

As the literature review, the low coupling efficiency in a HAMR system indicates an impedance mismatch between NFT and the media are found, anyway the tapered MIM waveguide design turns out to have a very large impedance that better matches the load and thus outperforms the lollipop and the E-antenna [9]. An optimization of the media that the maximum coupling efficiency is achieved when the resistance (real part of the impedance) of the plasmonic waveguide matches that of the load [58]. Further, the smallest nano-focusing is based on the plasmonic MIM

waveguide structure are found, but the manufacturing of them has a direct impact on the manufacturing requirements because it is a difficult process when integrated with the HAMR.

For fabrication technique of MIM waveguide with a linear taper, Choo and et al. demonstrated an Au-SiO$_2$-Au SPP waveguide with a three-dimensional linear taper and numerically found the optimum taper angle to be 20 deg. Vertical tapers with angles as large as 15-30 deg. were realized by employing an electron-beam-induced deposition (EBID) technique of SiO$_2$. However, EBID has an extremely small throughput and is difficult to apply to mass-production, because the SiO$_2$ layer is piled up by repeatedly scanning a single electron beam. In addition, the minimum thickness of the SiO$_2$ layer remained 14 nm due to the insufficient deposition resolution, although sub-10 nm thickness is required for intensity enhancement higher than 10^3 [57].

Vertical tapers have been important structures for spot size converters which are used to connect optical fibers and planar optical integrated circuits. Numbers of mass-productive techniques to fabricate vertical tapers have been proposed such as the wet etching of a substrate masked with photoresist with controlled dip speed [59], gray-tone photolithography followed by dry etching [60], dry etching using a shadow mask [61], and an anisotropic wet etching using the deflection of crystal orientation [62]. However, taper angles realized by these techniques are very small: typically < 0.1 deg. and only 4 deg. at most. These taper angles are too small for 3D NPCs.

In order to solve the manufacturing of MIM waveguide problem, this dissertation proposal proposes the fabrication of the linear tapered MIM waveguides with angles as large as 20 deg. by an efficient, mass-productive process based on standard dry etching technique by employing a mixed gas for taper fabrication and the realization of an ultra-thin waveguide by the thin film addition following the taper process. Furthermore, although, the MIM waveguide has superior lateral confinement because of the relatively shallow field penetration into the metal claddings (about a skin depth usually tens of nanometers). However, the loss in the MIM waveguide is substantial due to the strong absorption of metal in the visible or near-infrared spectrum. Therefore, the design, simulation, and measurement of the loss in the MIM waveguide are critically important in the development of SPPs-based nano-focusing [63]. Therefore, to improve the coupling efficiency of the NFT based on MIM waveguide by

using metamaterial are focused. In metamaterial properties such as negative permeability (ε), permittivity (μ), reflective index (n), and localize surface plasmon (LSP) resonance could help to overcome the diffraction limit, by modify the properties with designing them using engineering techniques. The detail of metamaterial will be shown in the next section.

2.4 Introduction to Metamaterials

Metamaterial are a class of composite materials fabricated to obtain unusual electromagnetic properties such as the electric field (E), the magnetic field (H) and the wave vector (k) of an electromagnetic wave propagating in its form a left-handed system that are not found in nature. The nonmetallic structure of metamaterial acts like artificial atoms that can be coupled to both the electric and magnetic field components of electromagnetic waves, leading to novel optical properties [64]. Compared with conventional materials, the negative refraction of metamaterial occurs because the phase velocity of the light propagating inside metamaterial is pointed in the opposite direction to the energy flow. The composite of the metamaterials is natural materials with different shapes or structures. The developments in structured electromagnetic materials have given rise to negative refractive index materials.

In 1968 V.G. Veselago proposed the first idea of metamaterial with negative permittivity (ε) and permeability (μ) [65]. Negative index of refraction is achieved when at the same frequency,

$$\varepsilon(\omega) < 0, \text{and } \mu(\omega) < 0 \tag{2.23}$$

Using Maxwell's equations to calculate the index of refraction gives,

$$n = \pm\sqrt{\varepsilon\mu} \tag{2.24}$$

and conventional materials take the positive sign. V. G. Veselago showed that, if the condition (2.24) is met, the negative sign for n is the one that satisfies causality.

For the experiment, in 1996, J.B. Pendry and et al. [66] reported the experiment results of negative permittivity by using the array of wires and in 1999, J.B. Pendry and et al. [67] also reported the negative permeability by using an array of split

ring resonators. Next, in 2000, D.R. Smith and et al. [68] went on to manufacture the first negative refraction index metamaterial made by combining a negative permittivity and a negative permeability. In such materials, the index of refraction is less than zero, the phase velocity and group velocity of an electromagnetic wave can propagate in opposite directions such that the direction of propagation is reversed with respect to the direction of energy flow. Further, the double fishnet metamaterial is reported about phase time and group velocity delay in 2006 by Gunnar Dolling and et al. [69]. They investigated the propagation of femtosecond laser pulses through a metamaterial which is the dispersion system for wavelengths around 1.5 micrometers. From the interference fringes of a Michelson interferometer with and without the sample, they directly inferred the phase time delay and determined the group time delay. In a spectral region, phase and group velocity are negative simultaneous. This means that both the carrier wave and the pulse envelope peak of the output pulse appear at the rear side of the sample before their input pulse counterparts have entered the front side of the sample.

In dispersion less system [70], the wave function is expressed in the form

$$\frac{\partial^2 \psi}{\partial t^2} = c^2 \frac{\partial^2 \psi}{\partial x^2}. \tag{2.25}$$

The solutions to this equation can be built up from exponential function,

$$\psi(x,t) = A e^{i(kx-\omega t)} \tag{2.26}$$

in (2.25), so this gives

$$\omega^2 = c^2 k^2. \tag{2.27}$$

This is called the dispersion relation. The velocity of the wave is $\frac{\omega}{k} = \pm c$, which is independent of ω and k and is the constant. For a sinusoidal wave sin(kx-ωt), the qualification phase is used for the speed of a single sinusoidal traveling wave. So, the phase velocity, v_p is given by $\frac{\omega}{k}$. If the v_p is not a constant value, that is, the speed of a wave depends on its ω and k value. Therefore, the determining of this is in the dispersion system that means waves with different frequencies move with different speeds. The speed of the wave is the group velocity, v_g which a wave packet moves and is not the same as the phase velocity. The v_g is given by the slope of the $\omega(k)$ curve [70].

$$v_g = \frac{d\omega}{dk} \qquad\qquad (2.28)$$

For large wave vectors, the group velocity $v_g \rightarrow 0$, this is corresponding to the wavelength $\lambda = \frac{2\pi}{k}$, the shorten wavelength are also obtained.

Although the MIM waveguide has superior lateral confinement. However, the loss in the MIM waveguide is high in the visible or near-infrared spectrum. Therefore, the design, simulation, and measurement of the loss in the MIM waveguide are important in the development of SPPs-based nano-focusing [63]. To enhance the coupling efficiency of the NFT, the NFT based on MIM and using fishnet metamaterial for improving the coupling efficiency for NFT will be interested, because the fishnet metamaterial in dispersive system can control the phase and group velocity or the slow light which is the main mechanism can improve the coupling efficiency of NFT. The detail of design concept and the methodology will be shown in the next chapter.

CHAPTER 3
RESEARCH METHODOLOGY

3.1 Concept design

Nano-focusing, a technique to concentrate light into deep sub-wavelength dimensions, is one of the major challenges in nanophotonics for nanoscale microscopy, nano-optical devices, nanolithography, and data storage [72, 73]. To achieve efficient nano-focusing, different metallic nanostructures with the linear-tapering designs have been proposed [74-75], based on the propagation of SPPs along metal/insulator interfaces [44, 78-79], especially the MIM plasmonic waveguide structure. In particular, on-chip three-dimensional nano-focusing components for nanoscale lasers, detectors, modulators, and heat-assisted magnetic recording heads have attracted attention [80].

Therefore, in my research which is field enhancement of near field transducer, the development of NFT based on 3D MIM structure for confining light on the deep sub-wavelength scale is proposed, in order to solve the manufacturing of MIM waveguide problem, the fabrication of the linear tapered MIM waveguides with a mass-productive process based on standard dry etching technique will be also proposed, and for improving the coupling efficiency, the employ the metamaterial for extracting the light source will be applied. The conceptual model is presented schematically in figure 3.1.

The model has three functional sections: (I) the metamaterial for extraction from the light source (II), and (III) a MIM–SPP waveguide with a linear taper and single hole. From this structure, the SPPs, wavelength and direction of light, and the spot size are designed.
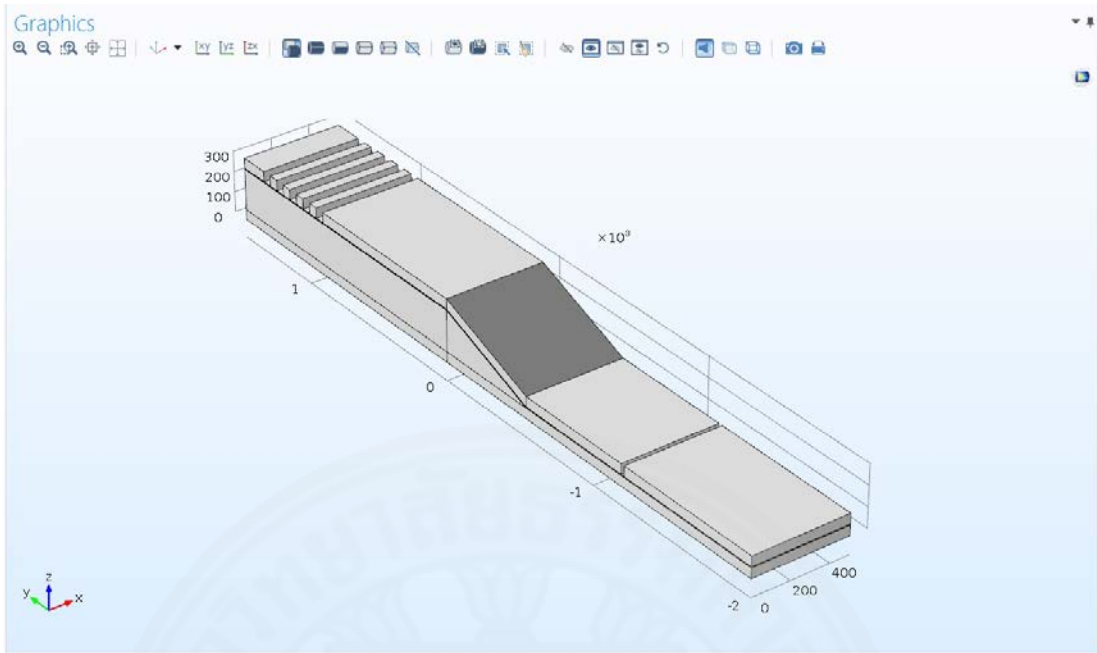
Figure 3.1 A schematic decomposition of a model concept of plasmonic light delivery mechanism which consists of three parts; light source extraction using metamaterial, intermediate guiding of light, and coupling of light into a focus in the tip.
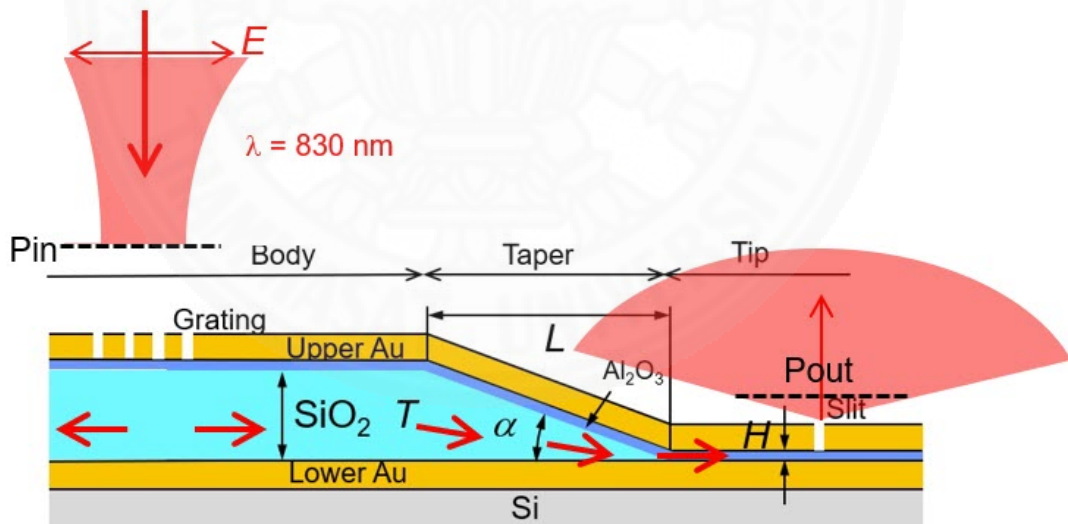
Figure 3.2 The geometry of the MIM-SPP waveguide with a linear taper composed of upper and lower Au layer with an insulator SiO_2 layer with an angle α at the taper section, the optical measurement strategy, Grating, Slit, P_{in}, and P_{out}.

The target structure of NFT based on a MIM waveguide with a linear taper, is presented schematically in figure 3.1 and 3.2. The configuration includes an upper and a lower Au layer with an intermediate SiO_2 layer which consists of three sections;

the body with a thickness T, the taper with a length L and a taper angle α, and the tip sections with a thickness H. The front of the structure will be dry etched for making the metamaterial, grating, for extracting the light source. This SPP mode is suitable for nano-focusing applications because its profile scales down with the size of the MIM cross-section and a highly localized hot spot inside the sub-100 nm scale waveguide. Not only the field of the fundamental anti-symmetric MIM-SPP mode can be focused down to a deep sub-wavelength space because they achieve very large wave-vectors and effective refractive indices, but also losses due to scattering and absorption in a 3D tapered MIM plasmonic waveguide. The single hole in the tip is provided for the light delivery in the characterize process.

To maximize the filed confinement and the coupling efficiency into the small area, the structure dimension of model structure is designed by running a series of finite element method (FEM) simulation using COMSOL software. For the simulation, the simulation are separated into three parts; (I) a MIM waveguide with a linear taper, for studying the SPPs phenomenal and to overcome the diffraction limit and to get the small spot size (II) the grating in body part design optimization, (III) the single hole in the tip part design optimization, for extracting the light source, improve the NFT performance, and Characterization preparation. This is advanced toward the concept design in the fourth simulation (IV), the integrated NFT of a MIM waveguide with a linear taper and the metamaterial.

3.2 Methodologies

To maximize the filed confinement and the coupling efficiency into the small area, the model structure are designed by running a series of finite element method (FEM) simulation using COMSOL software and preliminary fabrication both metamaterial and the waveguide with a taper for finding the feasibility and confirm the fabrication processes and check how much precisely dimension of specimens by SEM and TEM observation. The next step is to improve the structure and do the final specimen parallel with optical measurement and re-design for improving until the final specimen is optimized. The research methodologies are shown in the diagram as figure 3.3.
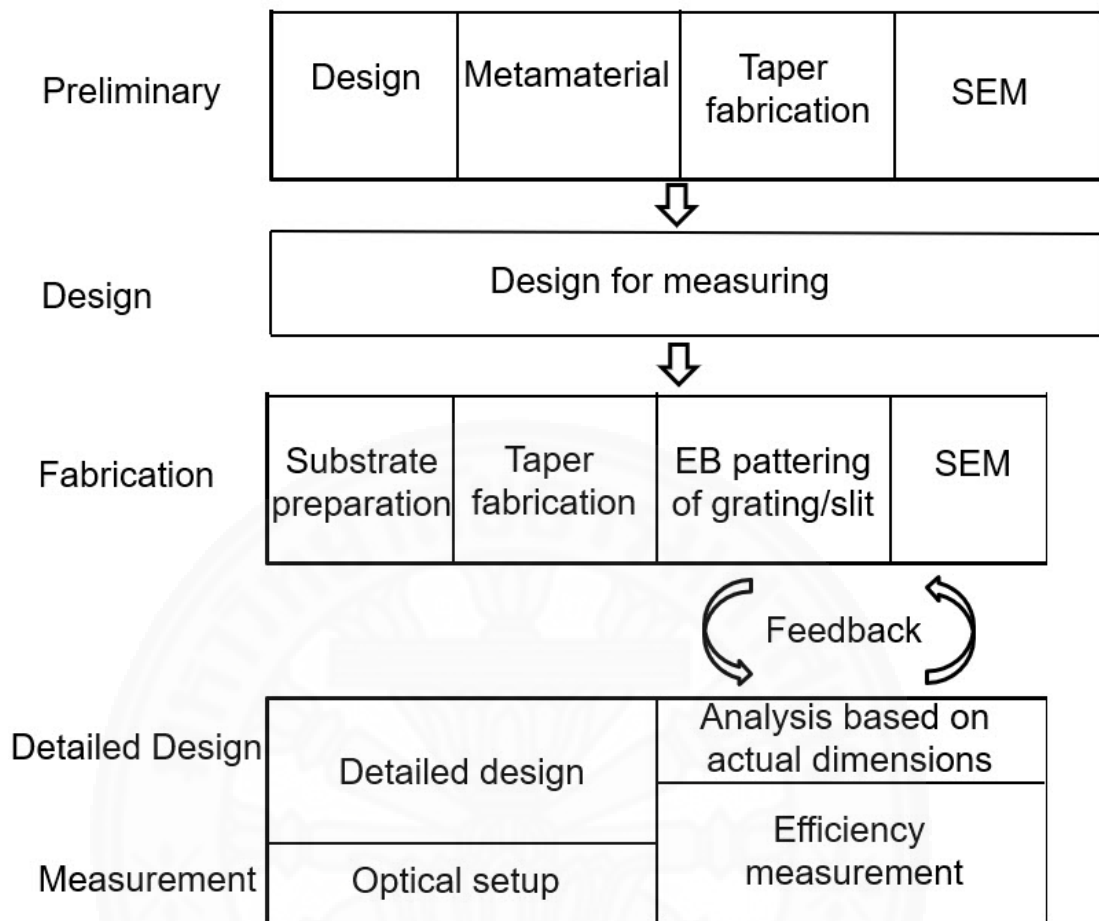
Figure 3.3 The research methodology flow chart.

3.2.1 Simulation Strategy

For preliminary simulation, to understand the MIM waveguide and the confinement, a two-dimensional structure is simulated. First, to compare the simulation results and analytical results. Next, to compare the MIM waveguide efficiency between Choo's paper [57] and our structure with a different material in order to investigate the influence of different material. The next simulation is separated into three parts; (I) a MIM waveguide with a linear taper, for studying the SPPs phenomenal and to overcome the diffraction limit and to get the small spot size (II) the grating in body part design optimization, (III) the single hole in the tip part design optimization, for extracting the light source, improve the NFT performance, and

Characterization preparation. This is advanced toward the concept design in the fourth simulation (IV), the integrated NFT of a MIM waveguide with a linear taper and the metamaterial. After that the fabrication results will measure and will improve the design and re-fabricate over again until the final specimen is optimized.

3.2.2 Fabrication strategy

For the fabrication, the feasibility of the MIM waveguide with the linear taper and metamaterial is investigated, then the final fabrication process and the final model structure with the light input/output ports and fabricate nano-focusing tapers with various taper angles are re-designed. To compare the efficiency of the several taper angles and find the optimum taper angle to apply in the HAMR. For the fabrication process, the specimens are fabricated which based on Lift-off technique [86], Electron beam lithography [87], and dry etching [88]. The detail of fabrication process will be shown in the next chapter.

3.2.3 Characterization strategy

For the characterization part, the feasibility of measurement is studied, because the signal output is too small and the SPP propagated suddenly decays when the observe point is far from the input area. The pre-observation of the pre-final specimen are measured and then the optimized position between the grating (input) and slit (output) is forecasted. The detail of the optical setup will be shown in the characterization chapter.

3.3 Preliminary Simulation of the MIM waveguide with the liner taper

For simulation, two important parameters of waveguide efficiency are computed; the coupling efficiency and the power enhancement. The nano-focusing is very correctly described "light intensity/amplitude enhancement" ("amplitude" here usually means the amplitude of the electric field). Two choices in discussing the enhancement factors are: intensity enhancement or electric field amplitude enhancement. The relationship between the electric field amplitude and the intensity, that is

$$I = \frac{n|E|^2}{2\eta_0} \tag{3.1}$$

where I [W/m^2] is the intensity, E [V/m] is the electric field amplitude, n is the refractive index of a material (here, the material is the dielectric layer), $\eta_0 = (\mu_0/\varepsilon_0)^{1/2}$ = 377 Ω is the impedance of the free space, μ_0 is the permeability of a vacuum, ε_0 is the permittivity of a vacuum. This "intensity" has the same meaning as all of "Poynting vector", "power density", "time-averaged power flow" and "power flux". The intense enhancement of the structure is, in short, the ratio of the profile curves of P_{out}/P_{in} as shown in figure 3.3 and P_T/P_B as shown in figure 3.4. Therefore, the intensity should be measured by selecting the maximum point at each cross section.
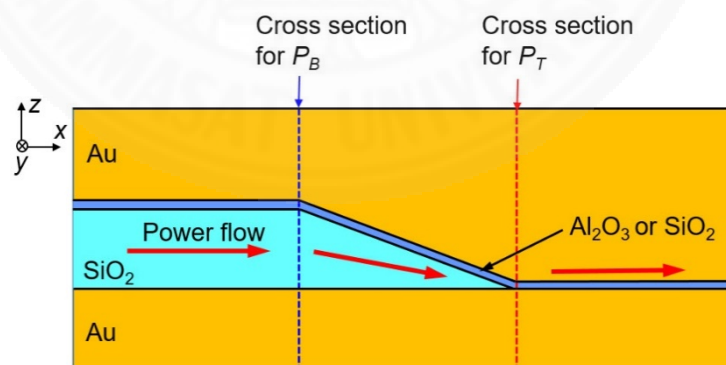
Figure 3.4 A two-dimensional Gaussian beam is incident on the left edge. To evaluate the coupling efficiency of the linear taper, power flow at two cross sections is monitored.

For the coupling efficiency, it is defined as the ratio of the x components of the total Poynting vectors, P_B and P_T, integrated over the cross sections just before and after the taper section, as shown in Fig. 3. The coupling efficiency is

$$\frac{P_T}{P_B} = \frac{I_T}{I_B} = \frac{n_{Al2O3}|E|^2}{2\eta_0} \; x \; \frac{2\eta_0}{n_{sio2+Al2O3}|E|^2} \tag{3.2}$$

In COMSOL software, the power flow through the ports is represented in term of S-parameters. The definition of the S-parameters in terms of the power flow is

$$S_{11} = \sqrt{\frac{Power\ reflected\ from\ port\ 1}{Power\ incident\ on\ port\ 1}} \tag{3.3}$$

$$S_{21} = \sqrt{\frac{Power\ reflected\ from\ port\ 2}{Power\ incident\ on\ port\ 1}} \tag{3.4}$$

The fields E_1 and E_2 should be normalized such that they represent the same power flow through the respective ports. The power flow is given by the time-average Poynting vector,

$$S_{av} = \frac{1}{2} Re(E \; x \; H^*) \tag{3.5}$$

The amount of power flowing out of a port is given by the normal component of the Poynting vector,

$$n \cdot S_{av} = n \cdot \frac{1}{2} Re(E \; x \; H^*) \tag{3.6}$$

The calculation in the model, the incidence of a z-polarized two-dimensional Gaussian beam propagating in the x direction with a wavelength of 830 nm was assumed to excite the TM-polarized guided SPP mode. So, for TM waves it holds that

$$H = \frac{1}{Z_{TM}} (n \; x \; E) \tag{3.7}$$

Where Z_{TM} is the wave impedance. Then the power becomes

$$n \cdot S_{av} = n \cdot \frac{1}{2} Re(E \; x \; H^*) = \frac{1}{2Z_{TM}} (n \cdot Re(E \; x(n \; x \; E^*)))$$

$$= \frac{1}{2Z_{TM}} |n \; x \; E|^2. \tag{3.8}$$

3.3.1 Simulation: To understand the MIM waveguide with a linear taper

In this section, the design and fabrication of a hybrid metal-insulator-metal (MIM) plasmon waveguide with a linear taper is presented. The target structure, a MIM waveguide with a linear taper, is presented schematically in figure 3.5 [57]. The configuration includes an upper and a lower Au layers with an intermediate SiO_2 layer which consists of three sections; the body with a thickness T, the taper with a length L and a taper angle α, and the tip sections with a thickness H.
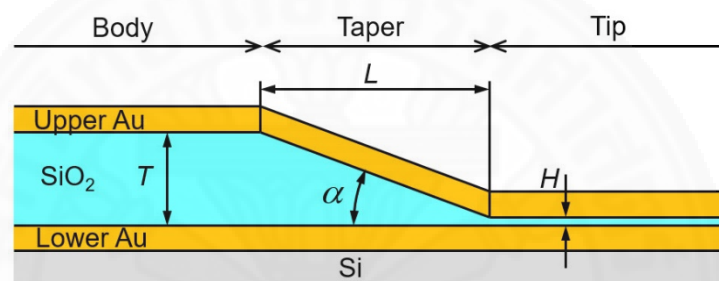
Figure 3.5 The geometry of the MIM-SPP waveguide with a linear taper composed of upper and lower Au layer with an insulator SiO_2 layer with an angle α at the taper section. [57].

To understand the MIM waveguide and the confinement, a 2D structure of MIM-SPP waveguide with a linear taper is used for simulation. The calculations are based on FEM. The simulation is two steps; 1) the comparison of the COMSOL results with analytical results and 2) to investigate the influence of the use of Al_2O_3 instead of SiO_2 as the ultra-thin dielectric film, the coupling efficiency. A linear tapered MIM waveguide made of only SiO_2 (ultra-thin SiO_2 film on a SiO_2 taper) and a hybrid one made of ultra-thin Al_2O_3 film on a SiO_2 taper were compared. For simulation condition, the incidence of a z-polarized two-dimensional Gaussian beam propagating in the x-direction with a wavelength of 830 nm was assumed [57] to excite the TM-polarized guided SPP mode. The Gaussian beam had a waist radius of 830 nm equal to the wavelength and was focused exactly on the entrance of the MIM waveguide. The

optical properties of Au and SiO$_2$ are the same values as those in Choo's work; the permittivity of Au and the refractive index of SiO$_2$ are -26.4 +1.65i and 1.45, respectively [57]. The refractive index of Al$_2$O$_3$ is 1.76 [89].

3.3.2 Analytical comparison

First, the comparison of the simulation results using COMSOL and analytical results is started. This comparison is based on Kurosawa's paper [79] that making a 2D straight MIM waveguide of SiO$_2$ as the insulator and hybrid MIM which is SiO$_2$ and Al$_2$O$_3$ as the insulator with T=100/30/10/3 nm. The geometry and parameters are set as shown in Fig 3.6. Then the power value in y-direction at y=-0.5 μm, -1.5 μm, and -2.5 μm is observed as shown in table 3.1.
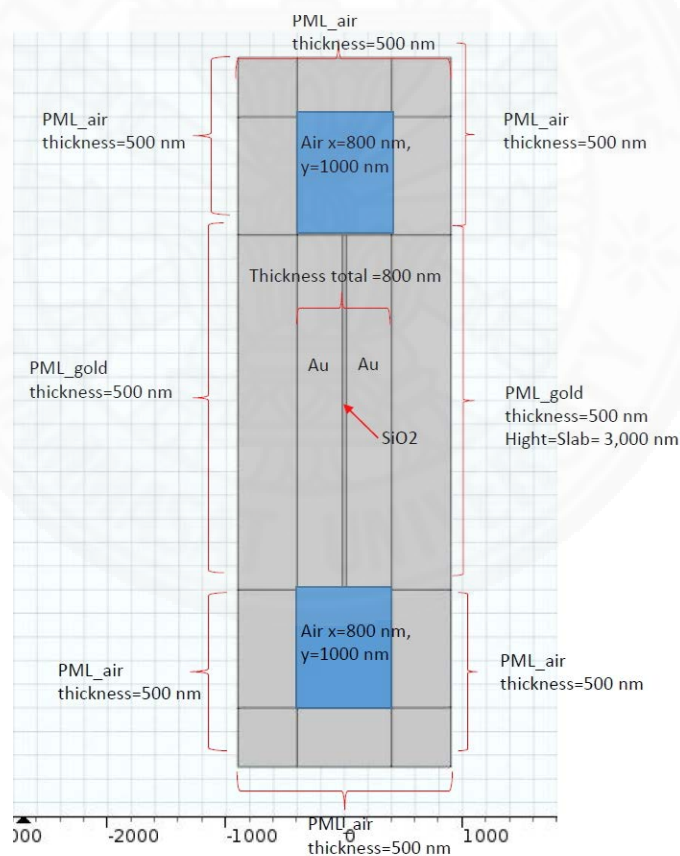
Figure 3.6 A 2D straight MIM waveguide and parameters setting.

Table 3.1 The power flow vs the thickness of the insulator.

Thickness (nm)	Power flow at -0.5 μm	Power flow at -1.5 μm	Power flow at -2.5 μm
100	-1.346E-10	-9.505E-11	-5.587E-11
30	-1.319E-10	-7.644E-11	-4.040E-11
10	-3.379E-11	-8.370E-12	-5.322E-13
3	-8.725E-13	-4.607E-15	2.438E-14

Next, the integrated power (I) of the straight MIM waveguide of SiO$_2$ and Hybrid taper with T=100/30/10 nm at y=-0.5 μm, -1.5 μm, and -2.5 μm, then the curve fitting of the results to an equation $I = Ae^{(-B(-y))}$ are shown in figure 3.7. The propagation length is $L_p=1/B$ as shown in table 3.2.
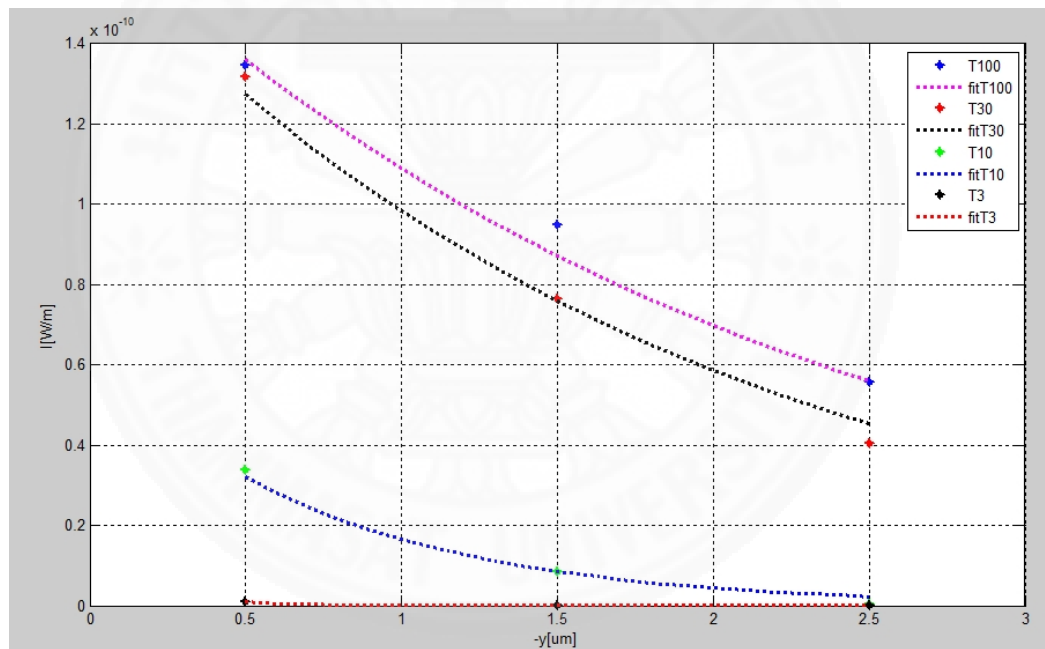
Figure 3.7 The integration of the power flow (I[W/m]) of T100, T30, T10, and T3 nm at y=-500, -1500, and -2500 nm respectively.

Table 3.2 The propagation length $L_p=1/B$ for each T.

T[nm]	L_p [m]
100	2.2472e-06
30	1.9342 e-06
10	7.5758 e-07
3	1.8868 e-07

As results, the value of T = 3 nm is positive values are found, probably this is just an accidental coincidence because it is too narrow. The positive values are not used for the fitting of T = 3 nm. As the curve fit graph, it tendencies agree with an analytical value and E_x inside SiO₂ layer for each T value is called λ_p, $k = \frac{2\pi}{\lambda_p}$ [79]. The obtained the values of L_p were very close to the λ_p, of Kurokawa's paper. Therefore, the COMSOL results agree with the analytical results.

3.3.3 The investigation of the influence of Al₂O₃

To investigate the influence of the use of Al₂O₃ instead of SiO₂ as the ultra-thin dielectric film, the coupling efficiency was evaluated numerically. A linear tapered MIM waveguide made of only SiO₂ (ultra-thin SiO₂ film on a SiO₂ taper) and a hybrid one made of ultra-thin Al₂O₃ film on a SiO₂ taper were compared. The structural model is shown in figure 3.4. The thickness of the main SiO₂ layer was set at $T\text{-}H$ = 200 nm and the angle α were vary to 10°, 15°, and 20°, respectively. The taper angle at α=20° will be observed because it is the optimum coupling efficiency by Choo et al. [57]. The resultant taper length L was 550 nm. On top of this structure, an ultra-thin dielectric film with a thickness of H = 5 nm was deposited. This dielectric taper structure was sandwiched between Au layers. The thicknesses of the upper and lower Au layers at the entrance were set at 300 nm, so only the guided power inside the waveguide was evaluated. Since the experimental structures have Au layers sufficiently thicker than the skin depth of Au (about 25 nm [79]), the discrepancy of the Au layer thicknesses between the simulation and the experiment had no effect. In this simulation structure, both the pure SiO₂ waveguide and the hybrid Al₂O₃-SiO₂ waveguide could be evaluated by simply changing the material properties of the ultra-thin dielectric film. The presence of Ti adhesion layers were neglected in the simulation. The coupling

efficiency is defined as the ratio of the *x* components of the total Poynting vectors, P_B and P_T, integrated over the cross sections just before and after the taper section [57].

The simulation structure and results are shown in figure 3.8-3.10 and table 3.3-3.6 that shows the comparison of the power flow at P_B and P_T of the only SiO$_2$ layer and for the hybrid layer. As the results, the power flow in both cases are not much different. The minimum wavelength of the surface plasmon polariton is 110 nm which is less than 7.57 times of the incident wavelength. With the smallest confinement area of 5 nm, the taper angle $\alpha=20°$, the highest coupling efficiency is 82.03% for only SiO$_2$ layer and 72.28% for a hybrid Al$_2$O$_3$ layer, respectively.
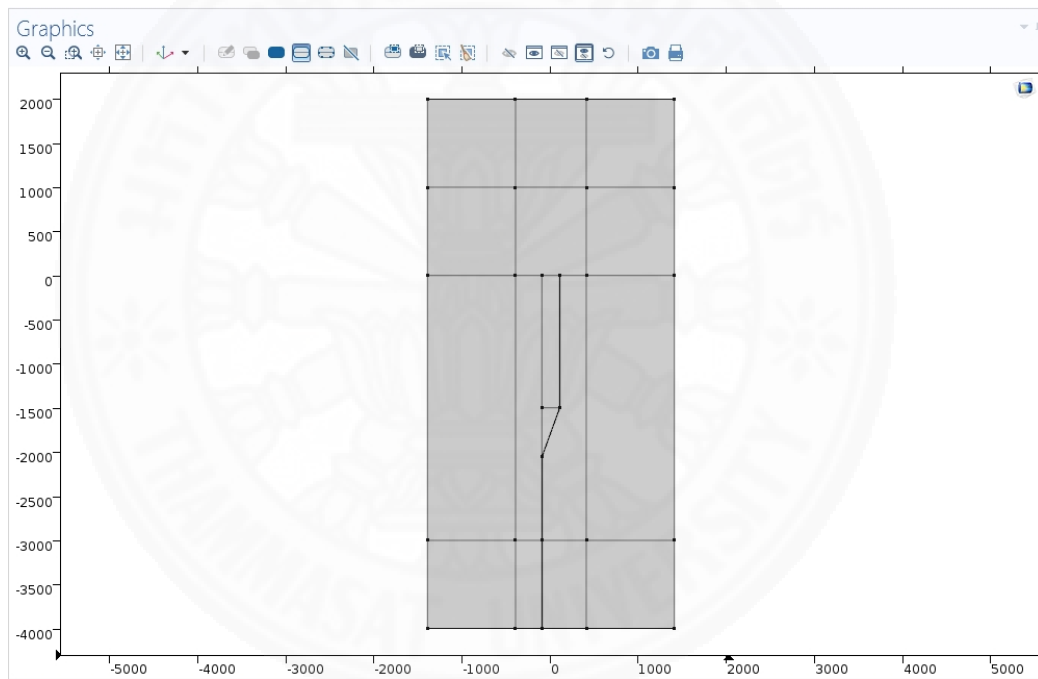
Figure 3.8 The geometry of the MIM-SPP waveguide with a linear taper composed of upper and lower gold plates with an insulator SiO$_2$ layer with angle α at taper section.
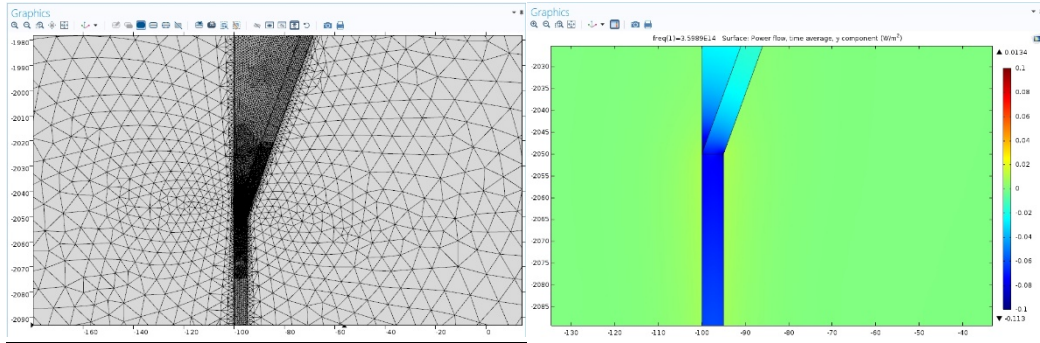
Figure 3.9 (Left) the enlarged mesh at the taper area (Right) the enlarge power flow at the waveguide tip.
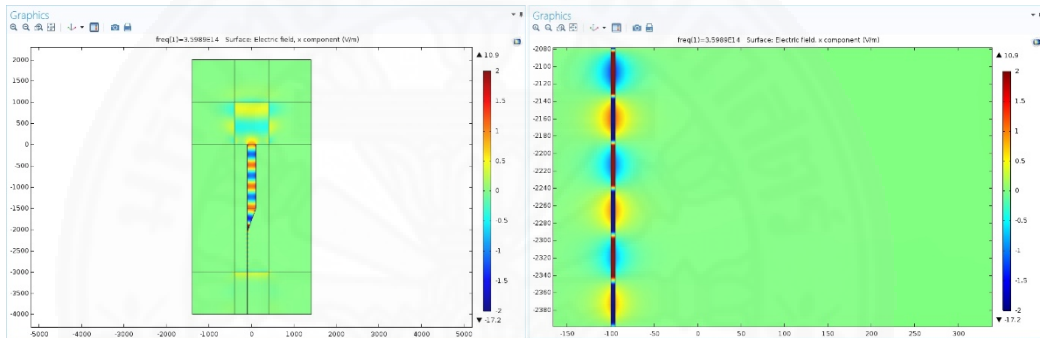
Figure 3.10 (Left) an electric field in the x component (Right) the enlarging of an eclectic field in the x component of the MIM waveguide with a linear taper.
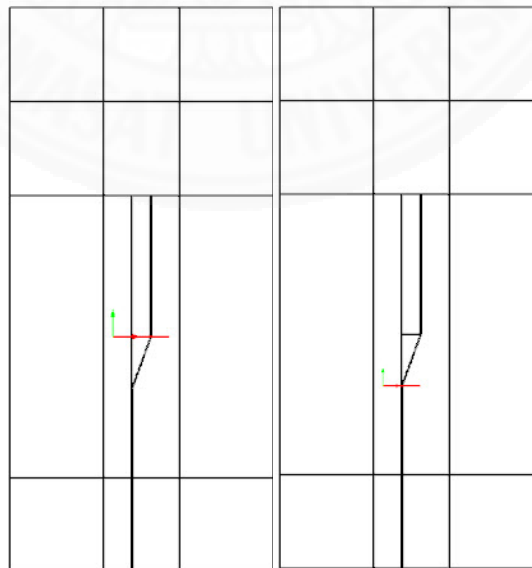
Figure 3.11 The cross section for observing the power flow across (Left) the body (Right) the tip.

Table 3.3. The profile of P_B and P_T cross section with α=10°, 15°, and 20°.

P_B and P_T	Pure SiO2	SiO2/Al2O3 (Hybrid)
P_B (y=-1500), alpha=20 deg.		
P_T (at y=-2050 nm), alpha=20 deg.		
P_B (y=-1500), alpha=15deg.		
P_T (at y=-2246 nm), alpha=15 deg.		
P_B (y=-1500), alpha=10 deg.		

P_T (at y=-2634 nm), alpha=10 deg.		
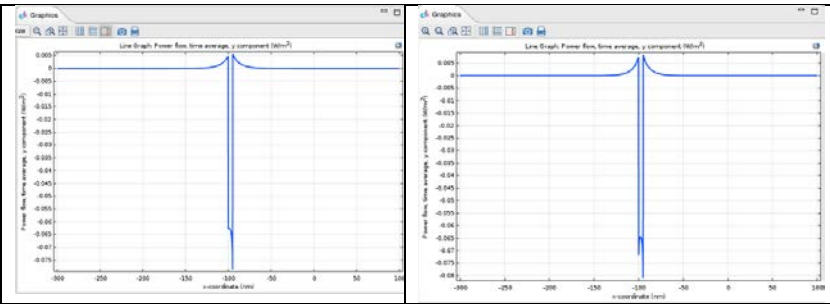
Table 3.4 the power flow value of P_B and P_T.

P_B and P_T value	Pure SiO$_2$	SiO$_2$/Al$_2$O$_3$(Hybrid)
P_B (y=-1500), alpha=20 deg.	-3.4529e-10	-3.0649e-10
P_T (at y=-2050 nm), alpha=20 deg.	-2.8324e-10	-2.4297e-10
P_B (y=-1500), alpha=15 deg.	-3.4999e-10	-3.1372e-10
P_T (at y=-2246 nm), alpha=15 deg.	-2.6582e-10	-2.3942e-10
P_B (y=-1500), alpha=10 deg.	-3.4011e-10	-3.3783e-10
P_T (at y=-2634 nm), alpha=10 deg.	-2.3447e-10	-2.19936e-10

Table 3.5 The coupling efficiency between the pure SiO$_2$ and the hybrid taper.

The taper angle	Pure SiO$_2$	SiO$_2$/Al$_2$O$_3$(Hybrid)
alpha=20 deg.	P_T / P_B =0.8203	P_T / P_B =0.7228
alpha=15deg.	P_T / P_B =0.7595	P_T / P_B =0.7632
alpha=10 deg.	P_T / P_B =0.7710	P_T / P_B =0.6493

Table 3.6 The λ_p of E_x inside the insulator layer of the MIM waveguide at the tip area.

The taper angle	Pure SiO$_2$ (nm)	SiO$_2$/Al$_2$O$_3$ (Hybrid)(nm)
MIM straight	500	500
alpha=20 deg.	140	110
alpha=15deg.	140	110
alpha=10 deg.	140	110

3.3.4 The influence of the insulator material of MIM structure

To understand the influence of the tip thickness layer and the refractive index of material in the insulating layer of MIM structure, only *H* is varied starting from 5 nm to 100 nm. The dielectric layer and *H* layer were sandwiched between Au layers. Furthermore, the refractive index of the dielectric layer varied from 1 to 3.

To vary the ultra-thin dielectric film thickness of *H*, the simulation results, the coupling efficiency and the power intensity enhancement at the junction between the tapered section and the sub-100 nm scale waveguide as a function of *H* for α=20° are shown in figure 3.12. As results, the highest coupling efficiency is 83% at *H* =10 nm, but the maximum power intensity was strongly enhanced for values of *H* less than 10 nm, the optimization of the two parameters is about 7nm-thickness of the ultra-thin dielectric film. This behavior results from the high spatial localization of the field and the increase in the effective refractive index, n_{eff} (increase of which results in slow propagation) [11].

To vary the refractive index of material in the insulating layer of MIM structure, the 205 nm-thickness insulator layer is varied. The result is shown in figure 3.13, the coupling efficiency and the power intensity enhancement are decreased when the *n* is higher. For figure 3.14, the main dielectric refractive index is fix at *n*=1.45 and varied the refractive index in the ultrathin-dielectric refractive index.
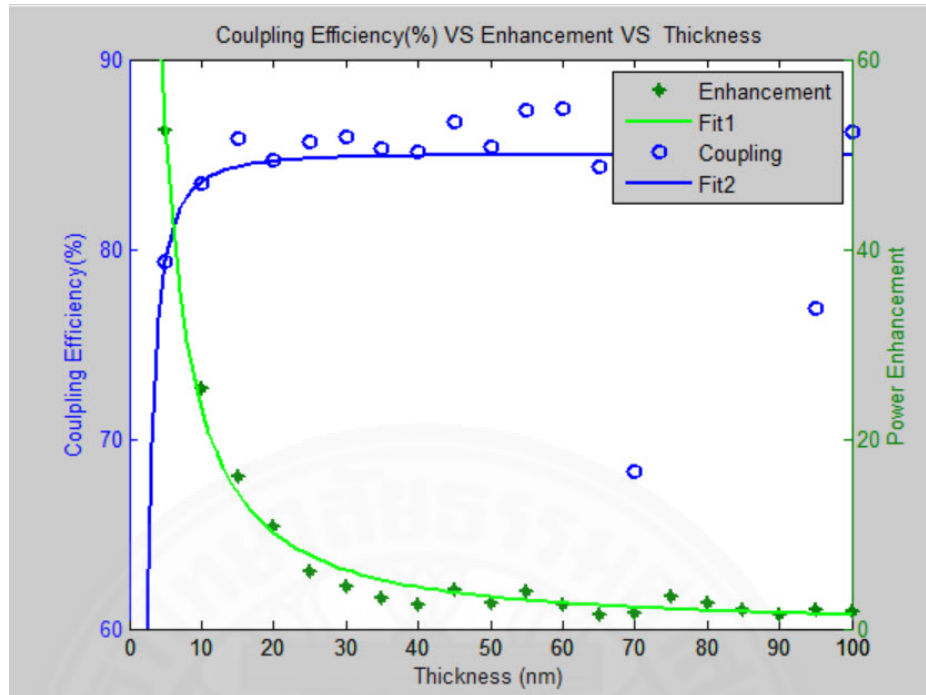
Figure 3.12 The coupling efficiency and the power intensity enhancement of the varied thickness of the ultra-thin dielectric layer.
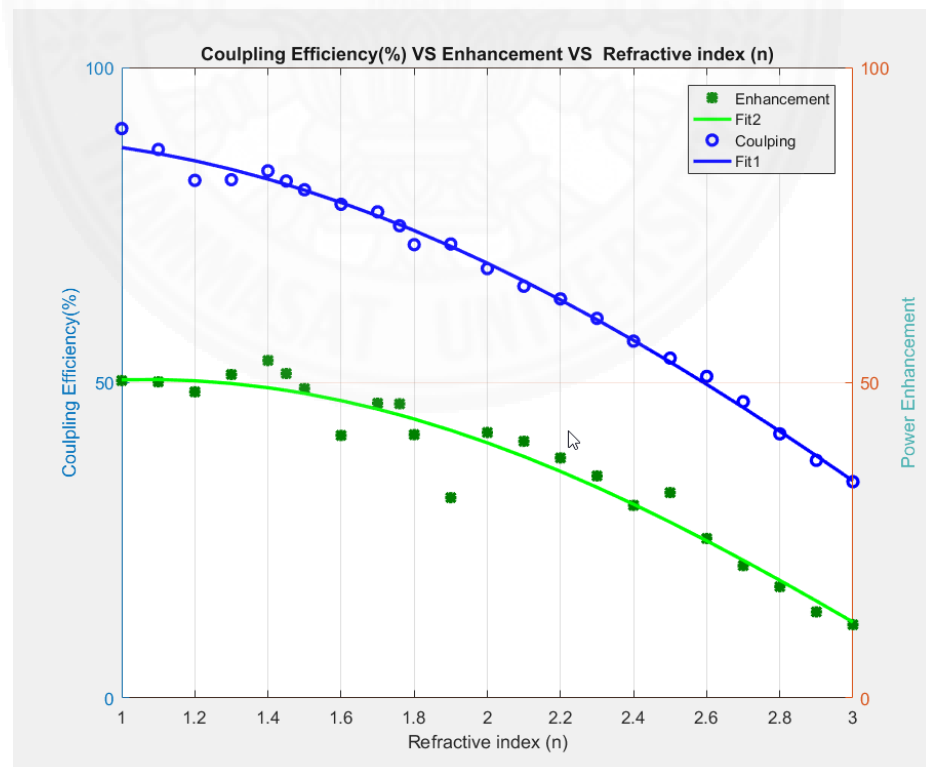
Figure 3.13 The coupling efficiency and the power intensity enhancement of the varied refractive index of the 205 nm-thickness insulator layer.
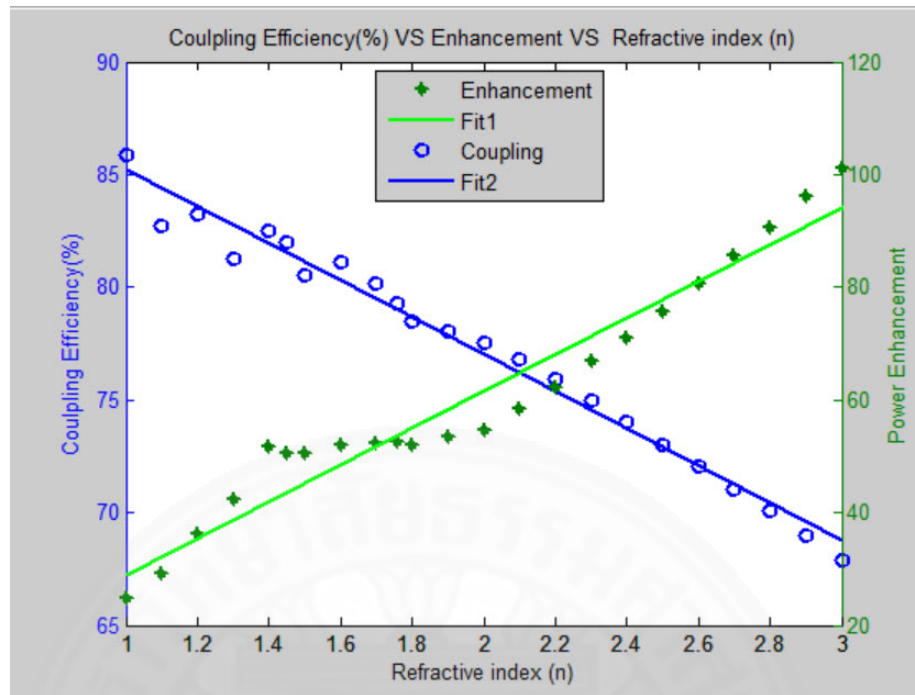
Figure 3.14 Fix the main dielectric refractive index *n*=1.45 and varied the refractive index in the ultrathin-dielectric refractive index.

3.3.5 Simulation: To understand the metamaterial

To understand the metamaterial, the double fishnet of Dolling's paper [71] is one of good example to reproduce by simulation and fabrication. They investigated how the light propagated when it went through the fishnet structure and measured the reflectance and transmittance. This fishnet structure consists of three layers; gold-Mgf$_2$-gold and structure parameters are shown in the table 3.7. The re-simulation, re-fabrication following Dolling's paper and characterization of the double fishnet are done for finding the optimized fabrication process and characterization to apply to the final structure model.

Table 3.7 The fishnet structure parameters [71].

Parameters	Dimension [nm]
A	600
Wx	307
Wy	100
Hx	293
Hy	500
T	25
S	35
d	85

Further, for finding the transmittance and reflections of the fishnet metamaterial, the Fresnel equation [83] is applied which shows how a plane electromagnetic wave propagating through free space which is incident on an infinite dielectric medium. For analytic expression of the reflectance and transmittance, reflection and transmission coefficients for *S*-polarization and *P*-polarization are defined respectively as

$$r_s = \frac{n_1 cos\theta_{incident} - n_2 cos\theta_{transmitted}}{n_1 cos\theta_{incident} + n_2 cos\theta_{transmitted}} \tag{3.9}$$

$$t_s = \frac{2n_1 cos\theta_{incident}}{n_1 cos\theta_{incident} + n_2 cos\theta_{transmitted}} \tag{3.10}$$

$$r_p = \frac{n_2 cos\theta_{incident} - n_1 cos\theta_{transmitted}}{n_1 cos\theta_{transmiitted} + n_2 cos\theta_{incident}} \tag{3.11}$$

$$t_p = \frac{2n_1 cos\theta_{incident}}{n_1 cos\theta_{transmiitted} + n_2 cos\theta_{incident}} \tag{3.12}$$

Reflectance and transmittance are defined as

$$R = |r|^2 \tag{3.13}$$

$$T = \frac{2n_2 cos\theta_{transmitted}}{n_1 cos\theta_{incident}} |t|^2 \tag{3.14}$$

Then, the transmittance and reflection are improved by following the Fraby-Perot Etalon [84], or interferometer for solving the transmittance and reflectance.

It can be considered as the best example of an optical resonator. This consists of a plane-parallel plate of thickness l and refractive index n that is immersed in a medium of index n'. If a plane wave incident to the normal on the etalon, the reflectance (R) and transmittance (T) are observed in term of intensity (I) or amplitude of the partial (A) waves as shown in the expression below.

The expression for the fraction of the incident intensity (I) that is reflected by the etalon;

$$\frac{I_r}{I_i} = \frac{A_r A_r^*}{A_i A_i^*} = \frac{4R\sin^2(\frac{\delta}{2})}{(1-R)^2 + 4R\sin^2(\frac{\delta}{2})}$$

(3.15)

and the transmitted fraction is shown;

$$\frac{I_t}{I_i} = \frac{A_t A_t^*}{A_i A_i^*} = \frac{(1-R)^2}{(1-R)^2 + 4R\sin^2(\frac{\delta}{2})}$$

(3.16)

$$\delta = \frac{4\pi n l \cos\theta}{\lambda} = 2m\pi, m = any\ integer.$$

(3.17)

For the simulation, the analyzation is running a series of FEM simulation using COMSOL software, based on 3D and periodic structure condition [82] for a unit cell of the double fishnet metamaterial as shown in figure 3.15. The Dielectric Constance of Au is from the curve fit with Johnson and Christy (see in detail in an appendix A) [45] and mgf$_2$ is 1.38. The results are shown in Fig 3.16-3.18.
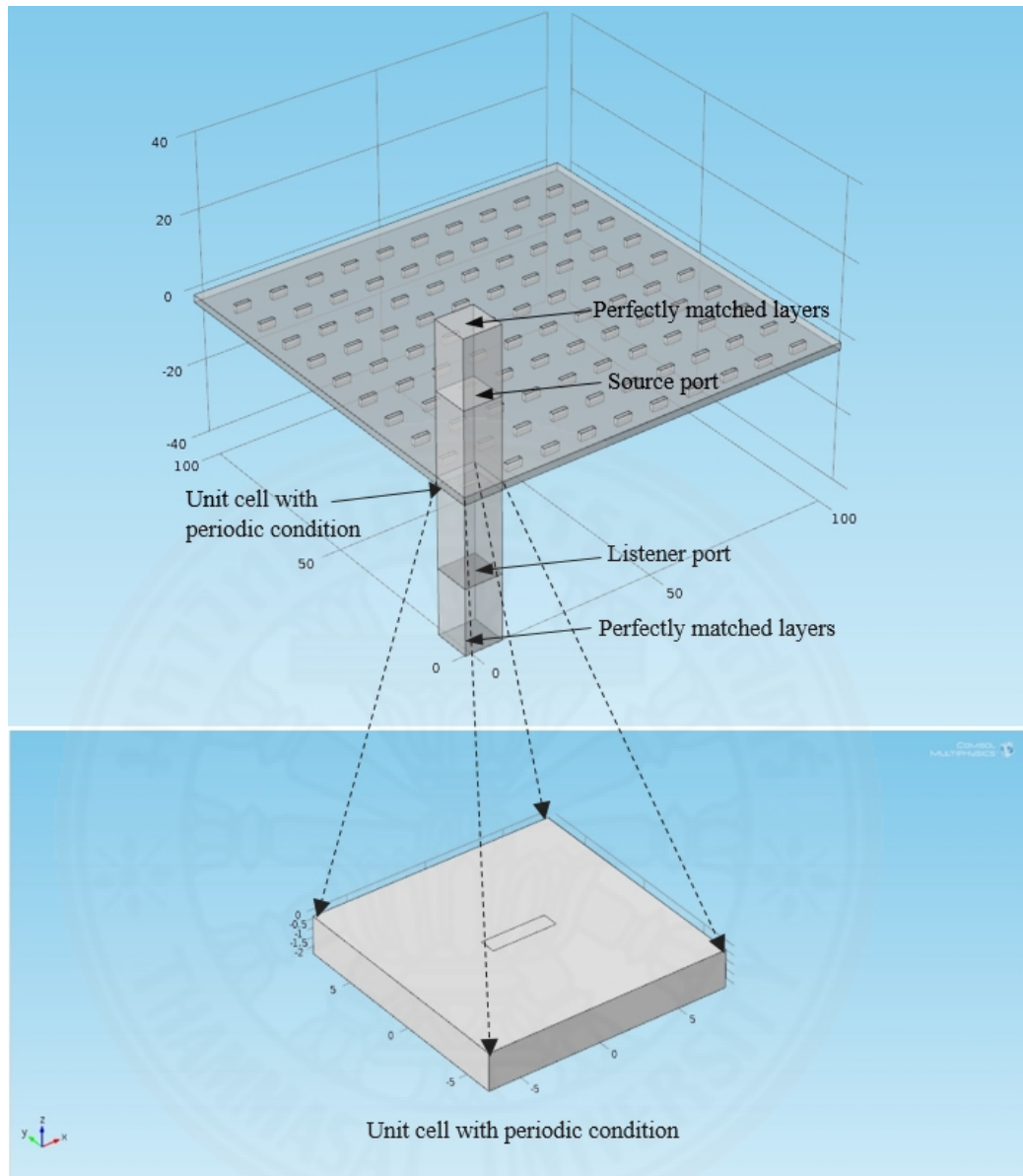
Figure 3.15 The double fishnet metamaterial with a unit cell structure.

Table 3.8 Parameters definition

Name	Expression	Description
n_air	1	refractive index, air
n_mgf2	1.38	refractive index, MgF2
lda0	800[nm]	wavelength
lda1	800[nm]	start point of wavelength sweep
lda2	1800[nm]	end point of wavelength sweep
ldastep	200[nm]	step of wavelength sweep
f0	c_const/lda0	start point of frequency sweep
f1	1.667e14[Hz]	end point of frequency sweep
f2	3.75e14[Hz]	step of frequency sweep
fstep	0.2e14[Hz]	start point of wavelength sweep
W	2*pi*f0	Frequency in rad/s unit
width	600[nm]	width of model
depth	600[nm]	depth of model
height	685.15[nm]	height of model
Az1	300[nm]	Air thickness
Glassz	300[nm]	Gold thickness
PMLz1	200[nm]	PML1 thickness
PMLz2	200[nm]	PML2 thickness
Gz1	25[nm]	First layer of Gold thickness
Gz2	25[nm]	second layer of Gold thickness
Mgz	35[nm]	MgF2 tihickness
Wx	300[nm]	Wx
Wy	100[nm]	Wy
Hx	width-Wx	Hold size in x direction
Hy	depth-Wy	Hold size in y direction
Hz	2*Gz1+Mgz	Hold size in z direction
EpS	1	Epsinlon infinity of science paper
WpS	1.32e16[rad/s]	Omega p of science paper
GamS	1.2e14[rad/s]	Gamma of science paper
x_pol	1	amplitude of incident polarization in x direction
y_pol	0	amplitude of incident polarization in y direction
n_glass	1.5	Reflective index of glass

Table 3.9 Variables definition

Name	Expression	Description
Ome1	freq*2*pi	frequency in rad/s unit
Ome2	(c_const/lda0)*2*pi	frequency in rad/s unit
epR	EpS-(WpS^2)/(Ome1^2-i*GamS*Ome1)	the dielectric function
n_gold	sqrt(epR)	reflective index of gold
n_slab	n_gold	reflective index of slab=n gold
theta	0[deg]	reflection angle in slab to glass
alpha	0[deg]	incident wave angle
beta	asin(n_air*sin(alpha)/n_slab)	reflection angle in slab
kax	ka*sin(alpha)	k vector of air in x direction
ka	emw.k0	k vector of air
kay	0	k vertor of air in y direction
kaz	ka*cos(alpha)	k vertor of air in z direction
kb	n_slab*emw.k0	k vertor of slab
kbx	kb*sin(beta)	k vertor of slab in x direction
kby	0	k vertor of slab in y direction
kbz	kb*cos(beta)	k vertor of slab in z direction
delta	(4*pi*n_slab*Hz*cos(theta))*f0/c_const	delta value for Fabry-Perot equation
kg	n_glass*emw.k0	k vertor of glass
kgx	kg*sin(theta)	k vertor of glass in x direction
kgy	0	k vertor of glass in y direction
kgz	kg*cos(theta)	k vertor of glass in z direction

<u>Simulation Results</u>
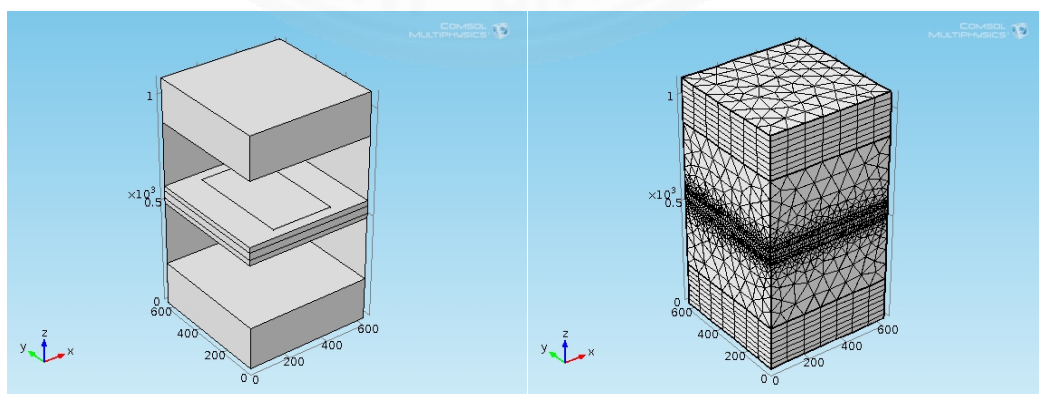
Figure 3.16 (Left) the geometry of the double fishnet unit and (Right) meshing
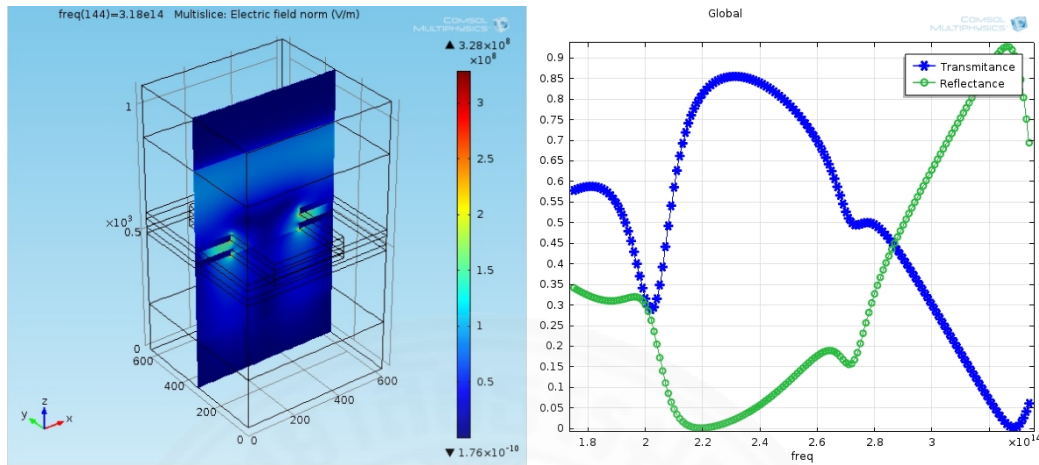
Figure 3.17 (Left) an electric field (Right) the transmittance and reflectance profile.

Table 3.10 The convergence of simulation mesh.

Air mesh size	1st normal	2nd Fine	3rd extra fine	4th fine
Maximum element size	108 [nm]	86.8 [nm]	38 [nm]	86.8 [nm]
Minimum element size	19.5 [nm]	10.8 [nm]	1.63 [nm]	10.8 [nm]
Maximum element growth rate	1.5	1.45	1.35	1.45
Curvature factor	0.6	0.5	0.3	0.5
Resolution of narrow regions	0.5	0.6	0.85	0.6
Fishnet size	1st extra fine	2nd manual	3rd manual	4th extremely fine
Maximum element size	38 [nm]	16.7 [nm]	10 [nm]	21.7 [nm]
Minimum element size	1.63 [nm]	0.217 [nm]	0.1 [nm]	0.217 [nm]
Maximum element growth rate	1.35	1.3	1.3	1.3
Curvature factor	0.3	0.2	0.3	0.2
Resolution of narrow regions	0.85	1	0.85	1
Hole size	1st finer	2nd extra fine	3rd extremely fine	2nd extra fine
Maximum element size	59.7 [nm]	38 [nm]	21.7 [nm]	38 [nm]
Minimum element size	4.34 [nm]	1.63 [nm]	0.217 [nm]	1.63 [nm]
Maximum element growth rate	1.4	1.35	1.3	1.35
Curvature factor	0.4	0.3	0.2	0.3
Resolution of narrow regions	0.7	0.85	1	0.85
Number of degree of freedom	163,726	666,498	2,318,428	399,532
Time duration	15 minutes	9 hours 30 minutes	Have got some errors.	4 hours, 18 minutes

1) Results of convergence1   2) Results of convergence 2

(3) Results of Hx 293 nm, Hy 500 nm
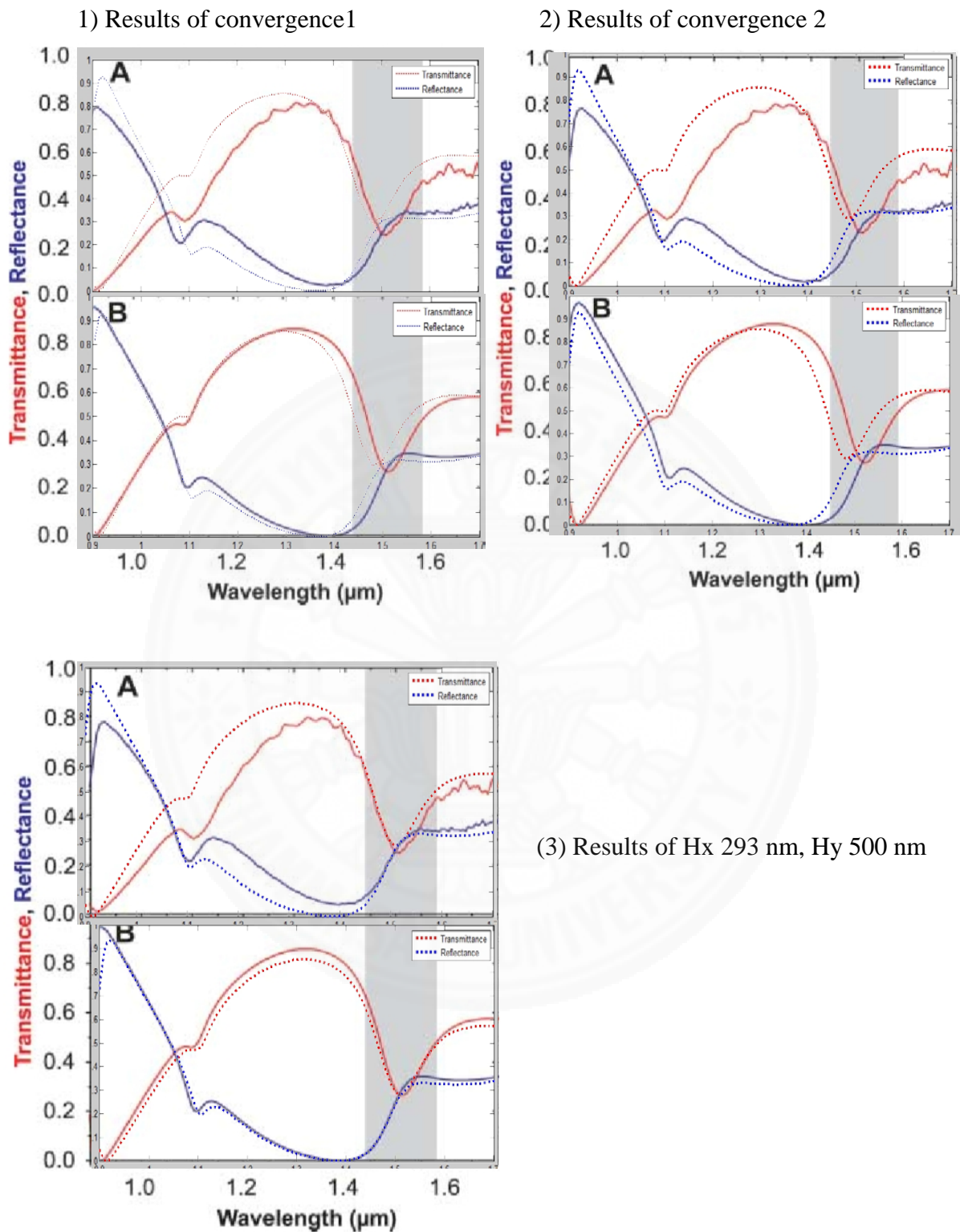
Figure 3.18 The comparison results between Dolling paper and our results.

After calculation by COMSOL, then analyzation results are further done by using MATLAB and are compared with Dolling paper. Furthermore, the convergence criterion of a 1% iteration strategy is done by reducing the mesh size that show in table 3.10. Finally, the results in figure 3.14, there are much close to Dolling theory results, so these results can be reliable. The next session will show the fabrication of the fishnet metamaterials.

3.4 Preliminary fabrication of the MIM waveguide

In this section, details of the fabrication processes are given. The hybrid Au-Al$_2$O$_3$-SiO$_2$-Au SPP waveguide structure was fabricated in four steps corresponding to figure 3.19 (a), (b), (c), and (d) -(f).
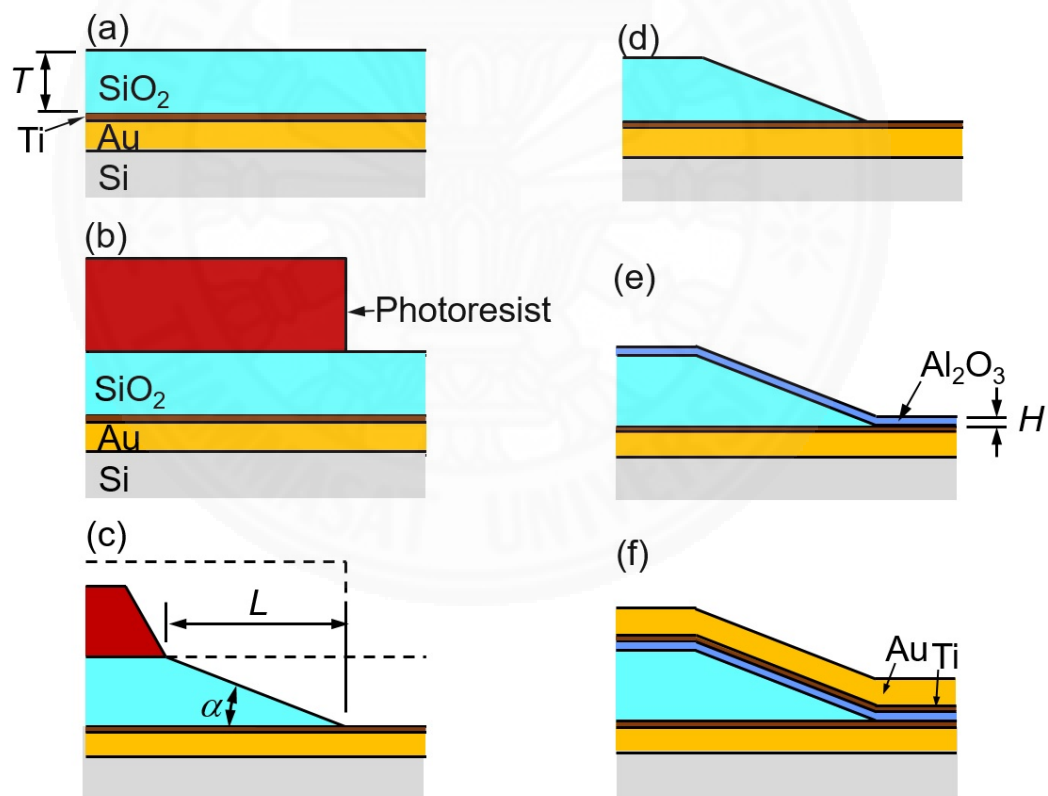
Figure 3.19 Schematic steps of the fabrication process. (a) Deposition of the lower Au layer and the main SiO$_2$ layer on a Si substrate. Intermediate layers between the lower Au layer and the Si substrate are not shown for simplicity. (b) Fabrication of the photoresist mask. (c) Dry etching using a mixed gas. (d) Photoresist removal. (e) Ultra-thin dielectric film deposition. (f) Deposition of the upper Au layer.

(1) A 50-nm-thick Ti film, a 50-nm-thick Pt film, and a 100-nm-thick lower Au layer were deposited on a Si substrate using electron-beam deposition. The Ti film was an adhesive layer to enhance the adhesion between the Pt film and the Si substrate. The Pt film was a barrier layer to prevent the diffusion of Si into Au during the successive high temperature processes. The main SiO_2 layer was deposited using chemical vapor deposition at 350°C. Before the main SiO_2 layer, a 3-nm-thick Ti film was deposited for adhesion on the lower Au layer.

(2) The next step was the fabrication of the photoresist masks. A 2.3 μm-thick photoresist (AZ5214E, Merck Co.) was spun at a speed of 1500 rpm for 60 s and prebaked at 110°C for 2 min. on the main SiO_2 layer, and then the stripe-shaped patterns were exposed by direct laser writing at a dose of 250 mJ/cm^2 at the wavelength of 405 nm. The photoresist was positively developed with 2.38% tetramethylammonium hydroxide for 150 s and stripe-shaped masks were fabricated.

(3) Capacitive coupled plasma reactive ion etching was used to obtain the linear tapered SiO_2 structure. The target here was to realize α = 20 deg., the optimum taper angle for the maximum coupling efficiency, by controlling the removal of the photoresist and SiO_2 is using two gases, CHF_3 and O_2. To find the optimum dry etching condition, the cross-sectional shapes of the etched SiO_2 layers were evaluated by scanning electron microscopy (SEM) for various compositions of gases and etching sequences. The total flow rate of CHF_3 and O_2, the gas pressure, and the RF power were set at 100 sccm, 3.0 Pa, and 150 W, respectively. The temperature of the substrate was uncontrolled. The representative conditions (from A to E) and the results are summarized in Table 3.11 and figure 3.15.

Table 3.11 Representative conditions and results of the vertical taper fabrication.

Condition	CHF_3/O_2 (sccm)	Etching sequence (min.)	Total etching time (min.)	α/α_2 (°)	Etched depth (nm)
A	40/60	6	6	15/5	79
B	40/60	3, (2), 3	6	10/-	107
C	60/40	3, (2), 3	6	20/-	131
D	70/30	3, (2), 3	6	35/20	125
E	60/40	3, (2), 3, (5), 3.	10	19/12	200

Bracketed figure, e.g. (2), is the waiting time for cooling the substrate.
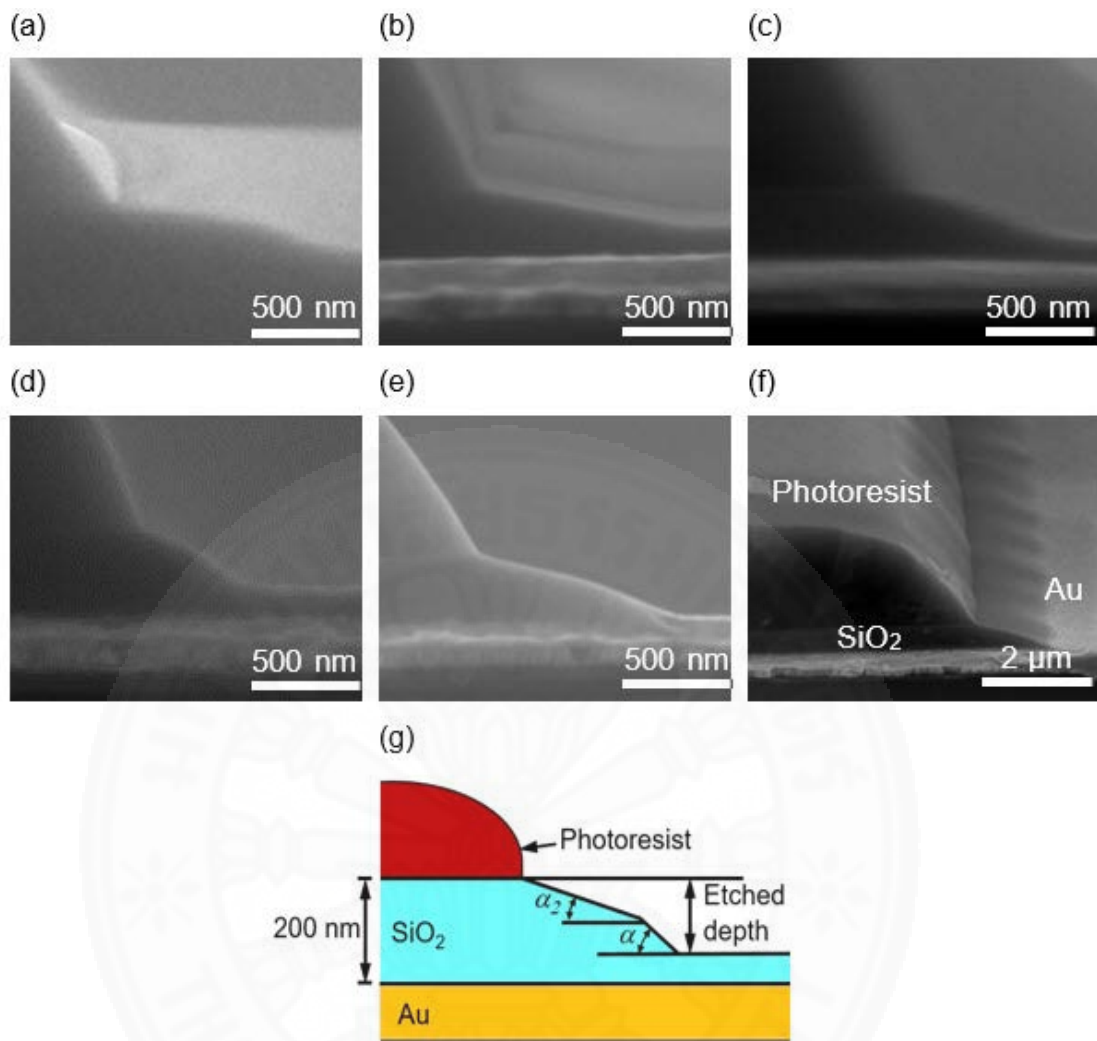
Figure 3.20 SEM micrographs showing the cleaved cross sections for various dry etching conditions. (a)-(e) correspond to Conditions A-E, respectively. (f) shows the perspective view of (e). (g) Schematic drawing showing the two-stage slopes.

The first finding was the importance of the temperature. In Condition A, the taper section exhibited two-stage slopes as shown in figure 3.20 (a). Here the angle of the upper taper is defined as α_2 as shown in figure 3.20 (g). The original taper angle α was 15 deg., which is not so far from the target value. However, the slope was drastically reduced on the way ($\alpha_2 = 5$ deg.) and a very long and shallow taper (depth was only 79 nm for 6 min-long etching) was obtained. This was probably due to the increased etching rate of the photoresist by the elevated temperature of the substrate during the process. Therefore, the etching process was stopped every 3 min and a waiting time inserted for cooling the substrate. In Condition B, the same gas composition and total etching time were used as in Condition A, but a waiting time of 2 min was inserted. In Table 1, the waiting time is shown in the parentheses in the etching sequence. The result is shown in figure 3.20 (b). Now the taper is linear and deeper, while α is reduced to 10 deg.; thus, the gas composition should be improved next.

For Conditions B, C, and D, the gas composition was varied while keeping the etching sequence the same. For a lower concentration of O_2, the taper angle and also the etched depth increased [figure 3.20 (b)-(d)]. This was reasonable because the regression of the photoresist mask decreased. For Condition C, the taper was linear and $\alpha = 20$ deg. [Figure 3.20 (c)]; therefore, it was concluded that the optimum flow rate ratio of $CHF_3:O_2$ was 60:40.

In the final Condition E, the 200-nm-thick main SiO_2 layer was completely etched by elongated total etching time of 10 min. The lower Au layer was exposed as shown in figure 3.20 (e) and (f). It was confirmed that the etching rate of Au of the mixed gas was negligibly small and the etching process stopped when the lower Au layer was exposed. In Condition E, the waiting time was gradually elongated to promote the cooling. However, figure 3.20 (e) shows a two-step feature and the taper is not completely linear. It seems that the waiting time was not sufficient. Nonetheless, $\alpha = 19$ deg. is close to 20 deg. Thus, it was decided to use Condition E for the final MIM waveguide.

Through these attempts, the insertion of proper waiting times between short etching periods was found to be crucial for realizing a linear taper with the target angle,

in addition to the optimization of the gas composition. By further optimization of the etching sequence, fabrication of more linear tapers could be possible.

(4) The final fabrication processes were to create the tip section and complete a linear tapered MIM waveguide. After removing the photoresist on the tapers using acetone, a 5 nm-thick Al_2O_3 film was deposited by ALD at 120°C. Then the surface was coated with a 3 nm-thick Ti adhesion layer and a 50 nm-thick upper Au layer using electron-beam deposition. The scanning electron micrograph and the cross-sectional pictures by transmission electron microscopy (TEM) are shown in figure 3.21. It is confirmed that $\alpha = 19$ deg. and $H = 5.6$ nm. The taper angle is closer to the optimum value and the minimum waveguide thickness is much thinner than Choo's results.
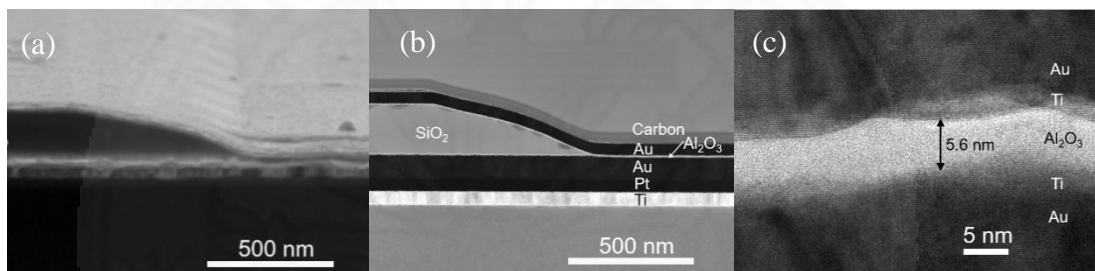
Figure 3.21 (a) SEM and (b), (c) TEM micrographs of the completed linear tapered MIM waveguide. (a) shows a perspective view of the cleaved cross section. (c) is the magnification of the tip section in (b), which clearly shows the ultra-thin dielectric film as thin as 5.6 nm.

An Au-Al_2O_3-SiO_2-Au SPP waveguide with a linear taper for nano-focusing was demonstrated. The vertical taper SiO_2 structures with a taper angle of nearly optimum 19 deg. was realized by mass-productive dry etching with a mixed gas and a photoresist mask using a standard etching instrument. In addition to the gas composition, the cooling of the substrate by inserting waiting times was found to be a key for the controlled taper shapes. The optimum CHF_3:O_2 flow rate ratio was found to be 60:40. At the tip section, an ultra-thin Al_2O_3 waveguide as thin as 5.6 nm, only one third of the conventional demonstration, was reproducibly realized by the employment of ALD technique. The coupling efficiency was numerically estimated at 72%.

This feasibility study offers practical mass-production of linear tapered MIM-SPP waveguides which is necessary for 3D NPCs. These are promising for on-

chip nano-focusing of light into a deep sub-wavelength spatial scale with high efficiency. In the future, by incorporating a substrate cooling system for the dry etching, quick and reproducible fabrication of highly controlled vertical taper structures would be realized. For complete 3D NPCs and its optical characterization, lateral patterning in the *y* direction is necessary as well.

3.5 Preliminary fabrication of the metamaterial

The fabrication processes are given in the figure 3.22, it started with fabrication on silicon substrate for checking the cross section because silicon substrate can break easily and then the fabrication is on ITO/Quartz substrate because of the optical characterization process reason. The details of this experiment will be described below. Substrate: Si dimension is10 mm x 10 mm x 0. 38 mm.

1) Pattern: Hole dimension consists of three sizes; a ($Hx = 300$ nm, $Hy = 500$ nm), b ($Hx = 320$ nm, $Hy = 520$ nm).

2) Nano-Fabrication processes consist of seven procedures as follows;

3) Cleaning: Acetone sonication 1 min, IPA, O_2 Plasma 1 min.

4) Resist: HMDS 3000 rpm 60 s, gL2000-14 3000 rpm 60 s, Baking 180 °C 5 min.

5) Electron Beam Lithography: 100 pA, Dose 0.75 us/dot, Pitch 2/2, Field. 150 μm Lithography time: 110 min for 23 Field (5 min/Field)

6) Development: Xylene 90 s, IPA 20 s.

7) Electron Beam Evaporator: Ti 3nm, Au 25 nm, MgF_2 35 nm, Au 25 nm.

8) Liftoff: NMP RT 18 h, NMP 80 °C 15 min, Sonication 10 s.

9) Cleaning: Acetone, IPA.
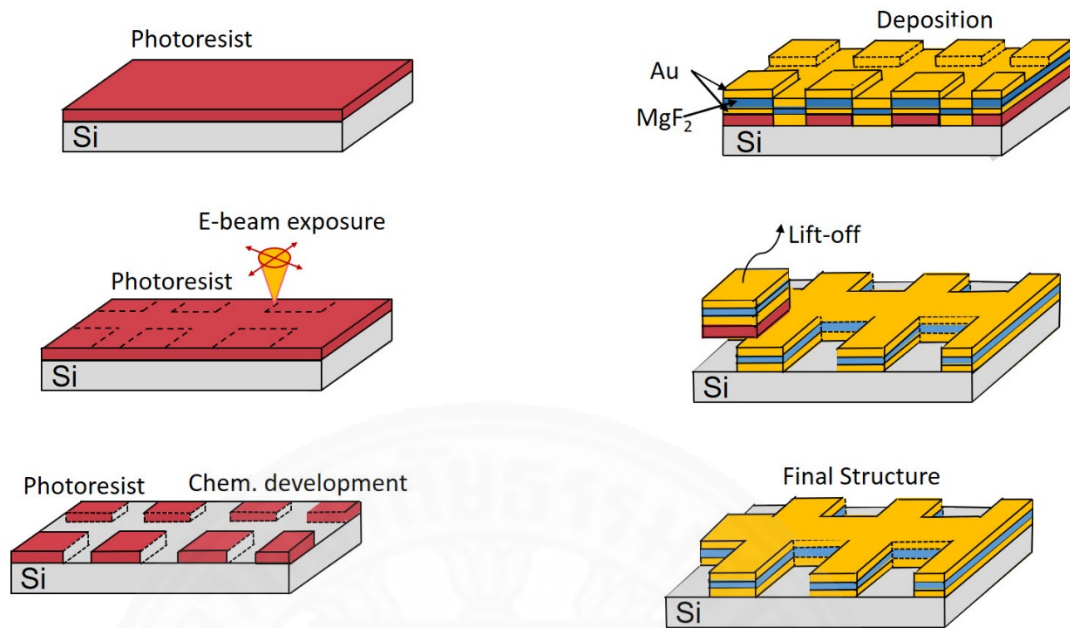
Figure 3.22 Electron Beam Lift-off methodology.
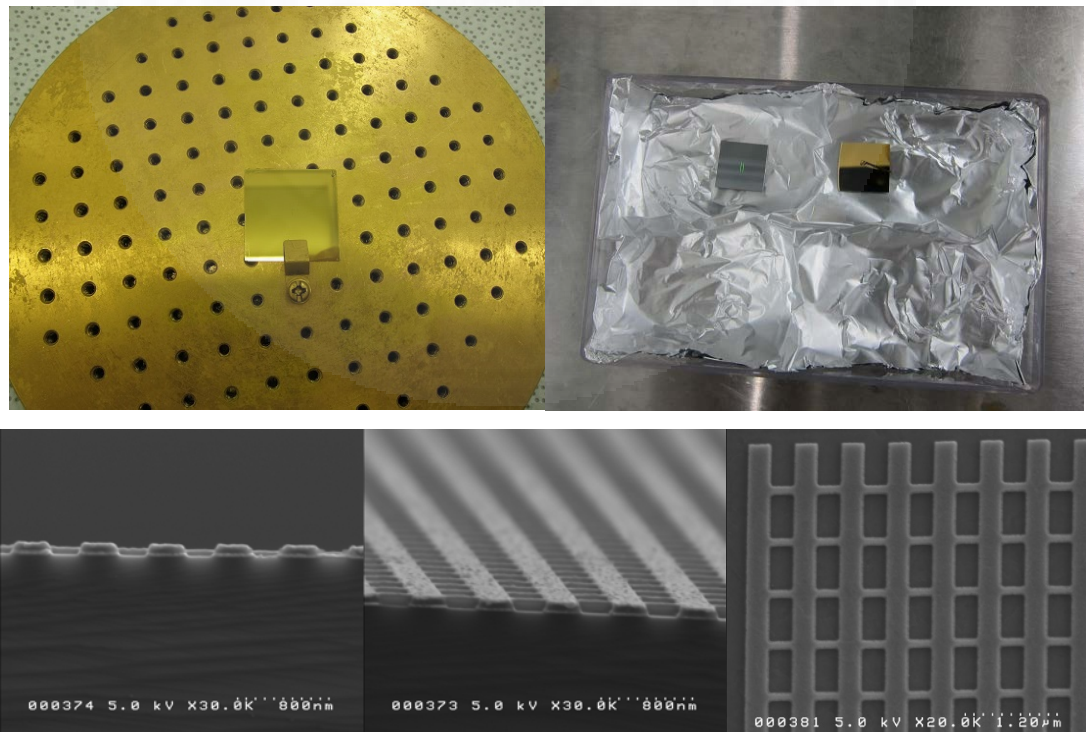
Figure 3.23 (Upper-left) after deposit MgF2 and Au (Upper-right) after lift-off process for 1 night (Lower) the SEM observation of the fishnet metamaterial.
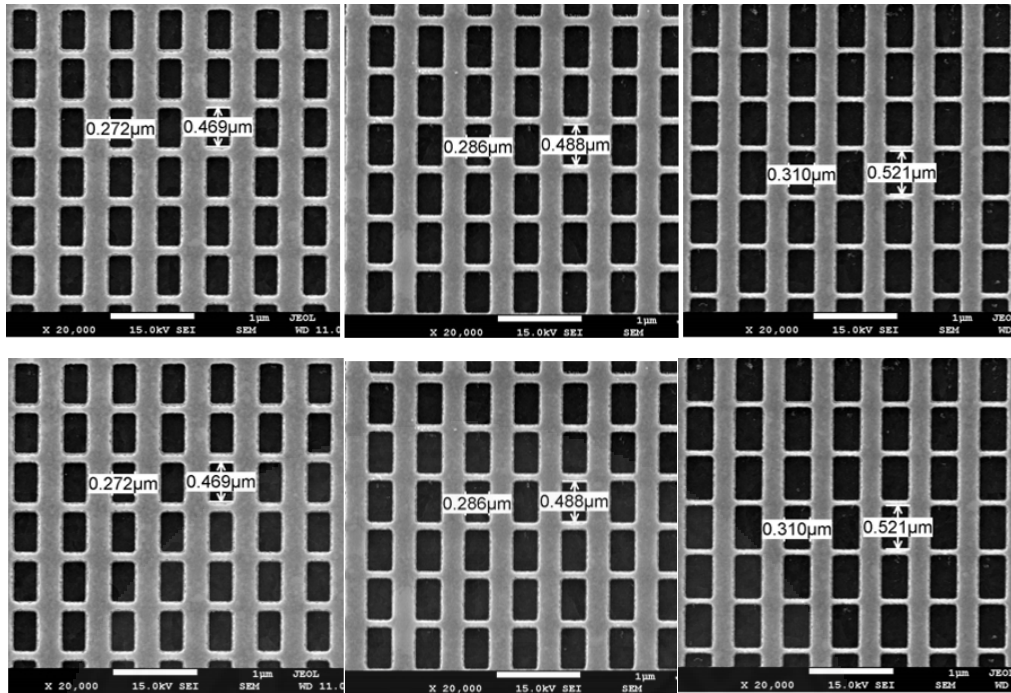
Figure 3.24 The fishnet structure with dimensions of SEM observation.

3.6 Preliminary characterization of the metamaterial

This is the schematic of the experimental setup and the parameter of the optical part as shown in figure 3.25 and table 3.12. The transmittance and refraction of fishnet metamaterial compared with Dolling paper is shown in figure 3.28, the re-calculation and the results are fitting well with Dolling's paper.
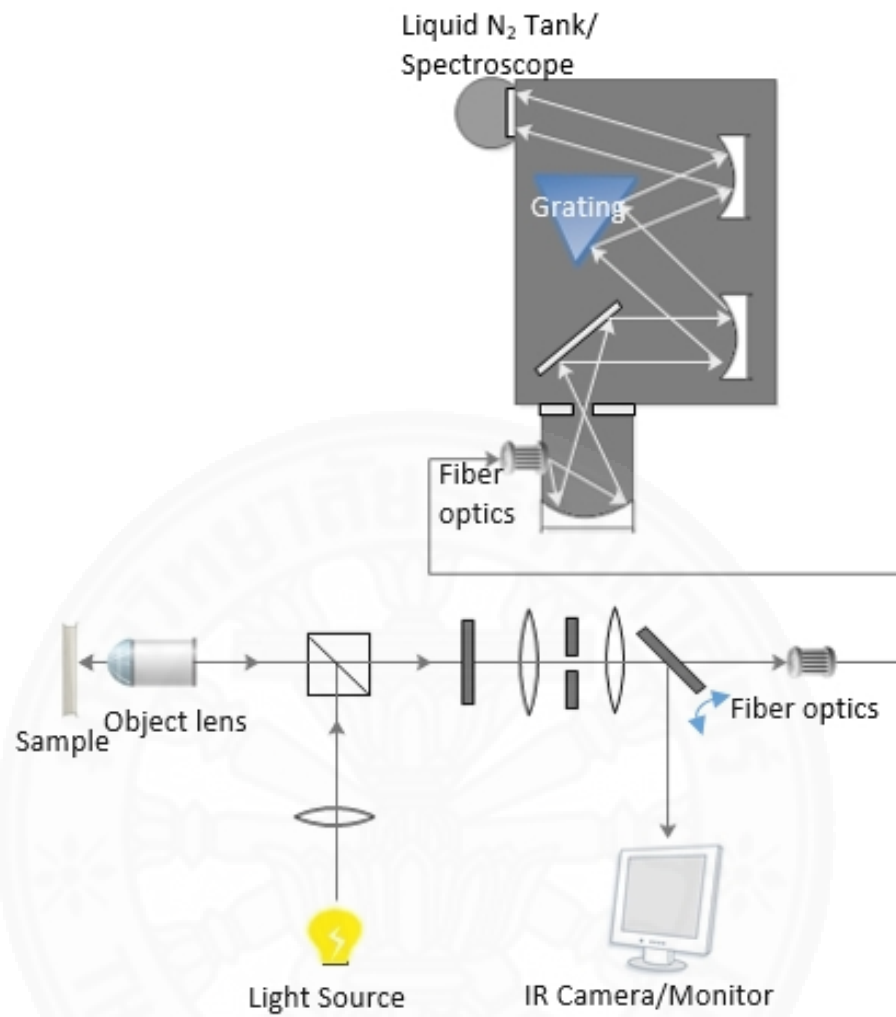
Figure 3.25 The schematic of the optical characterization experimental setup.

Table 3.12 The first optical characterized experimental parameter

Parameters	Values
Objective lens: Magnification	10X
Objective lens: Numerical Aperture (NA)	0.25
Aperture	no.3
Exposure time	0.4 second
Spectrometer temperature	-93° C
Grating	no.3# 150 grating/mm.

For characterization, the reflectance of pure gold, the sample on ITO substrate, and background are measured in horizontal polarization and vertical polarization as shown in figure 3.26 and 3.27.

For analysis, the reflectance expresses as

$$R = \frac{I_{sample} - I_{bg}}{I_{Au} - I_{bg}} \tag{3.18}$$
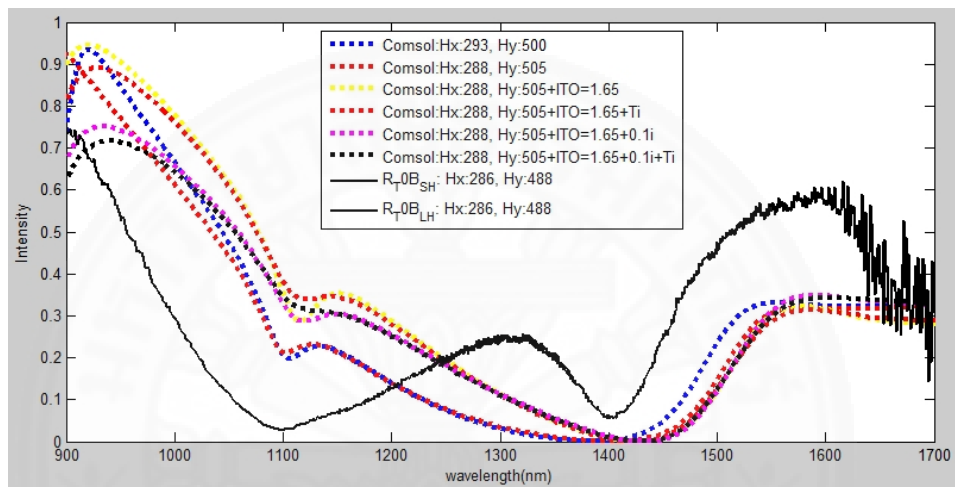
Figure 3.26 The reflectance in horizontal polarization.
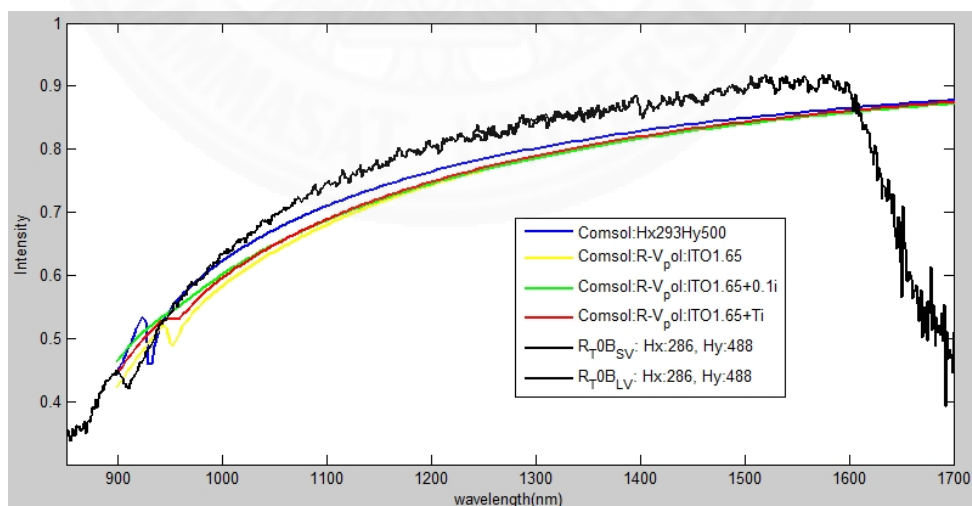
Figure 3.27 The reflectance in vertical polarization.

As the graph in figure 3.26-3.27, an experimental result with H_x 286 nm and H_y 488 nm is shown. In simulation setting, Ti is added and ITO's reflective index (n) is changed from1.9 to n=1.65 and n=1.65+0.1i.
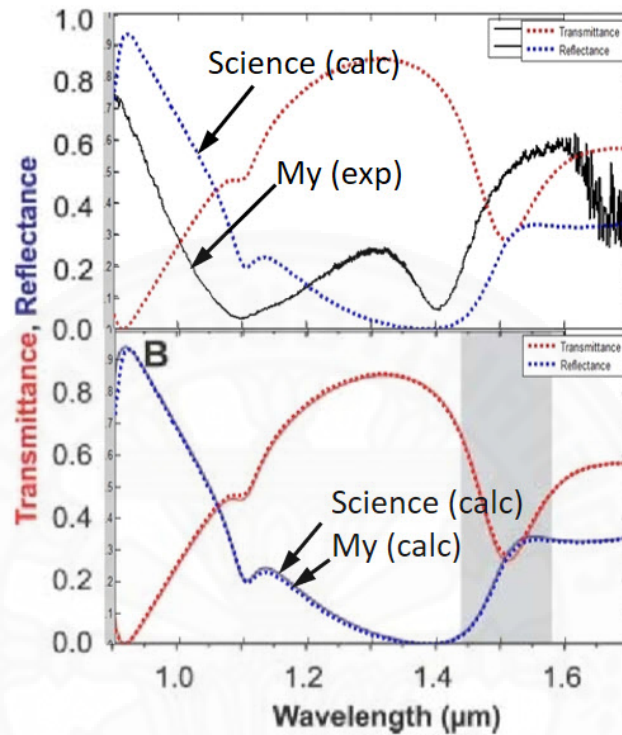
Figure 3.28 The transmittance and refraction of fishnet metamaterial compared with Dolling paper.

3.7 Conclusion

For preliminary study, the fabrication of a metal-insulator-metal plasmon waveguide with a linear taper based on Choo's configurations are succeeded, but using different fabrication technique which is a mass-productive process using a standard dry etching technique. The key improvements of our technique are to employ a mixed gas for taper fabrication and the realization of ultra-thin waveguide by the thin film addition following the taper process. By optimizing the compositions of a mixed gas and the etching sequence, the vertical tapers with an angle of 19 deg. is successfully produced, which is very close to the optimum angle given by Choo et al. The optimum CHF_3:O_2 flow rate ratio was found to be 60:40. The atomic layer deposition (ALD) technique

can produce thin films of a variety of materials and offer precise thickness with an atomic resolution to produce the ultra-thin dielectric film of Al_2O_3, instead of SiO_2. With this technique the hybrid structure had the minimum waveguide thickness as thin as 5.6 nm. For completing the MIM waveguide and its optical characterization, lateral patterning in the *y* direction is necessary as well.

Further, the fabrication of the fishnet metamaterial is also succeeded. As results, simulation calculations were reproduced, but experimental results were not because ITO thickness is much bigger than Dolling's paper and an influence of ITO seems to be dominant. In the next step, the design optimization of the fishnet dimension will be studied for it to be suitable for the integration with the MIM waveguide.

CHAPTER 4

SIMULATION AND RESULT

As the preliminary simulation, fabrication, and characterization, some information to re-design the MIM waveguide structure are considered. In this chapter, the design optimization of the grating in the body part and the single hole (slit) in the tip part are investigated for extracting the light source, to improve the NFT performance, and Characterization preparation are discussed. The total efficiency is also estimated for characterization feasibility. After that the fabrication results are confirmed and then for improving the design and re-fabricate over again until the final target is optimized. To calculate the total efficiency of our specimen, first, the dielectric constants at 830 nm-wavelength of Au, Ti, SiO$_2$, and Al$_2$O$_3$ are calculated and confirmed as shown in Table 4.1.

For Au dielectric constant by fitting to the experimentally determined dielectric function of gold [81] using 'lsqcuvefit' function of MATLAB, the suitable values of $\varepsilon_\infty, \omega_p, and \gamma$ are 6.5682, 8.2801, and 0.0820 respectively, the curve fit is shown in figure 4.1 and table 4.1 (Au), it shows the real and imaginary component ε_1 and ε_2 for a dielectric function of the 830 nm-wavelength.

Drude Model is

$$\varepsilon(\omega) = \varepsilon_\infty - \frac{\omega_p^2}{\omega^2 + i\gamma\omega} \tag{4.1}$$

when ε_∞ is constant $0 \leq \varepsilon_\infty \leq 10$, ω_p is the plasma frequency and γ is the collision frequency.

For Ti, SiO$_2$, and Al$_2$O$_3$ dielectric constants, there are fitted to the experimentally determined dielectric function of Ti [91] as shown in figure 4.2, SiO$_2$ and Al$_2$O$_3$ [89] using the cubic spline function of MATLAB as figure 4.1 and 4.3 respectively. The Ti's permittivity (ε) is -5.62+25.8i, n_{SiO_2}=1.45, and $n_{Al_2O_3}$=1.76, respectively.
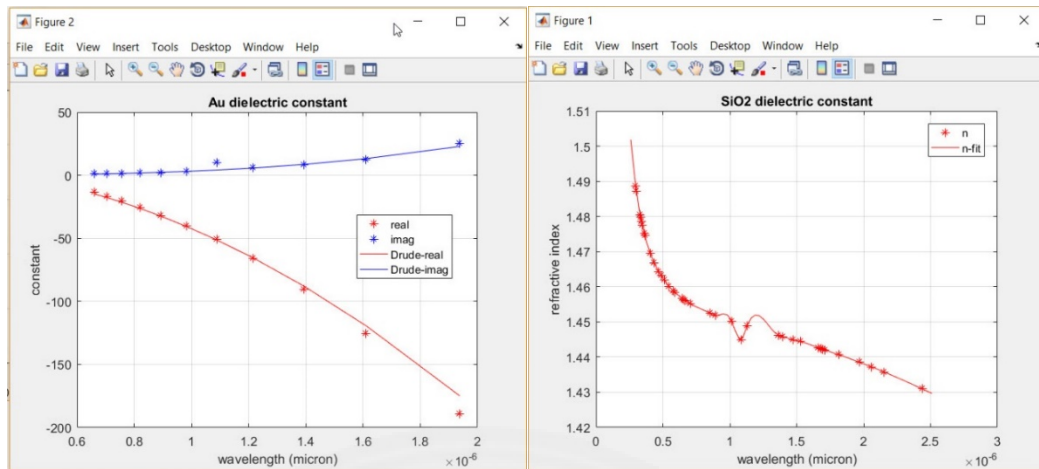
Figure 4.1 (Left) Au's dielectric constant, (Right) SiO₂'s dielectric constant.
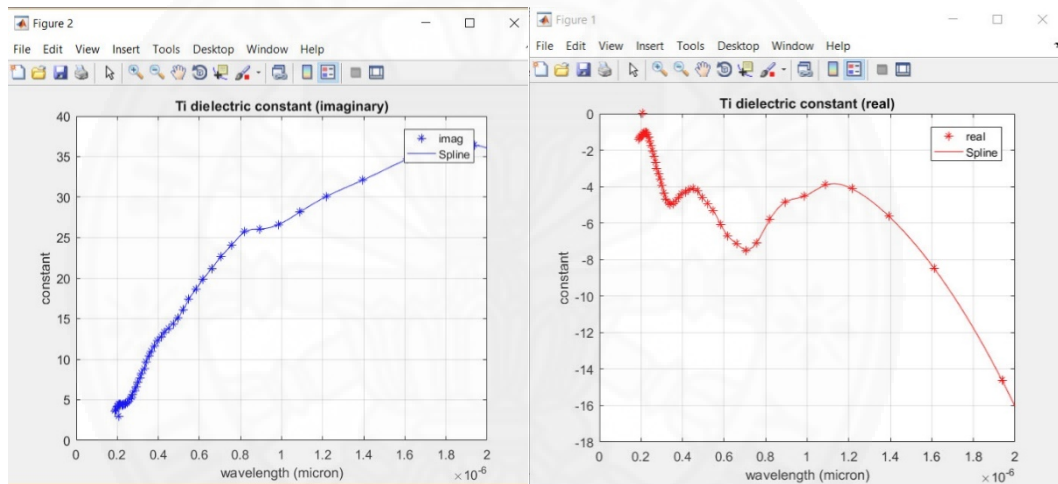
Figure 4.2 (Left) Ti-real part, (Right) Ti-Imaginary part of the dielectric constant.
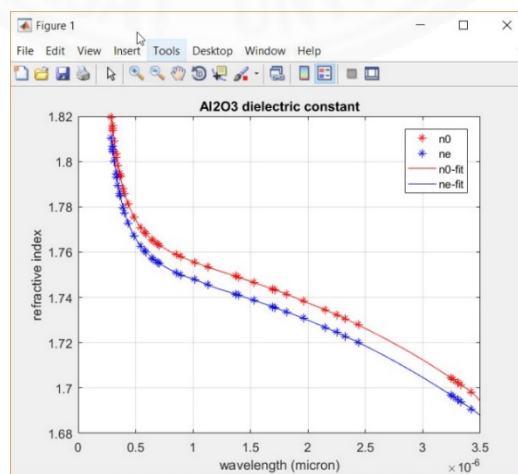
Figure 4.3 Al₂O₃'s dielectric constant.

Table 4.1 The dielectric constant of Au, Ti, SiO$_2$, and Al$_2$O$_3$ at 830 nm-wavelength.

@830 nm eV=1.49398	epsilon_in	Opmega_p	gamma	epsilon	n
auto expression @lsqcurvefit	6.5681	8.2801	0.0804	-27.2+1.81i	0.17+5.21i

Ti

@830 nm eV=1.49398	epsilon
cubic spline curve fit	-5.62+25.8i

SiO$_2$ dielectric constant from Palik handbook

@830 nm eV=1.49398	n
cubic spline curve fit	1.45

Al$_2$O$_3$

@830 nm eV=1.49398	n
cubic spline curve fit	1.76

4.1 Preliminary for re-designing

These simulations are prepared for the characterization process, a light propagated in the free space (it is assumed that the incident light is supplied as a Gaussian beam.) converts to a propagating mode in the MIM waveguide using the grating and deliver the SPPs through the MIM taper out for observing at the output part by using the single hole or silt. The wavelength of the propagating mode of the waveguide is different from that in the free space. When the period of the grating is equal to the wavelength of the propagating mode, the vertical incident light is turned by +/-90 deg. and efficiently converted to the propagating modes of the waveguide because the places with the same phases in the waveguide is simultaneously excited. Thus the period should be adjusted at the wavelength of the propagating mode. The wavelength of the propagating mode in a wide Au-SiO$_2$-Au waveguide is approximately $\frac{\lambda}{n_{SiO_2}}$. Therefore this dimension is applied for the first trial. The exact wavelength of the propagating mode is determined by the exact structure of the MIM waveguide and the next step is to numerically determine the optimum value. The

simulation used an initial value of $p\_hole = \dfrac{\lambda}{n_{SiO2}}$, and then optimal p_hole and w_hole in the body part, after that the optimal of p_hole and w_hole in the tip part are calculated, and then finally the combination of two parts are integrated and to calculate the coupling efficiency and power enhancement.

4.1.1 The optimization of the input part

The optimization of period grating, the geometry, the parameters, and variables are set as shown in the figure 4.4-4.7. The Gaussian beam wavelength is 830 nm, the polarized in the x direction. First, optimize the period of the grating by fixing the hold width at 100 nm. The starting period is $\dfrac{\lambda_0}{n_{SiO2}} = \dfrac{830\ nm}{1.45} = 572.4\ nm$ and rough adjustment at first. The results are shown in figure 4.8-4.15.
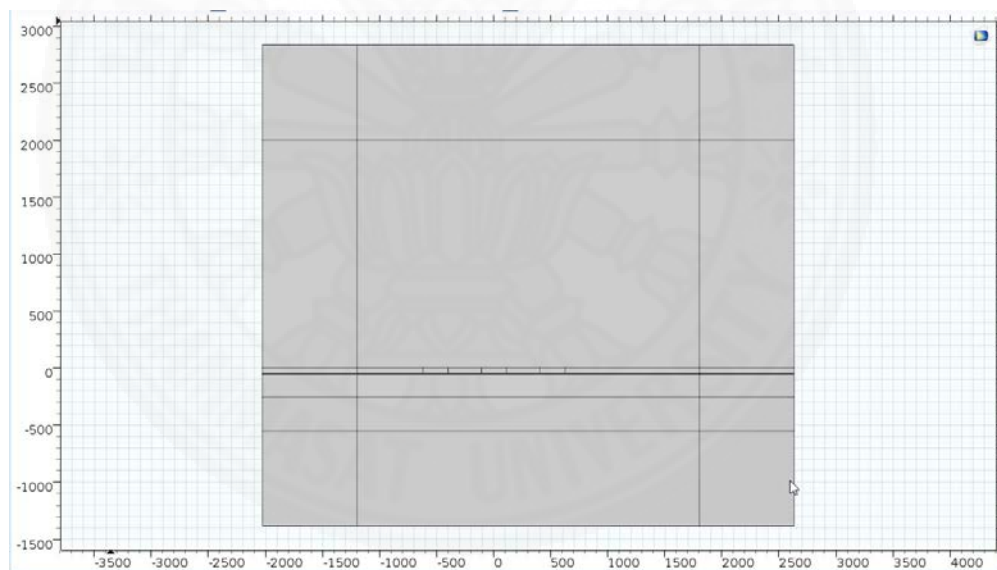
Figure 4.4 The geometry, direction, and dimension.

Figure 4.5 The parameters setting.

Figure 4.6 The variable setting.
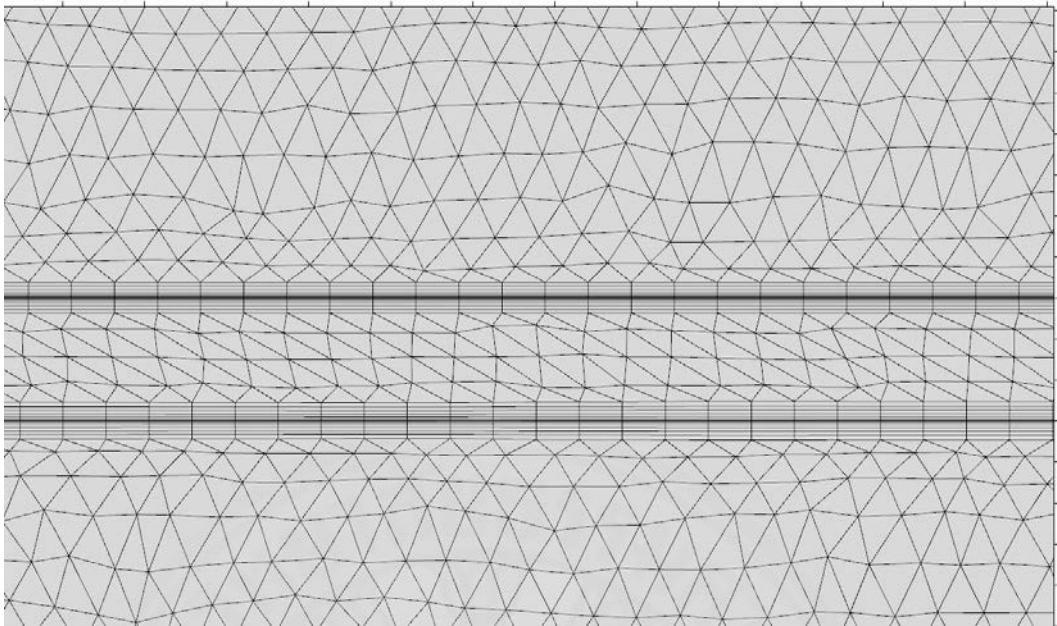
Figure 4.7 The magnified mesh.
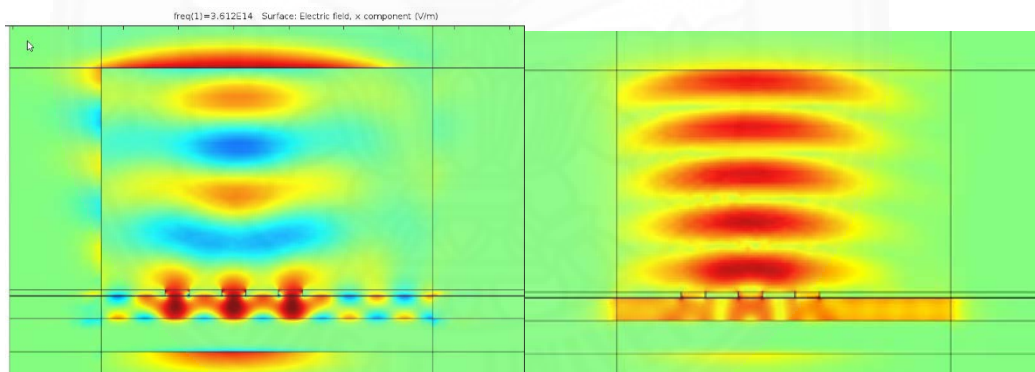
Figure 4.8 (Left) Electric field, x-component (Right) Electric field norm E.
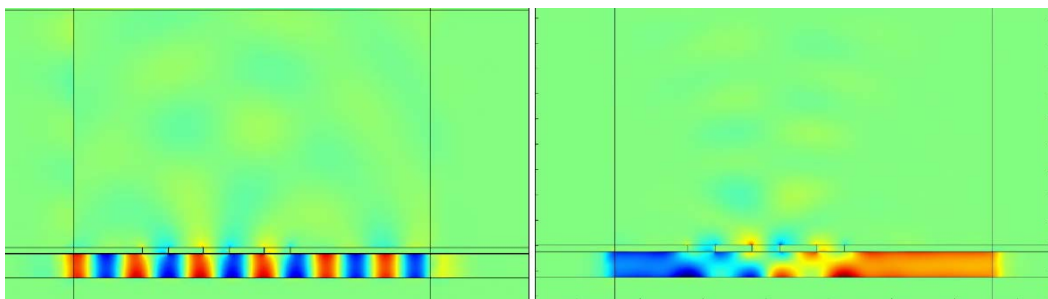
Figure 4.9 (Left) Electric field, y-component, the wavelength in the sio2 layer (peak to peak) is about 500 nm. (Right) Power flow in y direction.
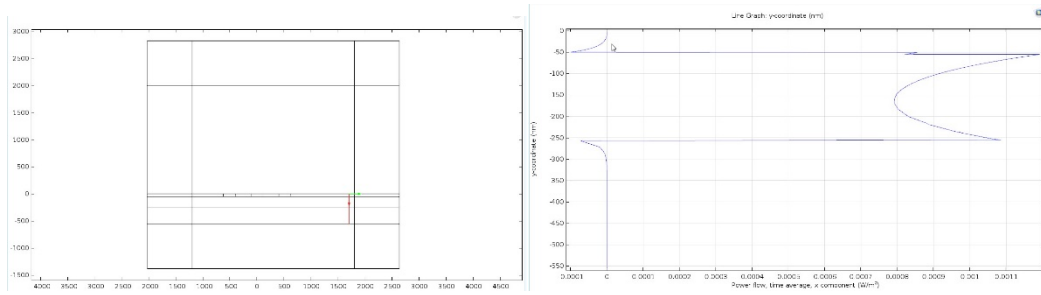
Figure 4.10 (Left the 2D for observing the Pt of a body part in x direction at the body part at x=1,700 nm. (Right) The profile of the power flow in the body.
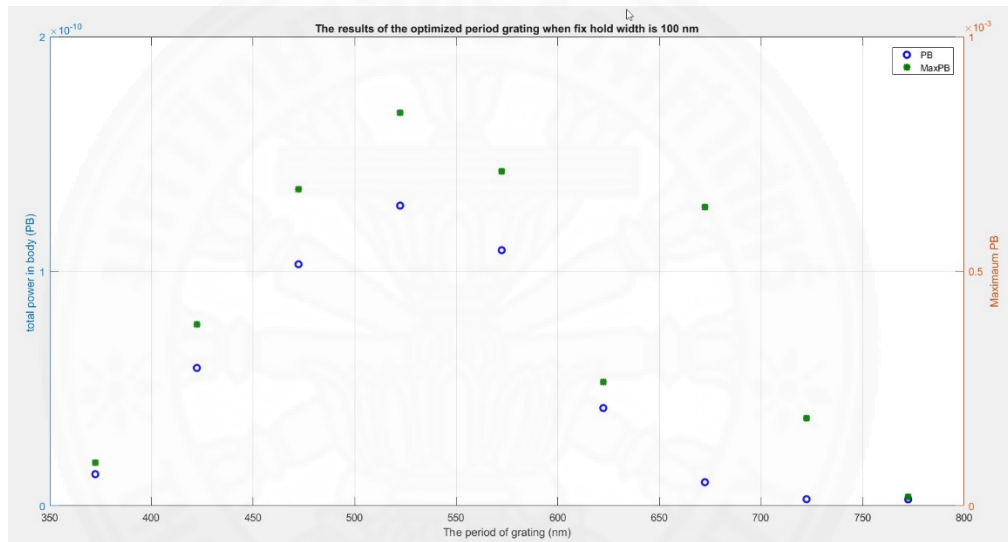
Figure 4.11 The optimum hholdsperiod grating when fix holds width is 100 nm.

From the results, the highest value is at 522.4 nm, then the period grating is adjusted, the results are shown in figure 4.12.
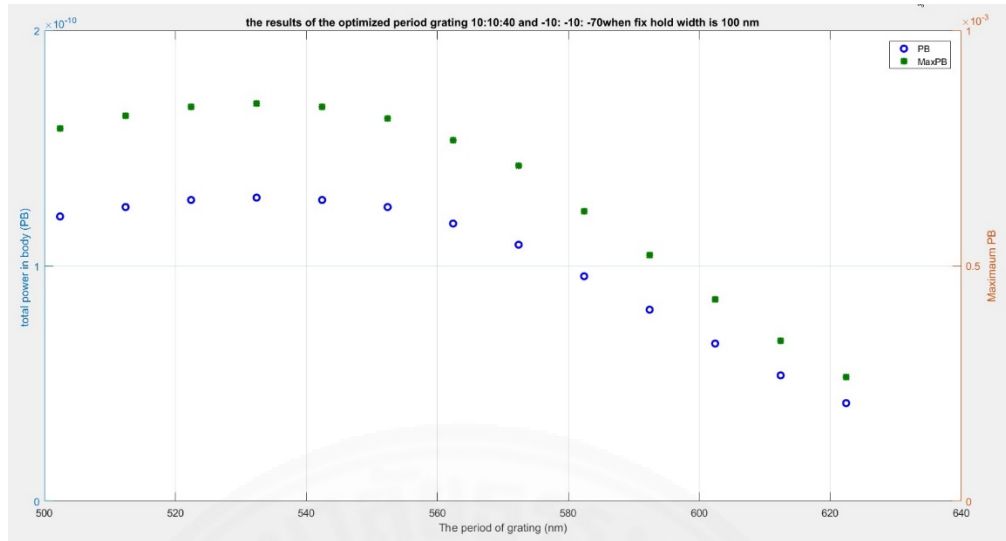
Figure 4.12 The optimized period grating 10:10:40 and -10: -10: -70 when fix hold width is 100 nm.

From the results, the highest value is at 522.4 nm, then the period grating is adjusted, the results are shown in figure 4.13.
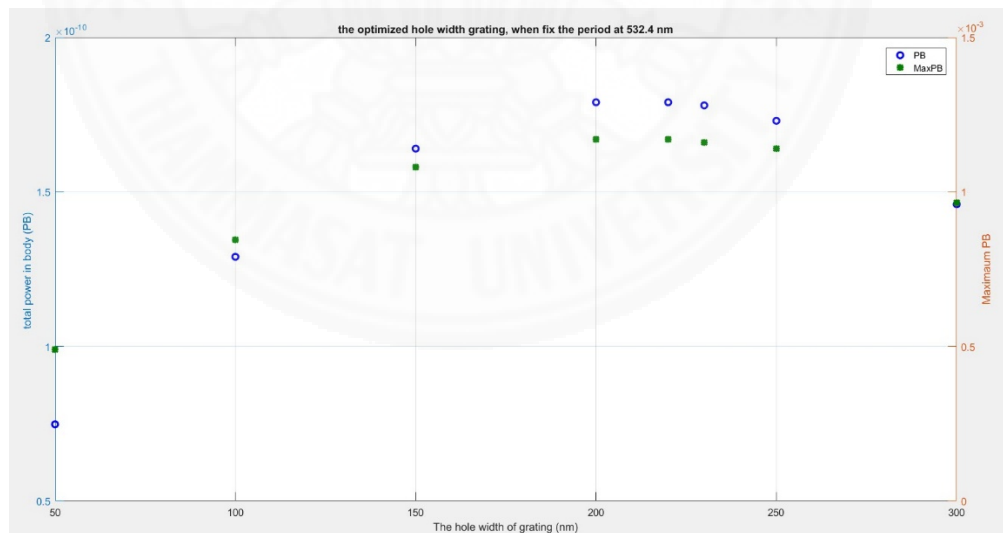
Figure 4.13 The optimized hole width grating, when fix the period of 522.4 nm.

The highest PB and Max_PB values of the hole width is about 200 nm, after that the hole is adjusted, then the highest PB and Max_PB are obtained when the hole width is 220 nm. After the optimization of the period grating is repeated by

fixing the hole width at 220 nm. The result of the second p_holes are shown in the figure 4.14.
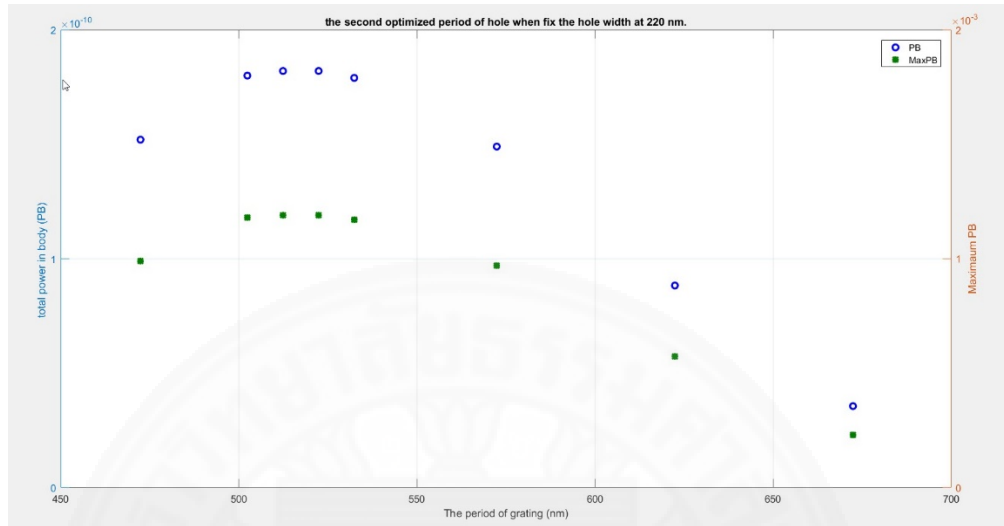
Figure 4.14 The second optimized p_hole when fix the hole width at 220 nm.

Then, the second value of w_hole is optimized using the hole width as 512.4 nm. The results are shown in figure 4.15.
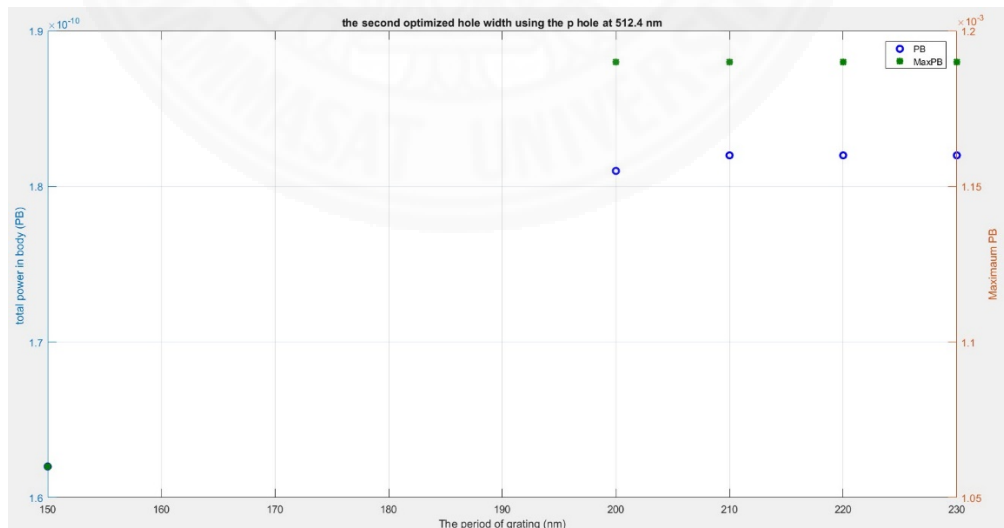
Figure 4.15 The second optimized w_hole using the p_hole at 512.4 nm.

Therefore, the optimized p_hole and w_hole are 512.4 nm and 220 nm, respectively.

4.1.2 The optimization of the output part

The purpose of the grating at the tip is to convert the propagating mode in the MIM waveguide to the free-space wave propagating in the z direction. In the future experiment, the intensity of the light coming out from this grating at the tip will be measured using the microscopic system. However, in Optics, it is known that the efficiency in the reverse process is identical. Therefore, the grating is optimized by conversing a free-space wave to the MIM waveguide mode. The optimum condition could also be optimized for the reverse process: conversion of MIM waveguide mode to the free-space wave.

This time, the initial value of the period should be shorter. It should be set around the wavelength of the propagating mode of the MIM waveguide at the tip. It is 110nm according to the simulation result of our journal [2]. The width would start at 50 nm.

4.1.2.1 The grating at the tip

First, optimize the period of the grating by fixing the hold width (wt_hole) at 50 nm. The starting period (pt_hole) is 110 nm as figure 4.16.
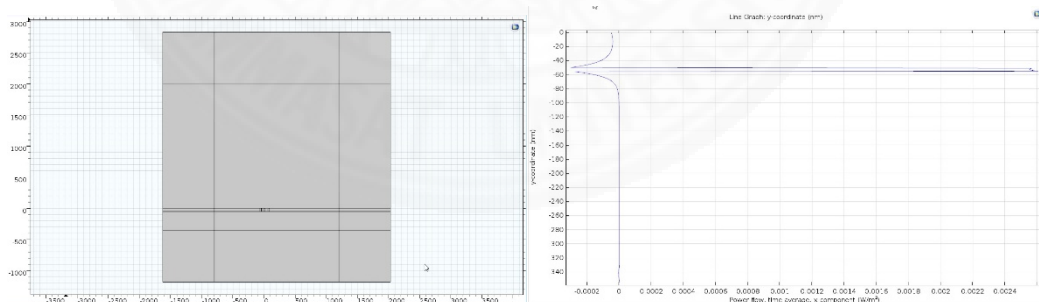
Figure 4.66 (Left) The geometry, direction, and dimension. (Right) the profile of the power flow at the tip.
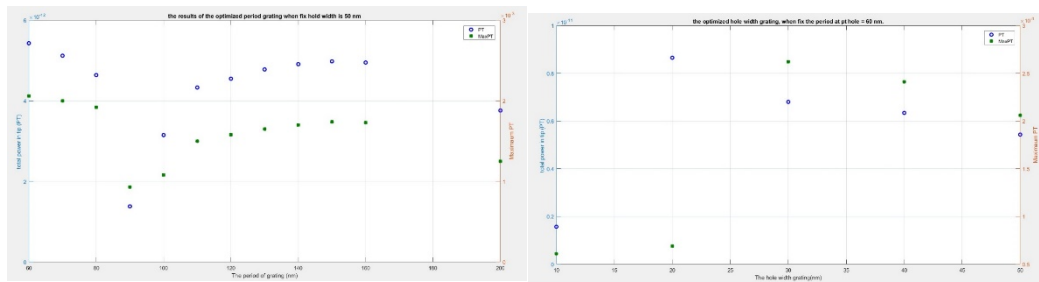
Figure 4.77 (Left) The results of the optimized period grating when fix hold width is on nm and fix pt_hole=60 nm on the right side.

From the results, the highest values were at pt_hole = 60 nm, then the hole width of grating is adjusted, the results are shown in figure 4.17 (right). The highest PT and Max_PT values are found when the hole width is 30 nm and the period grating is 60 nm. After that the optimization of the period grating is repeated by fixing the hole width at 30 nm. The results of the second pt_hole are shown in figure 4.18.
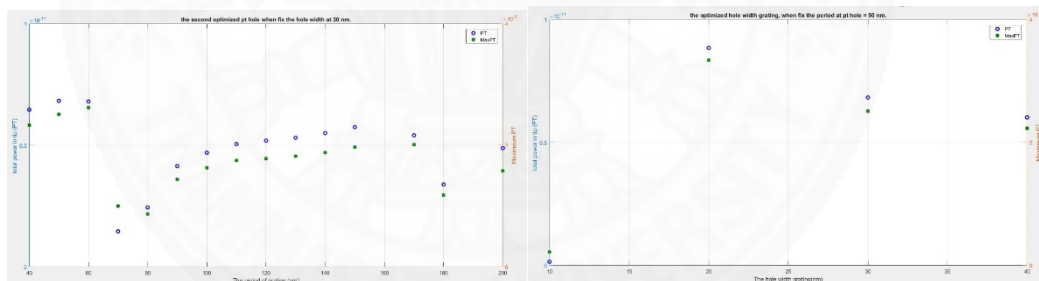
Figure 4.18 (Left) The second optimized pt_hole when fix the hole width at 30 nm and (Right) fix pt_hole=50 nm.

Because the values of pt_hole=50 and 60 is the highest in different, the period is equal to the waveguide of the guided mode or, the period = m * waveguide of the guided mode (m = 1, 2, 3,...). So, optimum pt_hole appears periodically. This is a theoretically. The optimum m can be found only by detailed simulation. But refer to our results, the optimum pt_hole seems to appear periodically, but they are m = ~0.5 and ~1.5. So, something might be wrong. In the previous example for the body part, the period was very large, so if there are many periods it may need a

larger model. But previously the fields around the grating was sufficiently periodic, which means that the grating is exciting the guided mode efficiently. The 3 holes of grating in the body part are enough. So, the holes to 5, 7, 9, and 11 are added to the structure.
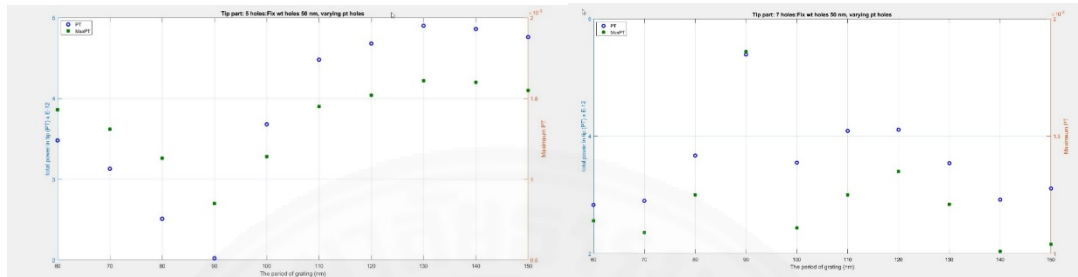
Figure 4.19 (Left) The 5 holes grating, the optimized period grating when fix holds width is 50 nm. (Right) The 7 holes.
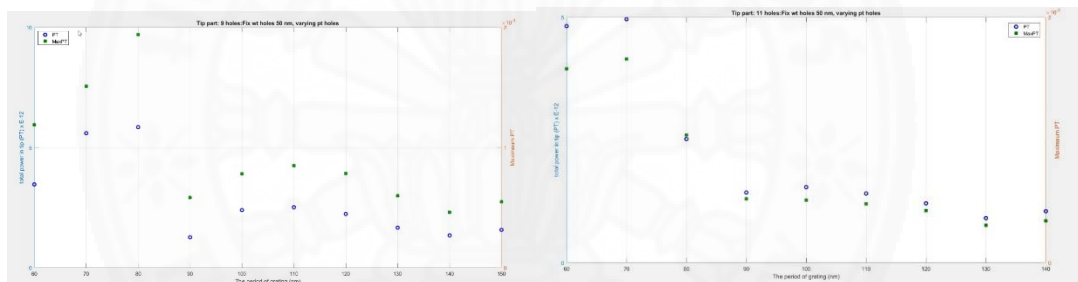
Figure 4.20 (Left) The 9 holes grating, (Right) the 11 holes.

From the results of adding 5, 7,9, and 11 holes grating in the tip part, the pt_hole close to 110 nm can be made the highest values of the power flow (PT) and the maximum PT are 130 nm and 90 nm when added 5 and 7 holes grating, respectively.

For the tip, the array of holes would not be a good solution. By increasing the number of the holes, the fields around the grating has become more periodic, which was a good result. However, the fields in the waveguide at the grating part is very much affected by the presence of holes. For a thick MIM waveguide in the Body part, the array of holes was good. Therefore, two ideas for solving this problem

are proposed, the first idea is a single hole or a slit and the second idea is the array of bumps instead of holes.

4.1.2.2 The slit at the tip

The wt_hole is set at 10:10:130 nm. The results are shown in figure 4.21-4.22. The highest PT when the single hole width is 60 nm and the highest maximum PT when the single hole width is 90 nm.
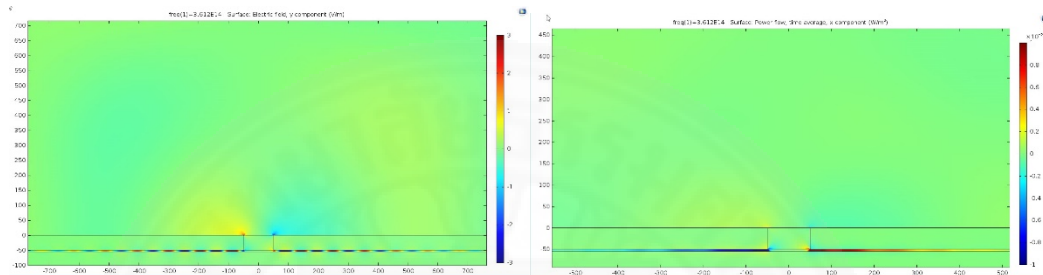
Figure 4.21 (Left) Electric field, x-component (Right) Power flow in y direction.

The cut 2D line for observing the power flow is in *x* direction at body part at 400 nm from the hole border and y is -0.5 to-355 (the upper gold to the lower gold). The hole width is varied as 10:10:130 nm, the results are shown in figure 4.22.
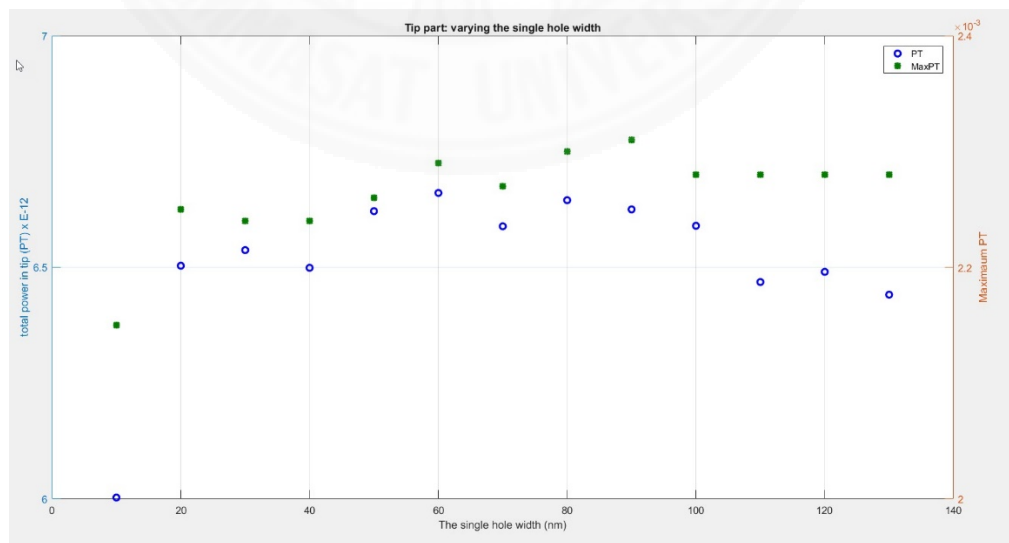
Figure 4.22 The varied single hole width, 10:10:130 nm.

4.1.2.3 The array of bumps at the tip

The second idea is the array of bumps instead of holes. The thickness of the bumps is set at 50 nm and the material is gold. The number of the bumps is set at 7. First, the wt_hole is set at 50 nm and varying the pt_hole, start with 110 nm. The results are shown in figure 4.23-4.24.
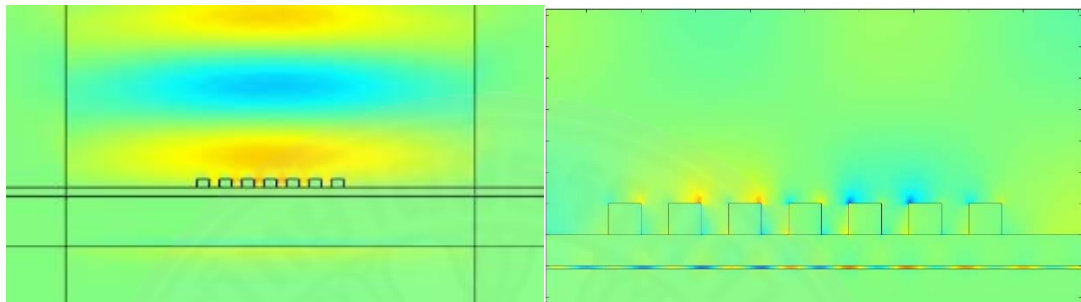
Figure 4.23 (Left) Electric field, *x*-component (Right) Power flow in *y* direction.
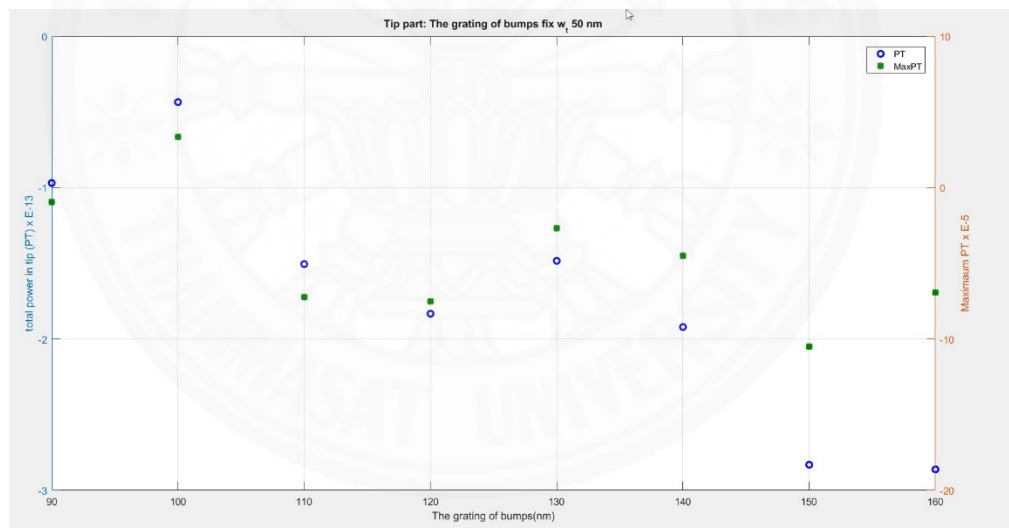
Figure 4.24 The results of the optimized pt_hole when fix wt_hole is 50 nm.

As the results, the graph of power flow is reversed, different from the single hole and previous grating in the tip. The bump array showed strange results (negative values), since the PML's were not functioning perfectly and produced an unphysical result. The MIM waveguide mode excited by the bump array was too small. But this is supposed that it would work well if we reduce w_gold.

Next, the effect of the grating and the single hole will be investigated by combine both with the MIM waveguide and observe the transmission efficiency of this taper structure with p_hole=510 nm and w_hole=220 nm and the tip part that should be a single hole with wt_hole=60 nm.

4.1.3 The first integration of the MIM waveguide and metamaterial
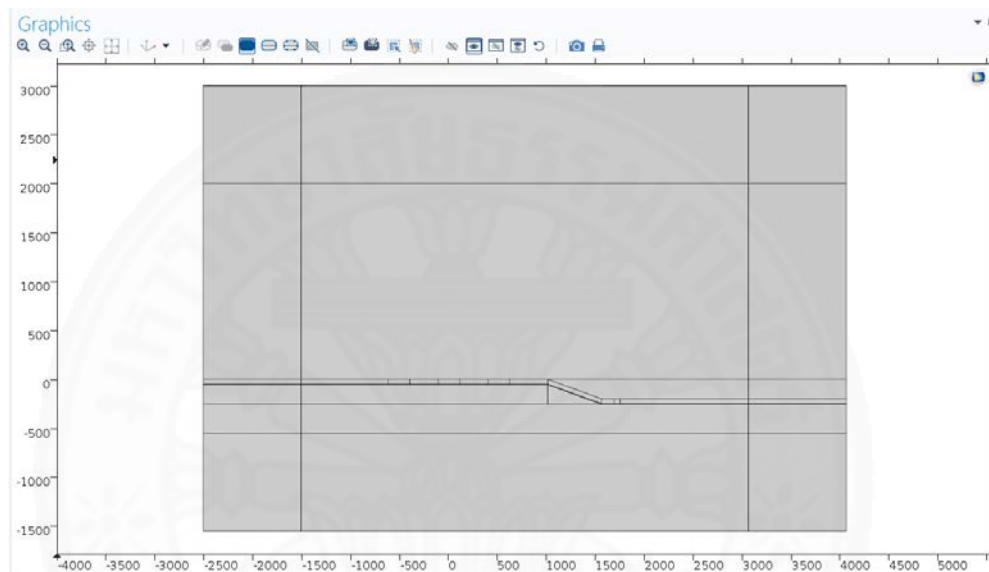
Figure 4.25 The geometry, direction, and dimension. The example is the case of the 500 nm-distance before the taper section (Before_T), w_hole 220 nm, p_hole 510 nm, and wt_hole 60 nm.

The distance between grating and taper are fix at 500 nm and 550 nm, then the position of wt_hole is optimized which starting from 100:10:300 nm of both cases. The results are shown in figure 4.26-4.36.
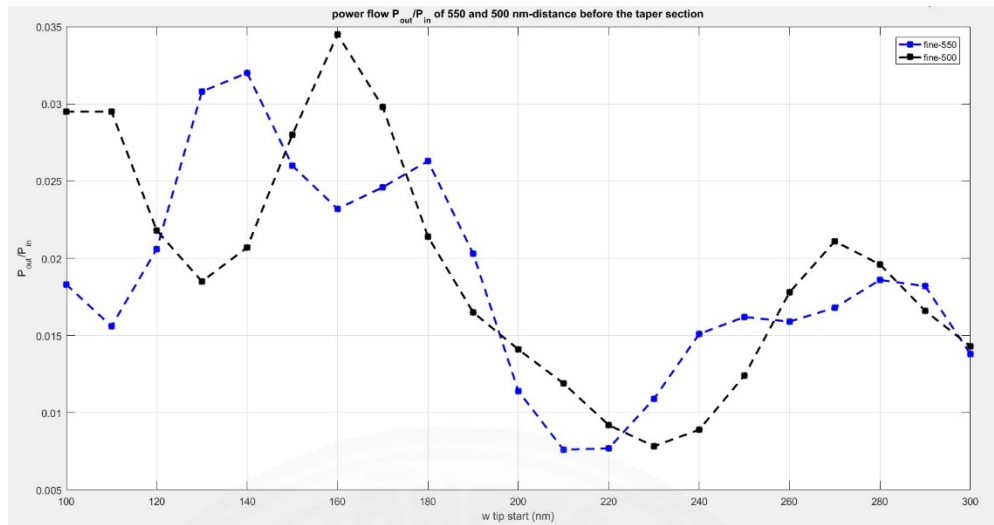
Figure 4.26 The optimum wt_hole is 160 nm.
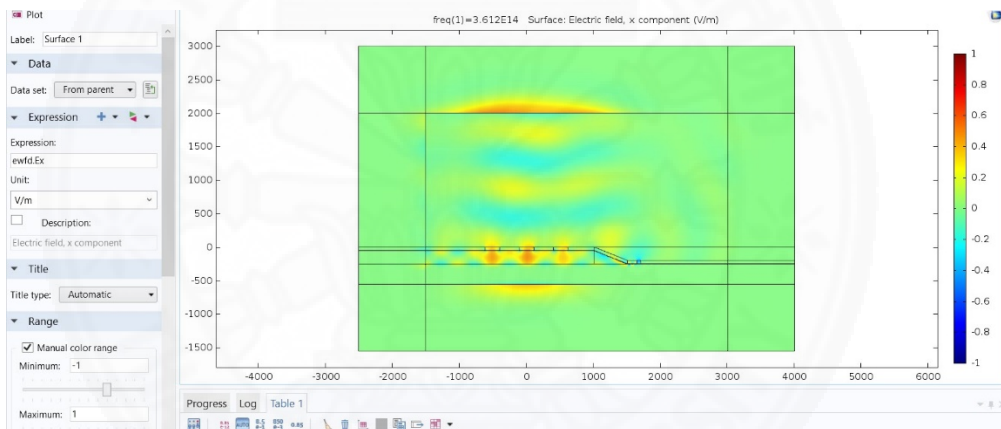
Figure 4.27 Electric field, *x*-component.
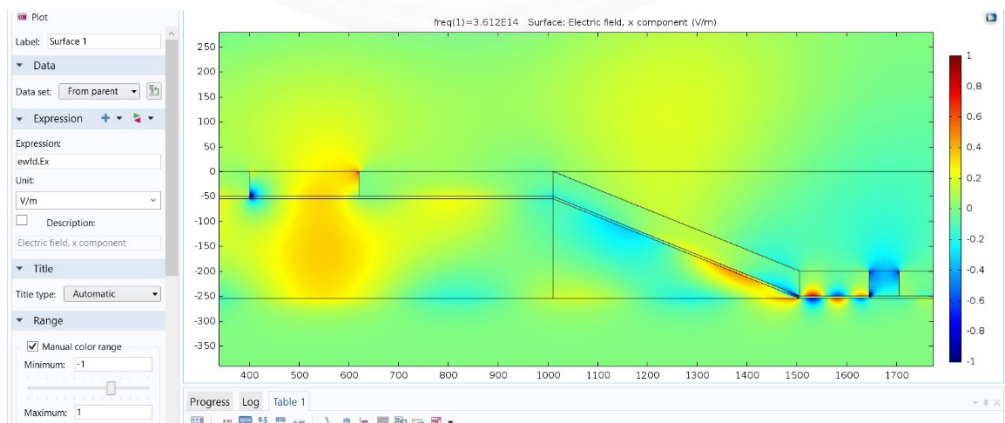
Figure 4.88 The magnified *Ex*.
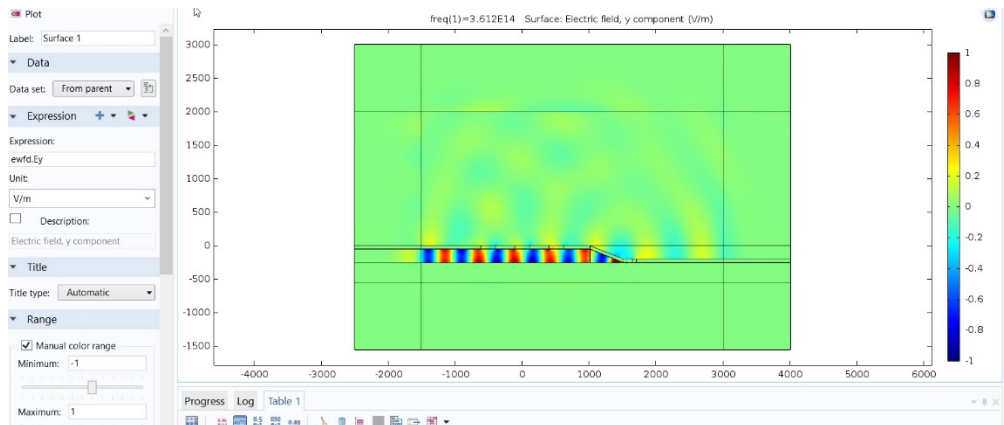
Figure 4.99 Electric field, *y*-component.
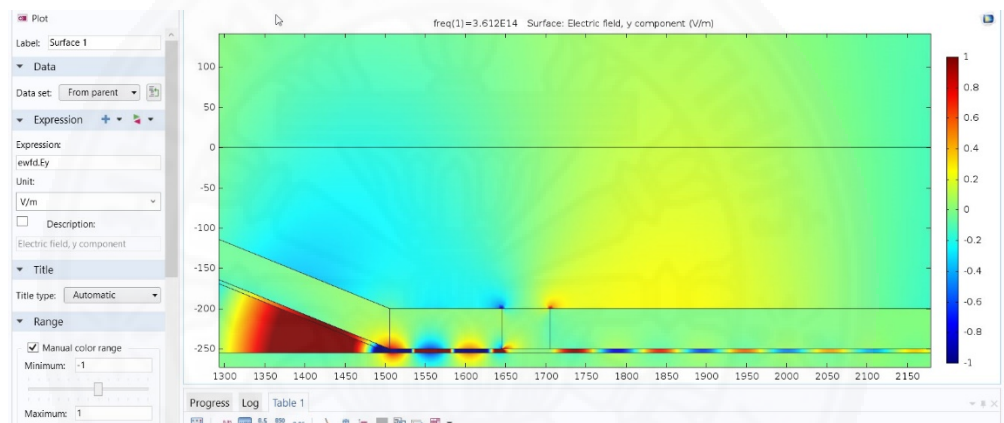
Figure 4.30 The magnified *Ey*.
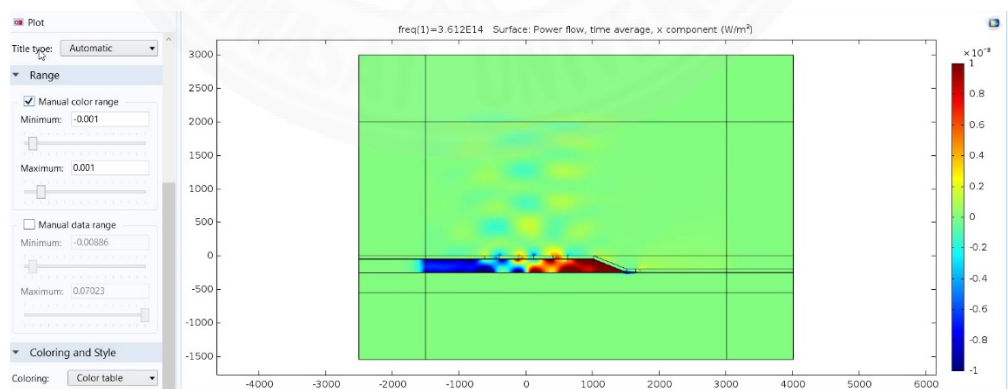
Figure 4.101 Power flow in *x* direction, range -0.001 to 0.001.
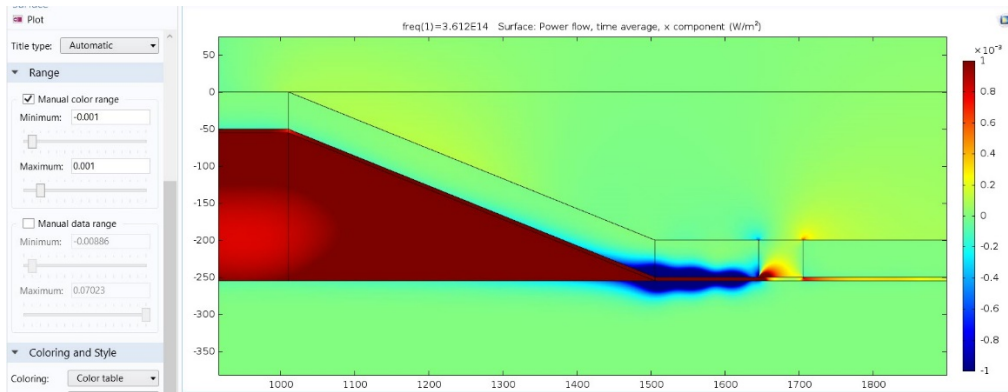
Figure 4.112 The magnified power flow in *x* direction, range -0.001 to 0.001.
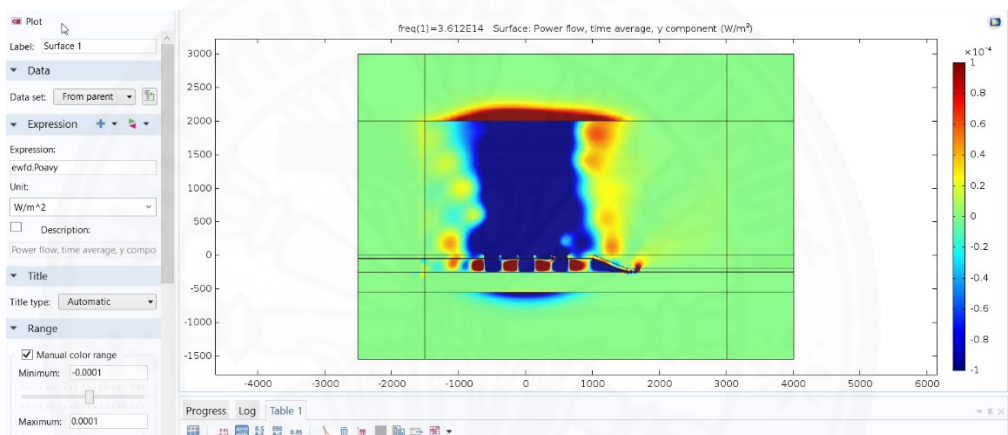
Figure 4.123 Power flow in *y* direction, range -0.001 to 0.001.
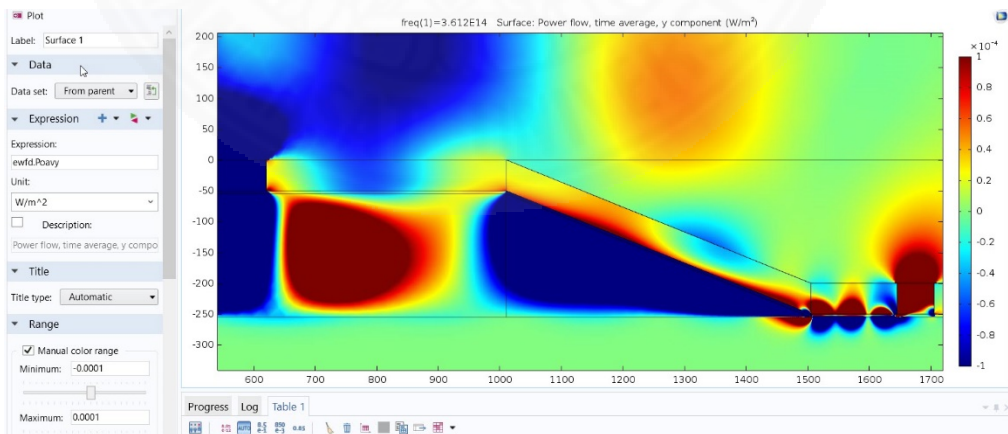
Figure 4.134 The magnified power flow in *y* direction, range -0.001 to 0.001.
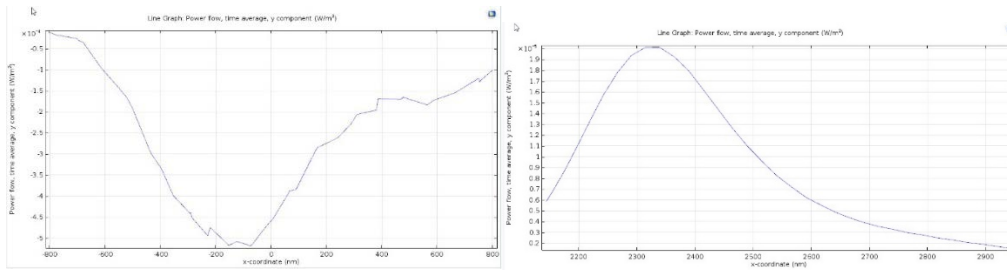
Figure 4.145 (Left) The profile of P_{in}, (Right) the profile of P_{out}.
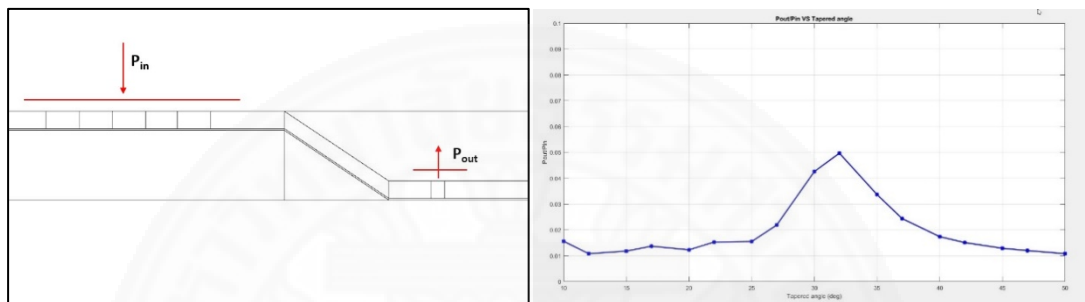
Figure 4.156 Pin and Pout Cut Line2D for observation, (Right) the optimum taper angle is 32 deg.

For the efficiency P_{out}/P_{in} of the grating input/slit output structure is P_{out}/P_{in} =1.8247e-10/ 6.6605e-12 = 3.65% that is efficient for doing the experiment that means about 3.65% of the incident light comes out from the hole. If light as high as 3% comes back, the experiment would be possible. It seems that our new target angle is 32 deg. The next experiment will be made to realize various angles from 10 to 50 deg. and compare their efficiency. In summary, so far, the first preliminary fabrication parameters will be as;

- Input grating   - Output hole
  p_hole=510nm   wt_hole=60 nm
  w_hole=220 nm

- Position of the input grating   - Position of the output hole
  before_T=500 nm   w_tip_start=170 nm
- Taper angle 32 deg.

4.1.4 The investigation of the input (Pin_0)
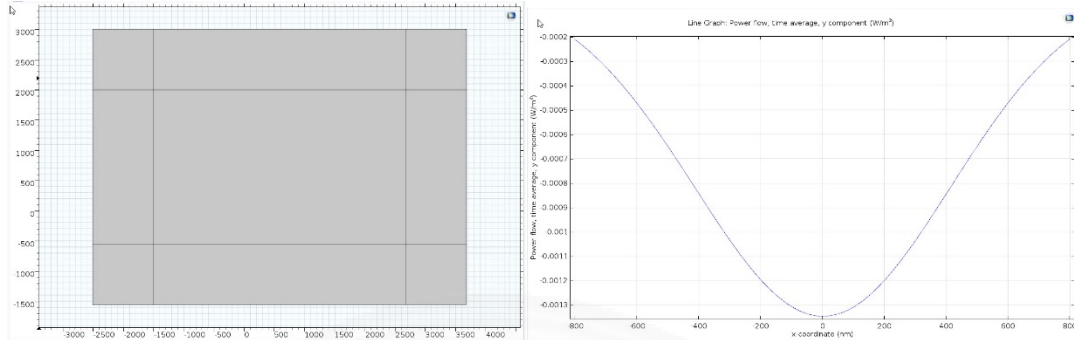
Figure 4.167 The geometry, direction, and dimension for no structure. (Right) The profile of power flow at P_in0, the integrated power of P_in0 is 1.3221E-9.
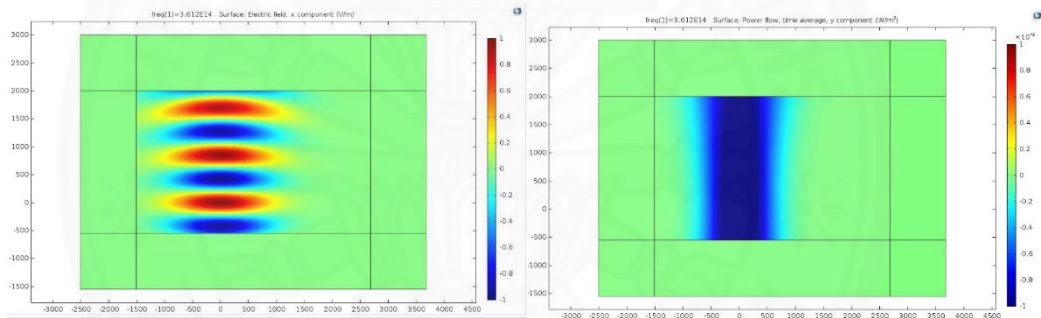
Figure 4.178 (Left) Electric field, x-component, (Right) Power flow in y direction.

4.2 The simulation of the first specimen

The thin layer of Al_2O_3 as 5 nm can produce the smallest spot size, but for the combination of the grating as input and the slit as output. As results, at 5 nm the propagated length will decay immediately as shown in figure 4.39 and table 4.2. The 20 nm- thickness is better. So, the 20 nm-thickness is selected and the parameters; the hole width (wt_hole), the distance between the taper and slit in the tip area (w_tip_start), and the taper angle for the 20 nm-thickness of Al_2O_3, are optimized as shown below.
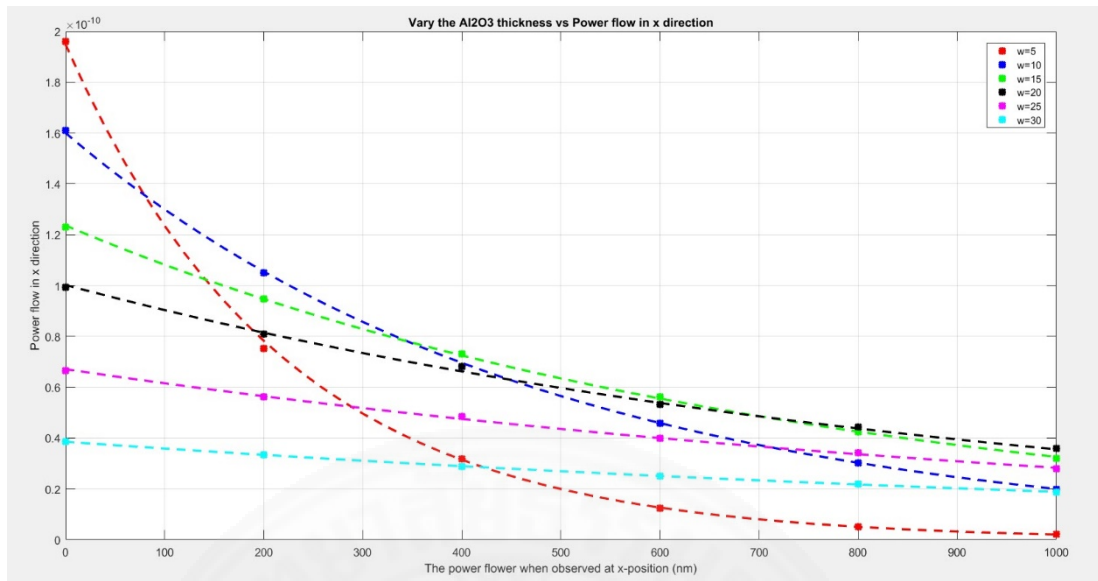
Figure 4.189 The power flow in *x*-direction when varied the Al$_2$O$_3$ thickness.

Table 4.2 The propagation length when varied the Al$_2$O$_3$ thickness.

W_ Al$_2$O$_3$ (nm)	Propagation length (nm)
5	219.2982
10	480.3074
15	749.6252
20	965.2510
25	1,158.6
30	1,396.8

For finding the wt_hole in case of the 20 nm-thickness of Al$_2$O$_3$, the structure without the taper is applied then varied the wt_hole 10-1000 nm. The Gaussian beam wavelength is 830 nm, the polarized in the *x* direction. The results are shown in figure 4.40.
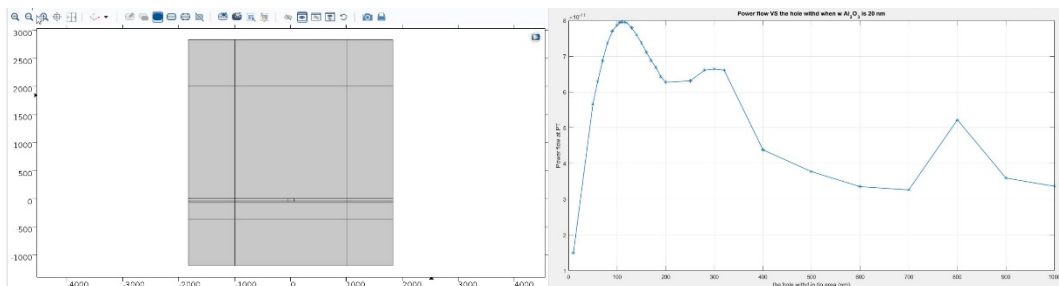
Figure 4.40 (Left) The geometry, (Right) the varied slit width starts 10 to 1000 nm, when w_Al$_2$O$_3$ is 20 nm. The optimum slit width is 110 nm.

89

For the w_tip_start (the position of the slit), the structure is combined with taper and fix w_hole (body) 220 nm, period 510 nm, before T 500 nm, w_Al$_2$O$_3$ 20 nm, and wt_hole is 110 nm then vary the w_tip_start 100:100:1000 nm, then varied w_tip_start around 200-400 nm. The results are shown in figure 4.41.
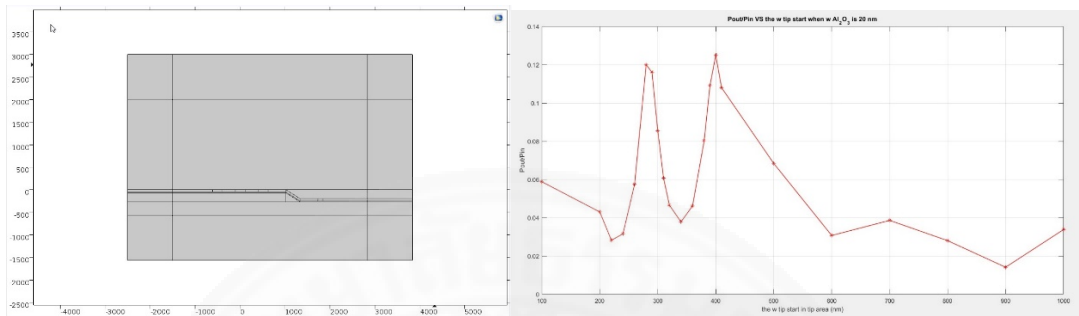
Figure 4.191 (Left) The geometry, (Right) The transmitting efficiency (P$_{out}$/P$_{in}$) vs the w_tip_start, the optimum the w_tip_start is 400 nm.

The structure is fixed w_hole (body) 220 nm, period 510 nm, and before T 500 nm, w_Al$_2$O$_3$ 20 nm, wt_hole 110 nm, and w_tip_start at 400 nm. Then the varying of taper angles are 10-50 deg. The results are shown in figure 4.42.
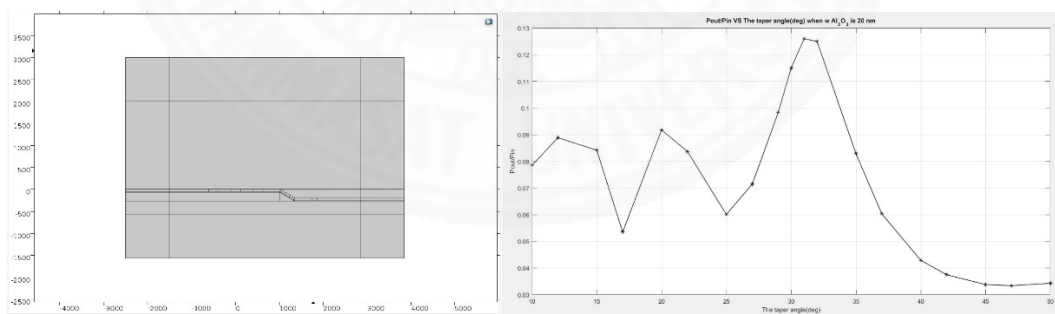
Figure 4.202 The geometry, (Right) the transmitting efficiency (P$_{out}$/P$_{in}$) vs the taper angle, when w_Al$_2$O$_3$ is 20 nm. The optimum the taper angle is 31 deg.

The first specimen's (T020) parameters are P=510 nm, W=220 nm, pt_hole 120 nm, w_tip_start 400, Taper angle 30 deg., number of grating is 20, Before T are 3, 5, and 10 μm.

4.3 The simulation for the second specimen

As the Atomic Layer Deposition machine for deposit Al_2O_3 is fixed. So, the material is changed to SiO_2, to study the effect of SiO_2 is important. Because of the fabrication reasons, Ti is added for adhesion inside the Au and SiO_2 layer, so the effect of Ti will calculate and will compare it with and without Ti layer by observing the propagate length (decay) as shown in figure 4.43-4.46 and Table 4.3-4.4. Because of the preliminary optical measurement, the guided wave through MIM waveguide could not observed, but the guided waves along the surface of the Au were easily observed. The suspect is that the effect of Ti was more serious than expected. Then, to add Ti at the outer surface for reducing the surface plasmon modes outside and the effect of the deviation of the grating period should be clarified by calculating the full width half maximum (FWHM) graph. Next, the grating, taper, and slit part will be combined into the simulation model, the distance between grating and taper should be carefully determined, the distance between the end of the taper and the slit will be optimized and finally the total efficiency will be calculated. All simulation parameters will be the second specimen parameters for the second fabrication.

4.3.1 The absorption loss of Ti

The simulation results are shown as follow;

(1) Thick part: SiO_2 200nm, with/without Ti, propagation length.

(2) Thin part: SiO_2 20nm, with/without Ti, propagation length.

(3) Taper part: optimum theta, with/without Ti, efficiency.

(4) Total efficiency: rough estimation, with/without Ti.
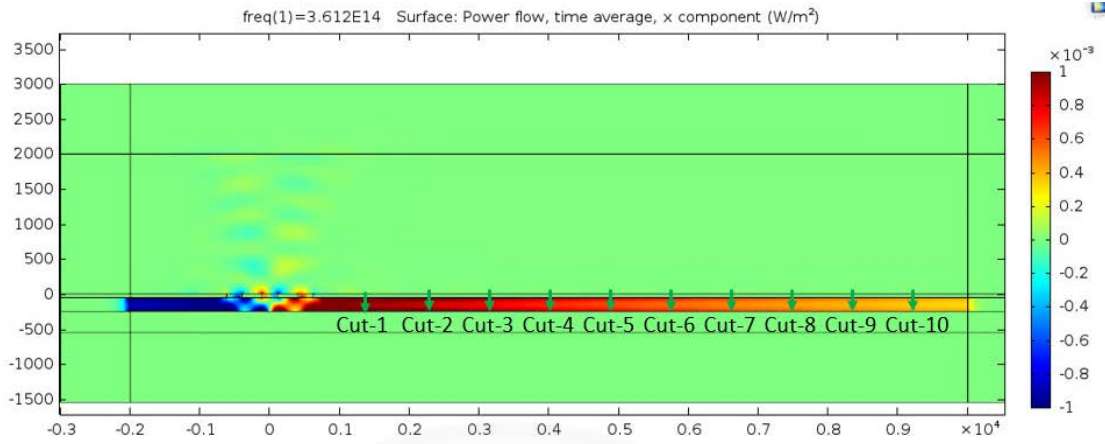
Figure 4.43 The cutline for observing the power in x direction every 1 μm from the grating for thick layer and 500 nm from the slit for thin layer.
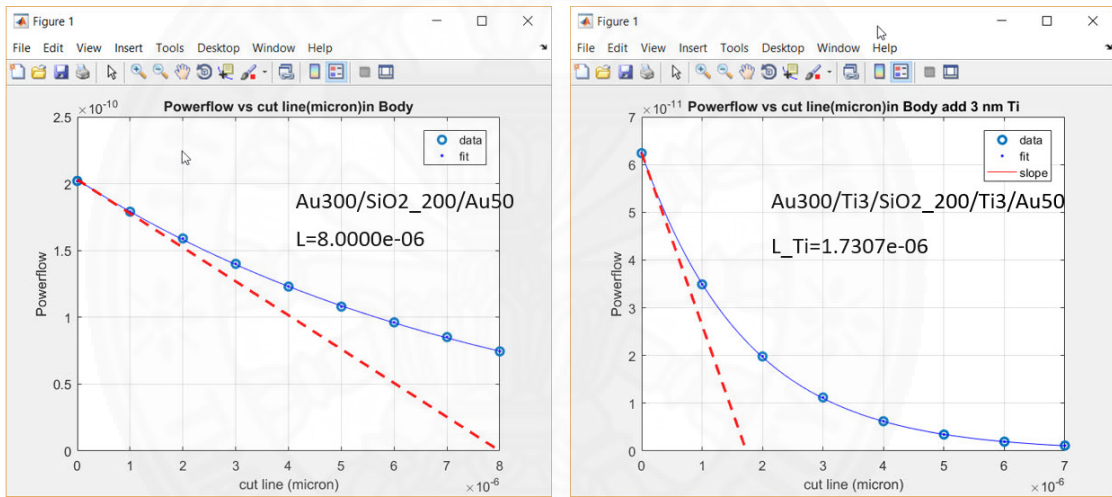
Figure 4.214 Thick layer with and without Ti (inside)
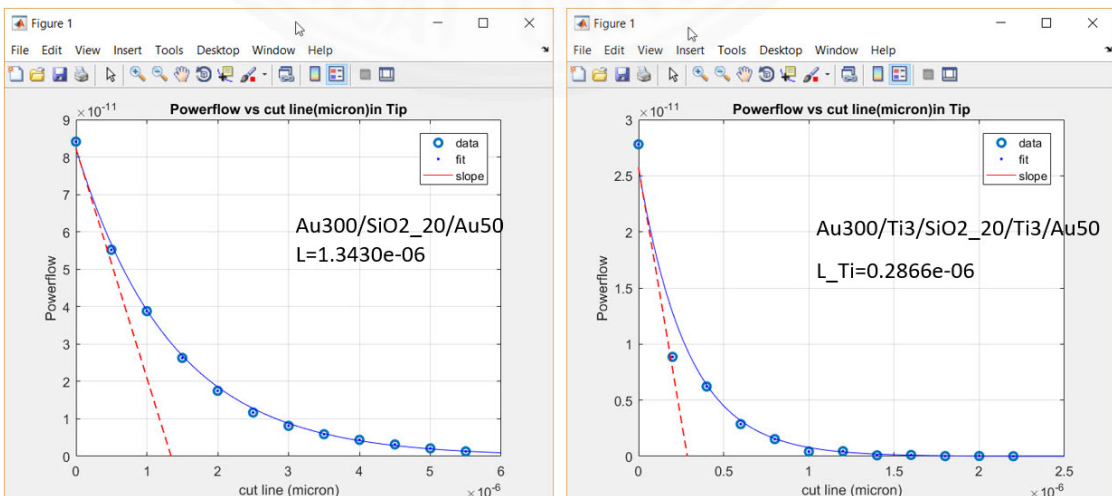
Figure 4.225 The propagate length of the thick layer with Ti and without Ti (inside)

Table 4.3 The propagate length of the first specimen

Structure		Propagate length: L	Dimension
Body	Au300/Ti3/SiO$_2$ _200/Ti3/Au50	1.7307E-06	P510, Hold width 220
	Au300/SiO$_2$ _200/Au50	8.0000E-06	P510, Hold width 220
Tip	Au300/Ti3/SiO$_2$ _20/Ti3/Au50	1.3430E-06	Hole width is 170 nm
	Au300/SiO$_2$ _20/Au50	0.2866E-06	Hole width is 170 nm
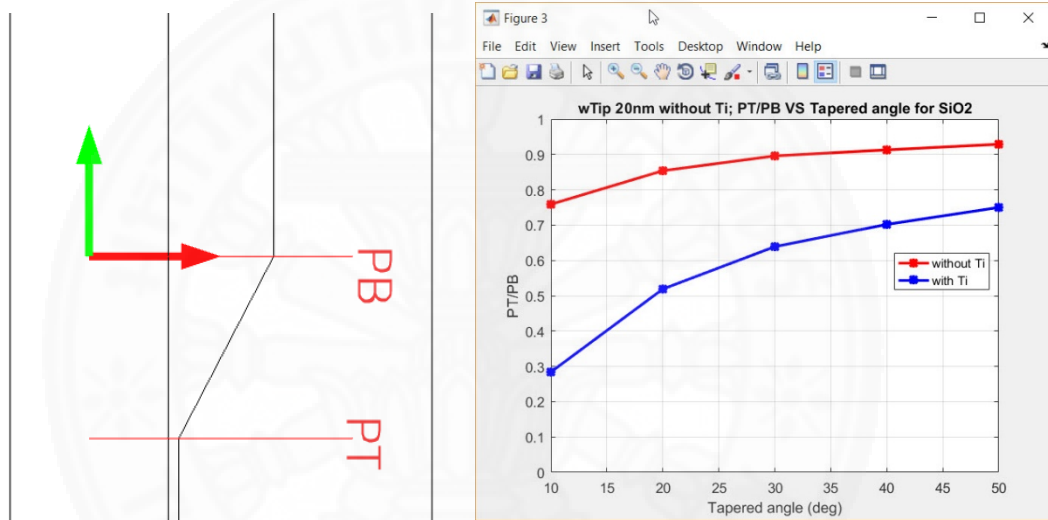
Figure 4.46 (Left) The Cutline for observing P_B and P_T (Right) the taper part: optimum theta, with/without Ti, efficiency.

$$\eta_{body} = \exp\left(-\frac{x_{body}}{L}\right) \quad \eta_{taper} = \frac{P_t}{P_B} \quad \eta_{tip} = \exp\left(-\frac{x_{tip}}{L}\right)$$

$$\eta_{total} = \eta_{body} \times \eta_{taper} \times \eta_{tip}$$
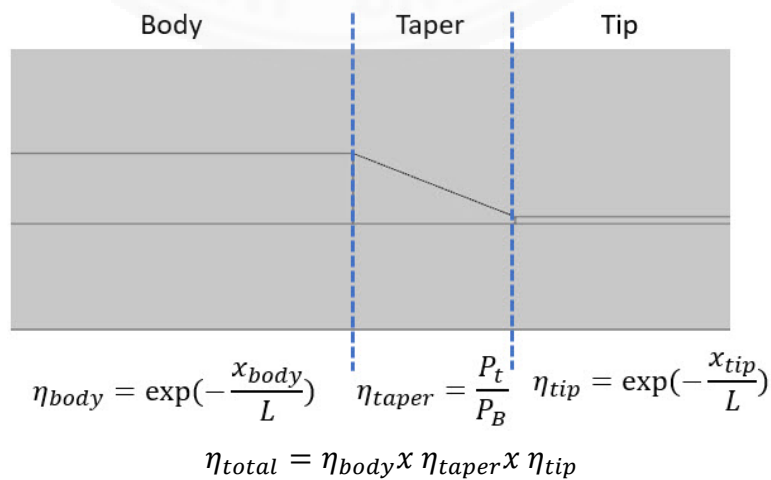
Figure 4.237 Total efficiency of the rough estimation, with Ti/without Ti.

Table 4.4. The estimation of total efficiency for with Ti and without Ti in our specimen

Ti effect	SiO$_2$ 200 nm	SiO$_2$ 20 nm	SiO$_2$ 200 nm		Taper angle (deg.)			SiO$_2$ 20 nm
	propagate length	propagate length	x= 5 μm	x=10 μm	10	30	50	x=0.4 μm
without Ti	8.0 μm	1.3 μm	5.3526E-01	2.8650E-01	0.759	0.869	0.929	0.7351
with Ti	1.7 μm	0.3 μm	5.2804E-02	2.7882E-03	0.284	0.639	0.75	0.2636

x=5 μm

Ti effect	body	taper		tip	total efficiency	
		30 deg.	50 deg.		30 deg.	50 deg.
without Ti	0.5353	0.869	0.929	0.7351	0.3420	0.3656
with Ti	0.0528	0.639	0.75	0.2636	0.0089	0.0104

x=10 μm

Ti effect	body	taper		tip	total efficiency	
		30 deg.	50 deg.		30 deg.	50 deg.
without Ti	0.2865	0.869	0.929	0.7351	0.1830	0.1957
with Ti	0.0028	0.639	0.75	0.2636	0.0005	0.0006

As the results, the Ti is added in MIM waveguide as an adhesion but the Ti is effective in reducing the power inside the waveguide, when the distance between the grating and taper is 5 μm and taper angle is 30 deg., then the total efficiency of 1% is obtained. For 10 μm, the total efficiency will be less than 0.05%, because of the long distance. Therefore, this case is omitted.

4.3.2. The effect of Ti outer

In preliminary characterization, the brightness of the SPPs outside of the MIM waveguide (Au/Air) is observed and it affects to the characterization. So, the 50 nm- Ti outer (on the top of the Au upper layer) is added, the results showed that it does improve the enhancement because the transmittance efficiency is decreased about 2.5 not times as shown in figure 4.49, but it can reduce the surface plasmon outside the waveguide that show in figure 4.47-4.48. Therefore, the 20 nm-Ti outer is selected to apply in the next structure.
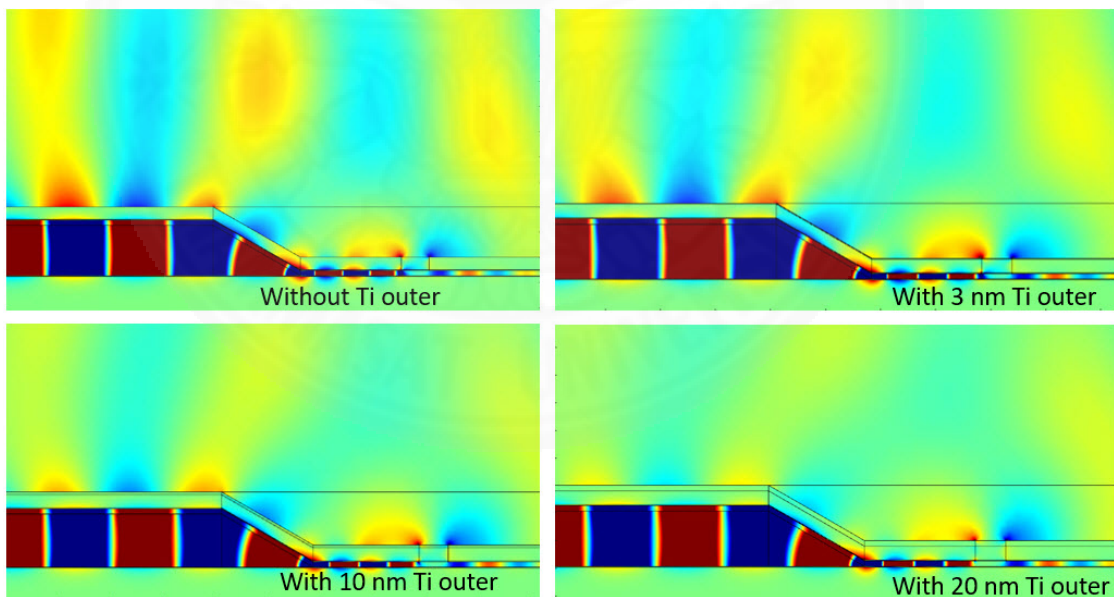
Figure 4.248 *Ey* for all cases
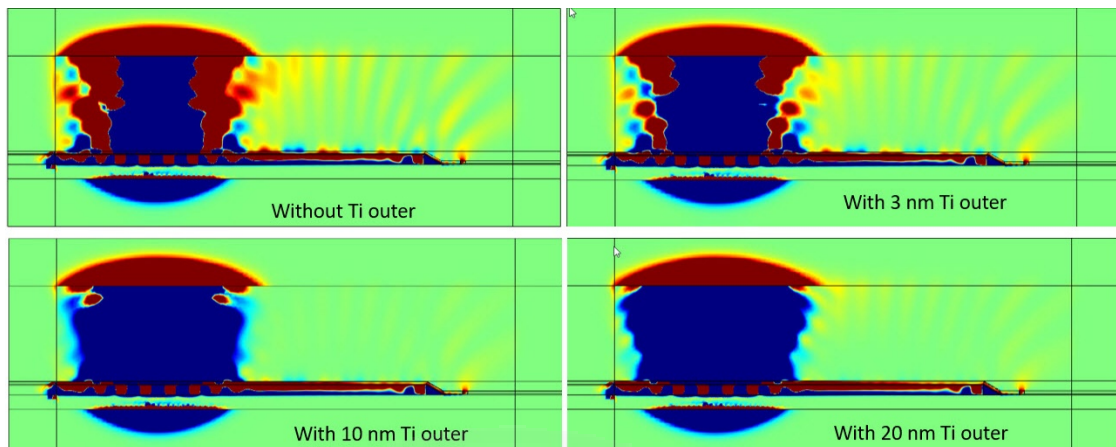
Figure 4.49 Power in *y* direction for all cases
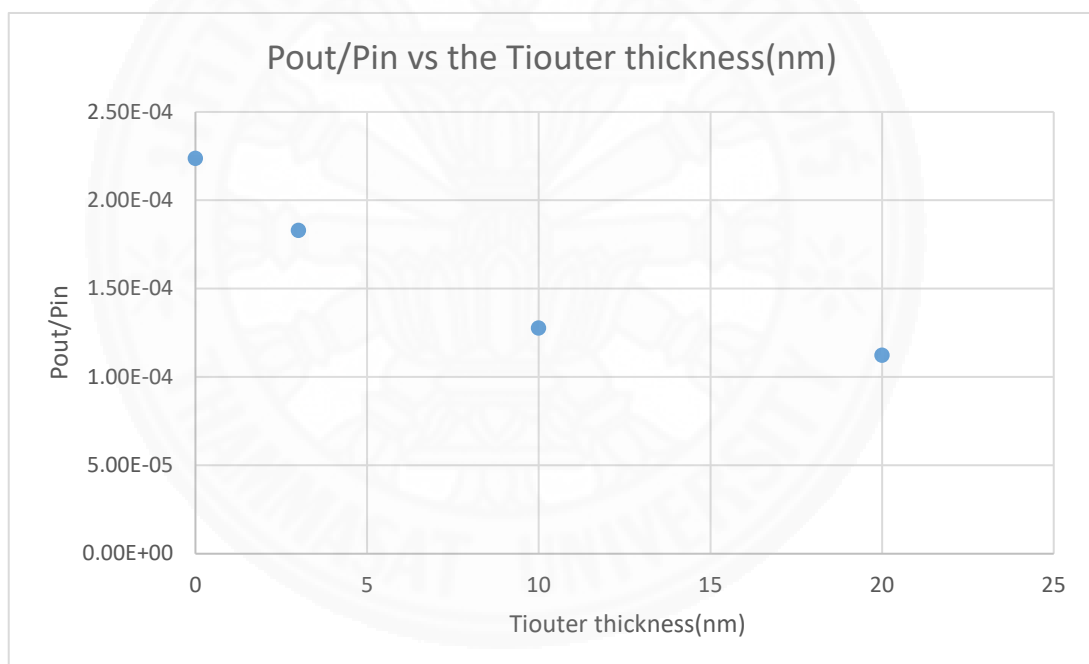
Figure 4.50 The power flow at P_{out} and P_{in} when varying the Ti outer thickness.

4.3.3. The optimization of the input part and the output part

As figure 4.50, for 220 nm-SiO_2, the power in *x* direction will be reduced by 50% for the 200 nm-SiO_2 and the optimized period of the grating is 505 nm and FWHM is 1.7394E-7 nm. For 200 nm-SiO_2, optimized period of the grating is 510 nm and FWHM is 1.7395E-7 nm as figure 4.51. Both are wide enough for optical measurement process.

SiO2 200 nm
Sp1=6.0791E-7
Sp2=4.3397E-7
FWHM= Sp1-Sp2=1.7394E-7

Cp= 5.10E-07
Halfmax=3.68E-11

SiO2 220 nm
Sp1=6.0684E-7
Sp2=4.3289E-7
FWHM= Sp1-Sp2=1.7395E-7

Cp= 5.05E-07
Halfmax=1.55e-11
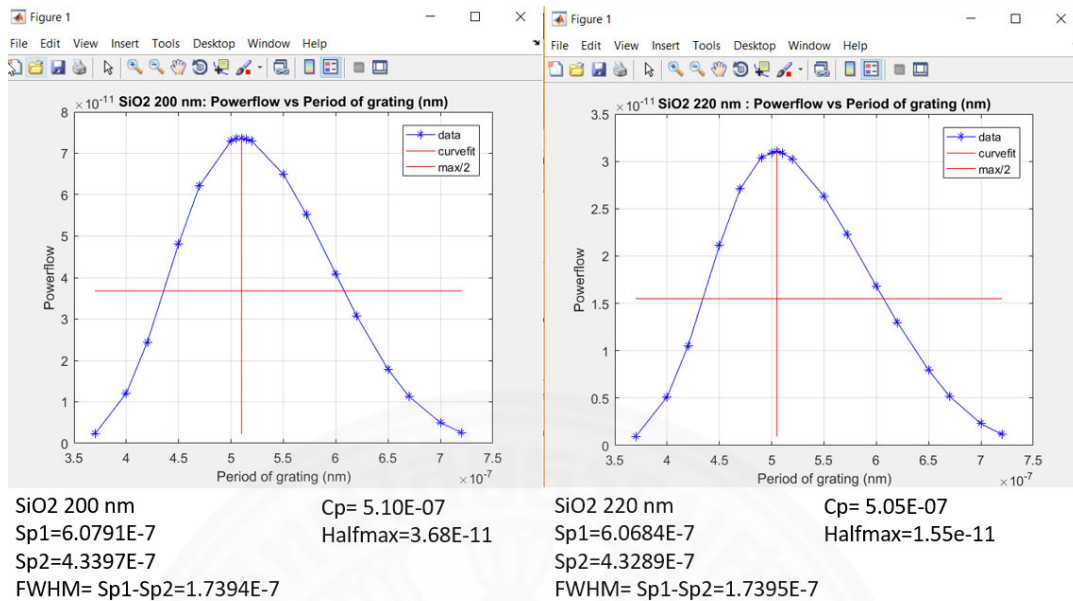
Figure 4.51 (Left) the FWHM of the 200 nm-SiO$_2$ (Right) the FWHM of the 220 nm-SiO$_2$.

As results, the optimum number of grating holes is 4 as shown in Table 4.5. The optimum grating hole width (w_hole) is 180 nm and optimum slit width (wt_hole) is 140 nm as shown in figure 4.52-4.53 respectively. The distance between the taper and the slit (w_t_start), the parameters are set as P=515 nm, W=180 nm, slit width is 140, taper angle is 30 deg., Before_T is 1um, and structure are with/without Ti outer and inside as shown in figure 4.54. The 4 peaks in the appropriate distance between the taper and slit are observed, that are 80 nm, 220 nm, 360 nm, and 500 nm. For with Ti case, the peak is shifted 20 nm and those are not sharp peaks. Although, the power of with Ti case is dropped, but it can average the output values, which is good to experiment because if the fabrication is not exactly 200 nm, the fair value output is still obtained. Figure 4.55 shows the optimum taper angle which is 30 deg. Figure 4.56 shows the comparison of the power flow in y direction of each typical angle, for the higher angle or higher slope, the power will be scattered at the taper, that means at a high taper angle, it is going to be a higher loss. The final optimization of the second specimen is shown in table 4.6, the 5 μm -distance between the taper and the grating (Before_T) is selected which is related to the viewpoint of the laser beam quality. The

total efficiency is 3.0413E-04 or (log10 (-3.5)) is necessary for successful optical measurement.

Table 4.5 The integrated power for each number of grating.

No. of grating	Integrated power
3	3.0981E-11
4*	3.1842E-11
5	2.9595E-11
6	2.7072E-11
10	1.4879E-11
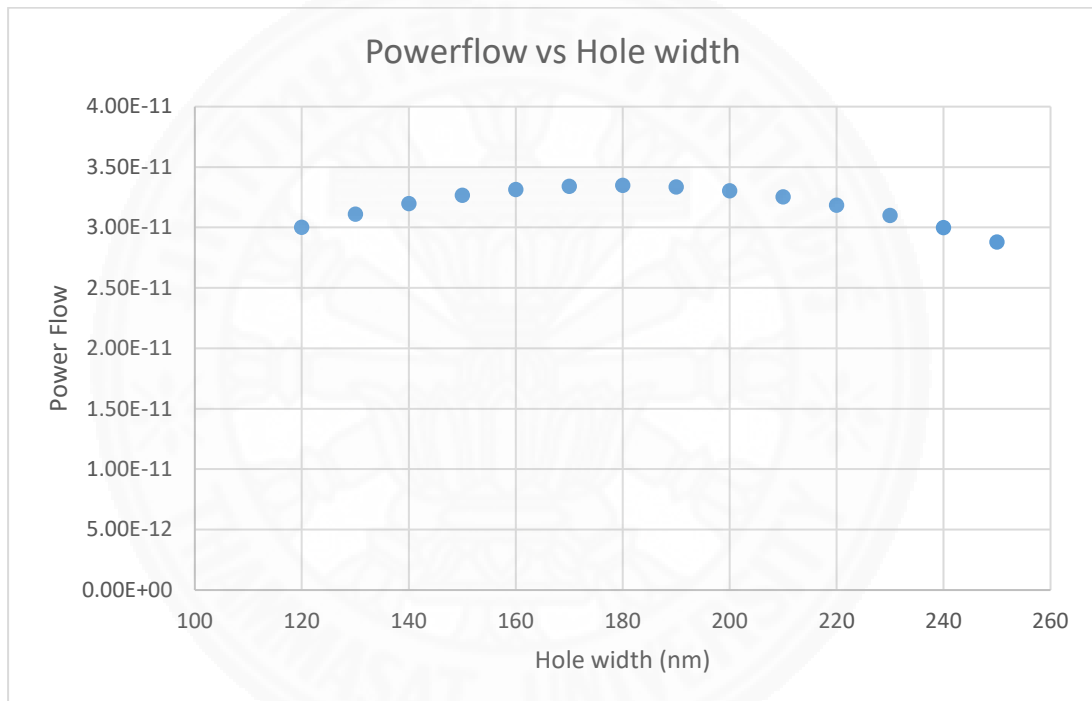
Figure 4.52 The optimum hold width is 180 nm.
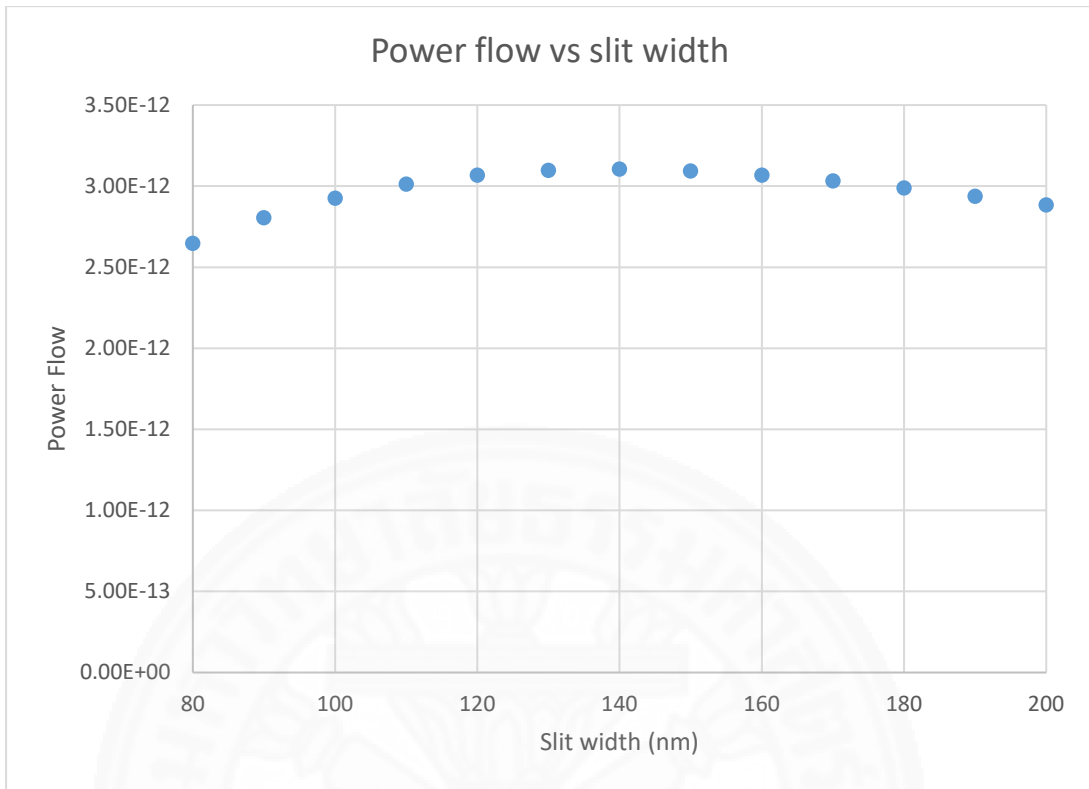
Figure 4.53 The optimum slit width (wt_hole) is 140 nm.
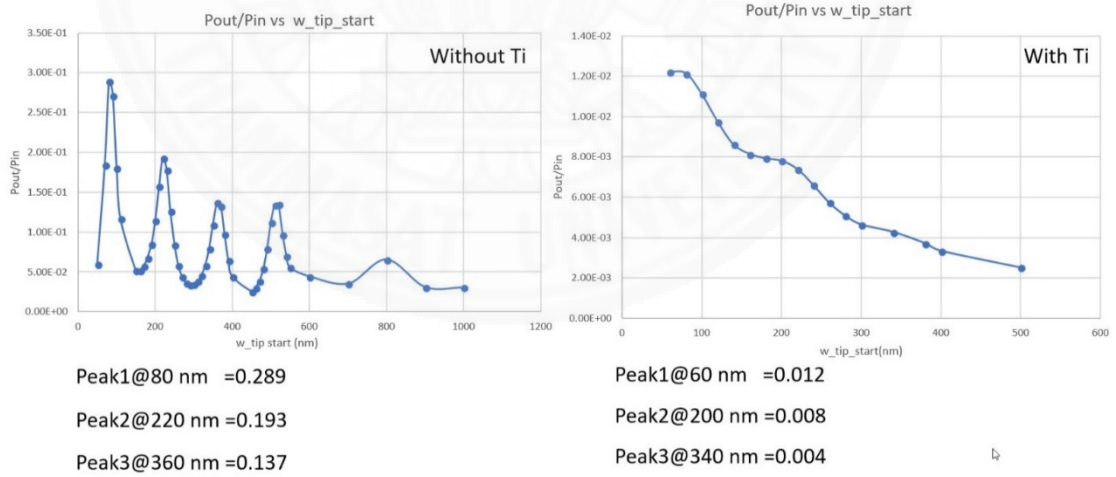
Figure 4.54 The P_{out}/P_{in} vs slit position.
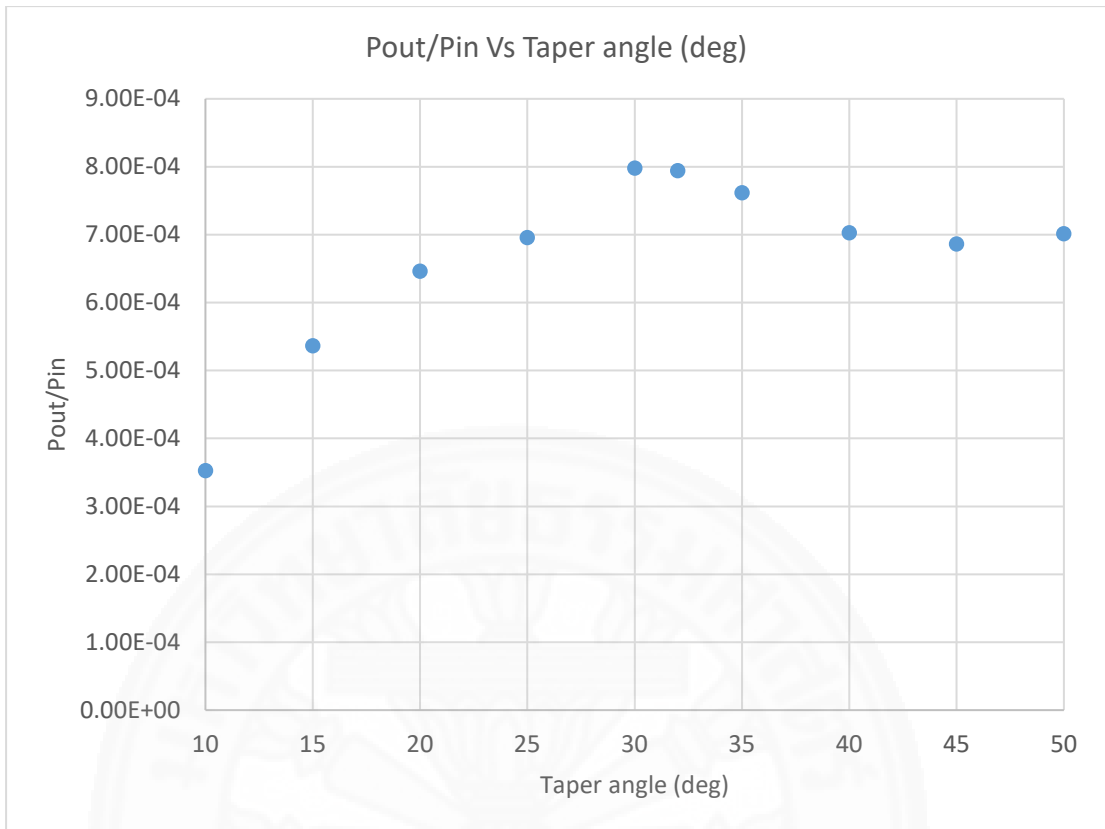
Figure 4.55 The optimum taper angle is 30 deg.

Range: -5E-7 to 5E-7
X depends on taper angle
Y(-300 to 700)

High angle, it will be scattered at the taper
(high slope, high loss).
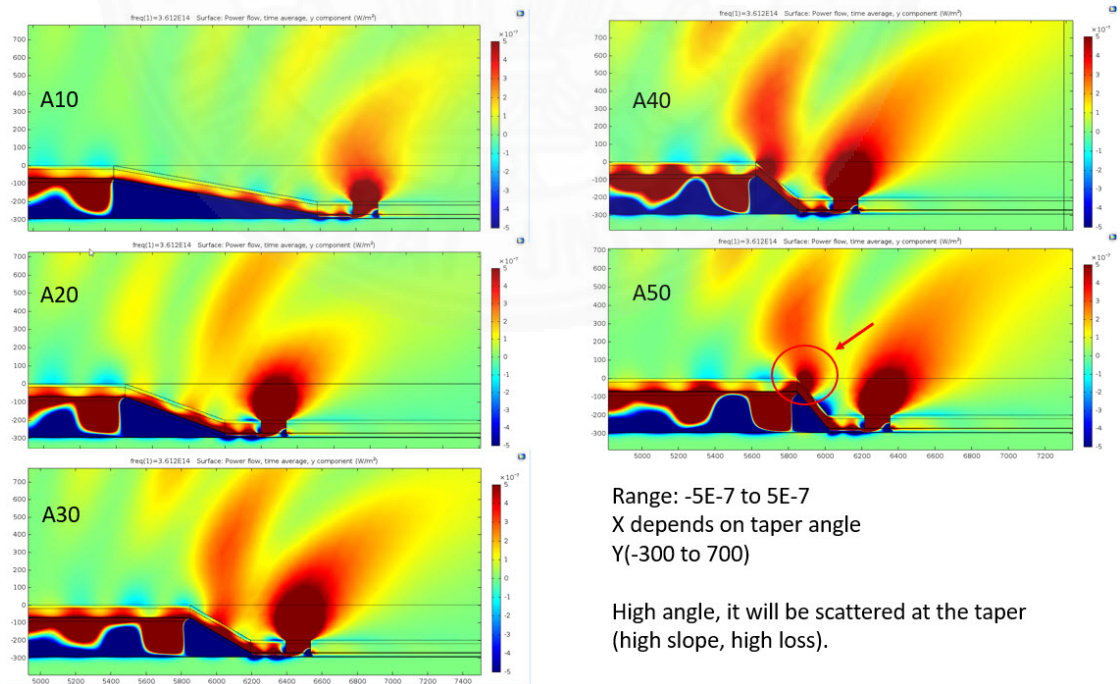
Figure 4.56 The comparison of the power flow in *y* direction of each typical angle.

Table 4.6 The parameter setting for the 200 nm-SiO₂.

Structure Layer	Thickness (nm)
w_Tiout	20
W_gold upper	50
W_Ti	3
W_SiO2	200
W_Ti	3
W_gold lower	300
	nm
Number of grating holes	4
Period of grating	510
FWHM	1.74E-07
Width of grating	180
slit width	140
Taper angle (deg)	30
distance between grating and taper	5,000
distance between taper and slit	200

4.4 The simulation for the third specimen

In the optical measurement process, the intense reflection of the input grating was the most serious problem. The signal guide of SPPs through the MIM waveguide could not observed and the measurement of very weak light at the output is practically difficult. So, the simulation can help to find some possible situations that can happen.

4.4.1 The magnitude order for measurement

The grating-grating model is simulated as shown in figure 4.57, the propagation for 3 μm, 5 μm, and 10 μm will be observed. Also, the effect of the outer Ti layer will be observed too. The use of grating-grating model to clarify the effect of each layer are as follows;

- Au 50/Ti 3/SiO₂_200/Ti3/Au300

- Ti 20/Au 50/Ti 3/SiO₂_200/Ti3/Au300

- Au 80/Ti 3/SiO$_2$_200/Ti3/Au300

- Ti 20/Au 80/Ti 3/SiO$_2$_200/Ti3/Au300

- Au 100/Ti 3/SiO$_2$_200/Ti3/Au300

- Ti 20/Au 100/Ti 3/SiO$_2$_200/Ti3/Au300

Figure 4.57 Cut line for observing the position of P$_{in}$, P$_{out}$, P1 and P2.

Table 4.7 Order of magnitude of the observing efficiency

Ti20/Au50/Ti3			n1		n2		n3	n_total
distance	Pin_0	P1	P1/Pin_0	P2	P2/P1	Pout	Pout/P2	n1*n2*n3
3 μm	1.3E-09	9.7E-11	7.3E-02	3.0E-11	3.1E-01	2.9E-12	9.7E-02	2.2E-03
5 μm	1.3E-09	9.7E-11	7.4E-02	9.6E-12	9.8E-02	8.5E-13	8.9E-02	6.4E-04
10 μm	1.3E-09	4.7E-10	3.6E-01	2.7E-12	5.8E-03	2.4E-13	8.7E-02	1.8E-04

Au50/Ti3								
distance	Pin_0	P1	P1/Pin_0	P2	P2/P1	Pout	Pout/P2	n1*n2*n3
3 μm	1.3E-09	1.2E-10	8.9E-02	3.8E-11	3.2E-01	5.0E-12	1.3E-01	3.8E-03
5 μm	1.3E-09	1.2E-10	9.0E-02	1.2E-11	1.0E-01	1.7E-12	1.4E-01	1.3E-03
10 μm	1.3E-09	1.2E-10	9.0E-02	7.0E-13	5.8E-03	4.0E-13	5.7E-01	3.0E-04

Ti20/Au80/Ti3								
distance	Pin_0	P1	P1/Pin_0	P2	P2/P1	Pout	Pout/P2	n1*n2*n3
3 μm	1.3E-09	1.2E-10	9.1E-02	4.0E-11	3.3E-01	4.9E-12	1.2E-01	3.7E-03
5 μm	1.3E-09	1.2E-10	9.1E-02	1.3E-11	1.1E-01	1.5E-12	1.1E-01	1.1E-03
10 μm	1.3E-09	1.2E-10	9.1E-02	8.9E-13	7.4E-03	7.0E-14	7.8E-02	5.3E-05

Au80/Ti3								
distance	Pin_0	P1	P1/Pin_0	P2	P2/P1	Pout	Pout/P2	n1*n2*n3
3 μm	1.3E-09	1.2E-10	9.0E-02	4.0E-11	3.4E-01	5.3E-12	1.3E-01	4.0E-03
5 μm	1.3E-09	1.2E-10	9.1E-02	1.3E-11	1.1E-01	1.7E-12	1.3E-01	1.3E-03
10 μm	1.3E-09	1.2E-10	9.1E-02	8.7E-13	7.3E-03	3.3E-13	3.8E-01	2.5E-04

Ti20/Au100/Ti3								
distance	Pin_0	P1	P1/Pin_0	P2	P2/P1	Pout	Pout/P2	n1*n2*n3
3 μm	1.3E-09	1.5E-10	1.1E-01	4.8E-11	3.3E-01	7.4E-12	1.5E-01	5.6E-03
5 μm	1.3E-09	1.5E-10	1.1E-01	1.6E-11	1.1E-01	2.1E-12	1.3E-01	1.6E-03
10 μm	1.3E-09	4.0E-10	3.0E-01	3.1E-12	7.9E-03	3.1E-13	1.0E-01	2.4E-04

Au100/Ti3

distance	Pin_0	P1	P1/Pin_0	P2	P2/P1	Pout	Pout/P2	n1*n2*n3
3 μm	1.3E-09	1.4E-10	1.0E-01	4.5E-11	3.4E-01	7.0E-12	1.5E-01	5.3E-03
5 μm	1.3E-09	1.4E-10	1.0E-01	1.5E-11	1.1E-01	2.1E-12	1.4E-01	1.6E-03
10 μm	1.3E-09	1.4E-10	1.0E-01	9.9E-13	7.3E-03	2.8E-13	2.8E-01	2.1E-04
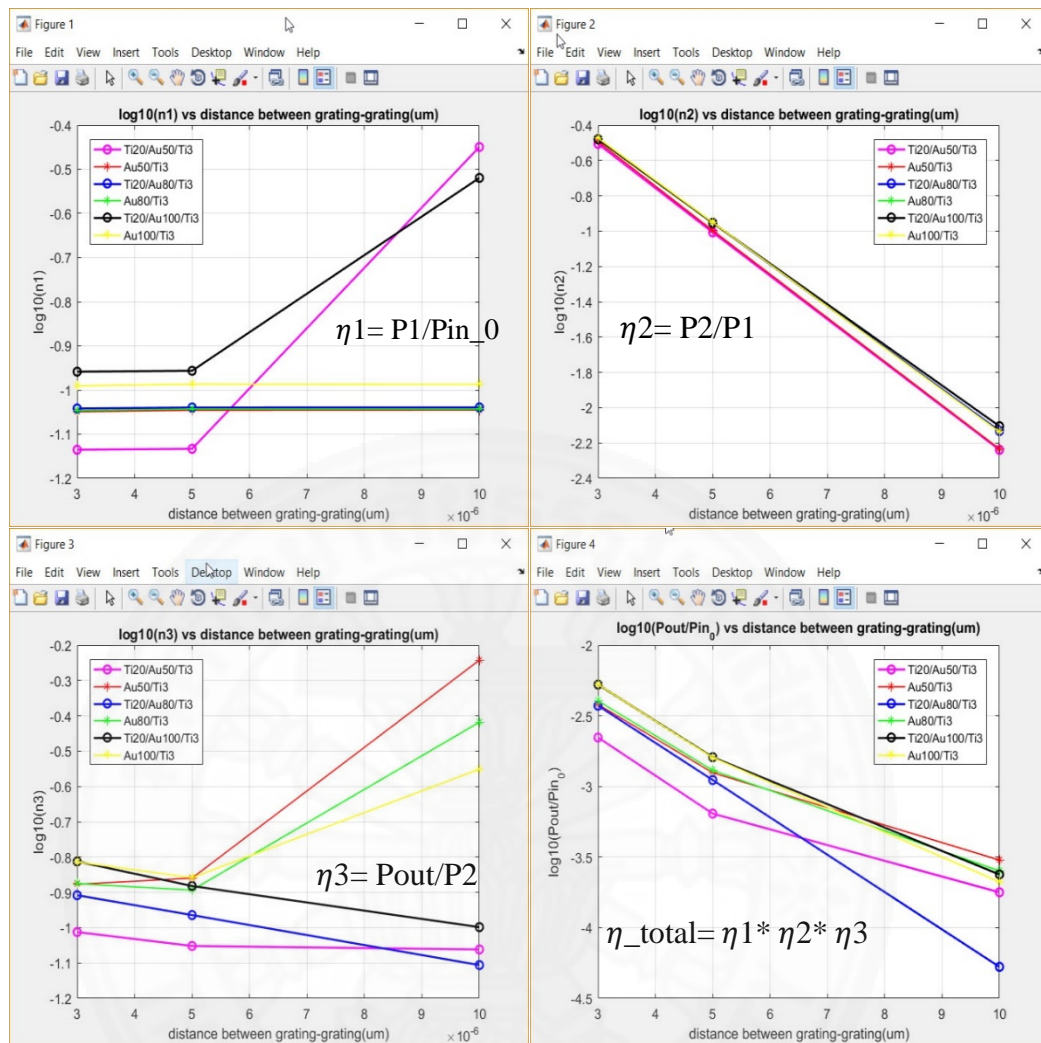
Figure 4.58 log10 (P_{out}/Pin_0) at each part (efficiency; η)

        As the results are shown in table 4.7 and figure 4.58, the efficiency for 5 μm can be observed. The outer Ti was surely effective to suppress the propagation of SPP outside. But it is suspected that it also reduces the inner SPP due to the thin Au layer. The absorption of the outer Ti layer was found to be negligible because as shown in the figure 4.58 ($\eta 2$) the efficiency of the middle part is not much difference from the efficiency graph of Au 50/Ti3 (for finding the propagate length (decay). But instead the grating coupling efficiency was found to be sensitive to the metal layers. Therefore, Ti 20/Au 100/Ti 3 is the best. But the compromise is with Ti 20/Au 80/Ti 3. In case of strange values of 10 μm, maybe the resonance inside happened because both grating input and output act as the mirror.

4.4.2 The reflection of the grating

When doing the preliminary characterization, there are too high reflection at the grating disturbs the measurement, as the results in table 4.8, the reflectance is about 50-60% comparing the Pin_0 as shown in figure 4.37-4.38 and it can be reduced by adding the 20 nm-Ti outer. To avoid the influence of the reflection is by improving the optical efficiency and setup.

Table 4.8 The reflection at the grating

Ti20/Au50/Ti3   ***R=(Pin_0-Pin)/Pin_0

distance between grating-grating	Pin	Pin_0	reflectance (R)
$3\ \mu m$	7.02E-10	1.32E-09	0.4691
$5\ \mu m$	7.01E-10	1.32E-09	0.4694
$10\ \mu m$	1.15E-10	1.32E-09	0.9127

Au50/Ti3

distance between grating-grating	Pin	Pin_0	reflectance (R)
$3\ \mu m$	5.05E-10	1.32E-09	0.6176
$5\ \mu m$	5.04E-10	1.32E-09	0.6184
$10\ \mu m$	5.02E-10	1.32E-09	0.6199

Ti20/Au80/Ti3

distance between grating-grating	Pin	Pin_0	reflectance (R)
$3\ \mu m$	7.37E-10	1.32E-09	0.4424
$5\ \mu m$	7.40E-10	1.32E-09	0.4402
$10\ \mu m$	7.37E-10	1.32E-09	0.4427

Au80/Ti3

distance between grating-grating	Pin	Pin_0	reflectance (R)
$3\ \mu m$	4.94E-10	1.32E-09	0.6261
$5\ \mu m$	4.98E-10	1.32E-09	0.6236
$10\ \mu m$	4.96E-10	1.32E-09	0.6248

Ti20/Au100/Ti3

distance between grating-grating	Pin	Pin_0	reflectance (R)
$3\ \mu m$	8.13E-10	1.32E-09	0.3849
$5\ \mu m$	8.14E-10	1.32E-09	0.3844
$10\ \mu m$	9.40E-10	1.32E-09	0.2888

Au100/Ti3

distance between grating-grating	Pin	Pin_0	reflectance (R)
3 μm	5.75E-10	1.32E-09	0.5649
5 μm	5.75E-10	1.32E-09	0.5647
10 μm	5.73E-10	1.32E-09	0.5662

4.4.3 Change the SiO$_2$ Thickness at the tip part

In the optical measurement, the SPPs inside structure is possible observed if the total efficiency is higher than $10^{-3.5}$ or 3E-4. Thus, The varying of the SiO$_2$ thickness at the tip part are as 20:10:60 nm as figure 4.59.
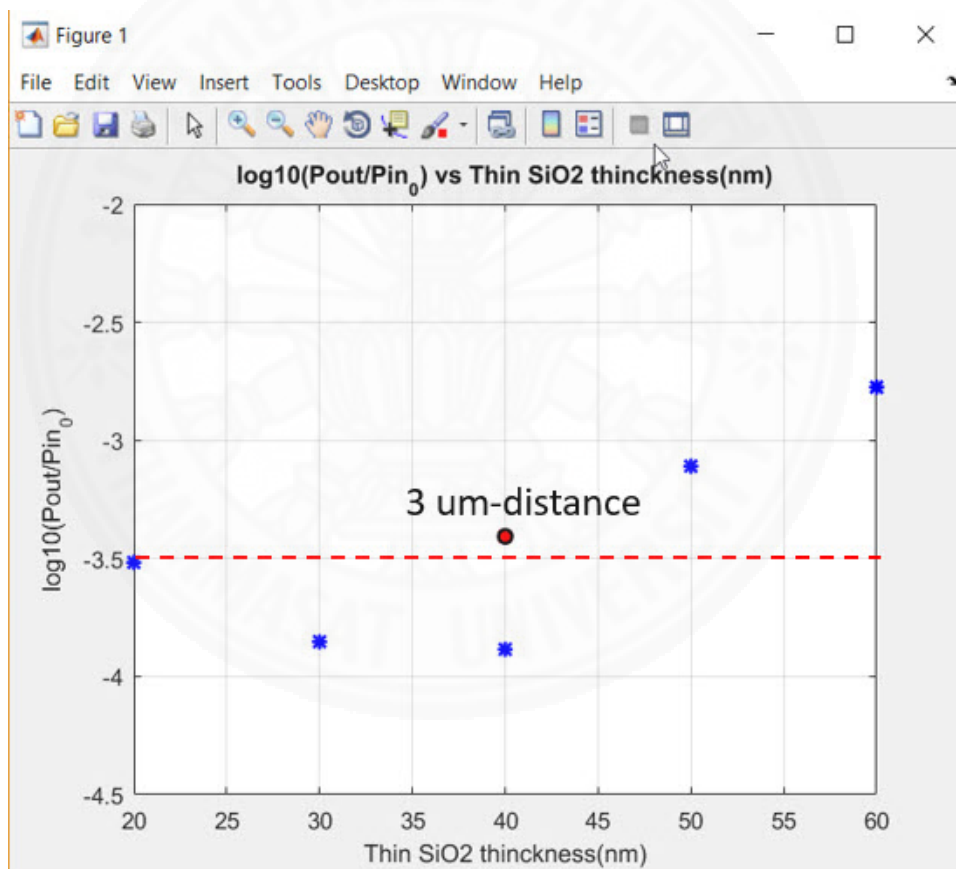
Figure 4.59 The log10 of total efficiency vs the SiO2 thickness.

As results, the efficiency of $10^{-3.5}$ or 3E-4 is possible by 40 nm-thickness of SiO$_2$ and grating distance of 3 μm. Then, the converging the mesh size of 40 nm is confirmed, the results are same as the previous one (red point), so the SiO$_2$ thickness is changed to 40 nm, but also try 20 nm in the third specimen.

4.4.4 The optimization of the input part and the output part for SiO$_2$

As the results in figure 4.60-4.64 and table 4.9-4.10, the fabrication of the third specimen with an appropriate taper are following these parameters.

- Thickness of Au layer: Ti 20/Au 100/Ti 3 (Ti 20/Au 80/Ti 3)

- SiO$_2$ sputtered layer: 40nm (and 20nm)

- Grating period, width: P=530nm, W=100nm for 40nm SiO$_2$,

P=505 nm, W=180nm for 20nm SiO$_2$

- Slit width, position: W=150nm, D=260nm for 40nm SiO$_2$,

W=140nm, D=200nm for 20nm SiO$_2$.
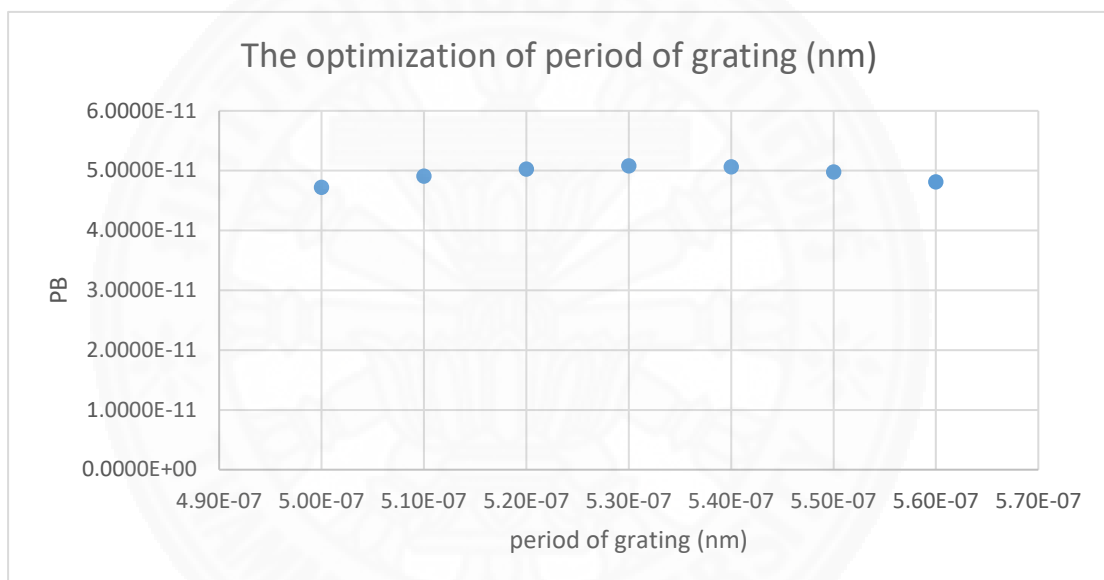
Figure 4.60 The optimized period of the grating is 530 nm.
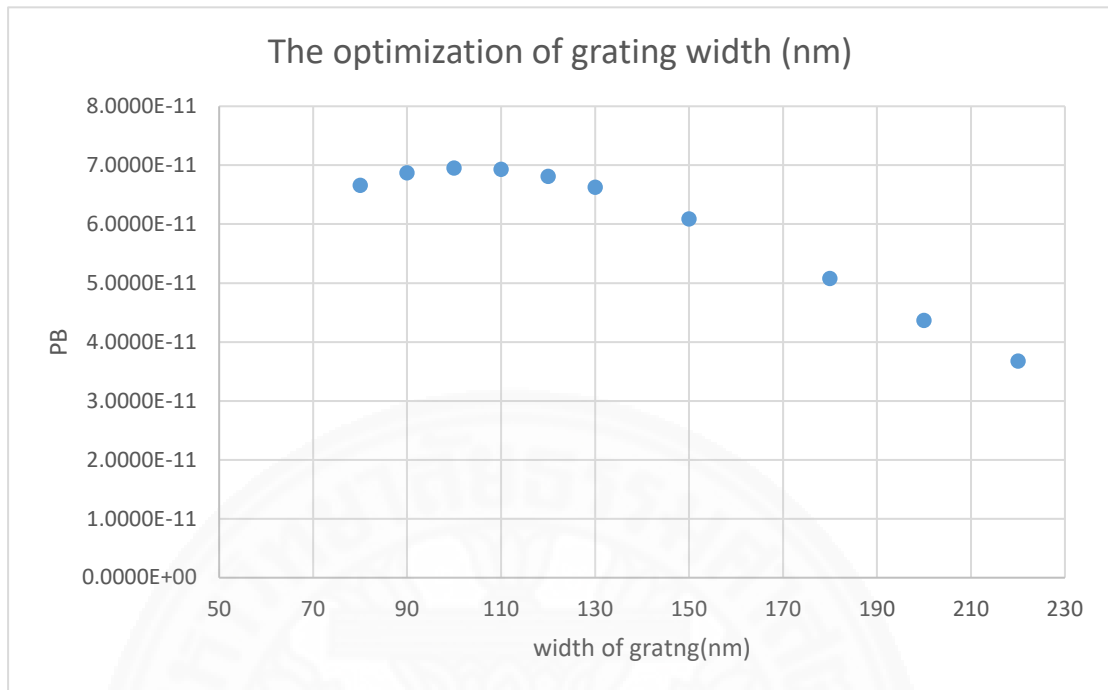
Figure 4.61 The optimized width of the grating is 100 nm.
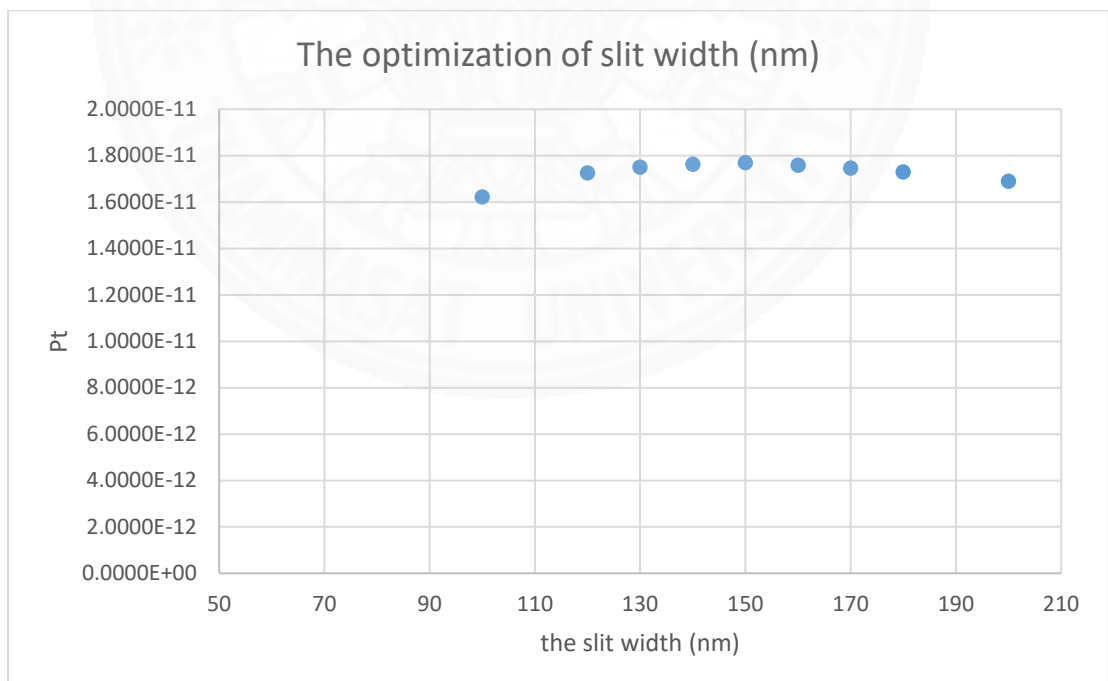
Figure 4.62 The optimized the slit width is 150 nm.
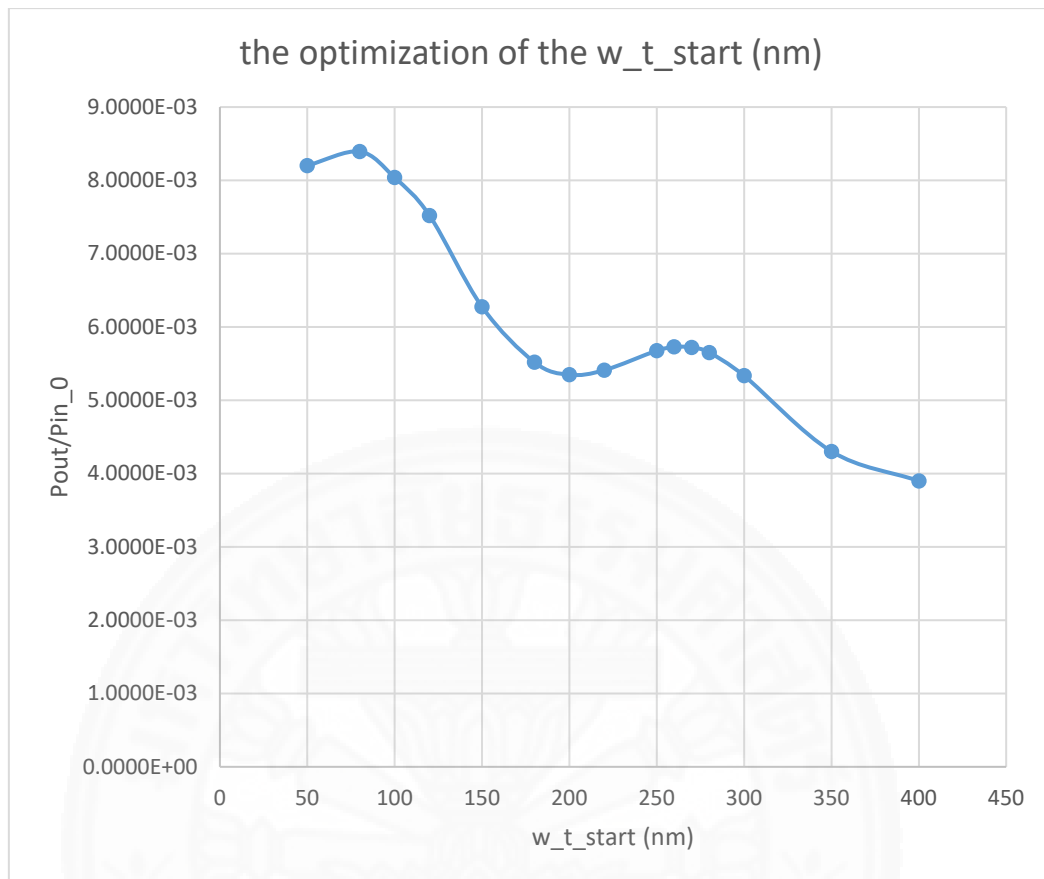
Figure 4.25 The optimized of the w_slit_start (the position of slit) Peak no. 1=90 nm, peak no. 2 is 260 nm.
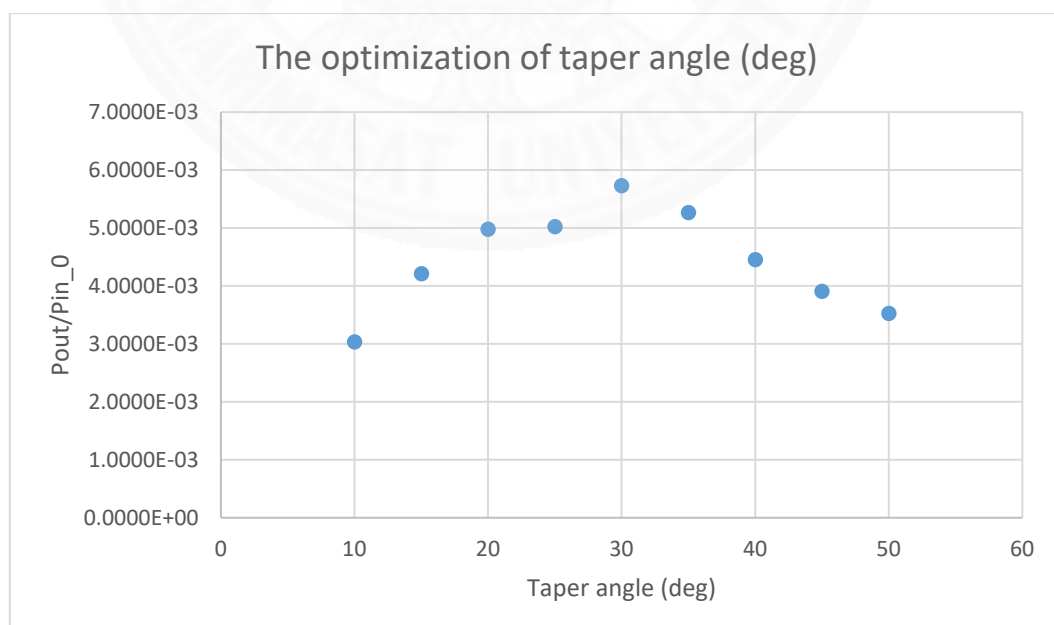
Figure 4.64 The optimized Taper angle is 30 deg.

Table 4.9 The coupling efficiency for the distance between grating and taper are 3, 4, and 5 μm.

Distance (μm)	Pin_0	Pout	Pout/Pin_0	log 10(pout/Pin_0)
3	1.3218E-09	3.5343E-12	2.6739E-03	-2.572862337
4	1.3218E-09	2.1179E-12	1.6023E-03	-2.795260297
5	1.3218E-09	1.2433E-12	9.4061E-04	-3.026589814

Table 4.10 The parameter setting for the thin SiO_2 40 nm, the third specimen.

Structure Layer	thickness (nm)
w_Tiout	20
W_gold upper	100
W_Ti	3
W_SiO2Thin	40
W_SiO2	200
W_Ti	3
W_gold lower	300
	nm
Number of grating holes	4
Period of grating	530
Width of grating	100
slit width	150
Taper angle (deg.)	30
distance between grating and taper	5,000
distance between taper and slit	260

4.5 Final optimization of the final specimen of Al_2O_3

By referring the optical measurement of SiO_2 specimen, the transmission for the 40 nm-thickness is surly observed, for the 20 nm-SiO_2 and grating 4 μm would be the limit and grating 3 μm would be too short due to the incident spot size, it covers both input and output area. Therefore, the grating 4 μm would be the optimum that confirmed check by varying the distance between grating and taper as shown in figure 4.12. Because in the third specimen, the spare sample of 70 vertical step and taper angle

as 50 deg. is selected, it reduced the efficiency very much, about 80-90% is reduced as shown in figure 4.65 and table 4.11. Finally, fabrication of the real final optimization with the final specimen of SiO_2 can be happened. Unfortunately, in the taper angle, making process by the etching machine, the Ti inside is etched, only bared lower Au layer is appearing and SiO_2 is not a good adhesion, for the lift-off process, SiO_2 is broke and gone, the detail in the fabrication chapter. So, for solving this problem, Al_2O_3 is used instead of SiO_2 and the optimum parameters for 20 nm-thickness and 40 nm-thickness are considered. Before that there are confirmed the optimum distance between the grating and taper by varying the distance $0.5:0.5:5$ μm. The highest efficiency increases when the distance decreases as shown in figure 4.66. For the optical measurement of the third specimen, we measure the radius of spot size (w0) and found that it is 620 nm, which is smaller than the previous simulation setting, 830 nm and the optimum angle is 30 deg. as shown in figure 4.79. Therefore, the effect of w0 is investigated and as we know, the efficiency is sensitive with metal thickness, so the optimized upper Au layer is done as shown in figure 4.78 and Table 4.12, and the efficiency reduced by the large vertical step. So, the vertical step effect of the final specimen is considered as shown in figure 4.90-4.92. The optimum parameters for Al_2O_3 20 nm are shown in figure 4.80-4.84 and table 4.13-4.14 for Al_2O_3 40 nm are shown in figure 4.85-4.89 and table 4.15-4.16.

As simulation results, Al_2O_3 reduces the efficiency about 30%-35% from sio2, but the transmission at the output can observe. Therefore, the final specimen with the optimum Al_2O_3 parameters can fabricate in the next. For vertical step considering, as shown in figure 4.92, the drop of the efficiency is linear, and if the trend is extrapolated, the efficiency at 70 nm step is about 1/6, as the case of SiO2 overcoat at first is confirmed. If a criterion of the vertical step of 15-30 nm is acceptable, the estimated distribution would be about +/-12%, which is reasonable scenario. Furthermore, the minimum observation limit about $10^{-3.5}$ was again confirmed.
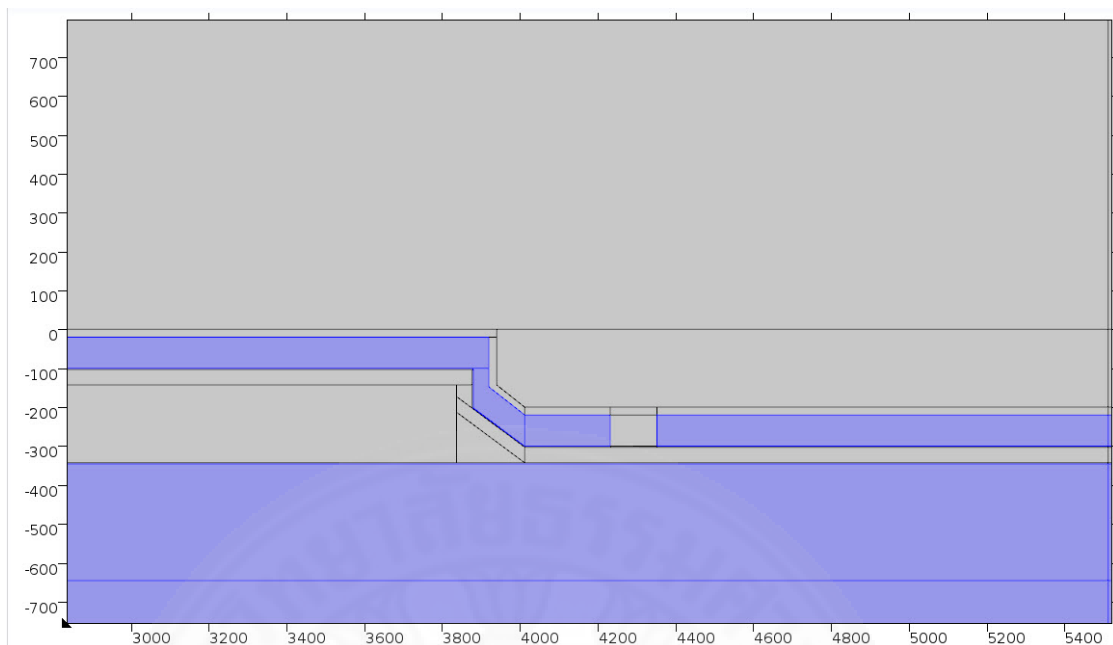
Figure 4.65 The 70 nm-vertical step of the final SiO$_2$ specimen.

Table 4.11 The coupling efficiency of the MIM waveguide with the 70 nm-vertical length.

For sio2 20 nm   Au80

Distance (μm)	Pin_0	Pout	Pout/Pin_0	log10(Pout/Pin0)
3	1.3218E-09	3.5516E-13	2.6869E-04	-3.5707417
4	1.3218E-09	2.3025E-13	1.7419E-04	-3.758966109
5	1.3218E-09	1.0689E-13	8.0867E-05	-4.09222867

For sio2 40 nm   Au80

Distance (μm)	Pin_0	Pout	Pout/Pin_0	log10(Pout/Pin0)
3	1.3218E-09	5.7124E-13	4.3217E-04	-3.364347137
4	1.3218E-09	5.1715E-13	3.9125E-04	-3.407549219
5	1.3218E-09	1.9694E-13	1.4899E-04	-3.826831814

4.5.1 The optimum distance between grating and taper

For optimum distance between grating and taper, the parameter named "Before_T" is starting from 0.5 - 5 μm, the results are shown in figure. 4.66, the increasing distance has reduced the efficiency. Because of the Gaussian beam source is too big, at the distance between grating and taper is short, the beam covered the grating and slit part. Therefore, the optimum value at 4 μm is selected.
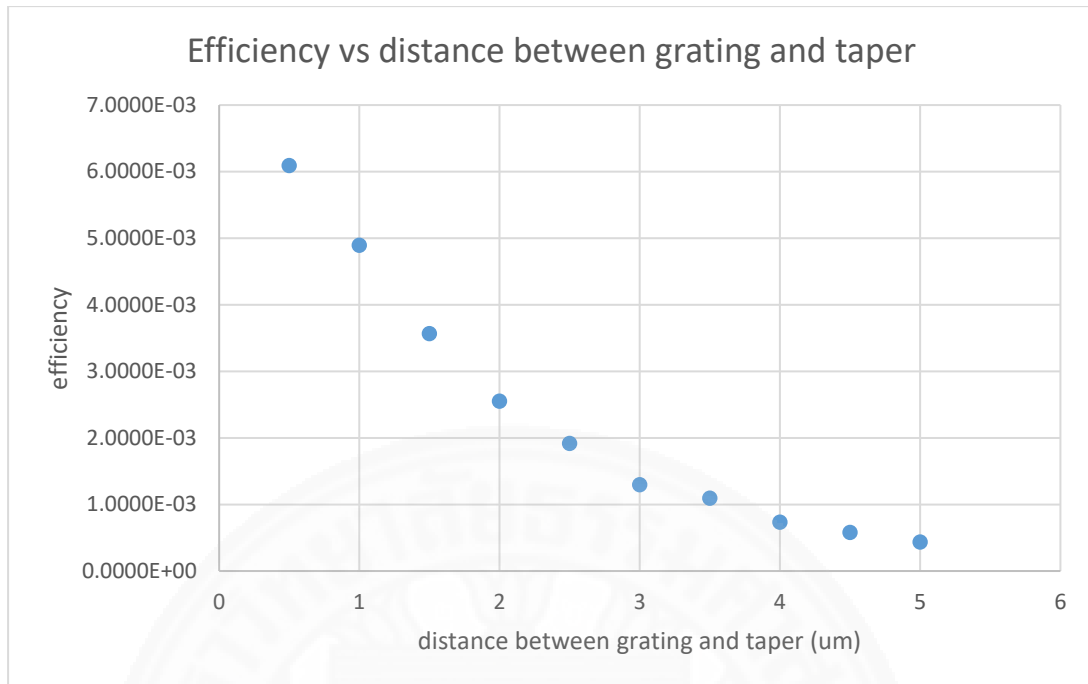
Figure 4.66 The efficiency when varied the distance between grating and taper.

4.5.2 The optimum parameters with Gaussian radius (w0) 620 nm

The optical setup, the light source is the semiconductor Laser at 830 nm-wavelength (En wave FSL-830-75ss), the radius (w0) is 620 nm. So, the simulation setting about the light source is set as shown in figure 4.67-4.74. The paraxial Gaussian beam is defined as shown in figure 4.66. It consists of the radius of curvature function, *R*, as a piecewise function, since it is infinite when its argument is zero, W(z), and *E* function. The w0 620 dropped the efficiency around 33% of the w0 830 nm as shown in figure 4.75 and the optimum number of grating holes with Gaussian radius (w0) 620 nm is 4 as shown in figure 4.76.

$$\frac{E(x,y,z)}{E_0} = \frac{w_0}{w(z)} exp\left[-\frac{r^2}{w^2(z)}\right] * exp\left\{\left[kz - tan^{-1}\left(\frac{z}{z_0}\right)\right]\right\} * exp\left[-j\frac{kr^2}{2R(z)}\right]$$

Radial Phase Factor:
Accounts for phase shifts due to measuring a spherical surface along a plane

Amplitude factor:
Describes beam spread

Longitudinal Phase Factor:
Describes shift from plane wave (tangent factor) to spherical wave behavior

$$z_0 = \frac{\pi w_0^2}{\lambda}$$

$$R(z) = \left[1 + \left[\frac{z_0}{z}\right]^2\right]$$

$$w^2(z) = w_0^2\left[1 + \left[\frac{z}{z_0}\right]^2\right]$$
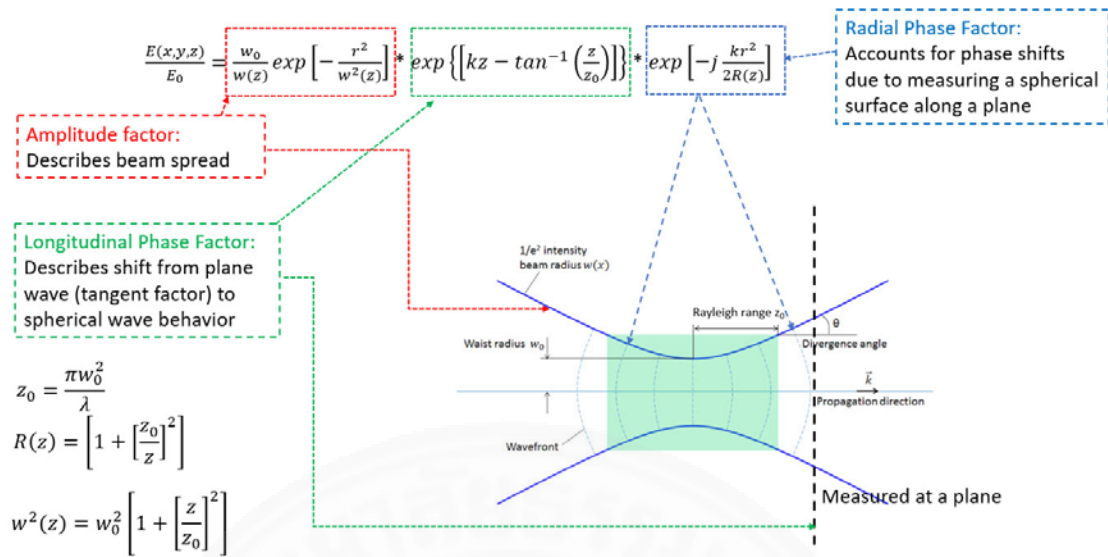
Figure 4.67 The definition of the paraxial Gaussian beam for COMSOL.

Parameters   freq(1)=3.612E14 Surf

Name	Expression	Value	Description
z0	pi*w0^2/lda	1.455E-6 m	Rayleigh range
w0	620[nm]	6.2E-7 m	Spot radius
w_tip_start	220[nm]	2.2E-7 m	length of start hole in the tip
w_Tiout	20[nm]	2E-8 m	Ti outside width
w_Ti	3[nm]	3E-9 m	Ti inside width
w_t_hole	120[nm]	1.2E-7 m	hole width in the tip
w_sio2	200[nm]	2E-7 m	sio2 thickness
w_pml	lda	8.3E-7 m	Thickness of PML domains
w_hole	110[nm]	1.1E-7 m	hole width in body
w_gold_lo...	300[nm]	3E-7 m	lower gold width
w_gold	80[nm]	8E-8 m	gold thickness
w_body_s...	1000[nm]	1E-6 m	body start width
w_al2o3	40[nm]	4E-8 m	sio2Thin layer
w_air_up	2000[nm]	2E-6 m	air width
w_air	1000[nm]	1E-6 m	air thickness
theta	0[deg]	0 rad	incident wave angle
p_hole	520[nm]	5.2E-7 m	period of hold
n_Ti	3.23-4.0i	3.23-4i	refrectrive index of Ti
n_sio2	1.45	1.45	refrective index of sio2
n_gold	sqrt(Ep_gold)	0.17343-5.2182i	gold properties
n_al2o3	1.76	1.76	refrective index of al2o3
lda	830[nm]	8.3E-7 m	Wavelength
k	2*pi/lda	7.5701E6 1/m	Propagation constant
h_tip	1500[nm]	1.5E-6 m	tip lenght
h_taper	346[nm]	3.46E-7 m	taper length
h_body	w_body_start+3*p_hole+w_hole+before_T	6.67E-6 m	body length
f	c_const/lda	3.612E14 1/s	Frequency
Ep_gold	-27.2-1.81i	-27.2-1.81i	elsilon of gold
E0	1[V/m]	1 V/m	Electric field amplitude
cut1	1000[nm]	1E-6 m	cut line at the first position
before_T	4[um]	4E-6 m	distance between grating and taper

Figure 4.68 Parameters setting
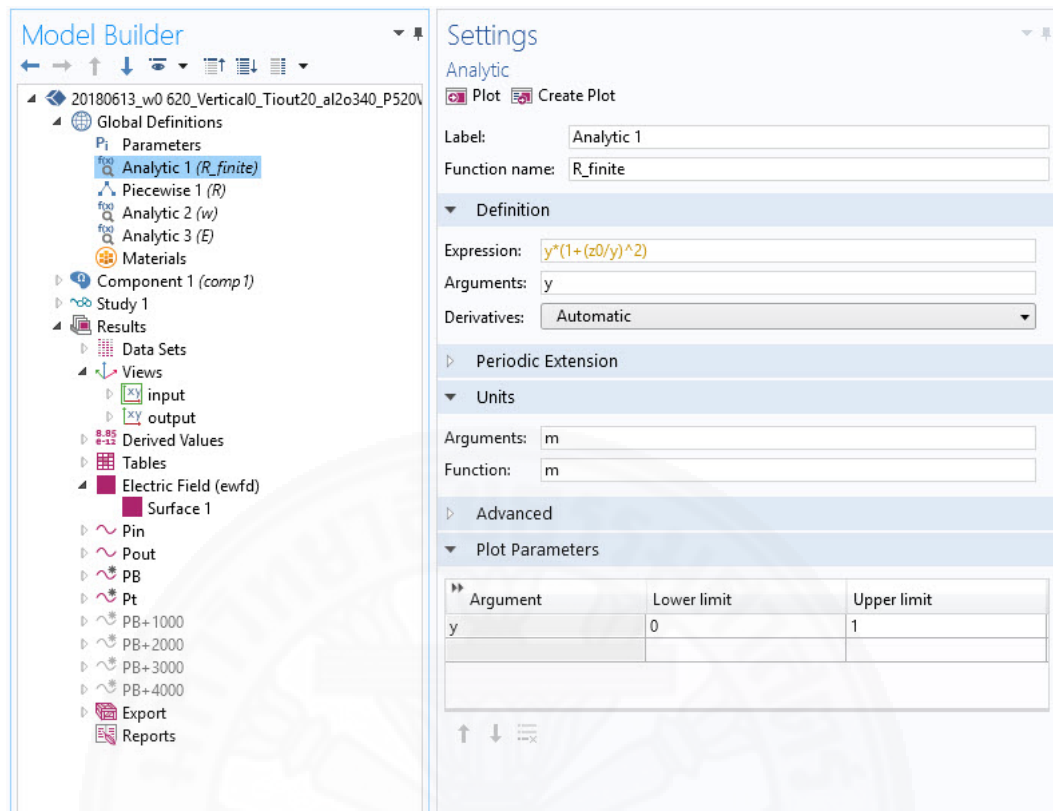
Figure 4.69 Define the radius of curvature function, *R*.
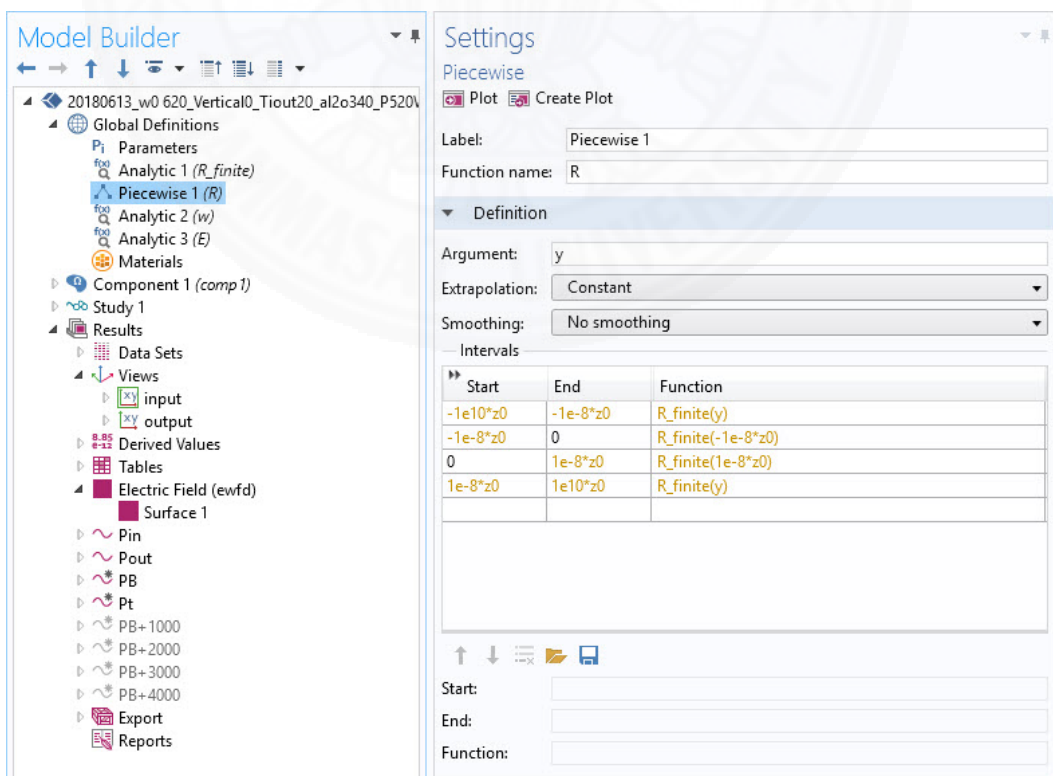
Figure 4.70 Define the radius of curvature function, *R*, as a piecewise function.
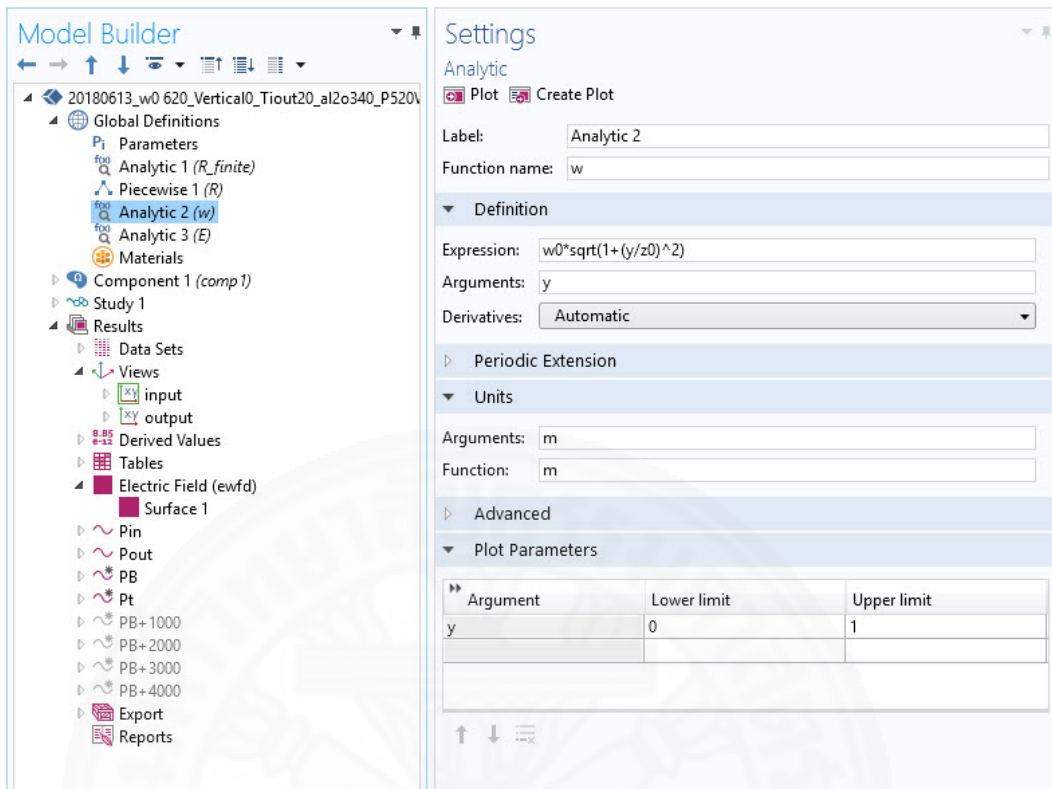
Figure 4.71 Define W(z) is the radius at which the field amplitudes fall to 1/*e* of their axial values at the plane *z* along the beam.
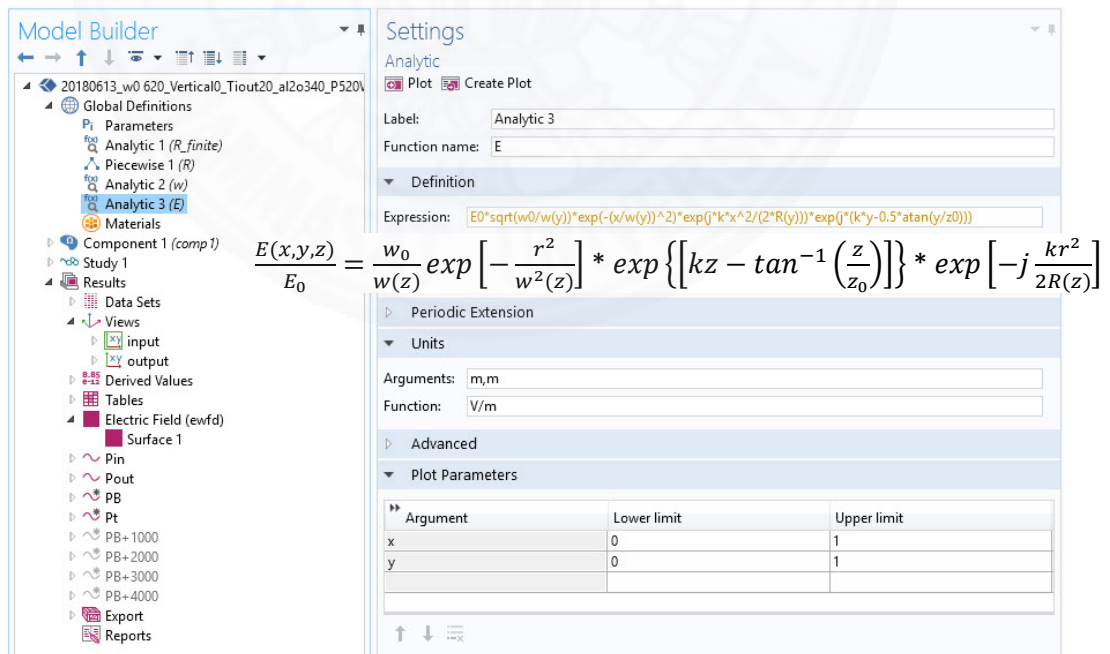
$$\frac{E(x,y,z)}{E_0} = \frac{w_0}{w(z)} exp\left[-\frac{r^2}{w^2(z)}\right] * exp\left\{\left[kz - tan^{-1}\left(\frac{z}{z_0}\right)\right]\right\} * exp\left[-j\frac{kr^2}{2R(z)}\right]$$

Figure 4.72 Define the paraxial Gaussian beam as function *E*.
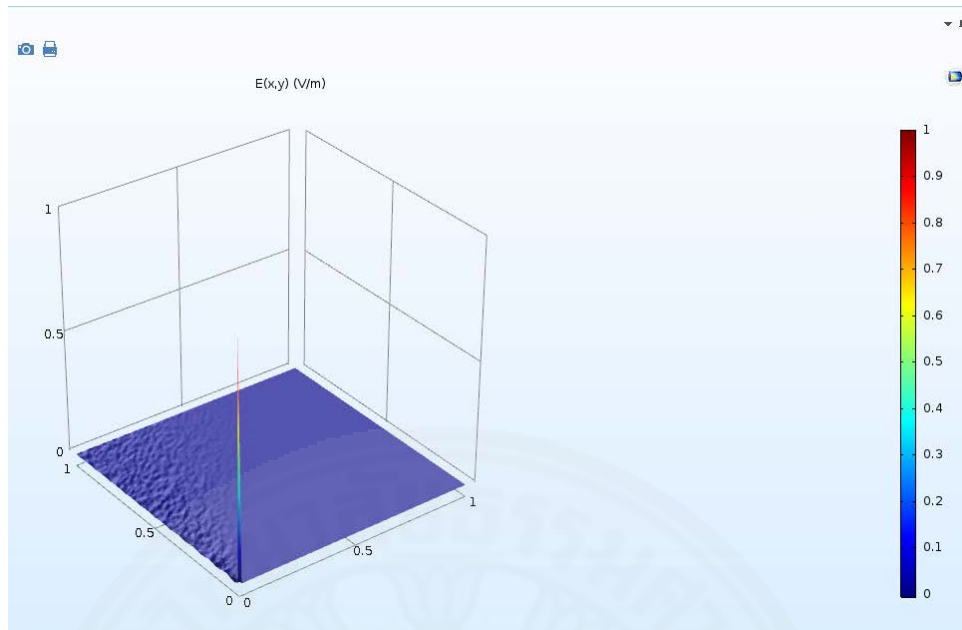
Figure 4.73 The feature of the Gaussian beam.
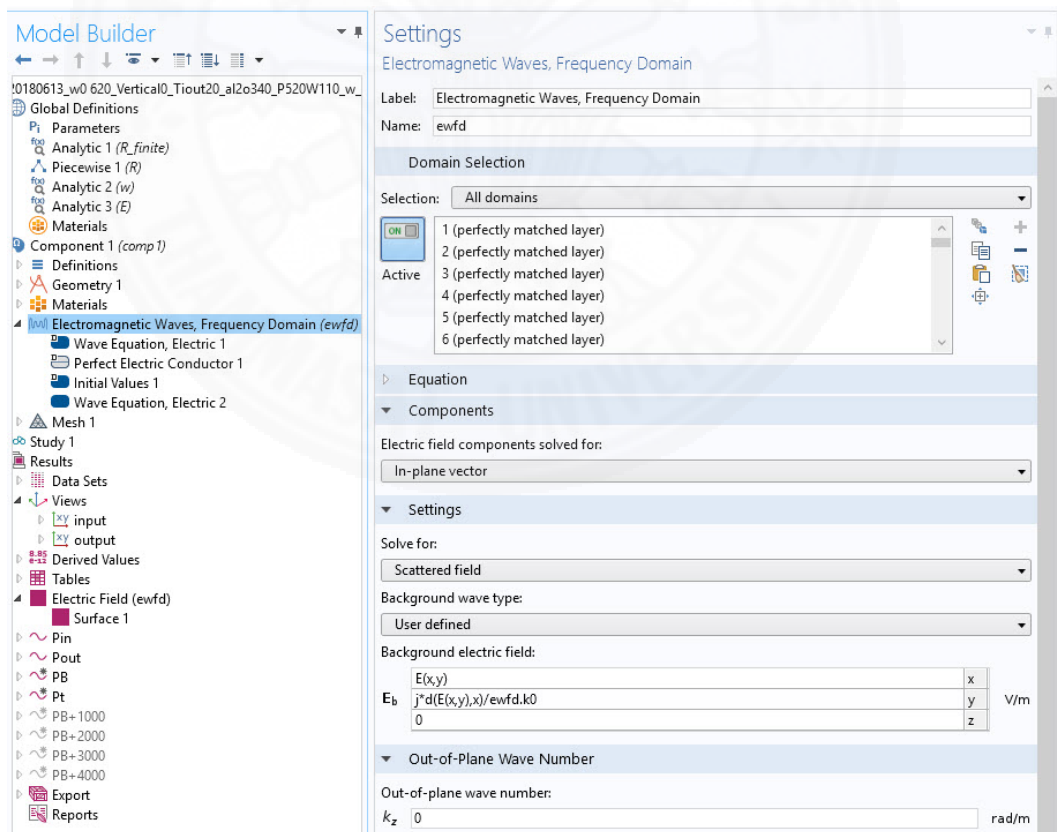
Figure 4.74 EM setting by called function E, to set the light source of the model.
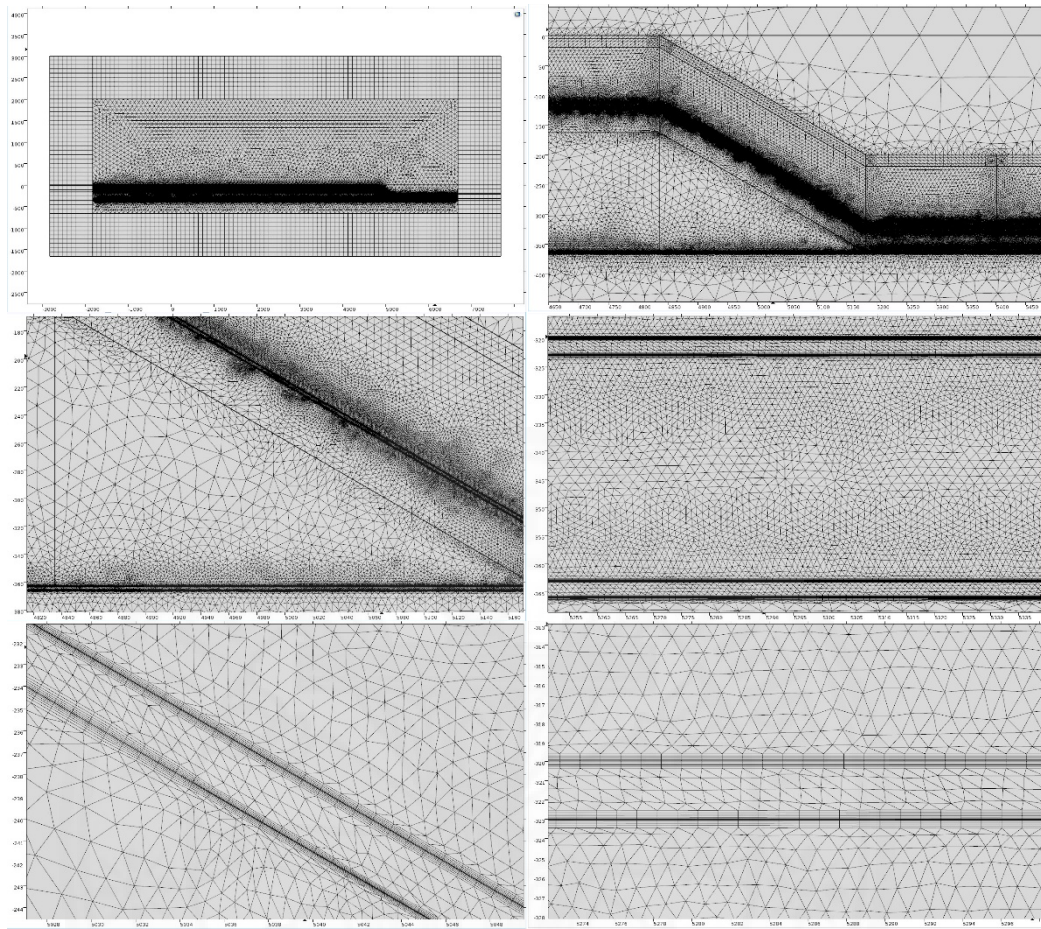
Figure 4.75 Mesh setting, overview, magnified at the taper, tip, taper border, and tip border.
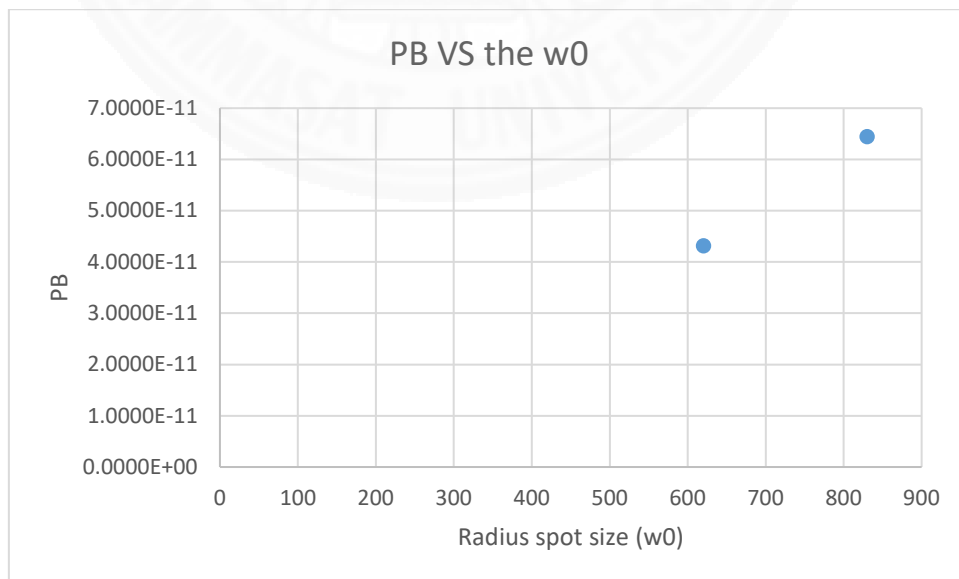
Figure 4.76 The w0 620 is dropped the efficiency around 33% of the w0 830 nm.
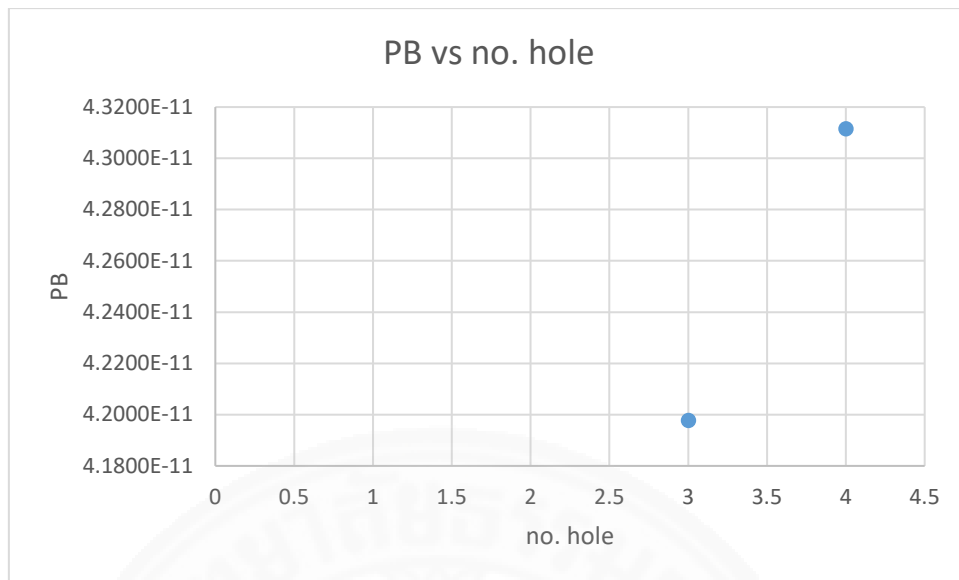
Figure 4.267 The optimum number of grating holes with w0=620 nm is 4.
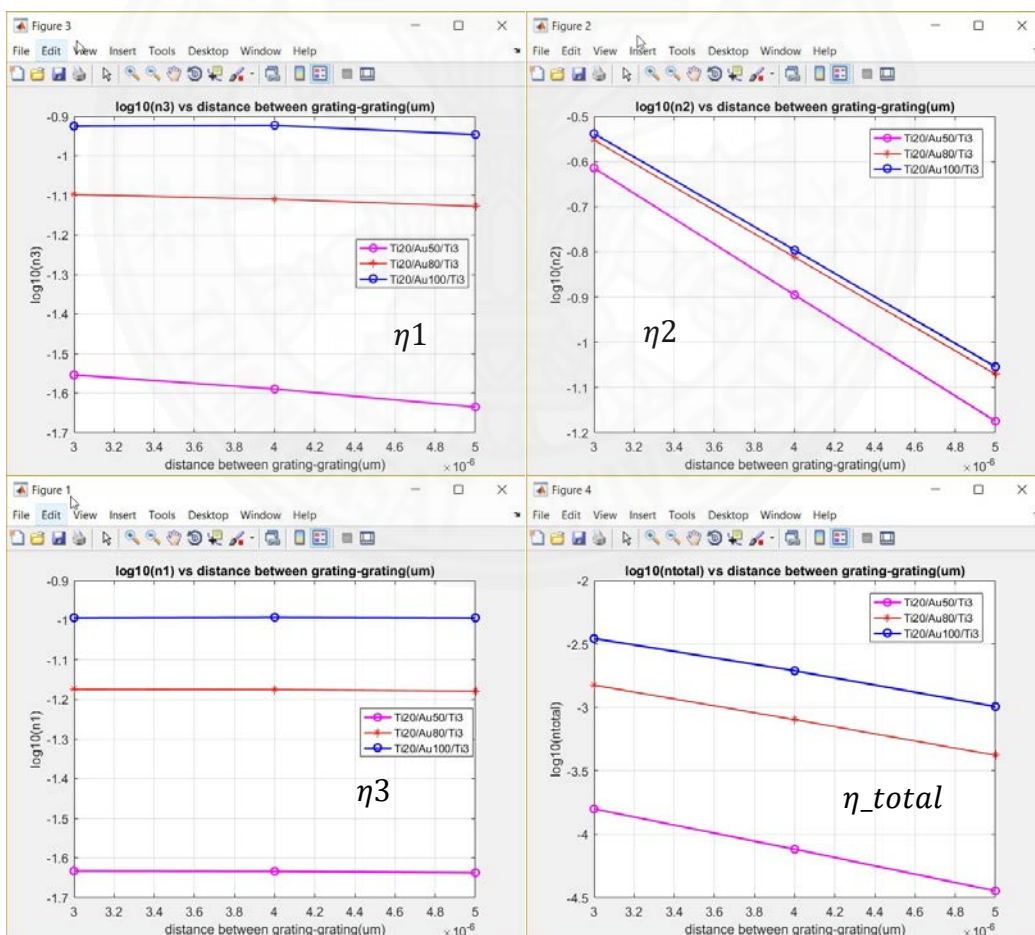
Figure 4.78 Log 10 (P_{out}/Pin0) at each part (efficiency; η) of Al$_2$O$_3$ 40 nm

Table 4.12 The optimum the lower Au layer thickness

Au 50

distance between grating-grating	Pin	Pin_0	Pout	Pout/Pin	pout/Pin_0	P1	P1/P_0 n1	P2	P2/P1 n2	Pout/P2 n3	n1*n2*n3
3 μm	5.31E-10	1.32E-09	2.09E-13	3.94E-04	1.58E-04	3.08E-11	2.33E-02	7.48E-12	2.43E-01	2.79E-02	1.58E-04
4 μm	5.32E-10	1.32E-09	1.01E-13	1.89E-04	7.62E-05	3.07E-11	2.33E-02	3.91E-12	1.27E-01	2.57E-02	7.62E-05
5 μm	5.32E-10	1.32E-09	4.72E-14	8.88E-05	3.57E-05	3.05E-11	2.31E-02	2.04E-12	6.69E-02	2.32E-02	3.57E-05

Au80

distance between grating-grating	Pin	Pin_0	Pout	Pout/Pin	pout/Pin_0	P1	P1/P_0 n1	P2	P2/P1 n2	Pout/P2 n3	n1*n2*n3
3 μm	8.53E-10	1.32E-09	1.98E-12	2.32E-03	1.50E-03	8.84E-11	6.69E-02	2.48E-11	2.80E-01	7.99E-02	1.50E-03
4 μm	8.50E-10	1.32E-09	1.06E-12	1.24E-03	8.00E-04	8.83E-11	6.68E-02	1.36E-11	1.54E-01	7.77E-02	8.00E-04
5 μm	8.45E-10	1.32E-09	5.55E-13	6.56E-04	4.20E-04	8.76E-11	6.63E-02	7.44E-12	8.50E-02	7.45E-02	4.20E-04

Au100

distance between grating-grating	Pin	Pin_0	Pout	Pout/Pin	pout/Pin_0	P1	P1/P_0 n1	P2	P2/P1 n2	Pout/P2 n3	n1*n2*n3
3 μm	1.20E-09	1.32E-09	4.62E-12	3.85E-03	3.49E-03	1.34E-10	1.01E-01	3.88E-11	2.90E-01	1.19E-01	3.49E-03
4 μm	1.20E-09	1.32E-09	2.57E-12	2.15E-03	1.94E-03	1.34E-10	1.02E-01	2.15E-11	1.60E-01	1.19E-01	1.94E-03
5 μm	1.19E-09	1.32E-09	1.34E-12	1.12E-03	1.01E-03	1.34E-10	1.01E-01	1.18E-11	8.83E-02	1.13E-01	1.01E-03
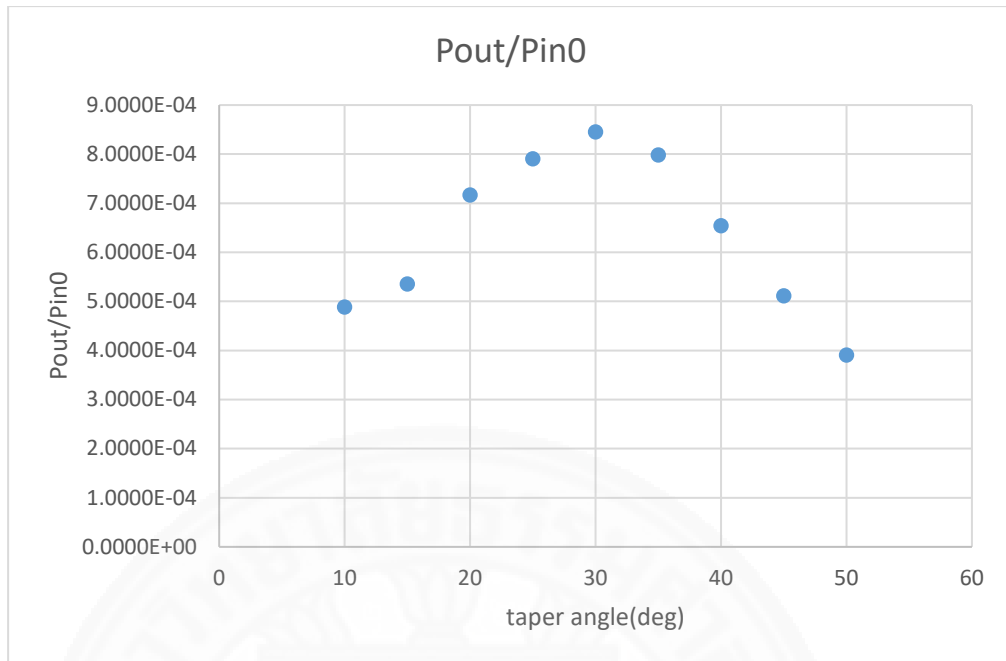
Figure 4.79 The optimum taper angle with Gaussian radius (w0) 620 nm is 30 deg.

4.5.3 The optimum parameters for the 20 nm-thickness of Al₂O₃
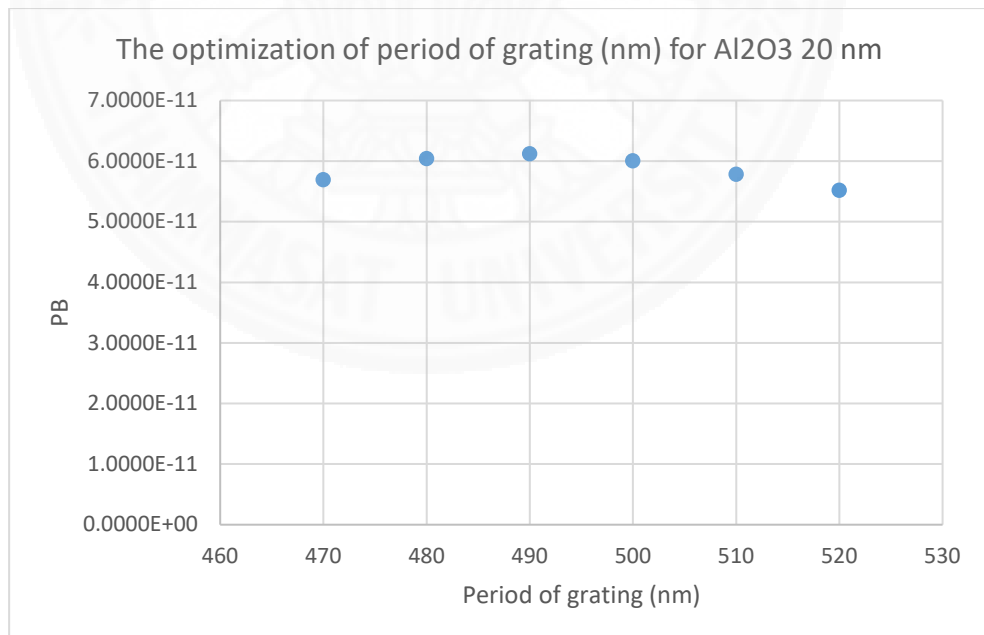
Figure 4.80 The optimized period of grating is 490 nm.

The optimization of grating width (nm) for Al2O3 20 nm
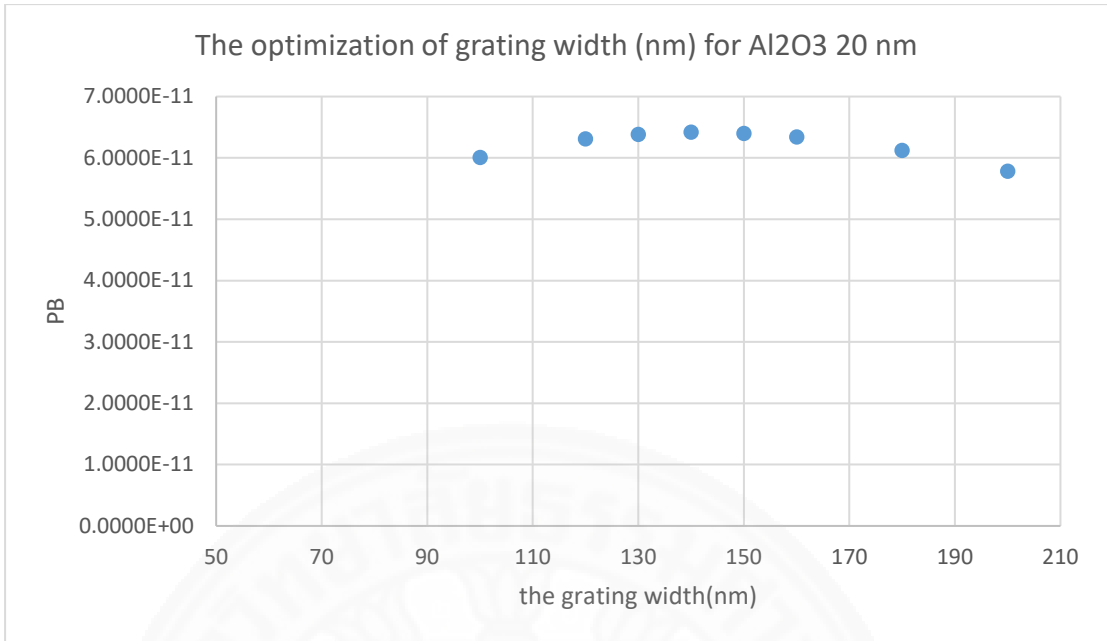
Figure 4.81 The optimized width of the grating is 140 nm.

The optimization of slit width (nm) for Al2O3 20 nm
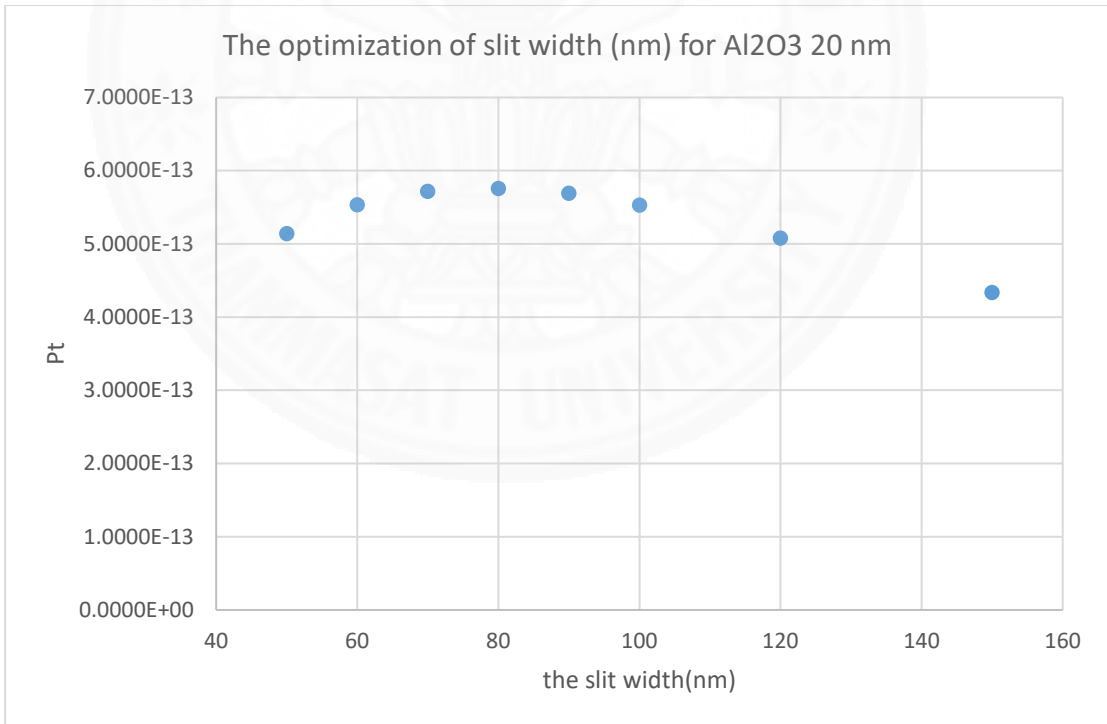
Figure 4.8227 The optimized the slit width is 80 nm.
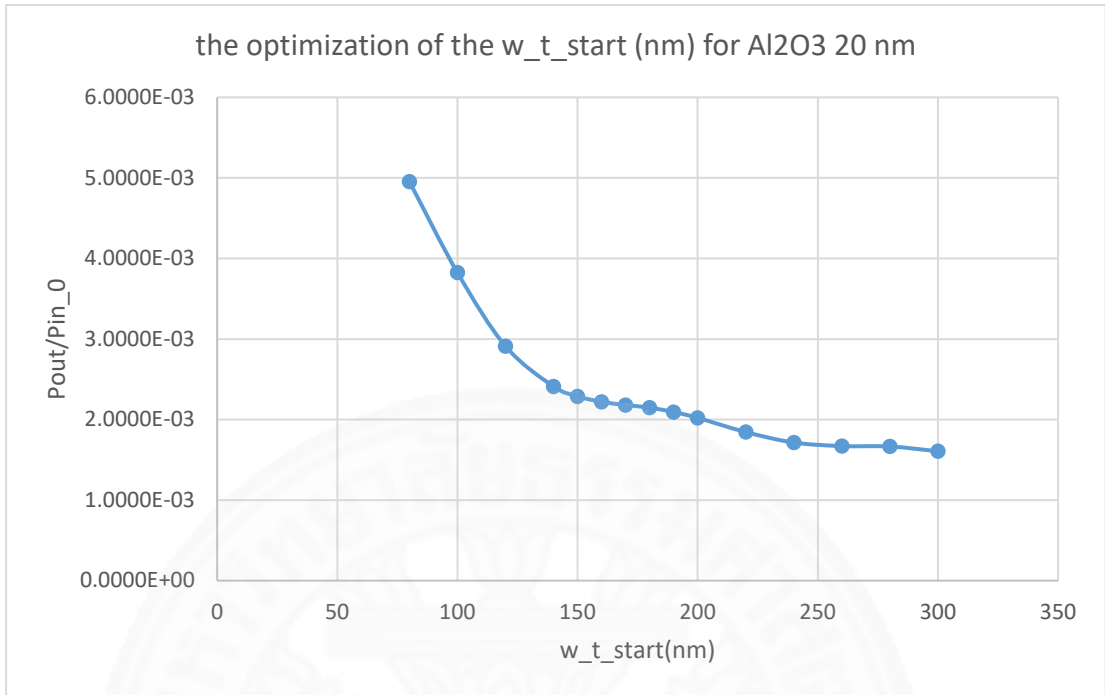
Figure 4.83 The optimized of the w_tip_start ; Peak no.1=80 nm, peak no.2 is 170 nm.
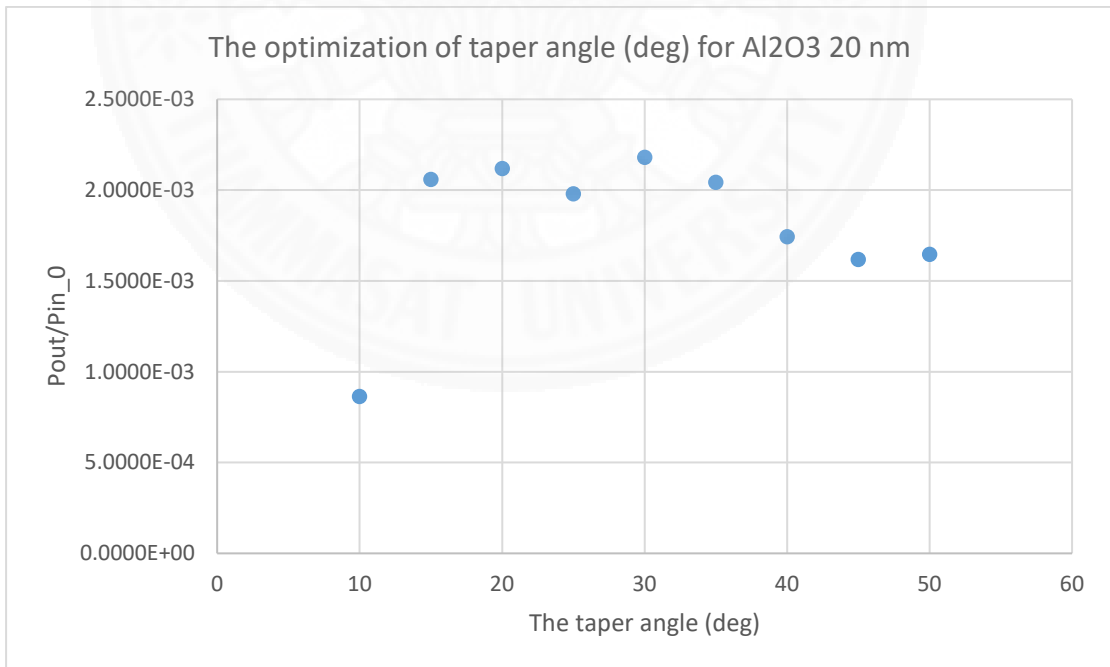
Figure 4.84 The optimized the taper angle is 30 deg.

Table 4.13 The coupling efficiency when varying the distance between grating and taper

Distance (μm)	Pin_0	Pout	Pout/Pin_0	log10(Pout/Pin0)
3	1.3218E-09	1.3302E-12	1.0064E-03	-2.997248804
4	1.3218E-09	6.5058E-13	4.9219E-04	-3.307865039
5	1.3218E-09	4.4726E-13	3.3837E-04	-3.470605688

Table 4.14 The parameter setting for the thin Al_2O_3 is 20 nm.

Structure Layer	thickness (nm)
w_Tiout	20
W_gold upper	80
W_Ti	3
W_Al2O3	20
W_SiO2	200
W_Ti	3
W_gold lower	300
	nm
Number of grating holes	4
Period of grating	490
Width of grating	140
slit width	80
Taper angle (deg.)	30
distance between grating and taper	4,000
distance between taper and slit	170

4.5.4 The optimum parameters for the 40 nm-thickness of Al₂O₃

The optimization of period of grating (nm) for Al2O3 40 nm
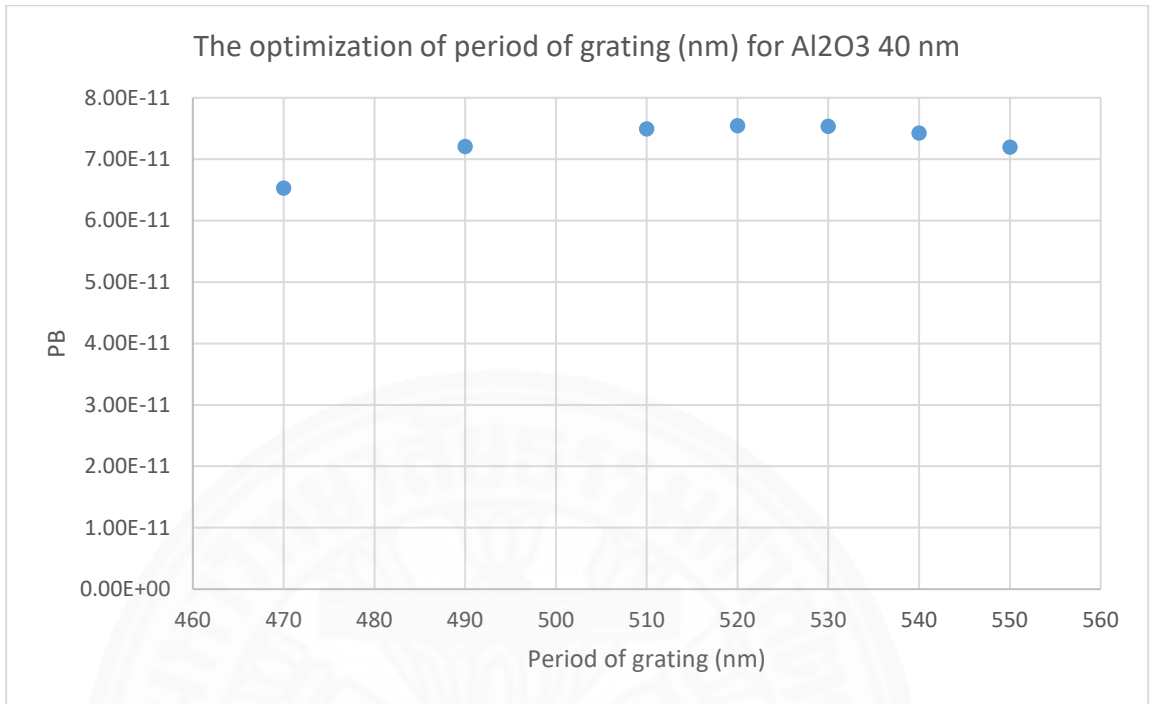
Figure 4.85 The optimized period of the grating is 520 nm.

The optimization of grating width (nm) for Al2O3 40 nm
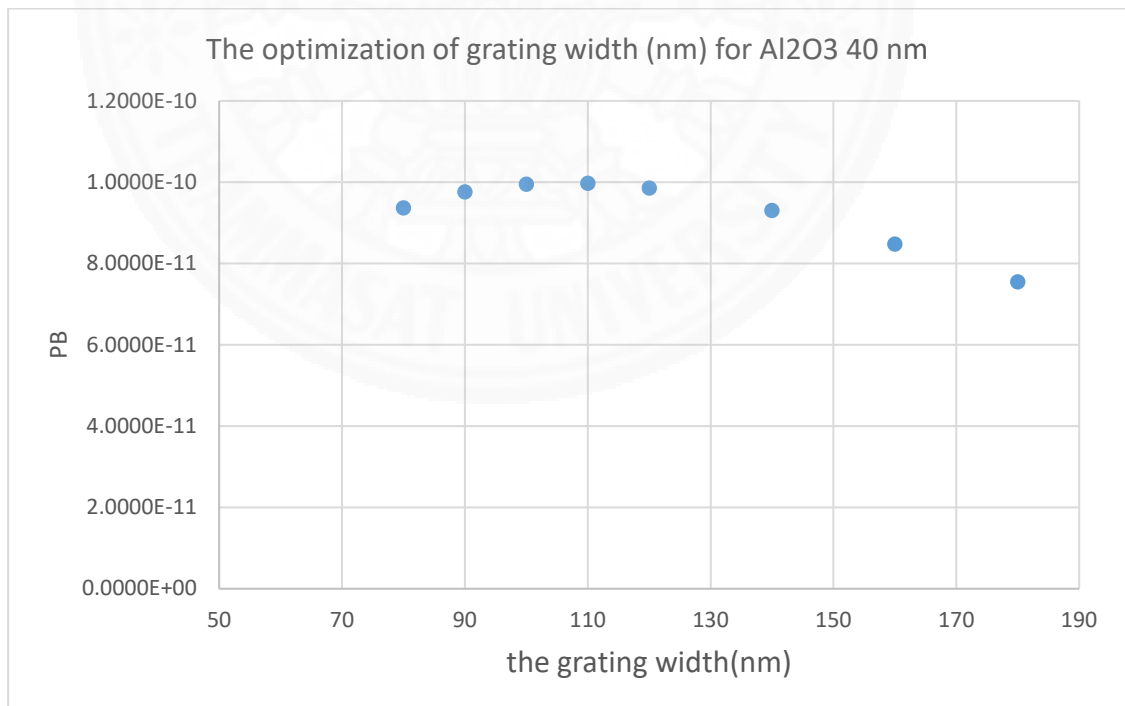
Figure 4.86 The optimized width of the grating is 110 nm.
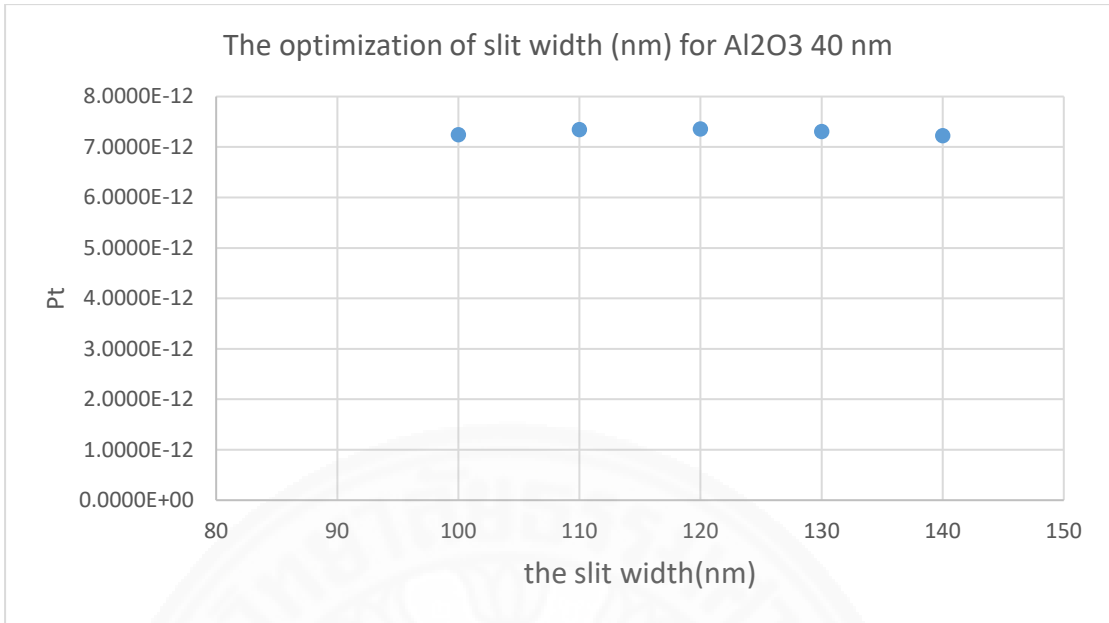
Figure 4.87 The optimized the slit width is 120 nm.
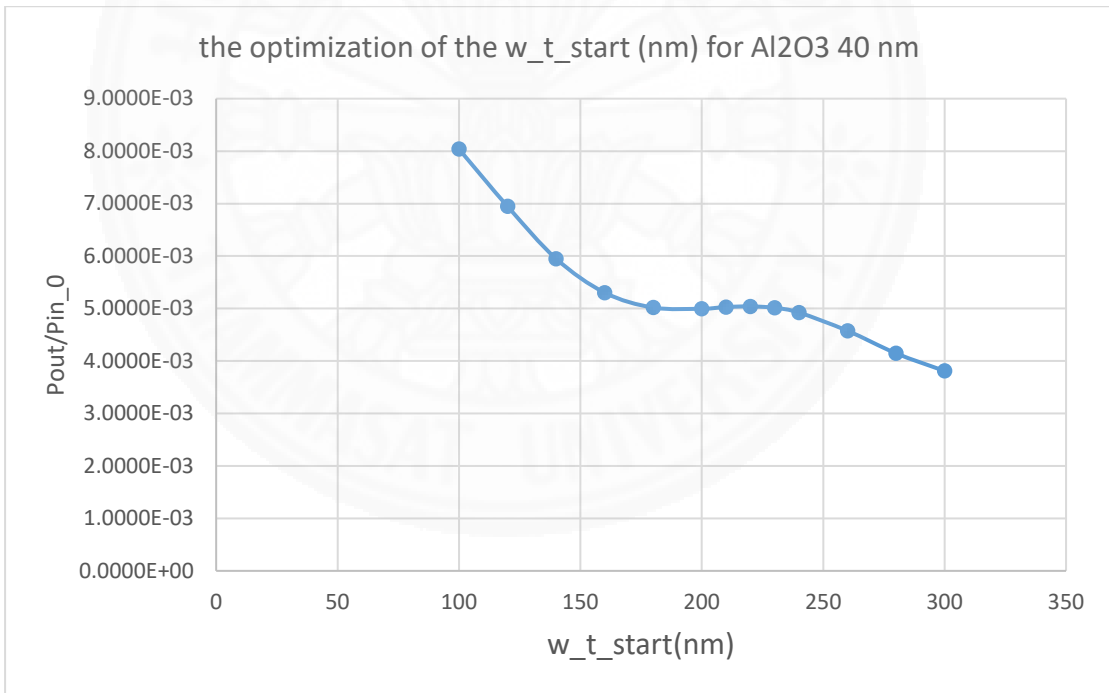
Figure 4.88 The optimized of the w_tip_start; Peak no.1=100 nm, peak no.2 is 220 nm.
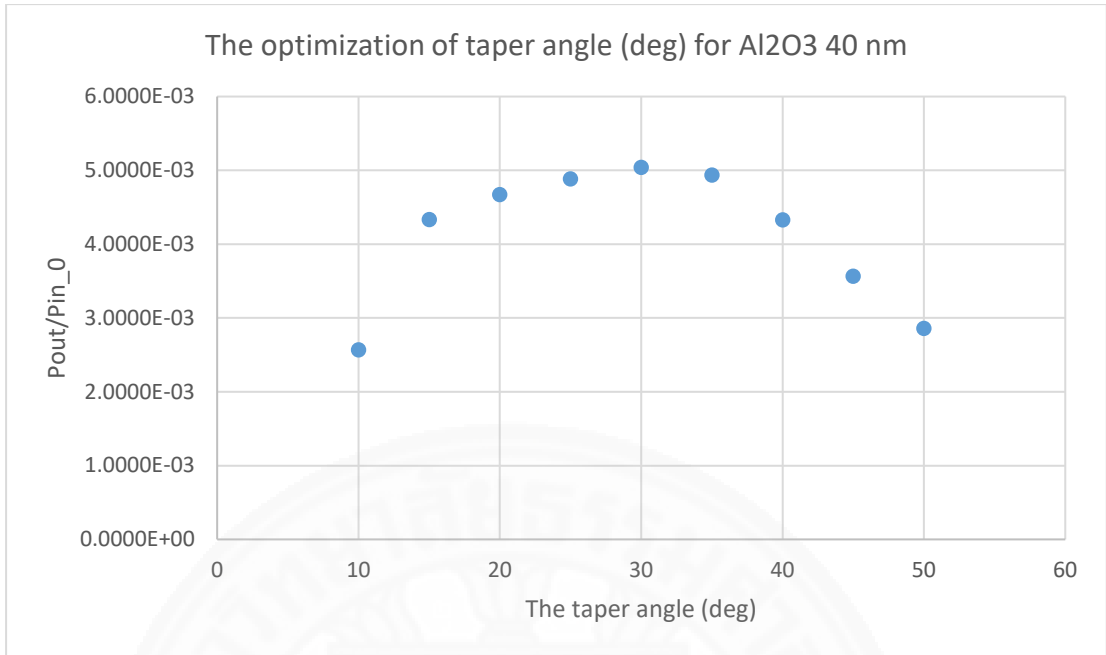
Figure 4.289 The optimized the taper angle is 30 deg.

Table 4.15 The coupling efficiency of the distance between grating and taper

Distance (μm)	Pin_0	Pout	Pout/Pin_0	log10(Pout/Pin0)
3	1.3218E-09	2.5733E-12	1.9468E-03	-2.710675328
4	1.3218E-09	1.3800E-12	1.0440E-03	-2.981286661
5	1.3218E-09	8.2450E-13	6.2377E-04	-3.204975088

Table 4.16 The parameter setting for the thin Al_2O_3 40 nm.

Structure Layer	thickness (nm)
w_Tiout	20
W_gold upper	80
W_Ti	3
W_Al2O3	40
W_SiO2	200
W_Ti	3
W_gold lower	300
	nm
Number of grating holes	4
Period of grating	520
Width of grating	110
slit width	120
Taper angle (deg.)	30
distance between grating and taper	4,000
distance between taper and slit	220

4.5.5 The optimum vertical step lenght for the final specimen
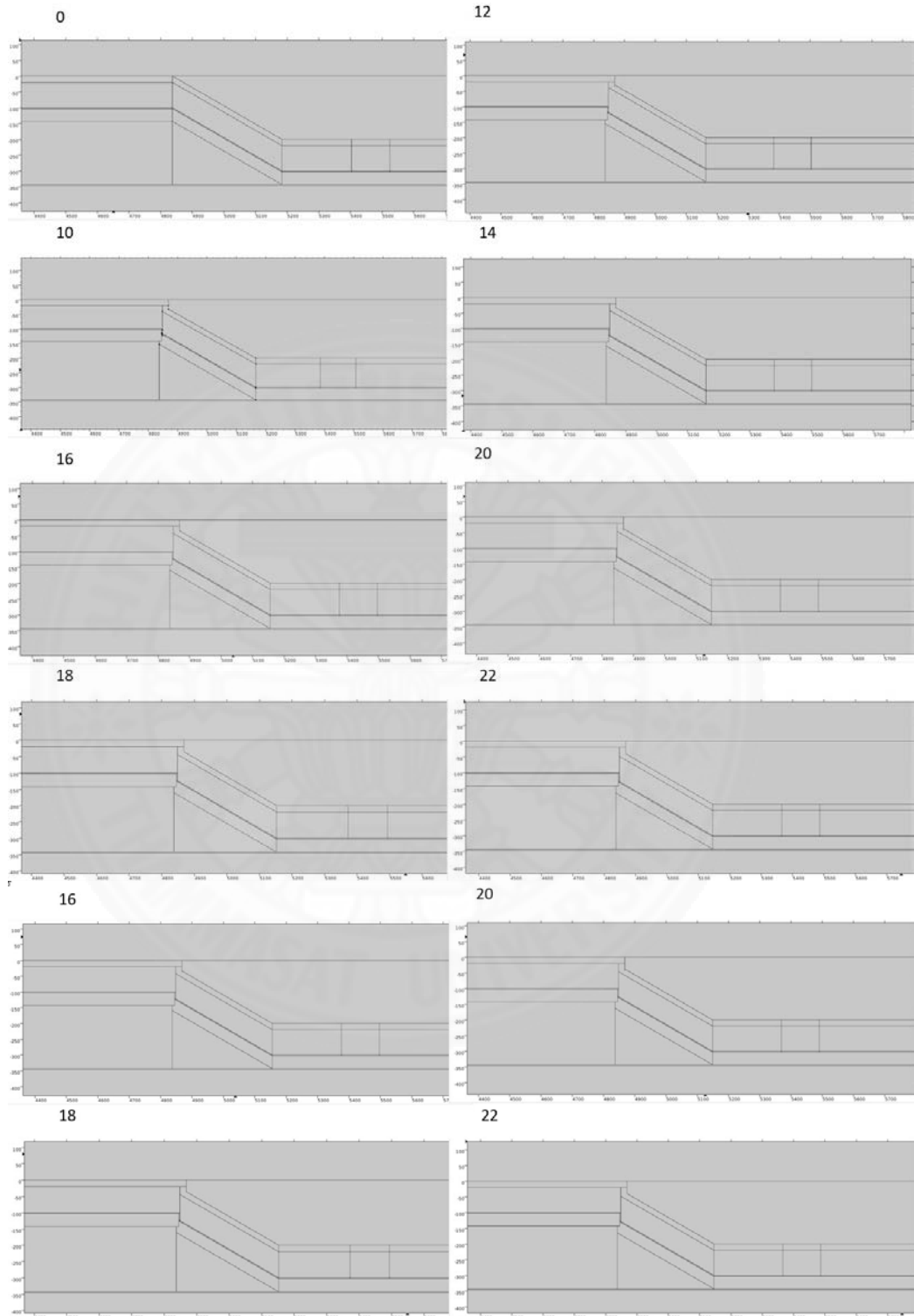
Figure 4.9029 The vertical step geometry of varying 10:2:30 nm calculation.

Name	Expression	Value	Description
z0	pi*w0^2/lda	1.455E-6 m	Rayleigh range
w0	620[nm]	6.2E-7 m	Spot radius
w_tip_start	220[nm]	2.2E-7 m	length of start hole in the tip
w_Tiout	20[nm]	2E-8 m	Ti outside width
w_Ti	3[nm]	3E-9 m	Ti inside width
w_t_hole	121[nm]	1.21E-7 m	hole width in the tip
w_sio2R	w_sio2-vl	1.8E-7 m	sio2 remain
w_sio2	200[nm]	2E-7 m	sio2 thickness
w_pml	lda	8.3E-7 m	Thickness of PML domains
w_hole	113[nm]	1.13E-7 m	hole width in body
w_gold_lo...	300[nm]	3E-7 m	lower gold width
w_gold	80[nm]	8E-8 m	gold thickness
w_body_s...	1000[nm]	1E-6 m	body start width
w_al2o3	40[nm]	4E-8 m	sio2Thin layer
w_air_up	2000[nm]	2E-6 m	air width
w_air	1000[nm]	1E-6 m	air thickness
vl	20[nm]	2E-8 m	vertical step
theta	0[deg]	0 rad	incident wave angle
Tangle	0.5774	0.5774	Tan angle
p_hole	520[nm]	5.2E-7 m	period of hold
n_Ti	3.23-4.0i	3.23-4i	refrectrive index of Ti
n_sio2	1.45	1.45	refrective index of sio2
n_gold	sqrt(Ep_gold)	0.17343-5.2182i	gold properties
n_al2o3	1.76	1.76	refrective index of al2o3
lda	830[nm]	8.3E-7 m	Wavelength
k	2*pi/lda	7.5701E6 1/m	Propagation constant
h_tip	1500[nm]	1.5E-6 m	tip lenght
h_taper	w_sio2R/Tangle	3.1174E-7 m	taper length
h_body	w_body_start+3*p_hole+w_hole+before_T	6.673E-6 m	body length
f	c_const/lda	3.612E14 1/s	Frequency
Ep_gold	-27.2-1.81i	-27.2-1.81i	elsilon of gold
E0	1[V/m]	1 V/m	Electric field amplitude
cut1	1000[nm]	1E-6 m	cutline 2D at the first position
before_T	4[um]	4E-6 m	distance between grating and taper

Figure 4.91 The parameter sitting of the vertical step calculation.
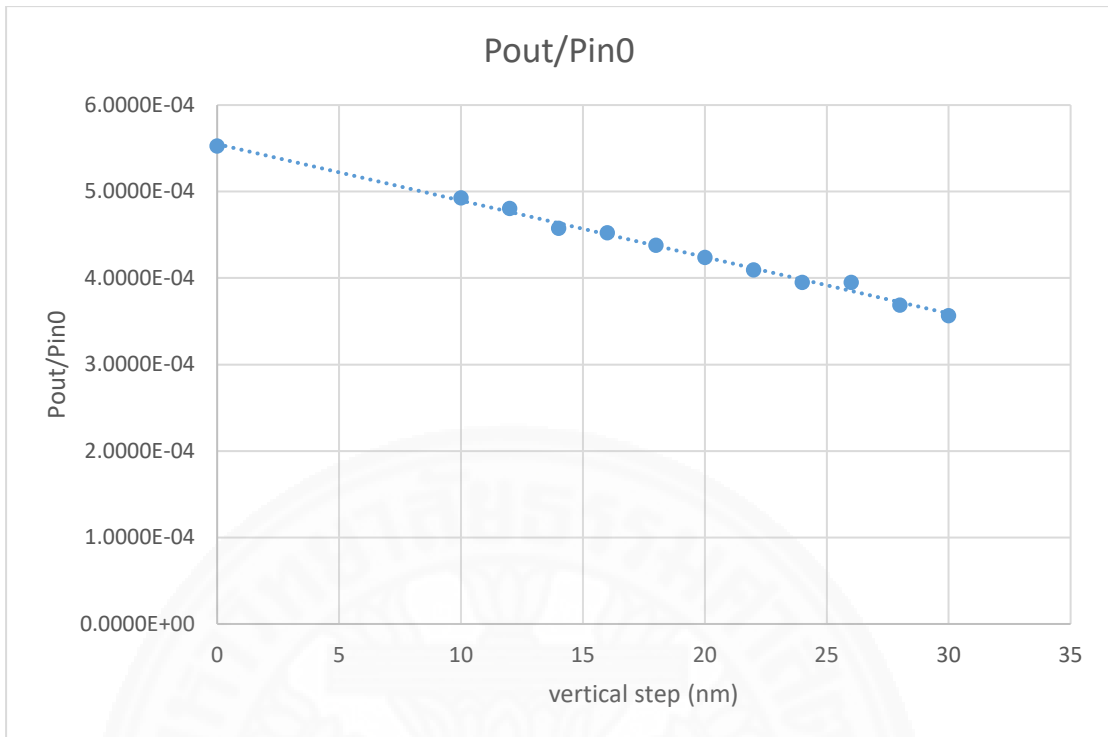
Figure 4.92 The efficiency of the vertical step varying.

4.5.6 The optimization of the final specimen

        The final specimen structure as shown in the figure 3.2, is operated at the 830 nm-wavelength. The light source is the Gaussian beam with radius beam 830 nm. The optimum parameters for fabricating are shown in the Table 4.17.

Table 4.17 The optimum parameters for the final specimen.

Materials: structure layer	Thickness (nm)
w_Tiout	20
W_gold upper	80
W_Ti	3
W_Al2O3	40
W_SiO2	200
W_Ti	3
W_gold lower	300

Input and Output parameter setting		nm
Input	Number of grating holes	4
	Period of grating	520
	Width of grating	110
	distance between grating and taper	4,000
	Taper angle (deg.)	30
	The Vertical step length	20-30
Output	Slit width	120
	distance between taper and slit	220

CHAPTER 5
FABRICATION AND RESULTS

The nano-focusing tapers with light input/output ports will fabricate in various taper angles and compare the efficiency and find the optimum taper angle according to the following simulation. Figure 5.1 shows the diagram of the nano-focusing device and figure 5.2 shows the fabrication process.
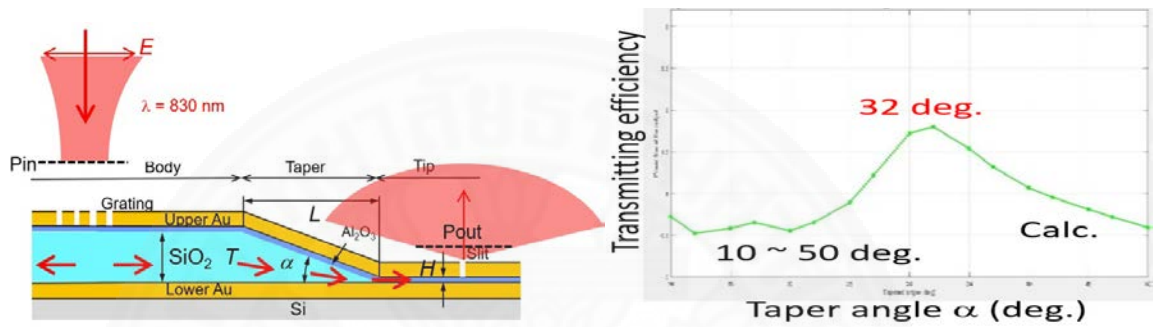
Figure 5.1 (Left) the optical characterization of nano-focusing taper and (right) the 32 deg. taper angle is our target.
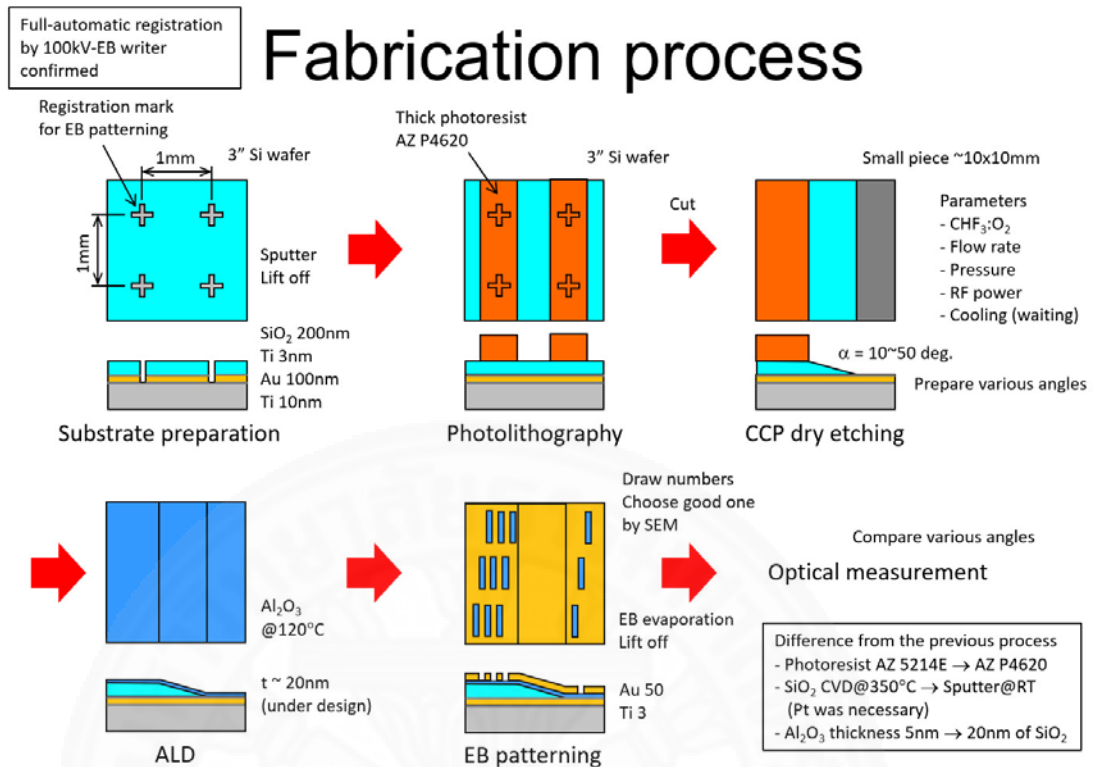
Figure 5.2 Fabrication process

The fabrication process consists of 5 steps as follow;

1) Substrate preparation

2) Photolithography for making the PR to make a taper angle

3) Taper angle using Oxide dry etching with a mixed gas

4) Cleaning, Al_2O_3 using ALD/SiO_2 Sputter

5) Grating and slit patterning by E-Beam lithography

5.1 The substrate preparation

The thin film of Au/SiO_2 are deposited on the Si wafer and make the cross mask to refer position when apply the E-Beam lithography for making the grating and slit in the step 5. The substrate preparation follows the steps below;

1) Si wafer surface checking

2) HMDS 3000 rmp 60 s, Drop the photoresist (PR) LOR5A 3000 rmp 60 s, then bake 180°C for 5 min, AZ5214E 3000 rpm 60s and bake 110°C for 2 min.

3) Exposure with the maskless lithography as the CAD data shown in figure 5.3 with Dose 100 mJ/cm^2 (Scanning mode; high speed).
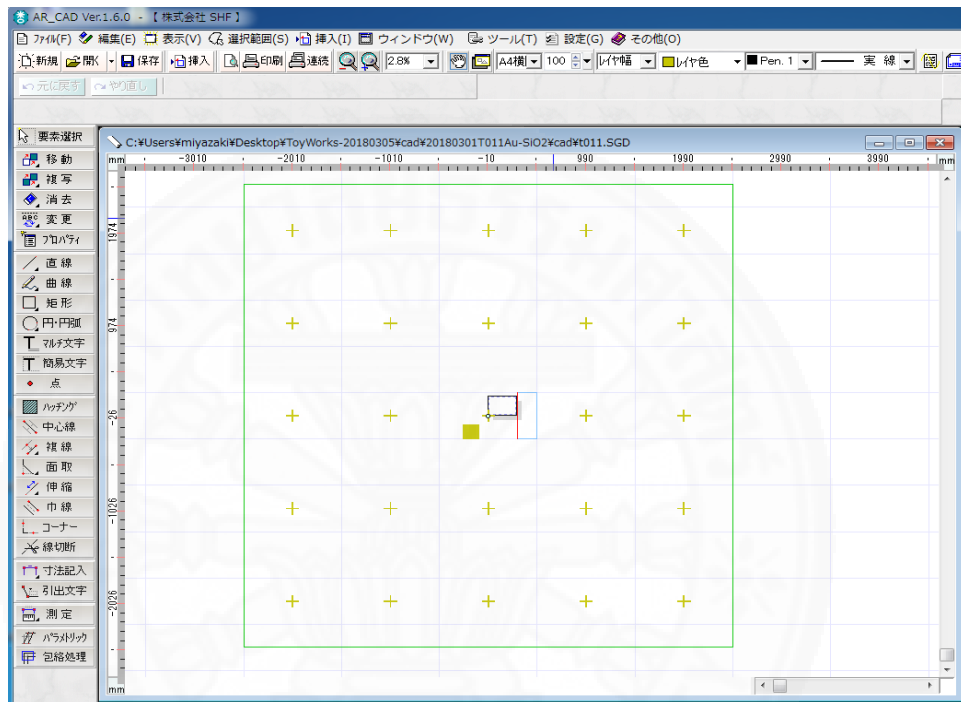
Figure 5.3 CAD data for making the pattern (cross mask) on the photoresist using the markless lithography.

4) Reversal bake 110°C for 2 min and UV exposure for 90 s (This process for making the negative resist; the exposure area, the cross mark, will be remained opposite with the positive resist).

5) Development, TMAH 2.38% 2.30 min and DI water longer than 30 s

6) Observed the sample (after developing the photoresist) by microscope as shown in figure 5.4

7) Do the sputtering process, to the deposition of the 10 nm-Ti, 100 nm-Au, 3 nm-Ti, and 200 nm-SiO$_2$ using the J-sputter machine as shown in figure 5.5-5.6

8) Then do the lift-off process by NMP solvent for 1 night as shown in figure 5.7.

9) Take the result from NMP after one night and clean the sample with acetone and put our sample with acetone in the vibrate 20 min and rinse with IPA, observed with a microscope and SEM observation as shown in figure 5.8 and 5.9, respectively.

Figure 5.4 After developing the PR, the pattern mark is clean, completed develop.

Figure 5.5 The J sputter and monitor for controlling operate to sputter Au-Ti-SiO$_2$ Film.
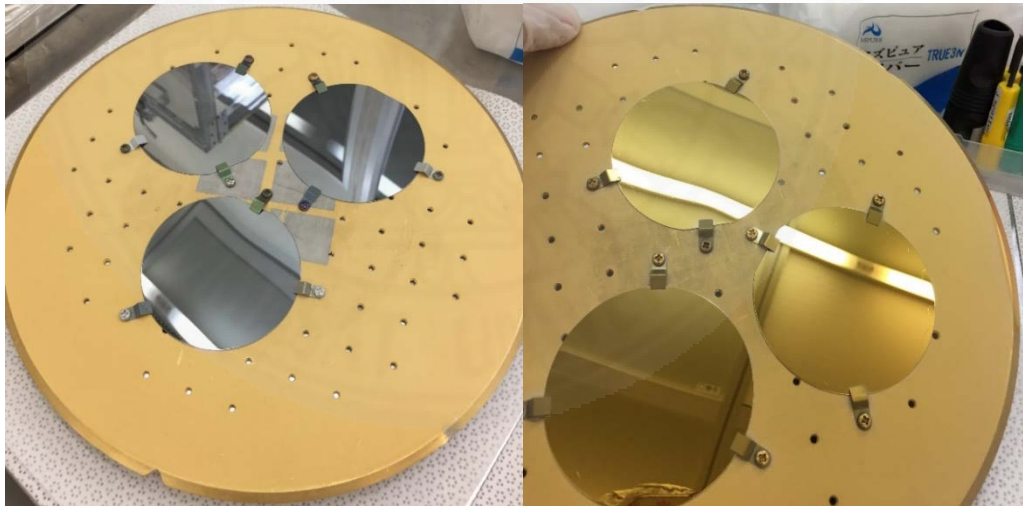
Figure 5.6 (Left) before and (Right) after the sputtering process.

Figure 5.7 (Left) NMP lift-off process for one night and (Right) after one night will add more temperature for complete lift-off remove.
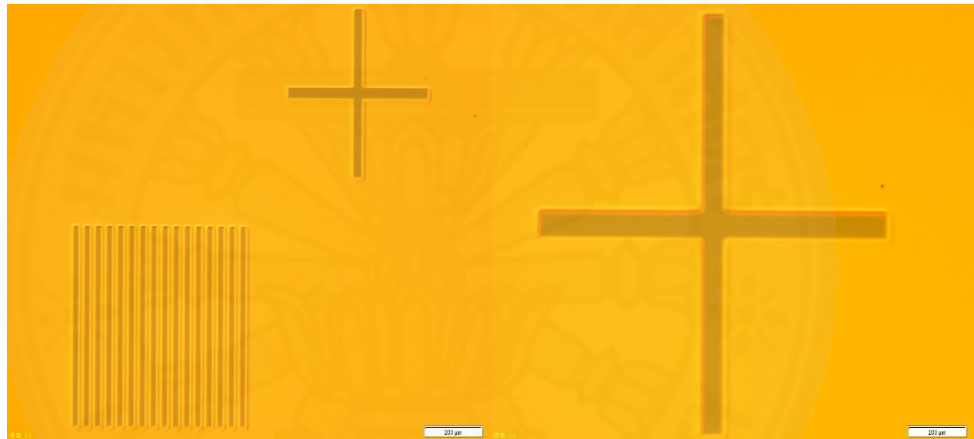
Figure 5.8 Microscope observation after the NMP Lift-off for one night.
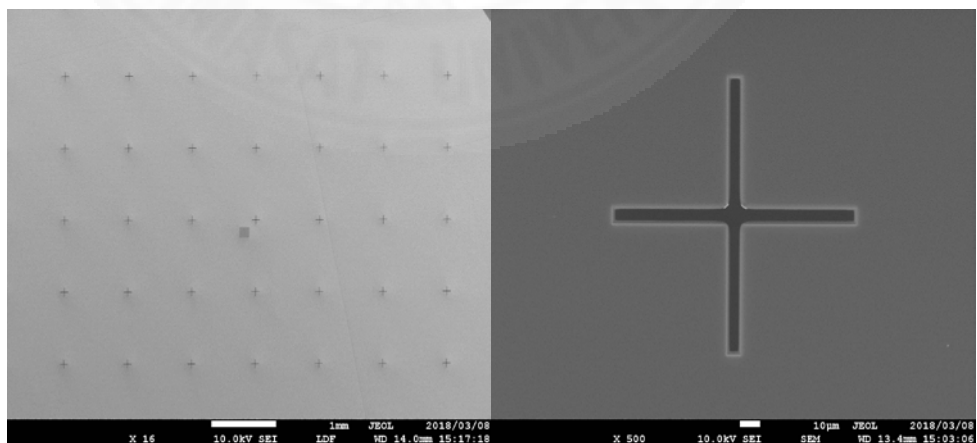
Figure 5.9 SEM observation after the NMP Lift-off for one night.

5.2 Photolithography for making the taper angle

5.2.1 The suitable does of laser lithography

 1) make a pattern on the small Si-wafer, first clean process with Acetone 1 min and IPA.

 2) For photoresist, HDMS 3000 rpm 1 min and AZP4620 1700 rmp 30s, then Bake 100 C 8 min. Our target to get the 10 μm-Photoresist thickness, following the instruction as shown in figure 5.10.

 3) For making a pattern with the markless lithography as shown in figure 5.11 and make recipes by use several doses at 500, 750, 1000, 1250, 1500 mJ/cm^2.

 4) Then develop with TMAH 2.38% 5 min and rinse by DI water 20 s.

 5) To observe the cross section with SEM, the 500 mJ/cm^2 dose is the best as shown in figure 5.12
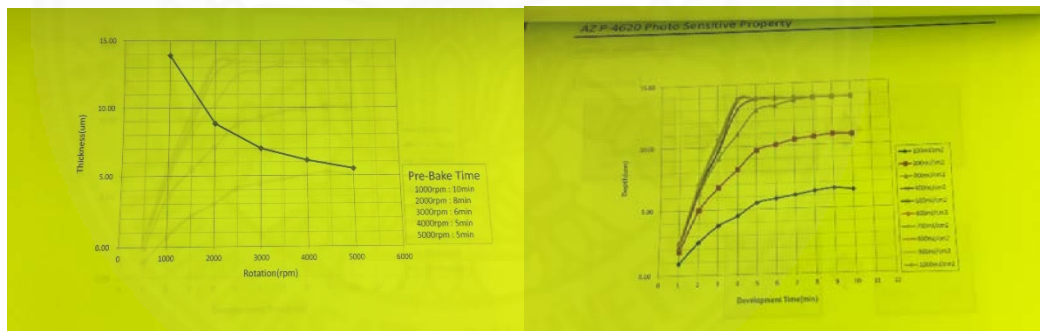
Figure 5.10 (Left) making, the thickness of AZP4620 making by using the spin coat rotation rate (right) the depth of the lithography making, using the different doses.
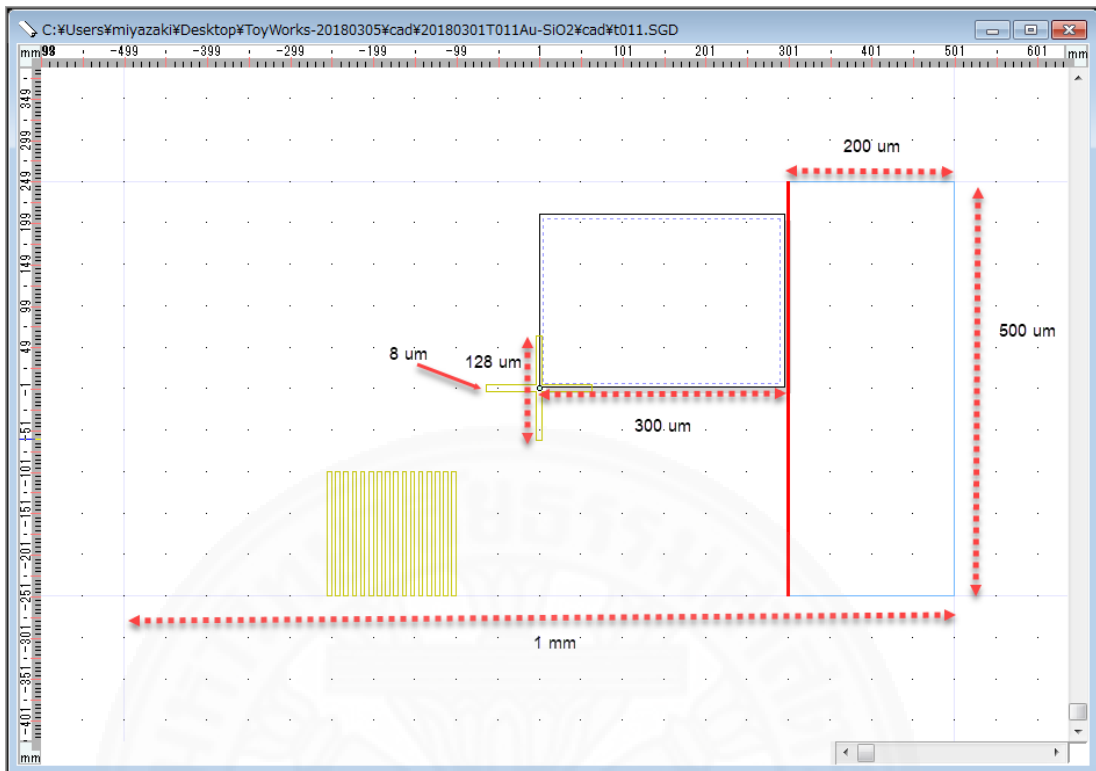
Figure 5.11 The CAD data for making the thick photo resist pattern before dry etching.
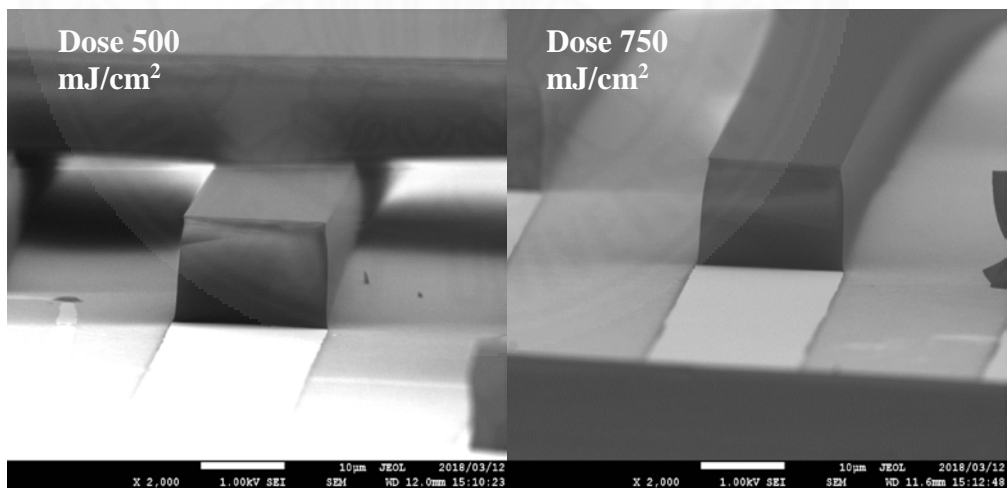
Figure 5.12 The SEM observation, cross section of the Dose 500 and 750 mJ/cm^2.
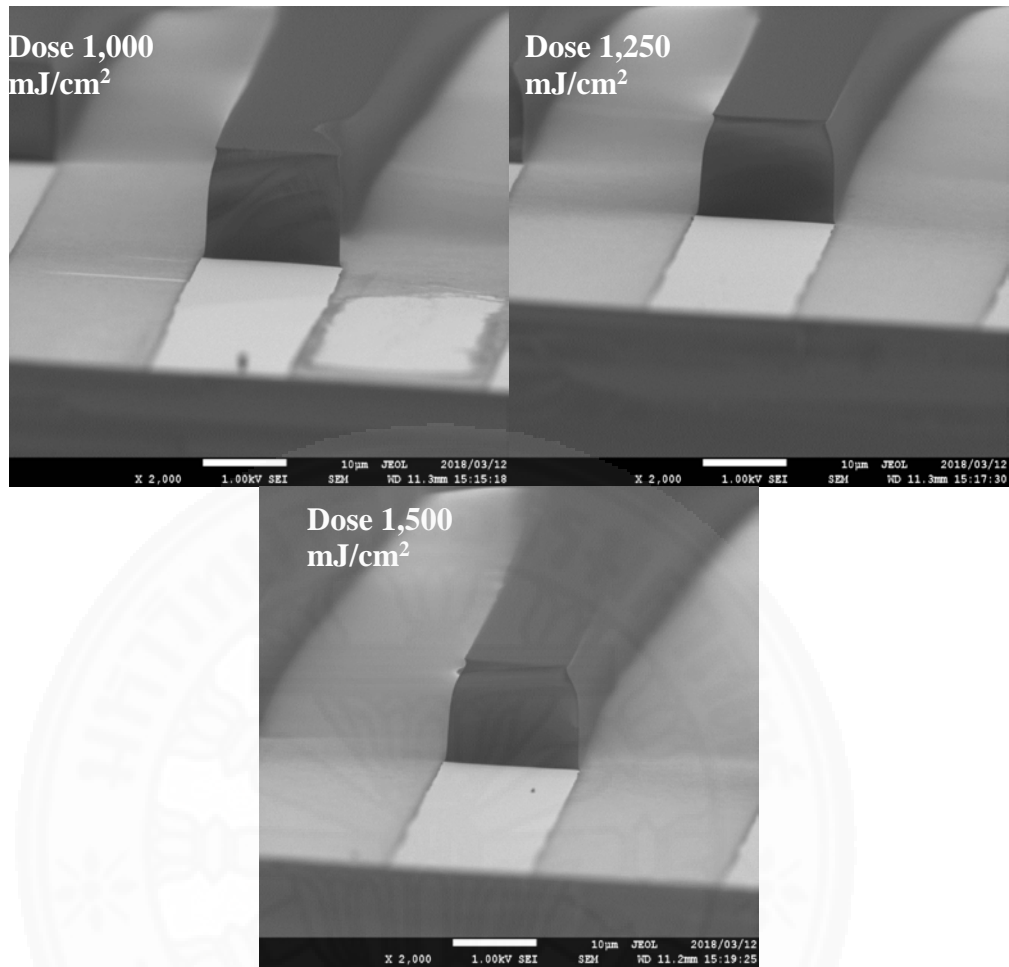
Figure 5.13 The SEM observation, cross section of the Dose 1,000, 1,250, and 1500 mJ/cm^2.

From SEM observation, the 500 mJ/cm^2 dose is the best because the shape of PR is a straight line at 90 deg. After getting the suitable dose, the next is to make the pattern for making the taper angle by using the 'B' and 'A' sample.

5.2.2 The Photoresist patterning for making the taper angle

1) Ashing the B sample by O$_2$ plasma for 5 min.

2) for photoresist, HDMS 3000 rpm 1 min + AZP4620 1700 rmp 30 s and Bake 100ºC 8 min. The target is the 10 micron-Photoresist thickness.

3) For making the pattern with the markless lithography, the dose 500 mJ/cm^2 is applied.

4) After that, develop sample with TMAH 2.38% 5 min and DI water rinse 30 s.

5) Microscopic observation and take some picture as shown in figure 5.14.

Figure 5.14 Microscope observation after developing with TMAH 2.38% 5 min and rinse by DI water 3 0s.

5.3 Making taper angle using the oxide dry etching with a mixed gas

After the simulation results, the next is doing the experiments to get the optimum taper angle which is 31 deg. and to get 8 typical taper angles start from 10 deg. to 50 deg. First, the 3 si-wafer of 'A', 'B', and 'C' are prepared for trial dry etching by separating it into small pieces as shown in figure 5.15. For Oxide dry etching machine as shown in figure 5.16, four parameters are adjusted which are the percentage of gases (CHF$_3$/O$_2$), RF Power, the pressure, and etch time to control a different taper angle by those conditions.

First, a data to forecast the taper angle is considered by making from start to dry etching within 3 min and applying the different percentage of gases as shown in the first trial etching in figure 5.17-5.18 then the remaining SiO_2 will measure by SEM observation and calculate the etch rate and taper angle. The results of second and third trial SiO_2 etching is shown in the figure 5.19-5.22 and table 5.1 shows all trials SiO_2 etching conditions. Figure 5.23 shows the sample of SEM observation.
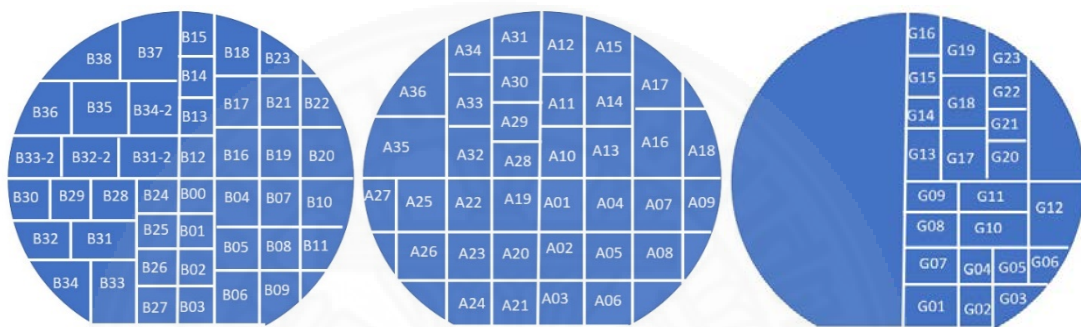
Figure 5.15 To cut 3″ Si wafer 'B','A', and 'G' into small pieces.

Figure 5.16 Oxide Dry Etching machine, user interface, Dry etching tray for loading the sample, and the sample preparation on dry etching holder.

5.3.1 The first dry etching (T015)

Sub: Si/10nm-Ti/100nm-Au/3 nm-Ti/200nm-SiO2

Gas	Pressure	RF	Time
CHF3/O2(Sccm)	3 Pa	250 W	3 min

Date: 20180320
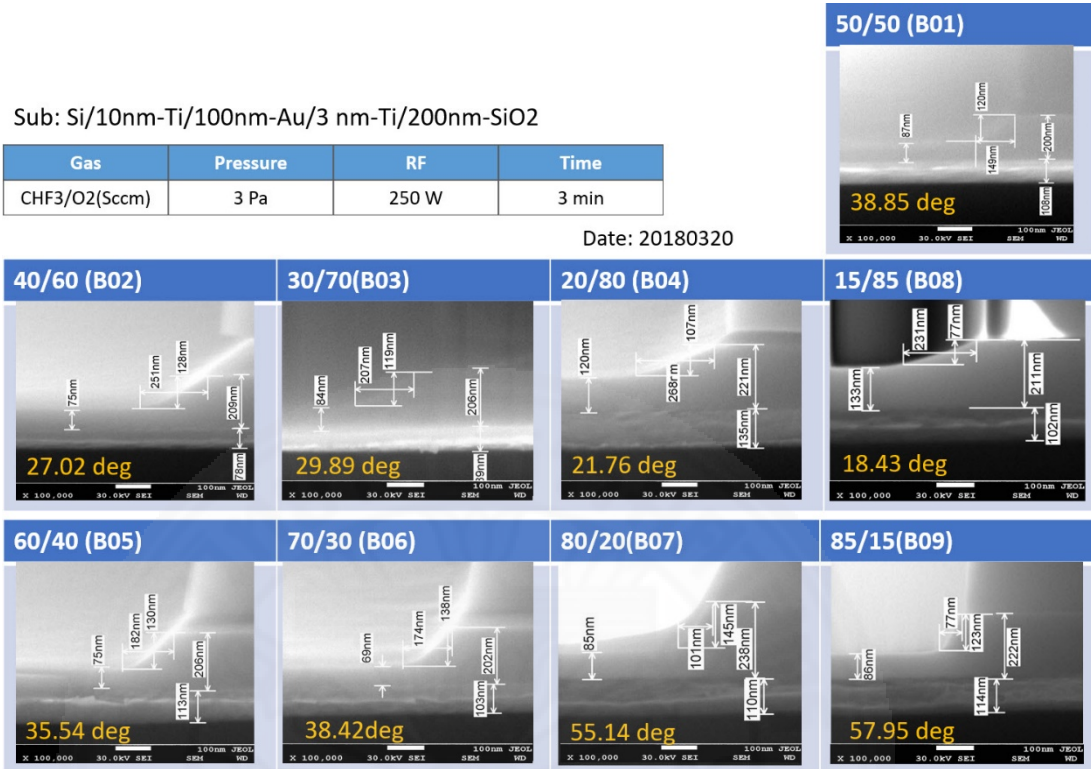
Figure 5.17 The SEM observation of the first trial etching.
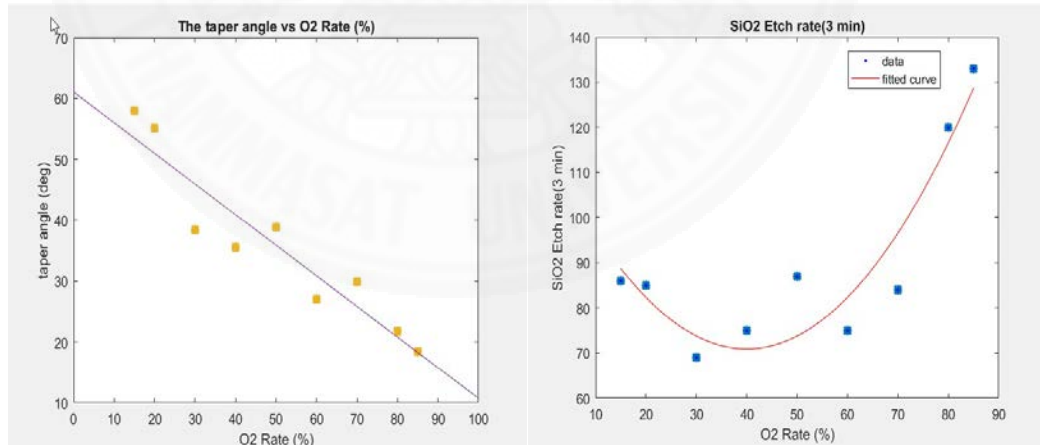
Figure 5.18 (Left) the taper angle vs the percentage of O_2 rate (Right) the SiO_2 etch rate vs the percentage of O_2 rate.

5.3.2 The second dry etching (T016 and T017)
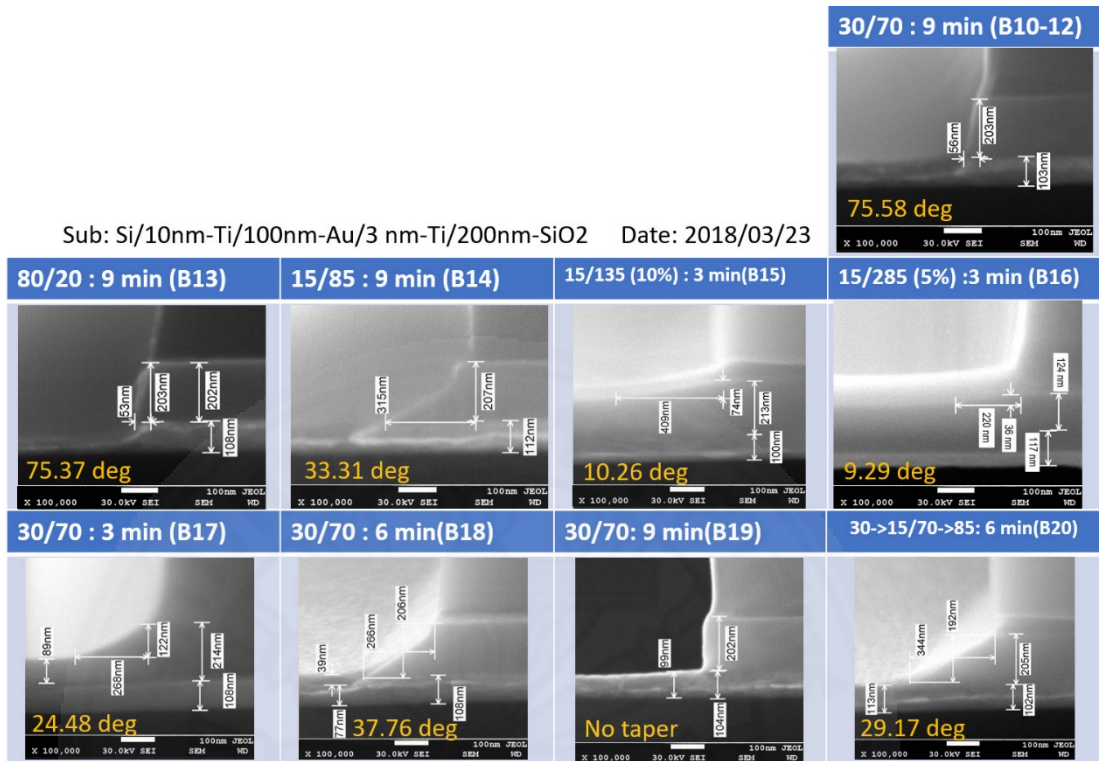
Figure 5.19 The SEM observation of the second trial etching.
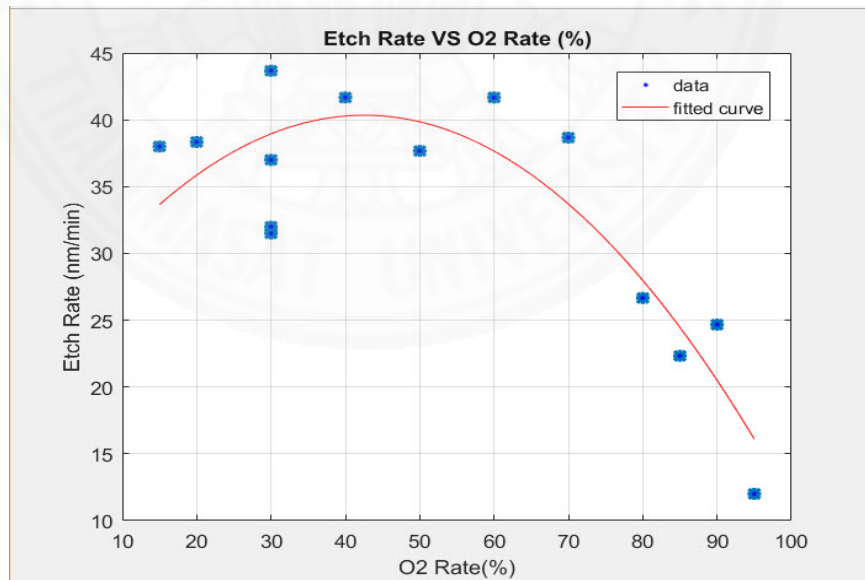
Figure 5.20 The SiO$_2$ etch rate vs the percentage of O$_2$ rate.

5.3.3 The third dry etching (T018 and T019)

Sub: Si/10nm-Ti/100nm-Au/3 nm-Ti/200nm-SiO2
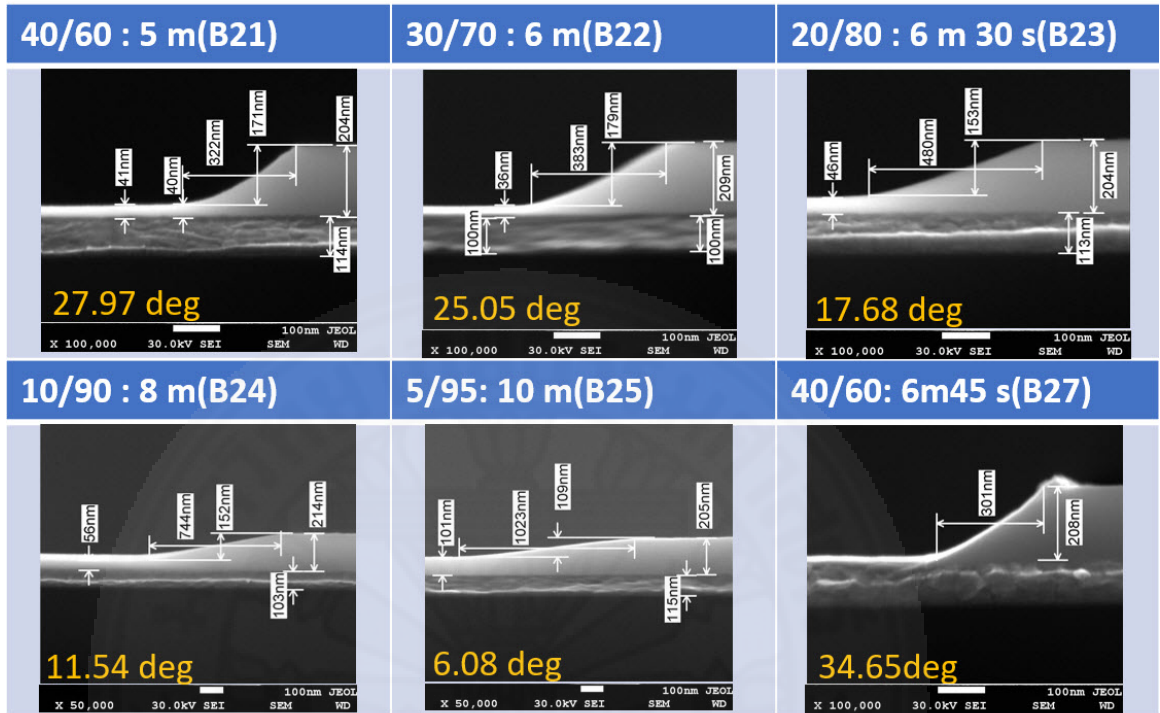
Date: 2018/04/06

Figure 5.21 The SEM observation of the third trial dry etching
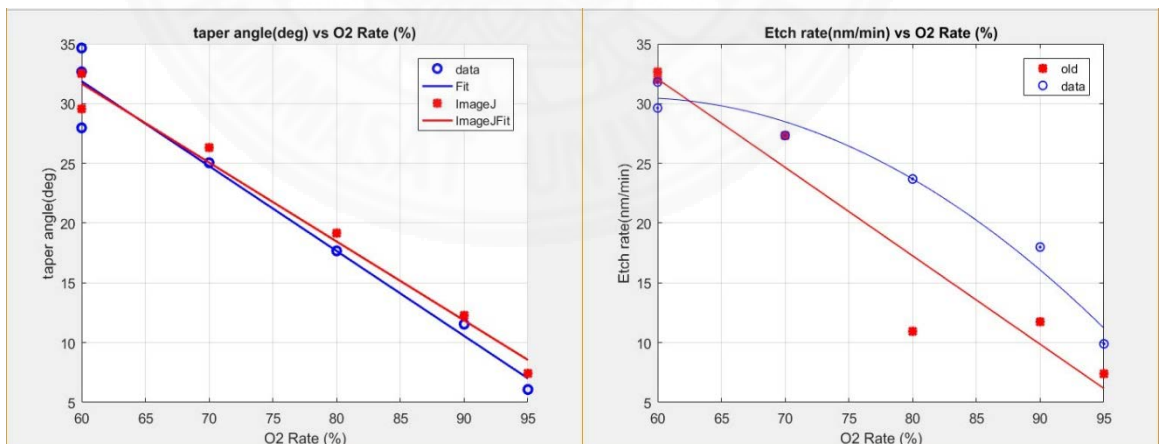
Figure 5.22 (Left) the taper angle vs the percentage of O_2 rate (Right) the SiO_2 etch rate vs the percentage of O_2 rate.

Table 5.1 The SiO$_2$ etch conditions and the SEM observation data.

Experiment	The SiO$_2$ etch conditions.						SEM observation			
	wafer name	CHF$_3$ %/Sccm	O$_2$%/Sccm	Time (min)	Pressure (Pa)	RF (W)	angle (deg.)	h_taper (nm)	w_sio2 (nm)	SiO$_2$ remained (nm)
T015	B01	50/50	50/50	3	3	250	38.9	149	120	87
	B02	40/40	60/60	3	3	250	27.0	251	128	75
	B03	30/30	70/70	3	3	250	29.9	207	119	84
	B04	20/20	80/80	3	3	250	21.8	268	107	120
	B05	60/60	40/40	3	3	250	18.4	182	130	75
	B06	70/70	30/30	3	3	250	35.5	174	138	69
	B07	80/80	20/20	3	3	250	38.4	101	145	85
	B08	15/15	85/85	3	3	250	55.1	231	77	133
	B09	85/85	15/15	3	3	250	58.0	77	123	86
T016 T017	B10	30/30	70/70	9	3	250				
	B11	30/30	70/70	9	3	250				
	B12	30/30	70/70	9	3	250	75.6	56	203	0
	B13	80/80	20/20	9	3	250	75.4	53	203	0
	B14	15/15	85/85	9	3	250	33.3/90	315	207	0
	B15	10/15	90/135	3	3	250	10.3	409	74	139
	B16	5/15	95/258	3	3	250	9.3	220	36	88
	B17	30/30	70/70	3	3	250	24.5	268	122	89
	B18	30/30	70/70	6	3	250	37.8/90	266	206	0
	B19	30/30	70/70	9	3	250	90	0	202	0
	B20	30->15	70->85	6	3	250	29.2	344	192	13
T018	B21	40/120	60/180	5	3	250	28	322	171	41
	B22	30/90	70/210	6	3	250	25.1	383	179	36
	B23	20/60	80/240	6m30s	3	250	17.7	480	153	46
	B24	10/30	90/270	8	3	250	11.5	744	152	56

Experiment	The SiO$_2$ etch conditions.						SEM observation			
	wafer name	CHF$_3$ %/Sccm	O$_2$%/Sccm	Time (min)	Pressure (Pa)	RF (W)	angle (deg.)	h_taper (nm)	w_sio2 (nm)	SiO$_2$ remained (nm)
	B25	5/15	95/285	10	3	250	6.1	1023	109	101
	B26	10/30	90/270	3x3=9	3	250	10.3	730	133	95
T019	B27	40/120	60/180	6m45s	3	250	34.7	301	208	8
	B28	30/90	70/210	9m10s	3	250	30/90	147	85	0
	B29	20/60	80/240	13	3	250	26.2/90	126	62	0
	B30	10/30	90/270	22	3	250	8	1489	208	0
	B31	5/15	95/285	31m24s	3	250	2.3	3239	131	0
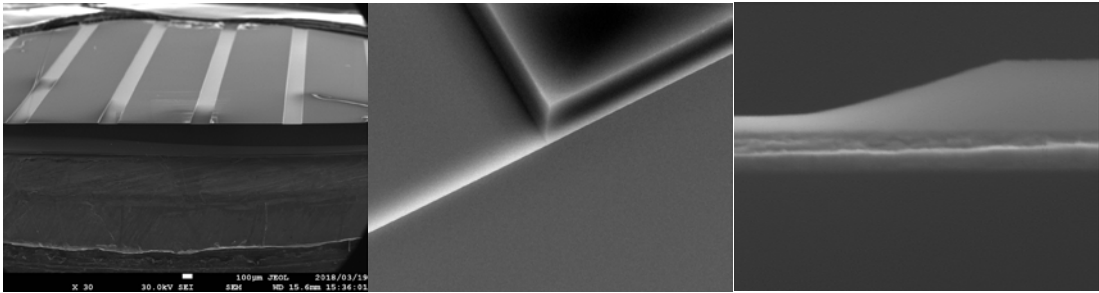
Figure 5.23 SEM observation (left) the top view of overview (middle) the 45 degrees view of the taper and PR, (right) the magnification of the taper.

From the SEM results, in the second trial, if the over etching SiO_2 is applied, the small vertical angle is appeared at the taper part and then the etch rate is suddenly changed because Au is the metal and the electron can charge and pass through the Au layer, so the Au layer will be etched. In case of over etching time, the SiO_2 completed etched (no taper part), it is only vertical 90 deg. appeared as shown in the second and third trial etching results. To solve this problem, the new structure by adding the Al_2O_3 layer between the lower Au layer and SiO_2 layer is applied because the Al_2O_3 is the dielectric material which electron cannot pass through that layer. The 20 nm-Al_2O_3 thickness layer is the optimum value to apply in the next structure.

5.3.4 The Al_2O_3 layer to stop the Au layer etched

To investigate the suspect, the Ti10/Au100/Ti3/ $Al_2O_3$20nm/ SiO_2_200 and Al_2O_3 100 nm is applying in the etching process. The process for preparing and making the pattern on Al_2O_3 wafer as shown in figure 5.24-5.26 which is same as the process to make the 'A','B', and 'C' wafer. Furthermore, only Ti10/ $Al_2O_3$100 is prepared for pre-etching and find the etch rate of Al_2O_3 and compare it with the etch rate of SiO_2.
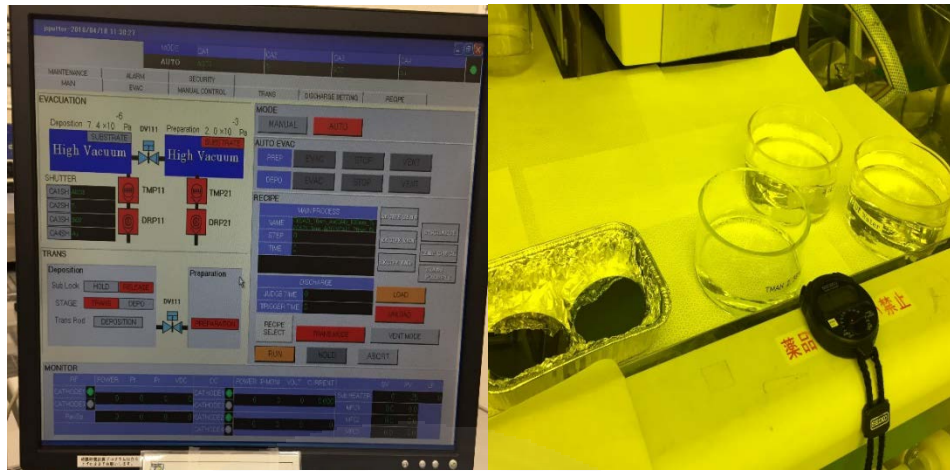
Figure 5.24 Al$_2$O$_3$ wafer making process
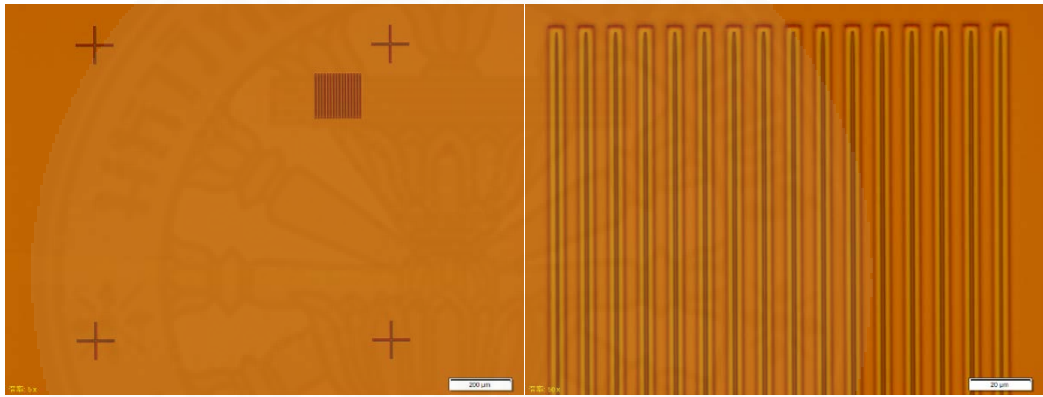
Figure 5.25 Al$_2$O$_3$ after development
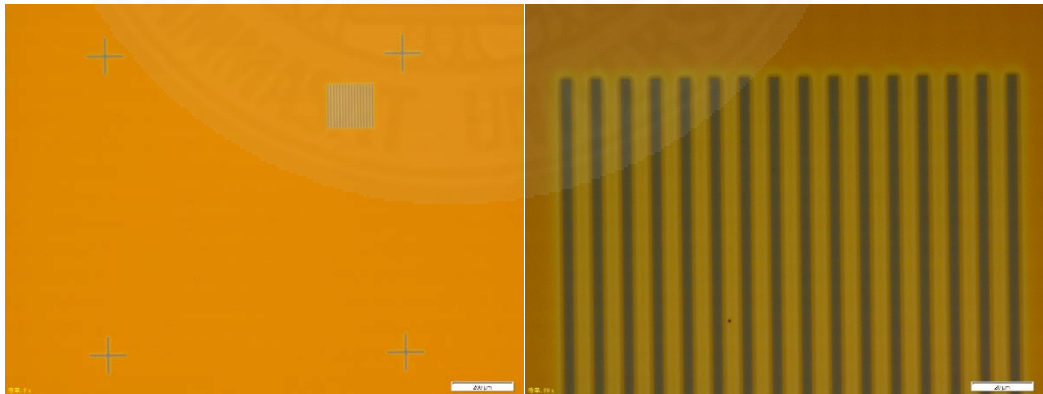
Figure 5.26 Al$_2$O$_3$ after NMP lift-off process.
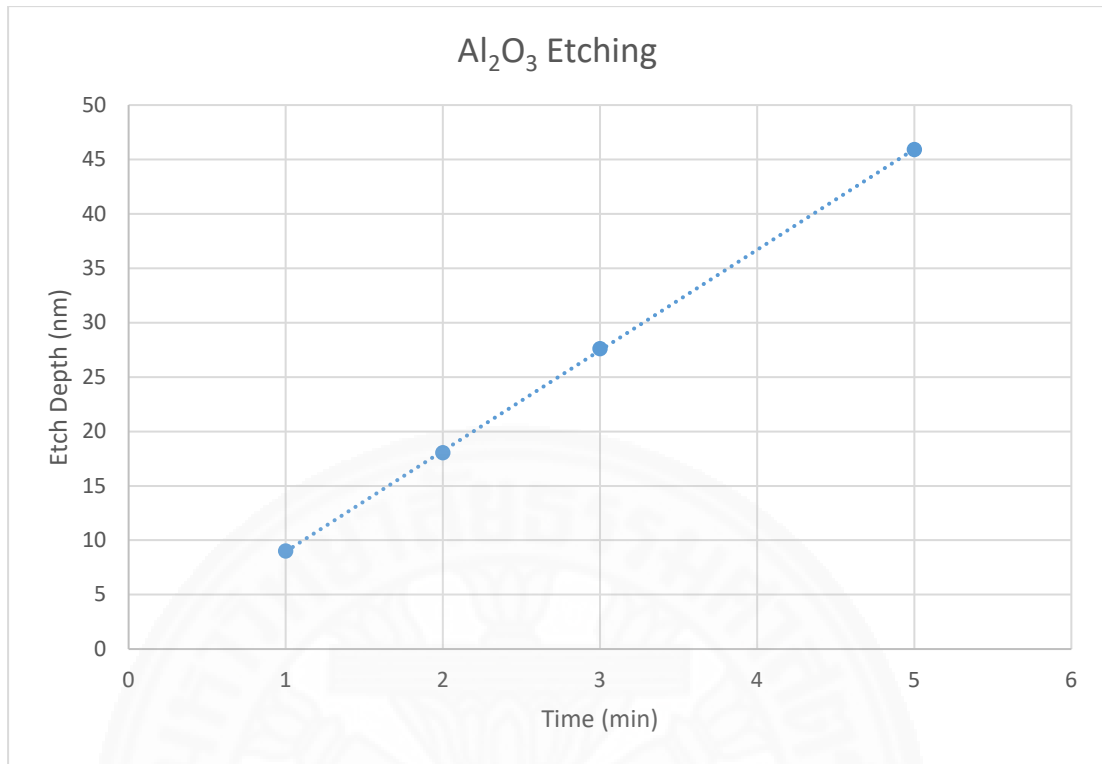
Figure 5.27 The Etch depth of the Al_2O_3.

For the results, the Al_2O_3 thickness is measured using the ellipsometer, some small amount of electron can pass through the Al_2O_3 layer, it is etched with rate 10 nm/min as shown in the figure 5.27. Although, it is lower than the SiO_2 etch rate, but it is also etched by CHF_3/O_2 gases. So, the bottom $SiO_2\_200/Al_2O_320/Au300$ would not be an appropriate solution to solve the problem. Finally, the original SiO_2 /Au substrate is selected. The small vertical length in the structure will be confirmed that the SiO_2 is completely etched.

5.3.5 The SiO_2 completed etch with the small vertical step

To confirm the SiO_2 etched part, the pure SiO_2 wafer is etched together with the sample, then time and etched rate are calculated by based on the previous data. The 100 nm-depth of SiO_2 will be etched then the remaining SiO_2 thickness and the pure Si wafer thickness are measured using the ellipsometer and to apply a bit over etched time to confirm that SiO_2 does not remain in the tip area by observing the small vertical, it will

be appearing in the taper part. After the 200 nm-thickness of SiO_2 on Si-wafer is made, named 'G' as figure 5.28, the small piece of G wafer will etch it with the sample to compare and forecast the exact etched depth and calculate the time for complete etching in the next step as figure 5.29. Results are shown in table 5.2 and figure 5.30-5.35. The summary of all samples is in table 5.3, and separate it into 2 groups, final specimen and spare specimen as shown in figure 5.36 and table 5.4, the realistic 8 final-specimens are shown in figure 5.37.
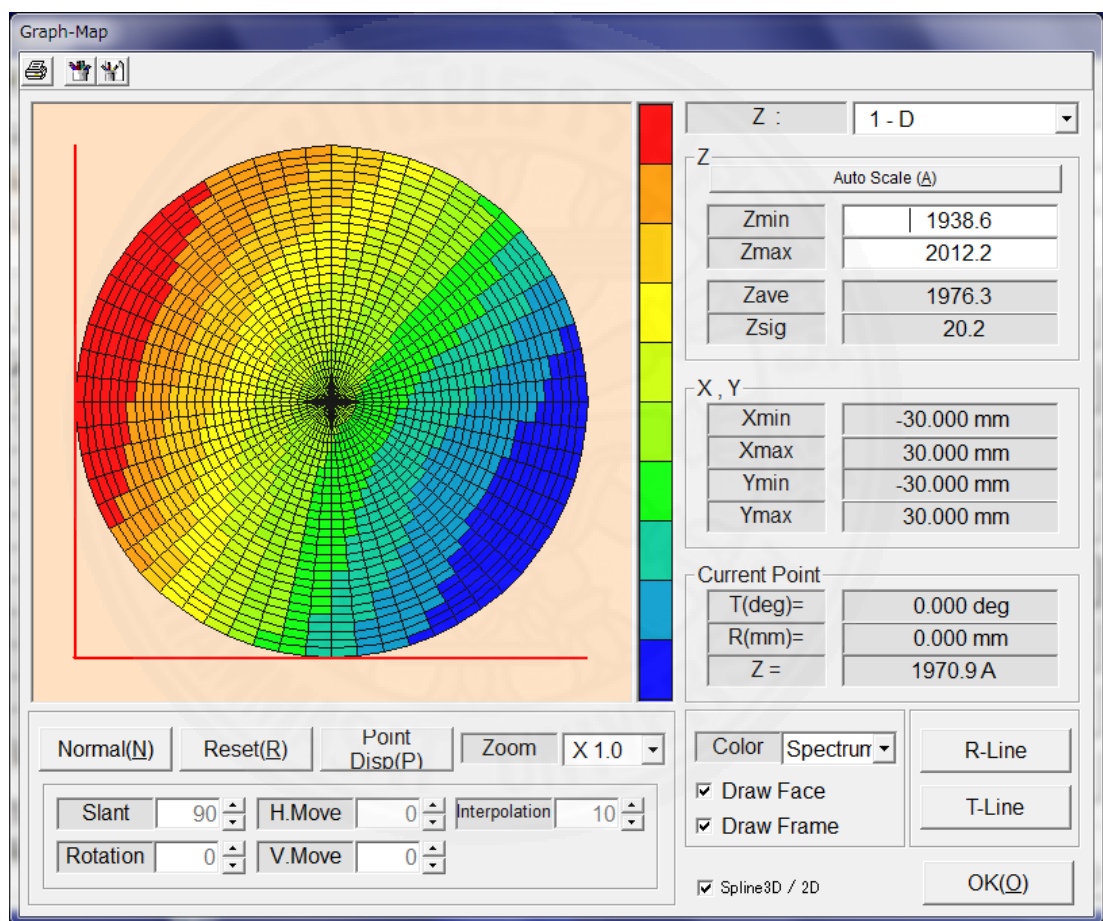
Figure 5.28 The 200 nm-thickness of SiO_2 is measured by the ellipsometer.

Figure 5.29 (Left) 'G'-pure 200 nm-SiO$_2$ thickness, (Right) Small piece of 'G' wafer and our sample for etching in the same condition.

Table 5.2 The trial etching to make various taper angles with different conditions

Experiment	Experiment conditions					SEM observation				Grade
	wafer name	target angle (deg.)	O_2%/ Sccm	Time#1 (min)	Time#2 (min)	angle (deg.)	h_taper (nm)	w_SiO_2 (nm)	vertical length(nm)	
24/03/2018	B14	30	85/85	9m		28.2	229	123	80	D
T016 T017	B18	35	70/70	6m		36.4	219	162	41	C
	B20	30	70->85	6m		28.4	325	176	21	A
24/04/2018	B38	10	93/279	6m40s	13m4s	4.4	2826	216	0	X
T026 T027	B35	15	84/252	4m46s	6m36s	13.9	873	216	0	X
	B32-2	20	78/234	4m	4m46	24.3	372	168	44	C
	B36	25	70/210	3m34s	3m47s	26.8	328	166	34	B
	B31-2	30	63/189	3m14s	3m47s	29.4	270	152	45	C
	B37	35	52/156	1m20s	4m41s	34.5	246	169	26	A
	B34-2	40	45/135	1m23s	4m43s	42.6	183	168	46	C
	A01	50	25/75	1m17s	4m10s	51.7	166	210	0	X
01/05/2018	A02	20	75/225	4m21	3m44s	21.4	420	165	32	B
T029	A03	20	75/225	4m21	4m4s	23.3	308	133	56	D
	A04	20	75/225	4m21	3m24s	22.6	437	182	18	A
	A05	30	60/180	3m27s	2m56s	32.3	291	184	24	A
	A06	30	60/180	3m27s	3m16s					EB Testing
	A07	30	60/180	3m27s	2m36s	29.6	348	198	0	X
	A08	40	45/135	2m56s	2m58s	41.3	199	175	26	A
	A09	40	45/135	2m56s	3m18s	41	154	134	61	D
	A10	40	45/135	2m56s	2m38s	34.8	294	204	0	X
02/05/2018	A11	25	68/204	3m42s	3m41s	30	327	191	24	A
T030	A12	25	68/204	3m42s	3m31s	26.4	405	201	0	X

Experiment	Experiment conditions					SEM observation				
	wafer name	target angle (deg.)	O$_2$%/ Sccm	Time#1 (min)	Time#2 (min)	angle (deg.)	h_taper (nm)	w_ SiO$_2$ (nm)	vertical length(nm)	Grade
	A13	25	68/204	3m42s	3m20s	24.9	388	180	18	A
	A14	15	82/246	5m53s	4m36s	14.4	669	172	16	A
	A15	15	82/246	5m53s	5m1s	13.4	734	175	28	A
	A16	15	82/246	5m53s	4m11s					No SEM
	A17	50	27/81	2m47s	3m1s	49.4	158	135	35	B
	A18	50	27/81	2m47s	3m11s	46.6	143	151	80	D
	A19	50	27/81	2m47s	2m51s	57.9	93	148	47	C
	A20	10	87/261	5m53s	8m20s	9.8	1146	190	0	X
	A21	10	87/261	5m53s	9m	10.9	847	163	20	A
	A22	10	87/261	5m53s	7m40s					No SEM
09/05/2018	B32-1	15	81/243	5m16s	4m42s	19.1	539	187	23	A
T031	B33-1	15	81/243	5m16s	4m12s	19.2	529	185	16	A
	B31	15	81/243	5m16s	3m42s	2.3	3239	131	0	X
	A23	20	79/237	4m5s	5m42s	20.8	392	149	48	D
	A24	20	79/237	4m5s	5m22s	20	457	166	28	A
	A25	20	79/237	4m5s	5m2s	16.9	622	189	0	X
	A26	30	61/183	3m16s	3m35s	33.8	236	158	33	B
	A28	30	61/183	3m16s	3m25s	29.4	333.8	188.4	21	A
	A29	30	61/183	3m16s	3m15s	29.1	326	182	14	A
	A30	50	26/78	2m53s	2m20s	48.9	185	212	0	X
	A32	50	26/78	2m53s	2m10s	52.6	153	200	0	X
	A31	50	26/78	2m53s	1m50s					No SEM

Experiment	Experiment conditions					SEM observation				
	wafer name	target angle (deg.)	$O_2\%/$ Sccm	Time#1 (min)	Time#2 (min)	angle (deg.)	h_taper (nm)	w_SiO_2 (nm)	vertical length(nm)	Grade
10/05/2018	A33-1	50	27/81	2m53s	2m27s	42	230	207	0	X
T032	A33-2	50	27/81	2m53s	2m24s	47.3	190	206	0	X
	A34	50	27/81	2m53s	2m22s	54.2	150	208	0	X
	B34-1	15	83/249	5m16s	5m49s	16	652	188	23	A
	A36	15	83/249	5m16s	5m54s	14.3	755	193	27	A
	A35-1	20	78/234	4m5s	5m21s	18.1	526	171	26	A
	A35-2	20	78/234	4m5s	5m16s	23.7	449	197	27	A

Sub: Si/10nm-Ti/100nm-Au/3 nm-Ti/200nm-SiO2
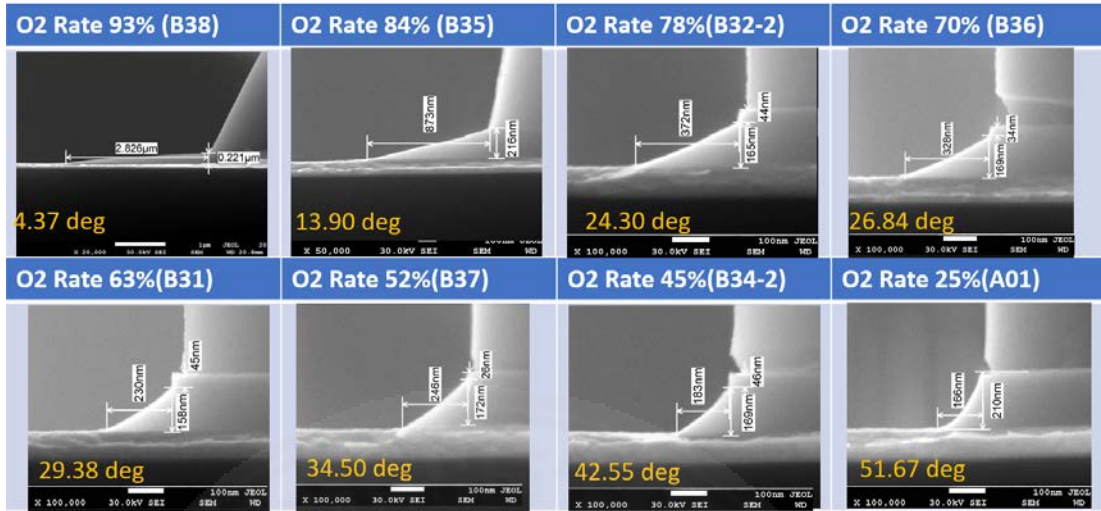
Figure 5.30 The trial dry etching of small vertical, T026 and T027.

Sub: Si/10nm-Ti/100nm-Au/3 nm-Ti/200nm-SiO2
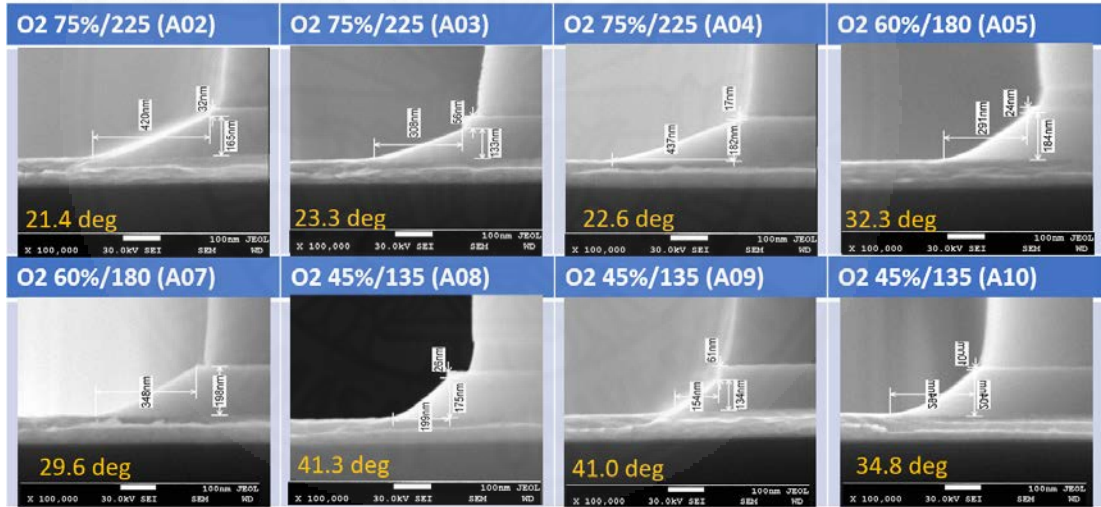
Figure 5.31 The trial dry etching of small vertical, T029.
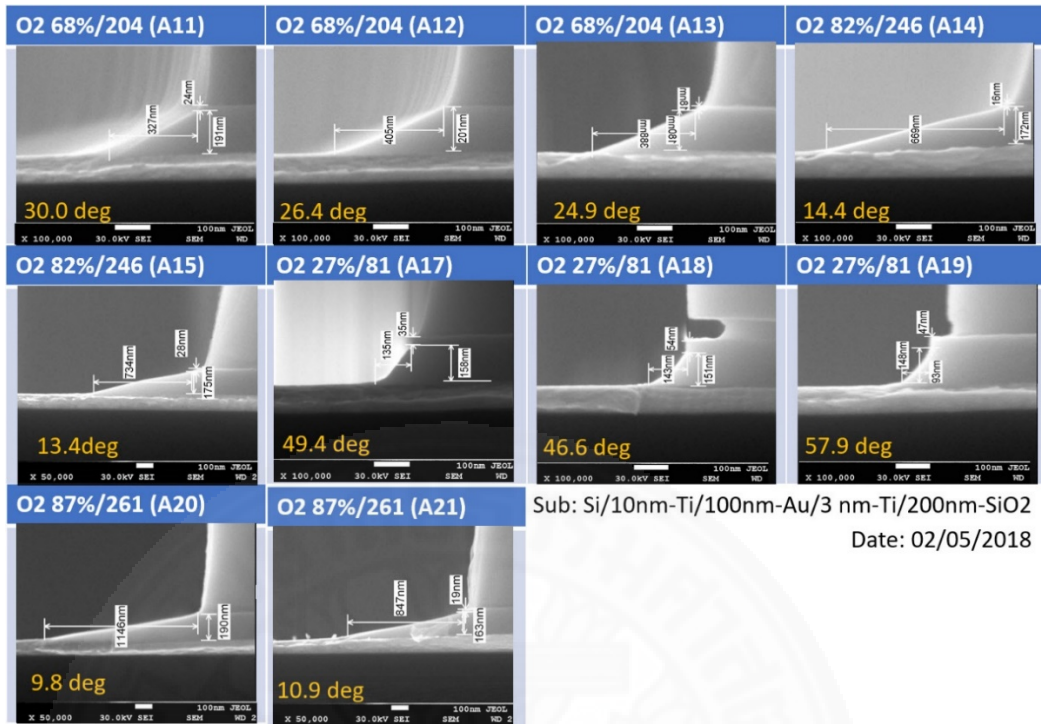
Figure 5.32 The trial dry etching of small vertical, T030.
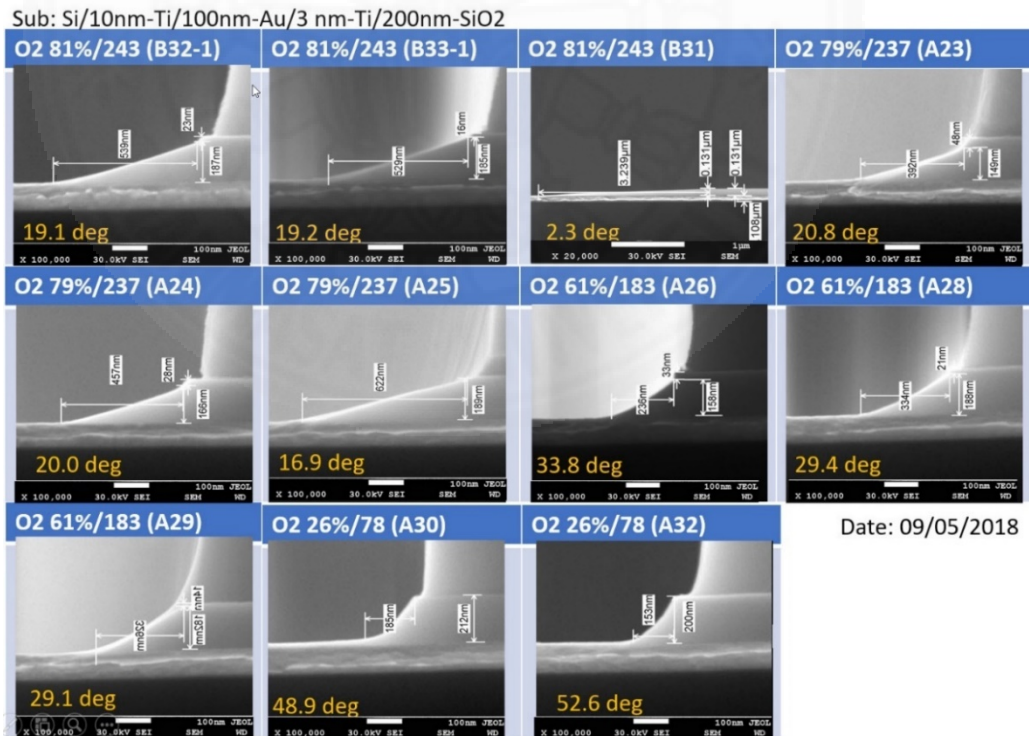
Figure 5.33 The trial dry etching of small vertical, T031.

Sub: Si/10nm-Ti/100nm-Au/3 nm-Ti/200nm-SiO2
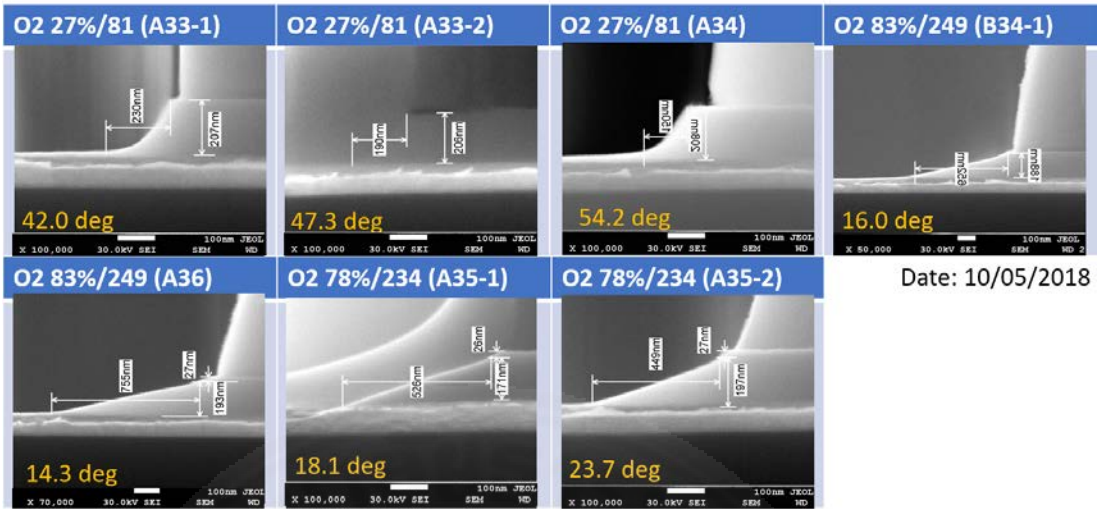
Figure 5.34 The trial dry etching of small vertical, T032.

Figure 5.35 The actual sample after dry etching process

Table 5.3 The final specimens

Target angle (deg.)	Measured angle (deg.)	h_taper (nm)	w_ SiO₂ (nm)	Vertical length (nm)	Gas O2 (%)	Time (min)
10	10.9	847	163	20	87/261	5m53s/9 m
15	14.4	669	172	16	82/246	5m53s/4m36s
15	19.1	539	187	23	81/243	5m16s/4m42s
25	24.9	388	180	18	68/204	3m42s/3m20s
30	29.1	326	182	14	61/183	3m16s/3m15s
35	34.5	246	169	26	52/156	1m20s/4m41s
40	41.3	199	175	26	45/135	2m56s/2m58s
50	49.4	135	158	35	27/81	2m47s/3m1s

Table 5.4 Two groups of final specimens and spared specimens

Taper angle	The best specimens (angle/vertical)	The spared specimens (angle/vertical)	Preliminary Test
10	A21(10.9/20)		
15	A14(14.4/16) B34-1(16/23)	A36(14.3/27) A15(13.4/28)	B31-1,31-2(15/45)
20	B32-1(19.1/23) B33-1(19.2/16) A04(22.6/18)	A35-1(18.1/26) A24(20.0/28)	A02(21.4/32) A23(20.8/48) A03(23.4/56)
25	A13(24.9/18)	A35-2(23.7/27)	B36(26.8/34) B32-2(24.3/44)
30	A29(29.1/14) A28(29.4/21) A11(30.3/24)	B20(28.4/21) A05(32.3/24)	B14(28.2/80) A06(31.0/80)
35	B37(34.5/26)	A26(33.8/33)	B18(36.4/41)
40	A08(41.3/26)	B34-2(42.6/46)	A09(41.0/61)
45	-	-	-
50	A17(49.4/35)	A19(57.8/47)	A18(57.0/80)
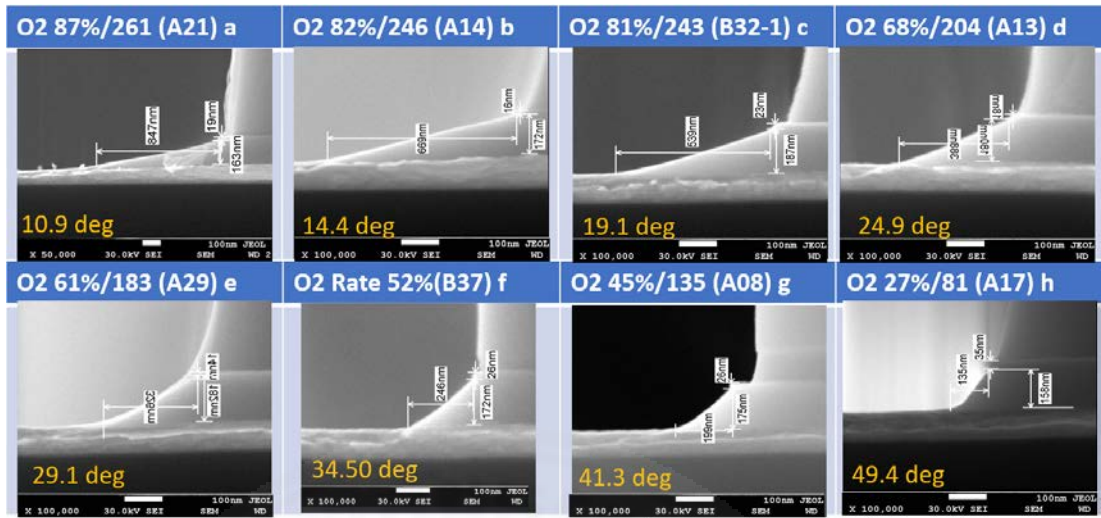
Sub: Si/10nm-Ti/100nm-Au/3 nm-Ti/200nm-SiO2

Date: 26/05/2018

Figure 5.36 The Final specimen; 10 to 50 deg.
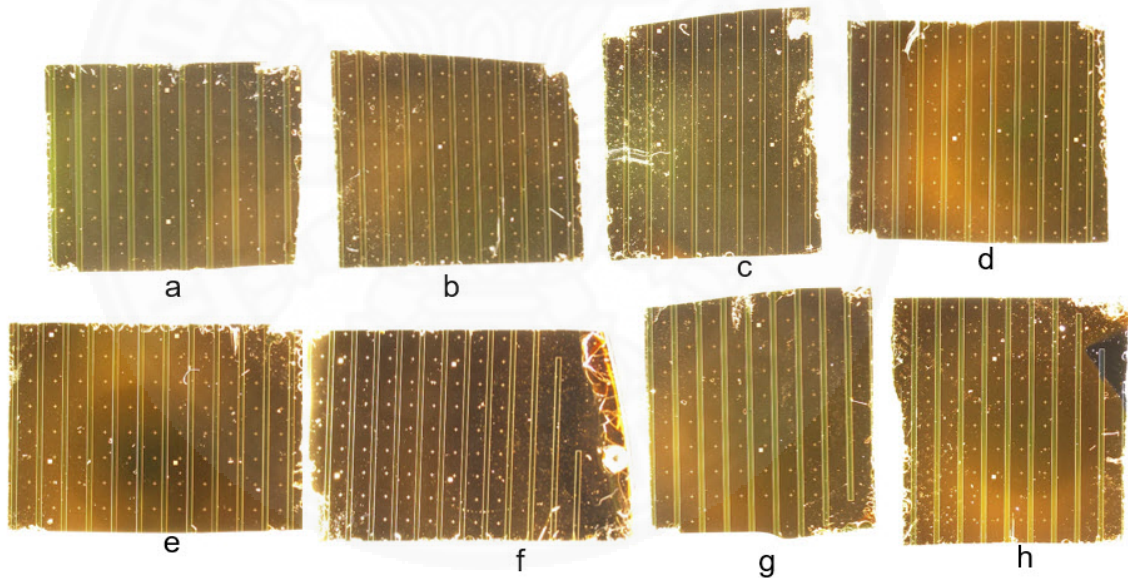
Figure 5.37 The realistic of final specimen's feature.

The best specimens are selected for the fabrication in the next process in 8 specimens for each of the angle as shown in table 5.4. The next process is to remove the PR and 40 nm-Al_2O_3 ALD, then deposit 3 nm-Ti layer and 80 nm-gold layers, finally the grating at the body part and the slit in the tip part will fabricate.

5.4 The cleaning and Al$_2$O$_3$ sputter using ALD

5.4.1 The cleaning of the first specimen (T020) and the second specimen (T023)

Because the sample is selected from the remaining SiO$_2$ at the tip area, so, the Al$_2$O$_3$/SiO$_2$ layer is skipped to sputter on top the main 200 nm- thickness of SiO$_2$. The PR removed processes are standard cleaning process as follow;

    1) Ashing by O$_2$ plasma 3 min

    2) NMP 1 min

    3) Acetone 2 min

    4) Rinse by IPA 20 Sec.
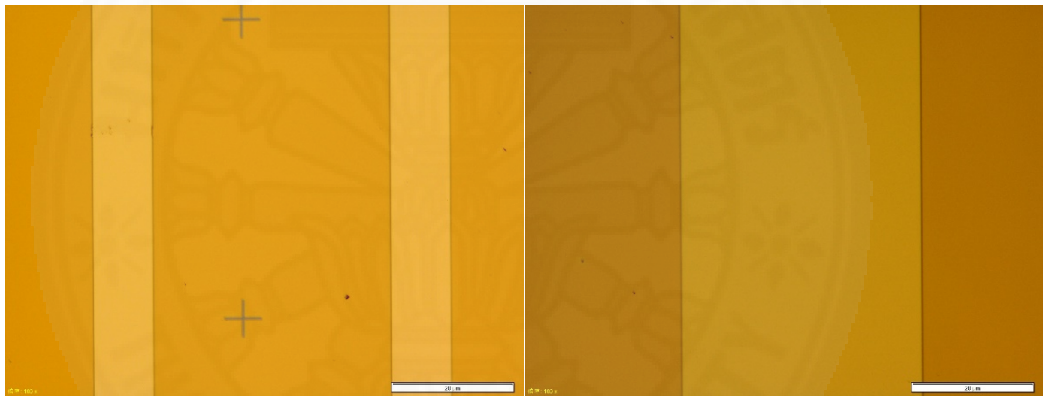
Figure 5.38 The first and second specimen after PR removed.

5.4.2 The cleaning of the third specimen (T034)

The 70 nm-vertical steps is selected for testing in the third specimen, before sputtering 20 nm and 40 nm-thickness of SiO$_2$, the standard cleaning process is applied as same as the first and second specimen cleaning.

5.4.3. The problem solving

After cleaning, the serious problem of photoresist residual film and surface hydrophobicity was found before ALD as shown in figure 5.39-5.40. The new resist removing process should be applied in the next.
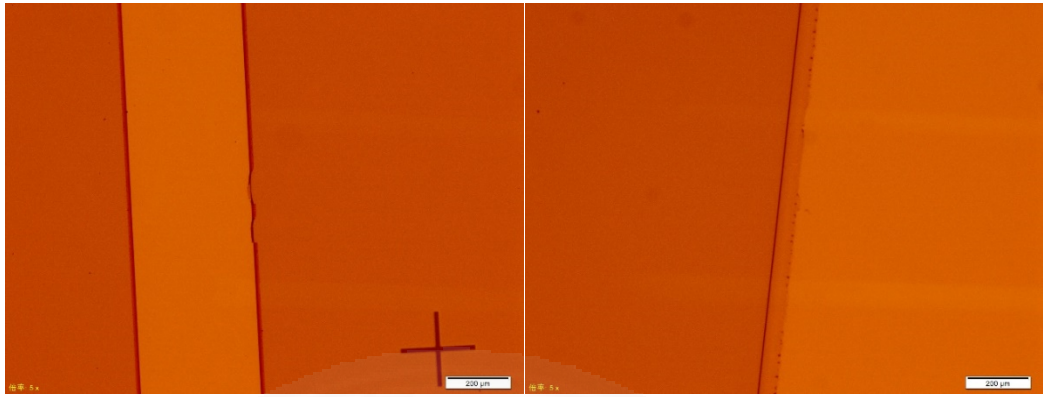
Figure 5.39 (Left) after cleaning by HFE, acetone, NMP, IPA (Right) after 10 min sonification.
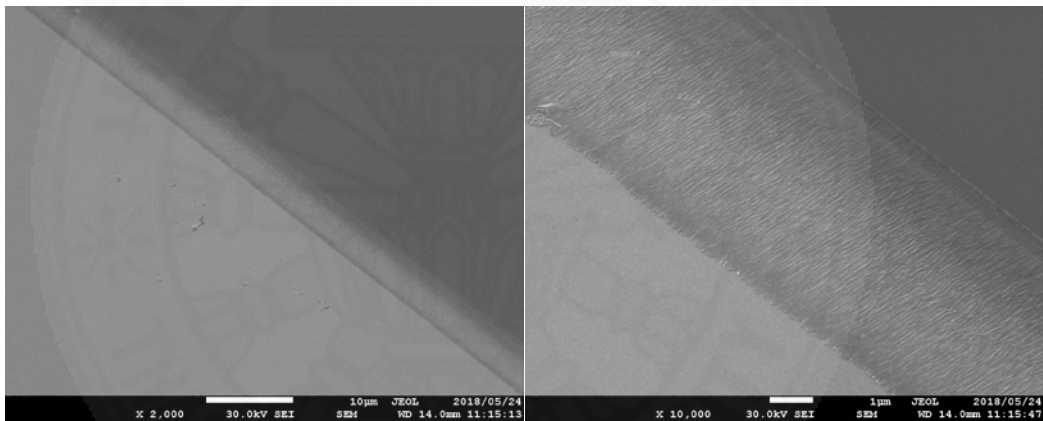
Figure 5.40 SEM observation shows some grease remained in the taper area.

The solving of this problem are as follows;
1) Reverse sputter 20 second and Acetone with sonification 10 min, IPA rinse, then ashing 5 min.

2) Reverse sputter 10 sec and replace the acetone to NMP with 10 min sonification, then acetone and IPA rinse, and ashing 5 min.

As the results, for the first method, the grease is removed with 20 second-reverse sputter, but the reverse sputtering is too long because the Au layer is also removed as shown in figure 5.41 For the second method, two types of specimens are found, first the complete

cleaning specimen and second the specimen where some part of resisting film was remaining as shown in figure 5.42-5.43, but it is out of using area, so the second method of cleaning process will apply to the final specimen.
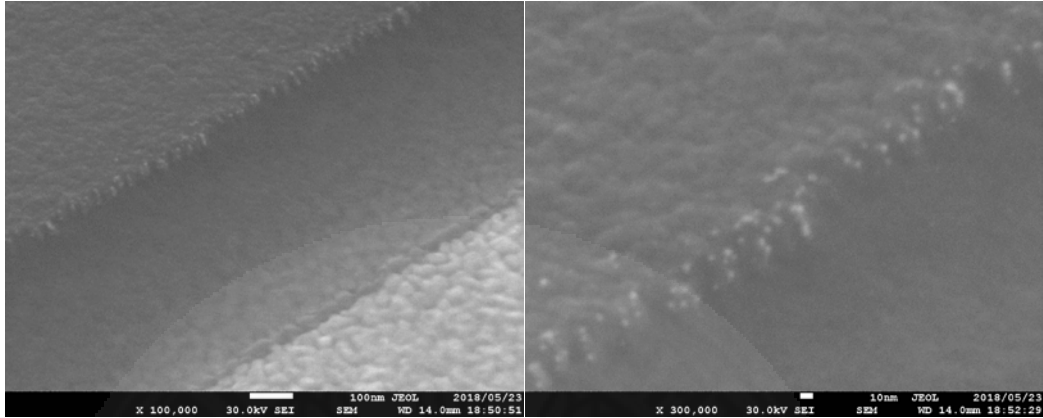
Figure 5.41 The grease is removed by the 20 second-reverse sputter, but the Au layer is also removed.
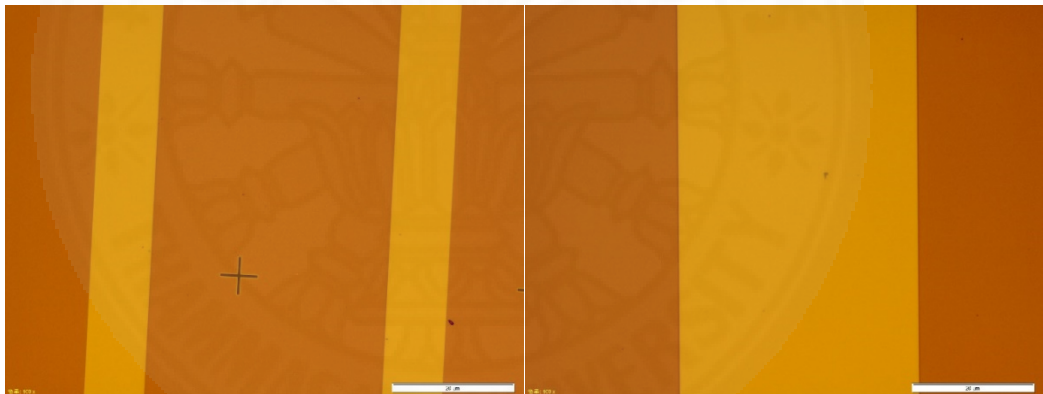
Figure 5.42 The first type; complete cleaning
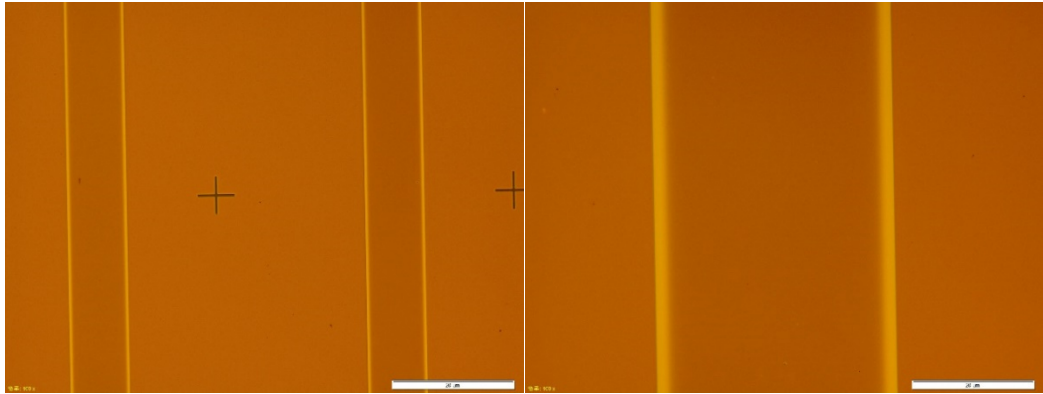
Figure 5.43 The second type; some part of photoresist film is still remained, but it is out of using area, we can use it

5.4.4. The cleaning of the final specimen

1) Reverse sputter, this process is applied to damage a few nanometer thickness layers of unknown thin film on PR layer which happens when applying the dry etching process as shown in figure 5.44.

2) Ashing 5 min

3) NMP and sonication 10 min as shown in figure 5.45.

4) Acetone and IPA, between that it is observed by a microscope as shown in figure 5.46. If it can observe some PR remain, the specimen is added in the acetone and vibrate it more for a long period of time. Finally, the specimen looks clean, after it is completely clean, take it out and blow it dry well.

5) Ashing 5 min.
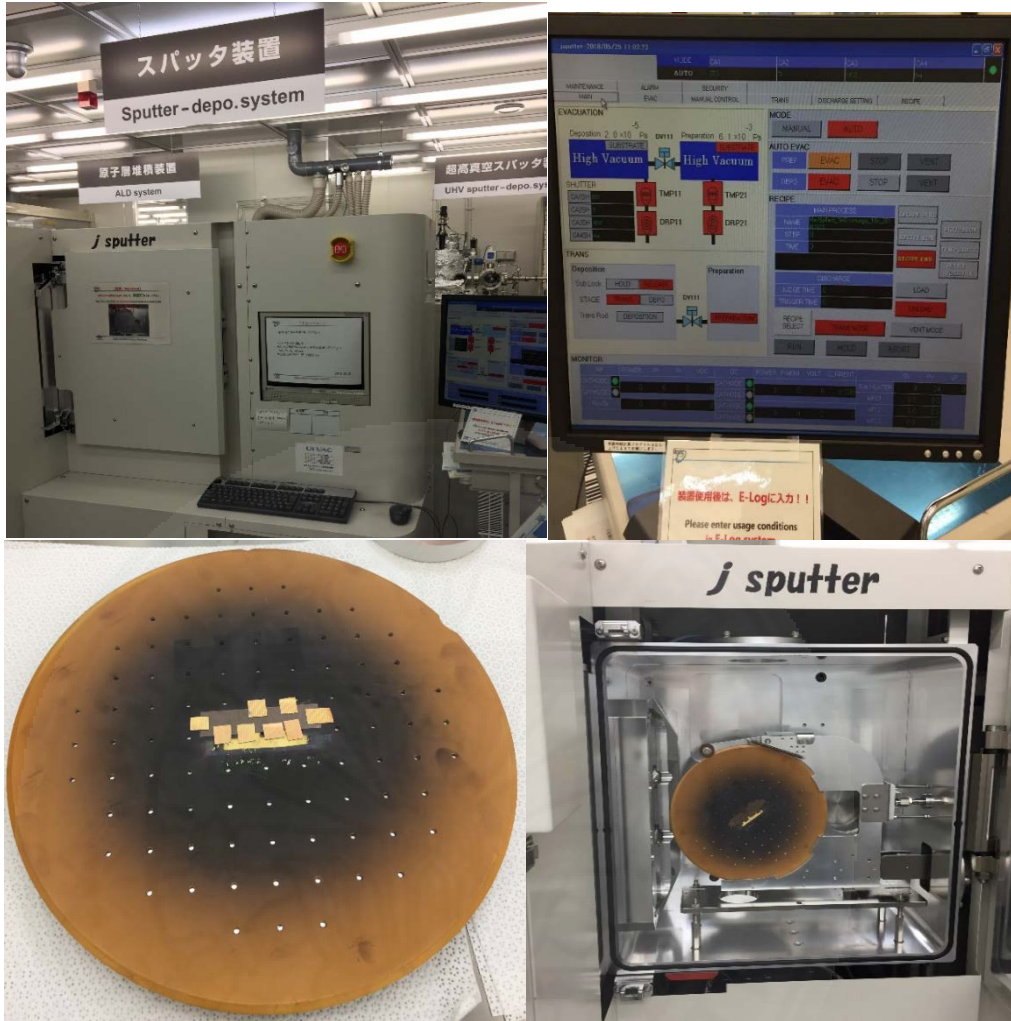
Figure 5.44 J- sputter-deposition system and our specimens stick in the sputter holder.

Figure 5.45 NMP sonication, acetone, and IPA cleaning.
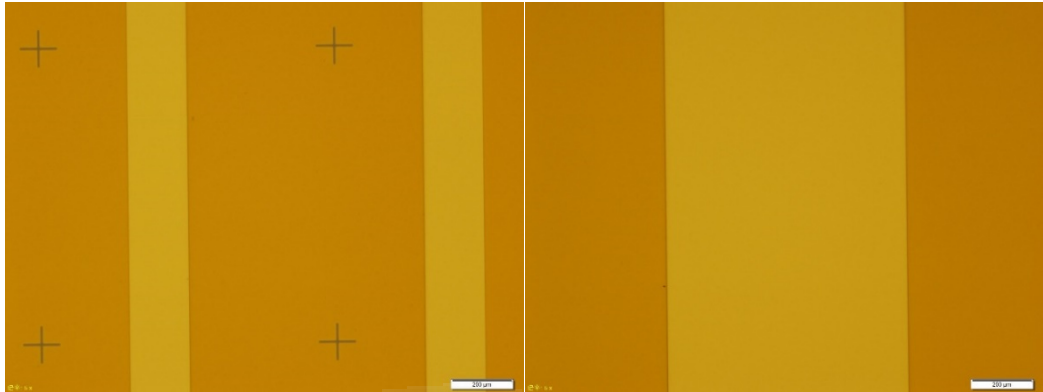
Figure 5.46 Microscope observation of a-specimen after cleaning process.

5.4.5 ALD of Al$_2$O$_3$

The 40 nm Al$_2$O$_3$ is deposited by using an atomic layer deposition (ALD) as shown in figure 5.47. The growth per cycle at 120°C is 0.99/1 second. The parameters are shown in Fig 5.48-5.49.
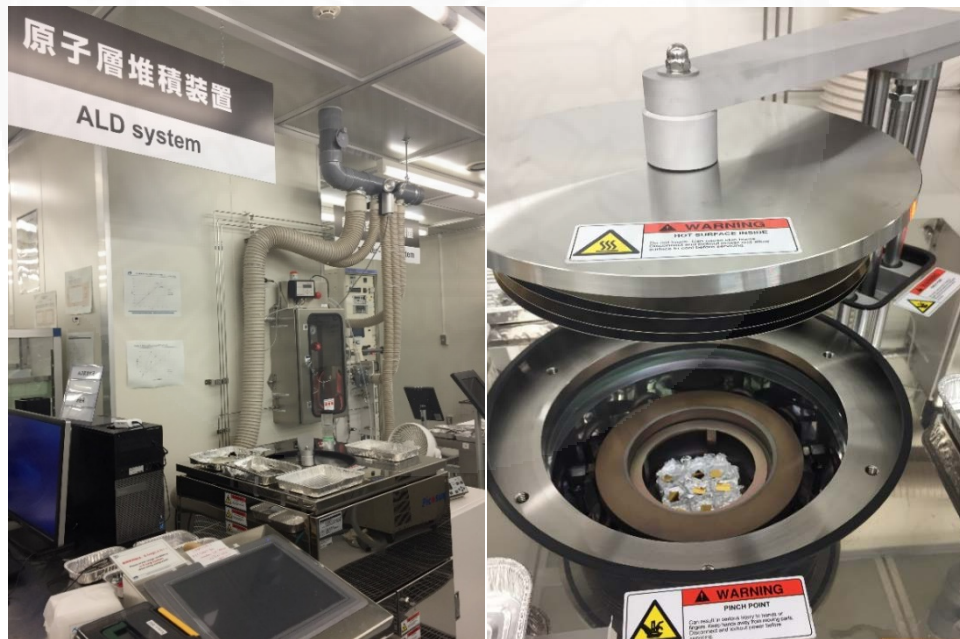
Figure 5.47 ALD of Al$_2$O$_3$
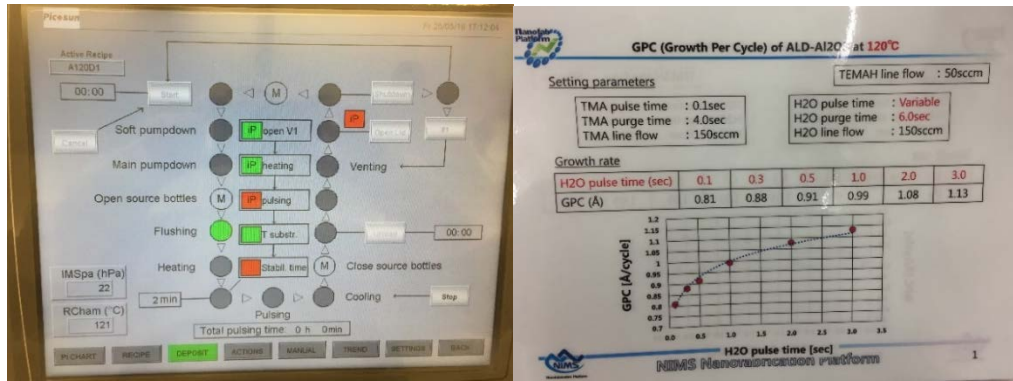
Figure 5.48 (Left) Al$_2$O$_3$ deposit process (Right) the parameters of Al$_2$O$_3$ deposit.

Figure 5.49 The recipe of ALD of the 40 nm-thickness Al$_2$O$_3$.

5.5 Grating and slit patterning by E-Beam lithography

5.5.1 The first specimen with SiO$_2$ (T020)

The parameters for making the first specimen are the grating (P510 nm, W220 nm) and slit width (120 nm hole width), slit position is 100-400 nm, the sample no. B21 is used. The processes follow;

1) E-Beam Photoresist remove by O$_2$ plasma ashing 3 min

2) Clean sample with acetone and vibrating 1 min and IPA 20 s.

3) PR drop and finding the optimized thickness follow from the experimental data as shown in figure 5.50.

3.1) The PR thickness target is 130 nm which is very close to the thinnest thickness of PR. Drop the HMDS 3000 rmp 60 s, GL2000 DR2.5 3000 rpm 60 s and bake 180° C for 5 min.

3.2) Target 230 nm-thickness of PR, drop the HMDS 3000 rmp 60 s, GL2000 DR2.0 2000 rpm 60 s and bake 180° C for 5 min.

4) Apply the Electron beam lithography as shown in figure 5.52; current 1 nA, 125 Kvolt, Dose 240 mJ/cm^2.

5) Developing; GL200 developer (Xylene) 1.30 min and rinse by GL-2000 Rinse (IPA) 30 s as shown in figure 5.51

6) Observe by Microscope.

7) To evaporate 3 nm-Ti, 80 nm-Au, and 20 nm-Ti by the 12-Evaporator as shown in figure 5.53.

8) NMP Lift-off process, boiled 20 min, clean with acetone, scratch the border of sample and eject by acetone, and rinse IPA, and observe by microscope.

9) SEM observation
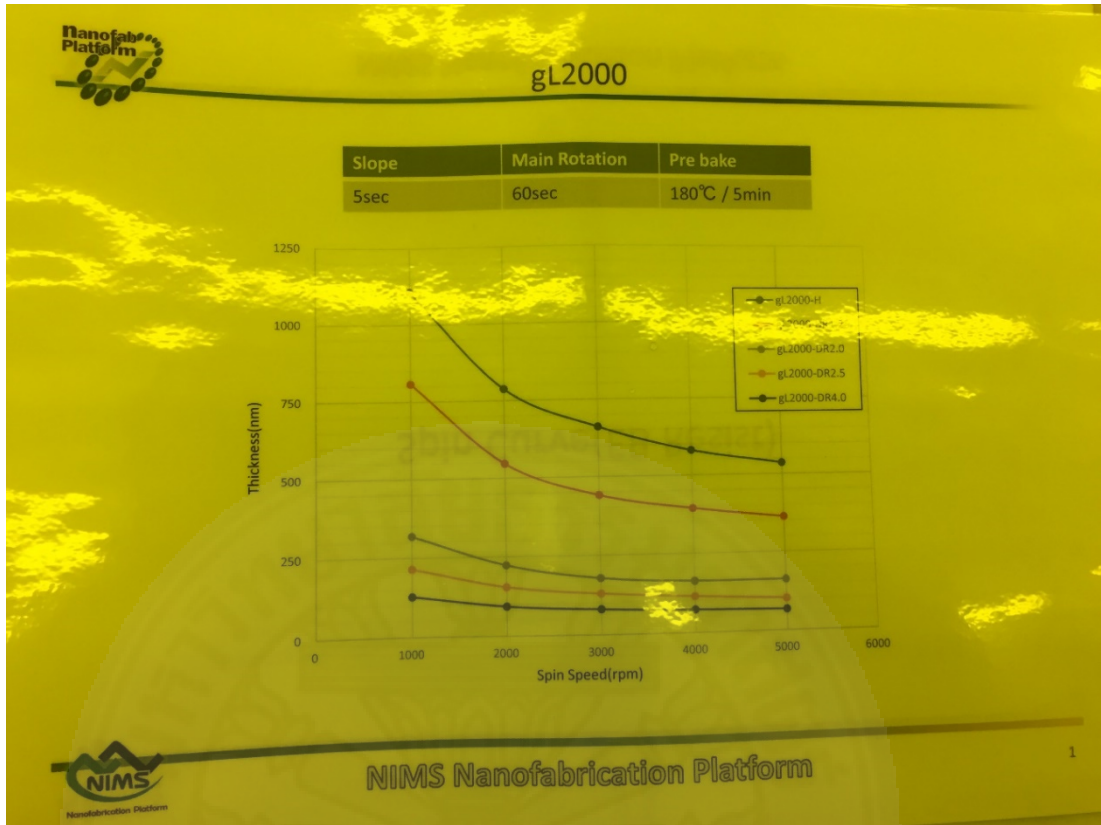
Figure 5.50 The experiment data for thickness of photo resist making.
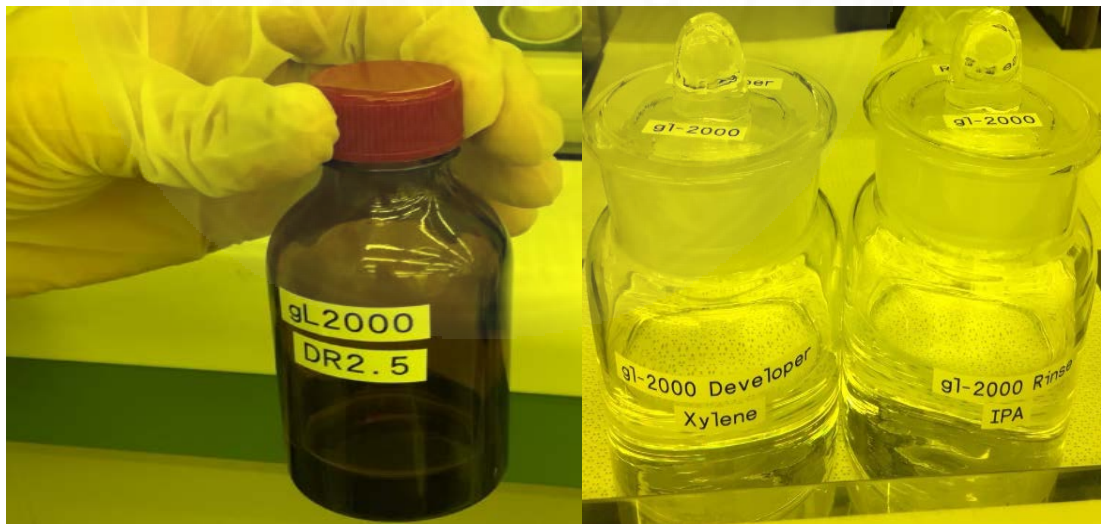
Figure 5.51 (Left) GL2000 DR 2.5-Photoresist and (Right) GL2000 Developer

Figure 5.52 The ultra-high precision electron beam lithography system (E-Beam lithography)
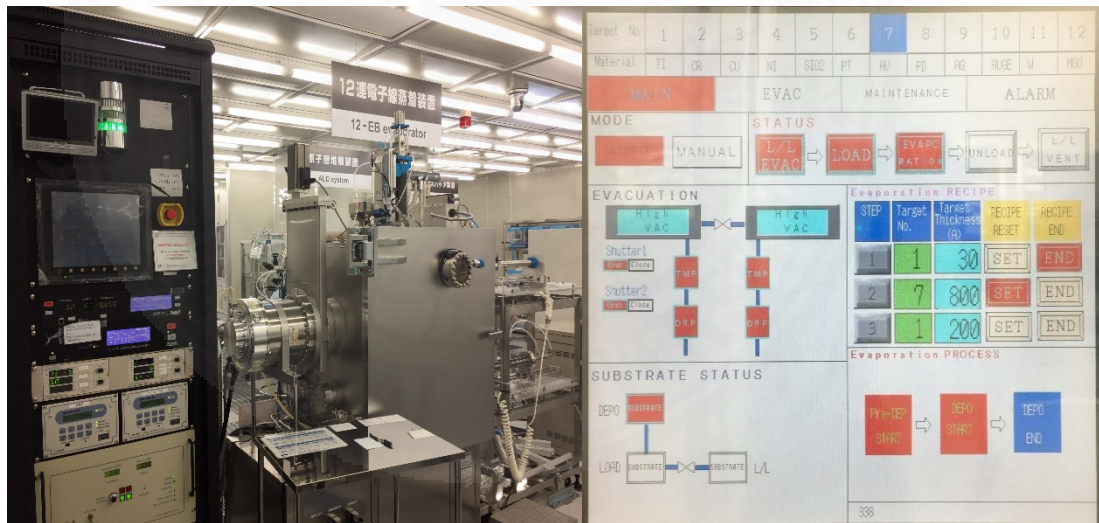
Figure 5.53 The 12-Evaporator for Ti and Au layer deposition.

Figure 5.54 Microscope observation of the 130 nm-thickness of PR after developed by
GL2000 developer (Xylene) 90 s and rinse by GL-2000 Rinse (IPA)
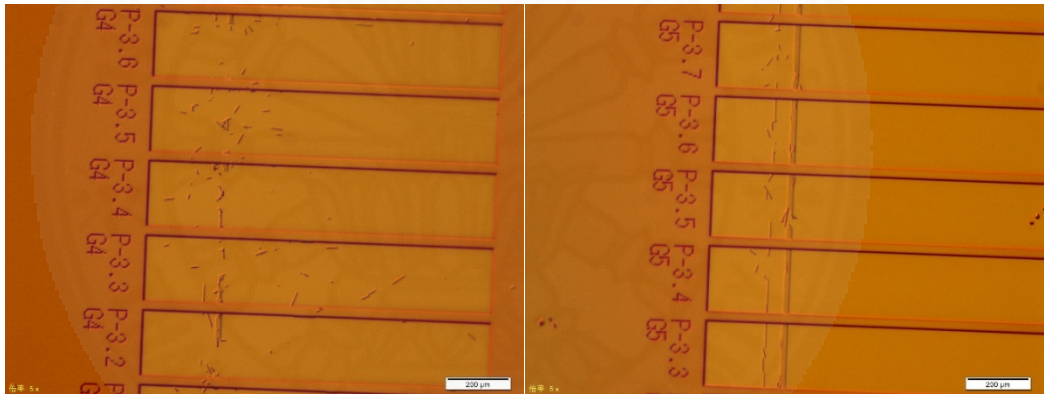
Figure 5.55 Microscope observation of the 230 nm-thickness of PR after development
process.
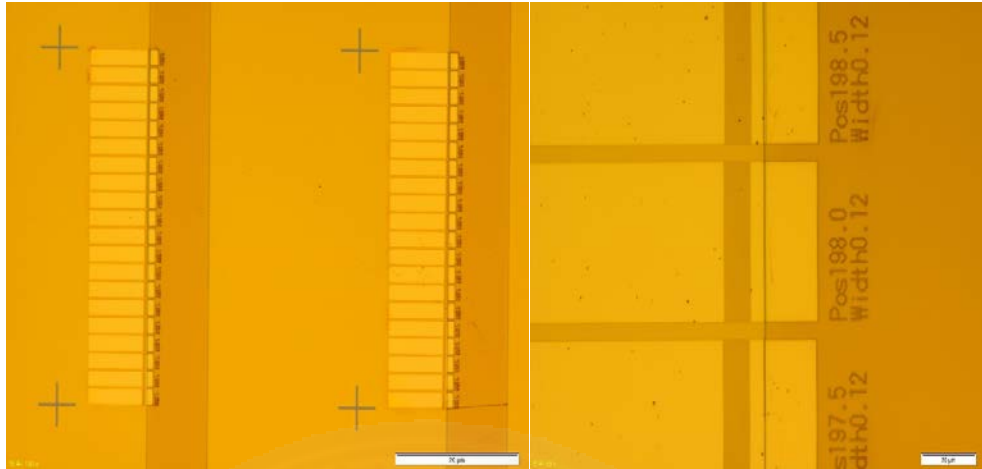
Figure 5.56 Microscope observation after NMP lift-off process for 2 hours.
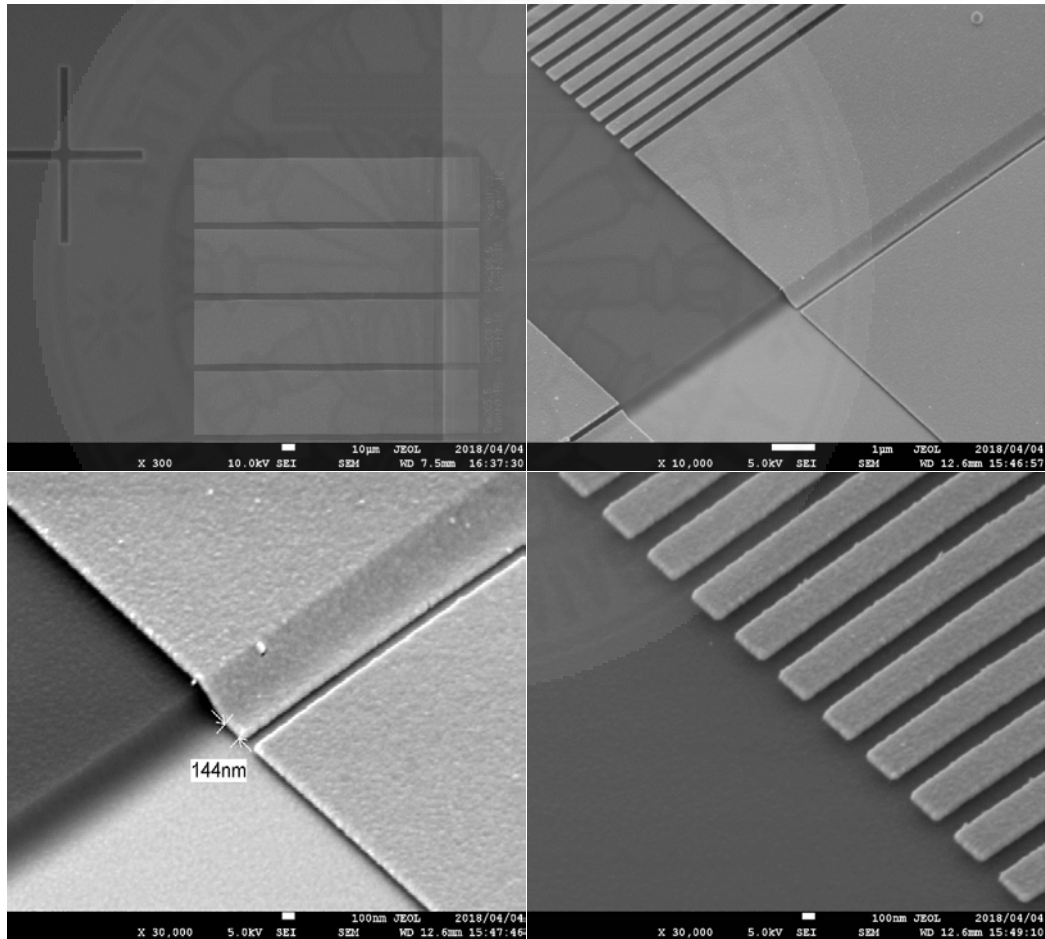
Figure 5.57 SEM observation of the first specimen (low-left) the slit in the tip area and (low-right) the grating in the body part.

After the development process, for 130 nm-thickness of PR as figure 5.54, there are the clear shape of the grating and slit pattern but for 230 nm-thickness of PR as figure 5.55, the pattern is broken, because of the PR thickness is too high and it is easy to fall down, therefore, for the actual pattern making, the photo resist is changed from GL2000 DR2.5 to GL2000 DR2.0 and reduce the thickness of PR by reducing the spin rate coating from 3000 rmp to 2400 rpm 60 s for making the PR about 200 nm-thickness. Then the entire process is applied again. the next experiment is only for 130 nm-thickness of PR case.

As the results, figure 5.56 shows the first specimen after the lift-off process looks clear by SEM observation as figure 5.57, the pattern of grating and slit looks clear and sharp. The smallest hole width is less than 100 nm. and the shorter w_tip start is around 144 nm. That means the grating and hole can be made by following the design (the optimum simulation values) base on the lift-off process. Furthermore, the smallest hole width around 50 nm can be made by using a dry etching process. The lift-off process is easier than dry etching, but the dry etching process can make the smaller hole width than the lift-off. The testing, pre-specimen cases are shown in Table. The simulation can be parallel done by characterize with the testing specimens.

5.5.2 The specimen with SiO_2 and Ti outer (T023)

The parameters for making the second specimen are the grating (P510 nm, W180 nm) and slit width (140 nm hole width), slit position is 200 nm, the sample no. B21 is used, and added 20 nm-thickness of Ti to the outside of the first specimen for reducing the SPPs outside. The grating and slit are made by following the same process which did for the first specimen making. The fabrication result as figure 5.58, the specimen after lift-off process looks good and SEM observation as figure 5.59 shows the pattern of grating and slit when they are completed.
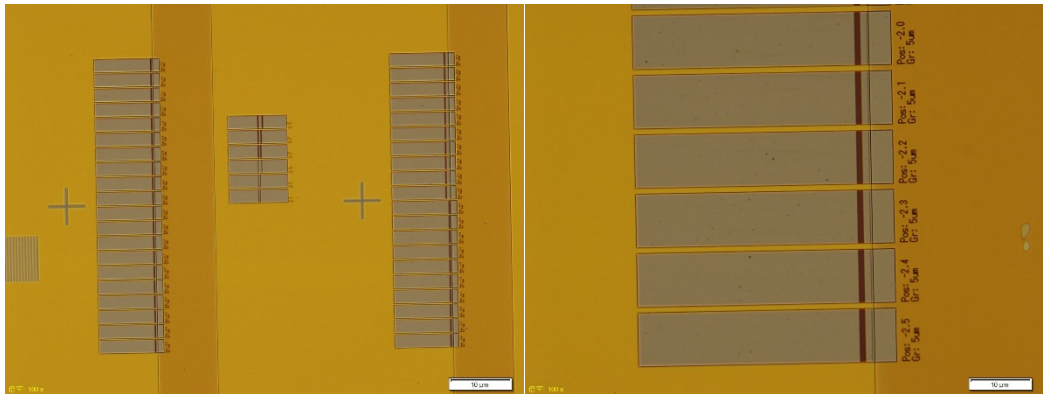
Figure 5.58 The second specimen after lift-off process.
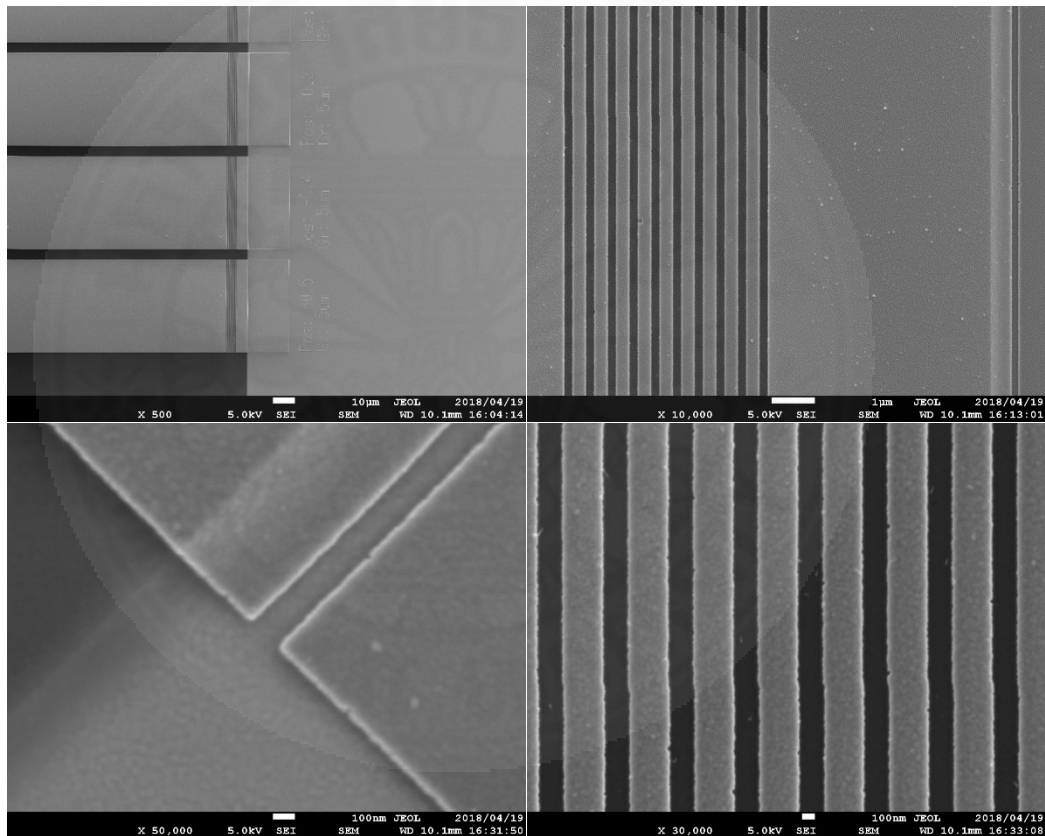
Figure 5.59 SEM observation of the second specimen (low-left) the slit in the tip area and (low-right) the grating in the body part.

5.5.3 The third specimen with SiO₂ (T034)

The parameters for making the third specimen are the grating (P530 nm, W100-130 nm) and slit width (150 nm hole width), slit position is 260 nm, the sample no.

A06 is used. The grating and slit are made in the same way as the first specimen making process. The fabrication results are shown in figure 5.60-5.63.
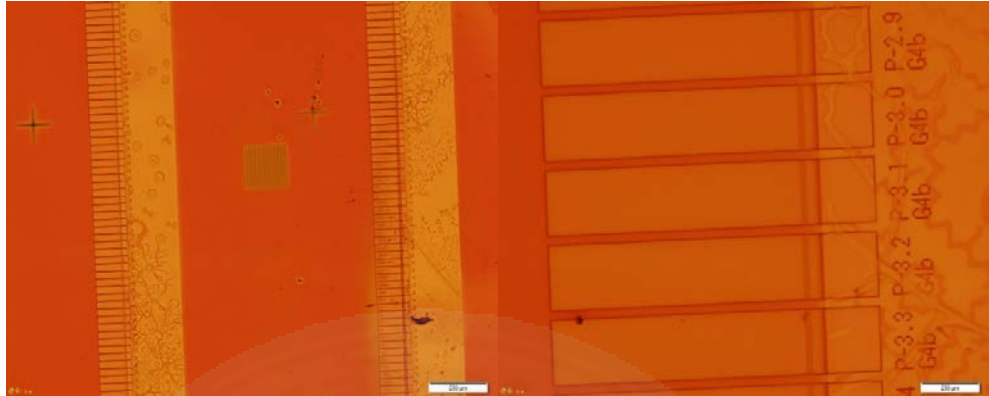
Figure 5.60 After developing the PR, SiO$_2$ layer peel off.
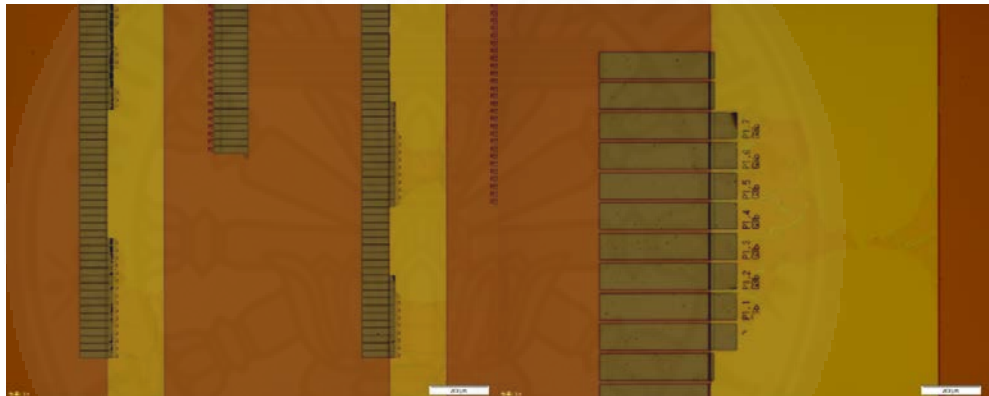
Figure 5.61 Microscope observation after NMP lift-off process, SiO$_2$ layer is broken that make the pattern is removed.
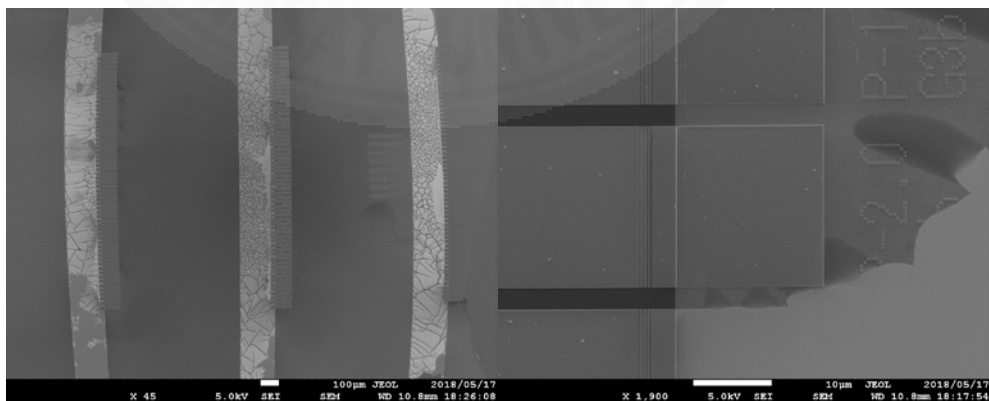
Figure 5.62 SEM observation, we found SiO$_2$ layer is broken.
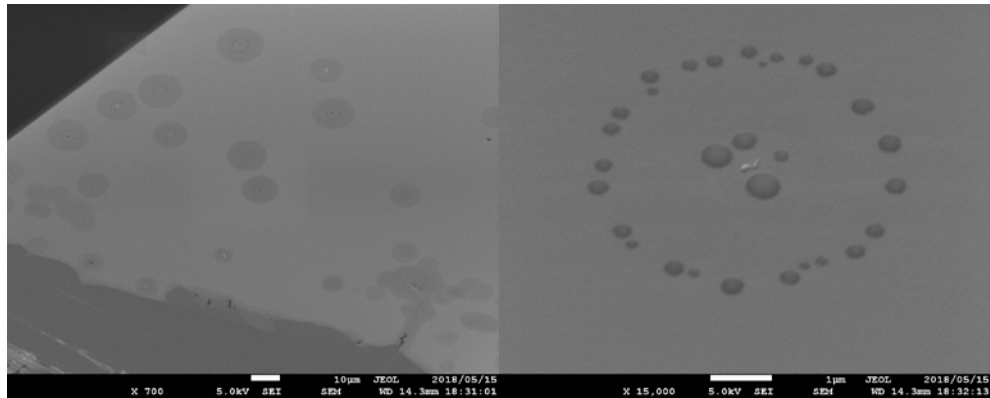
Figure 5.63 SEM observation, we found the watermark is on the specimen surface.

As the results, 2 big problems are found as shown above, first, after the development and lift-off process SiO$_2$ breaks and peels-off, affected by the weak adhesion with Au the pattern of grating and slit is removed, and second, we also found the water mask on the specimen surface even after the sufficient cleaning. Table 5.5 shows the pre-testing all specimen cases. the Al$_2$O$_3$ is used instead of SiO$_2$ in the next trial specimen and it will follow the simulation results.

Table 5.5 The pre-testing all specimen cases

Specimen	SiO$_2$ thickness (nm)	Period of grating (nm)	Width of grating (nm)	Before_T (μm)	Slit width (nm)	Slit position (nm)
#1	remained	510	220	5 and 10	120	100-400
#2	remained	510	180	3 and 5	140	200
#3	20 and 40	530	100-130	3,4, and 5	150	260
final	Al$_2$O$_3$ 40	520	110	4	120	220

5.5.4 The final specimen (A-H)

The parameters for making the final specimen are the grating (P520 nm, W110 nm) and slit width (120 nm hole width), slit position is 220 nm. The final specimens, A-H are used. The details of the grating and slit making are as follows;

1) Ashing by O$_2$ plasma 3 min

2) PR drop, HMDS 3000 rmp 60 s, GL2000 DR2.0 as figure 5.64 for 2,400 rpm 60 s (130 nm-thickness), and bake 180c for 5 min.

3) CAD data, drawing as shown in figure 5.65.

4) Apply the Electron beam lithography as figure 5.66-5.67; current 1 nA, 125 Kvolt, Dose 240 mJ/cm^2.

5) Developing; GL200 developer (Xylene) as figure 5.64 for 1.30 min and rinse by GL-2000 Rinse (IPA) 30 s. Figure 5.68 shows the microscope observation after developing.

6) To evaporate 3 nm-Ti, 80 nm-Au, and 20 nm-Ti outer as shown in figure 5.76.

7) NMP Lift-off process as figure 5.77, boiled 20 min, clean with acetone, scratch the border of sample and eject by acetone, and rinse IPA, and observe by microscope.

8) SEM observation as figure 5.78-5.86.

Figure 5.64 (Left) GL2000 DR 2.0 EBeam-Photoresist and (Right) GL2000 Developer
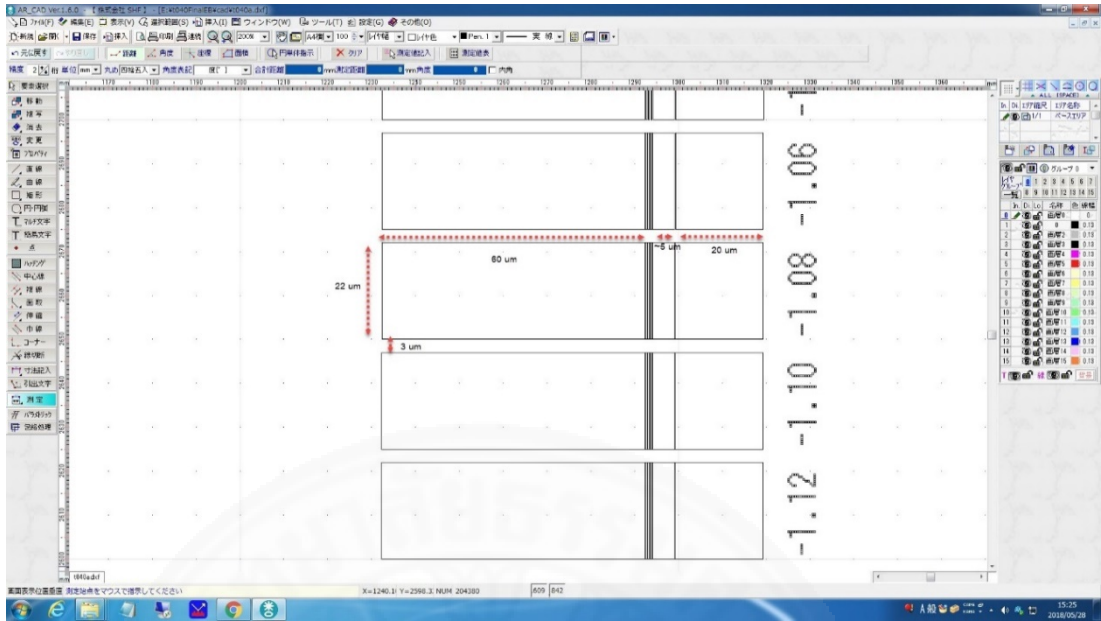
Figure 5.65 CAD drawing, for 'A' specimen, the grating (P520 nm, W110 nm) and slit (120 nm hole width), slit position is 220 nm. The position is -3.2 to 1.8, step 0.02.
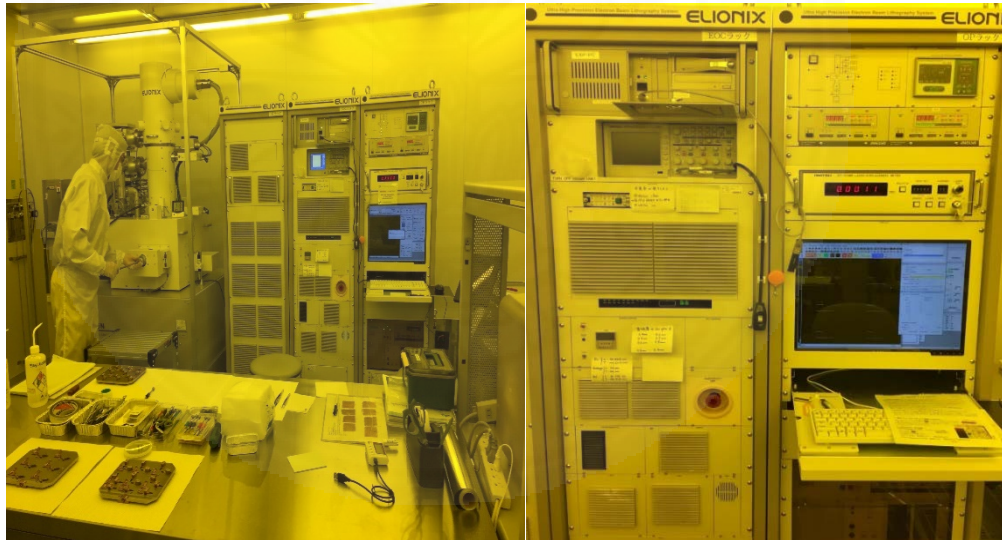
Figure 5.66 The ultra-high precision electron beam lithography system (E-Beam lithography)

Figure 5.67 (Left) the holder of the E-Beam lithography with 'A' and 'B' specimens (Right) the mask for origin point adjustment.
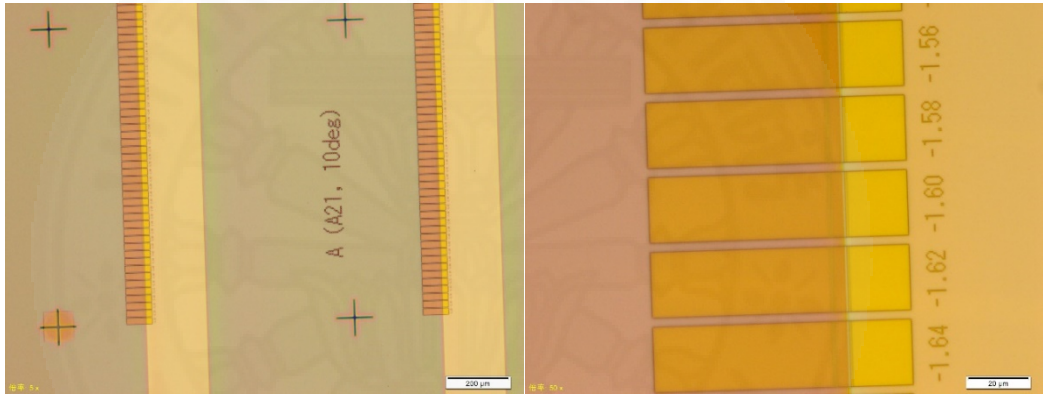
Figure 5.68 A specimen after development process.
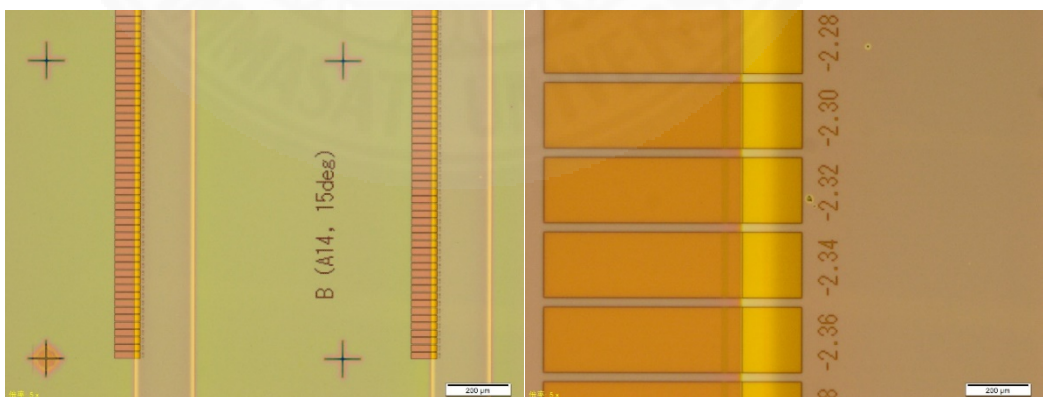
Figure 5.69 B specimen after development process.
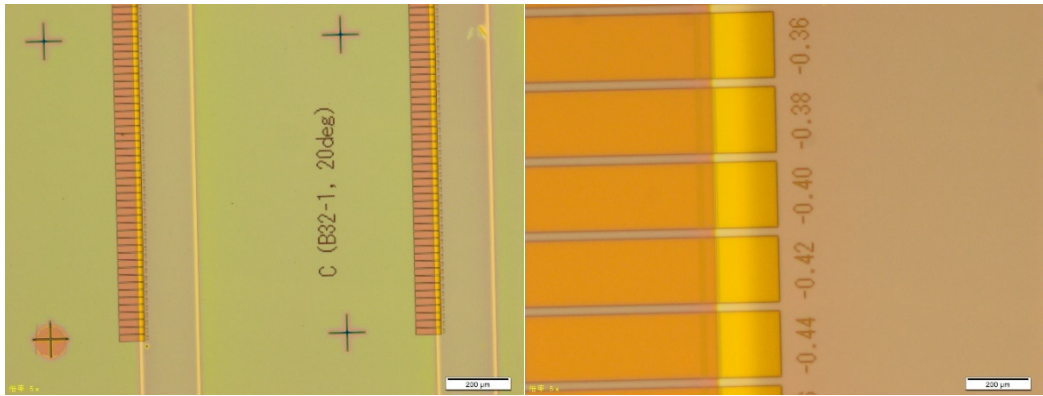
Figure 5.70 C specimen after development process.
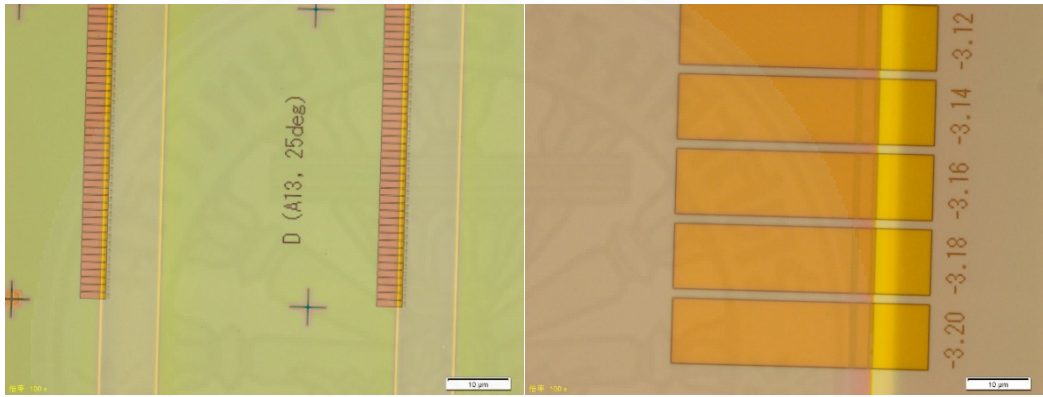
Figure 5.71 D specimen after development process.
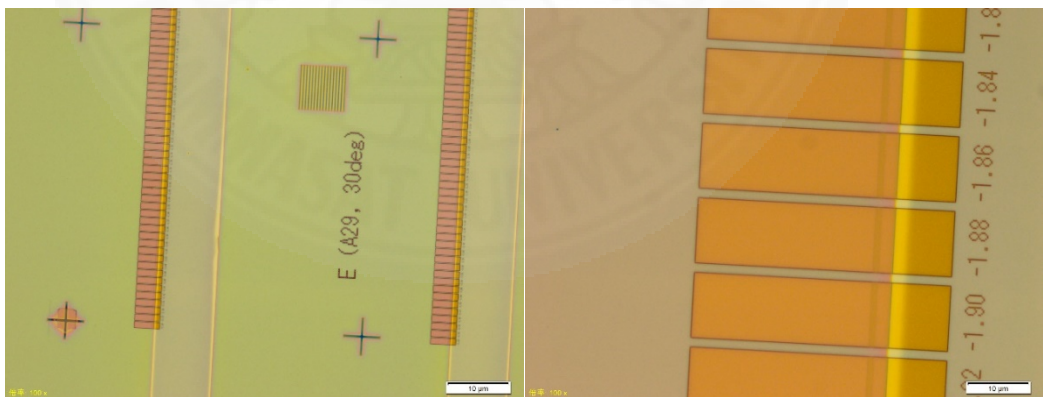
Figure 5.72 E specimen after development process.
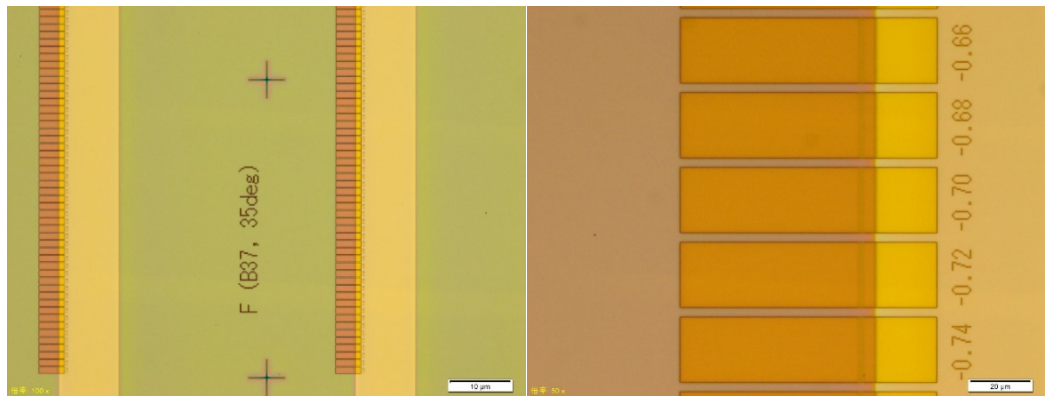
Figure 5.73 F specimen after development process.
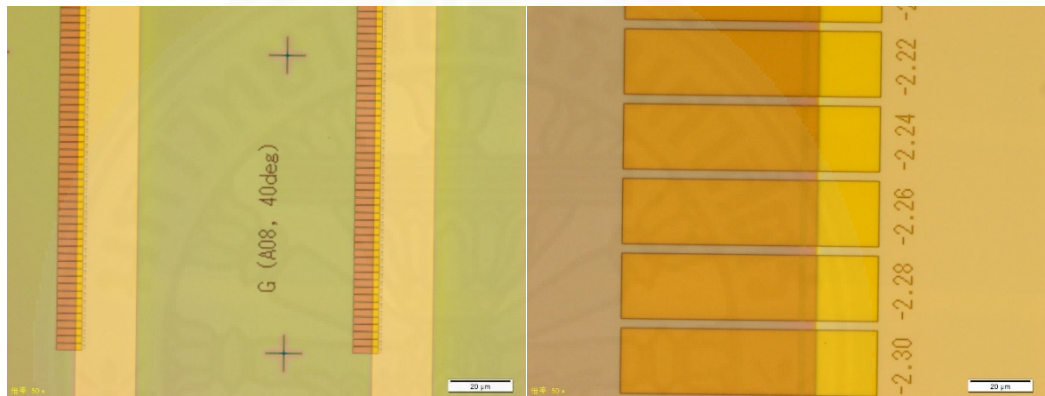
Figure 5.74 G specimen after development process.
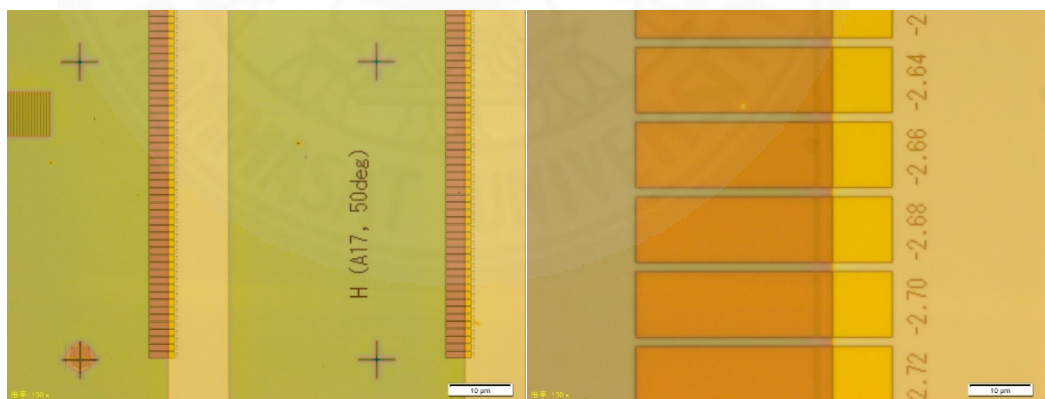
Figure 5.75 H specimen after development process.
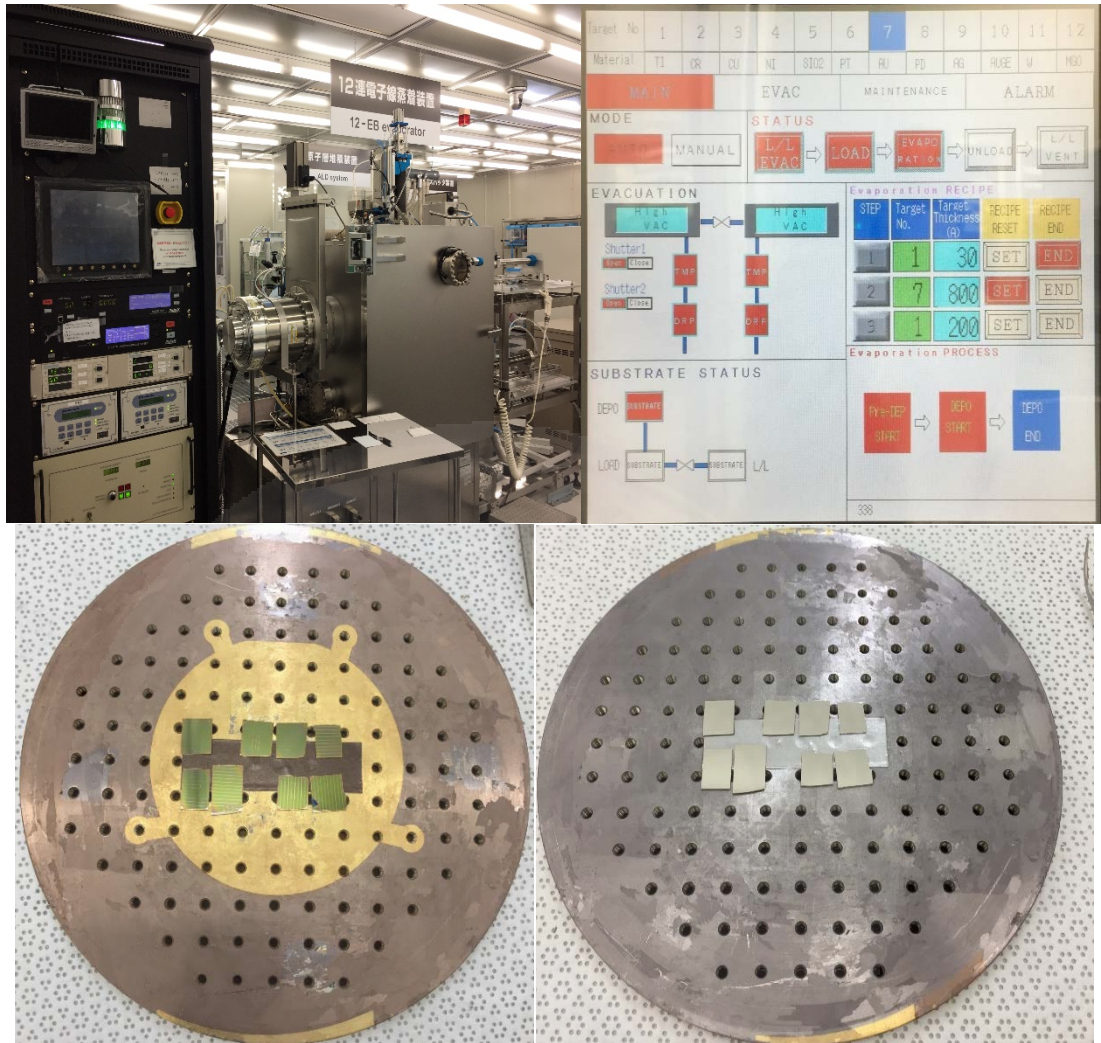
Figure 5.76 The evaporate 3 nm-Ti, 80nm-Au, and 20 nm-Ti outer.
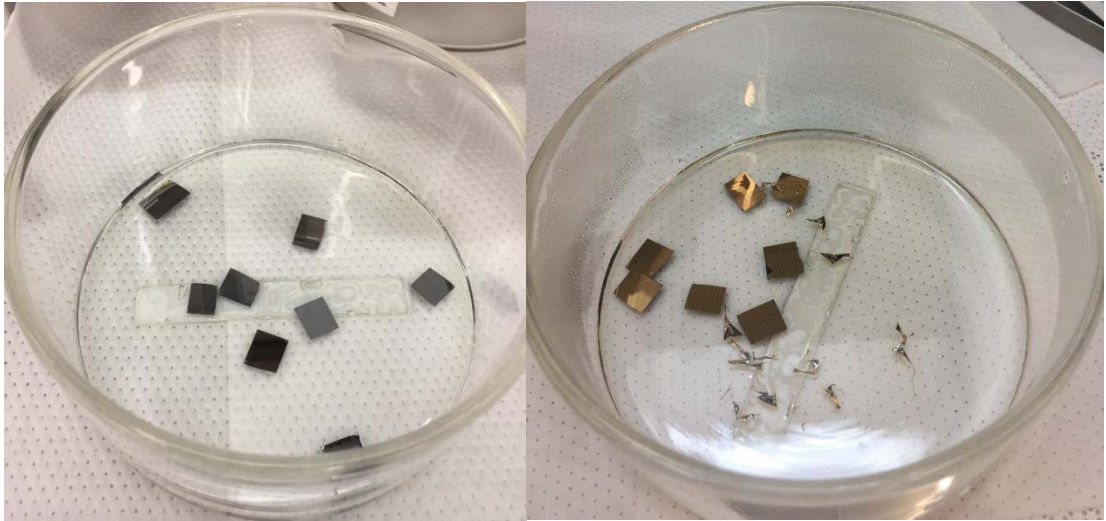
Figure 5.77 (Left) NMP lift-off process (Right) After 1 night lift-off.
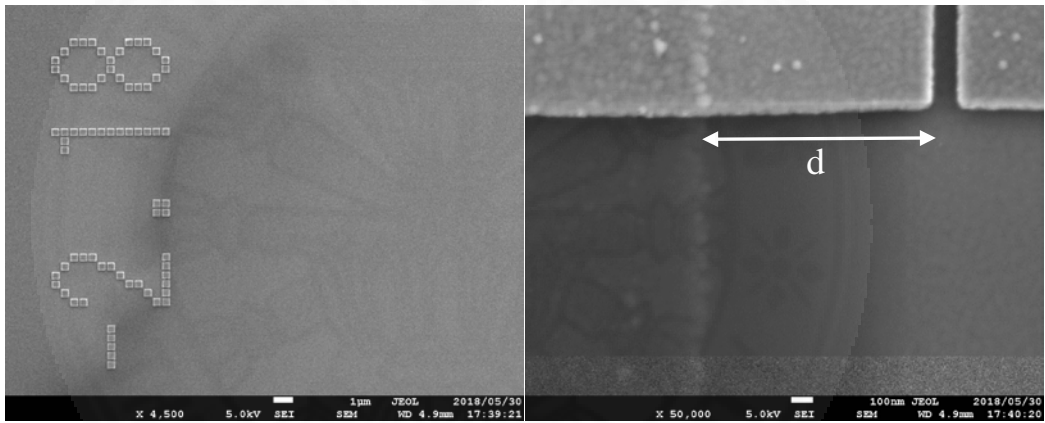
Figure 5.78 SEM of 'A' specimen.
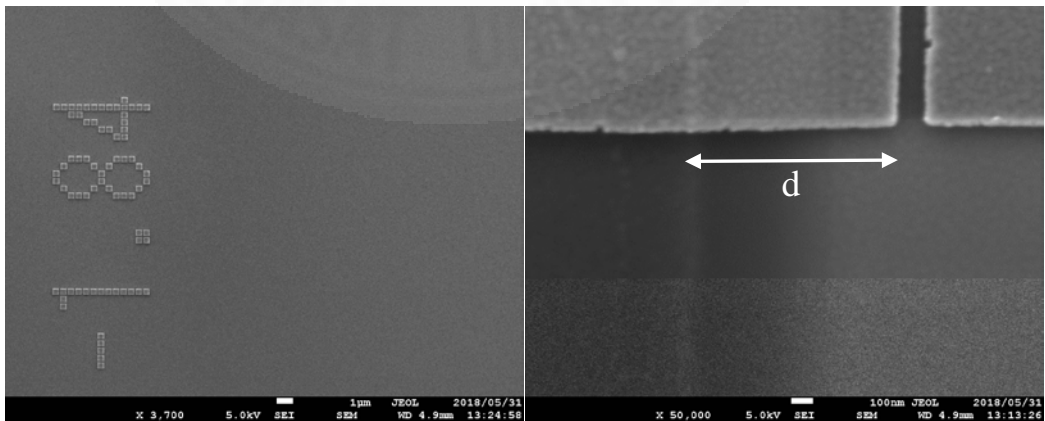
Figure 5.79 SEM of 'B' specimen.
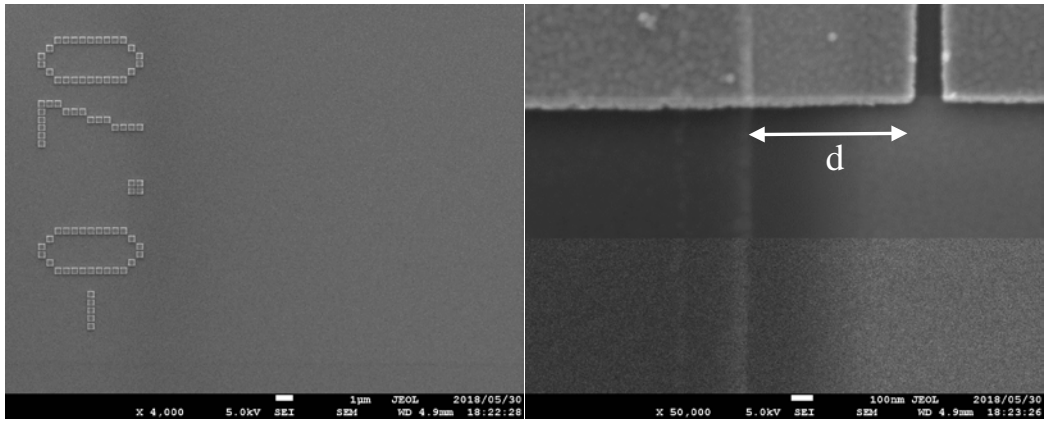
Figure 5.80 SEM of 'C1' specimen.
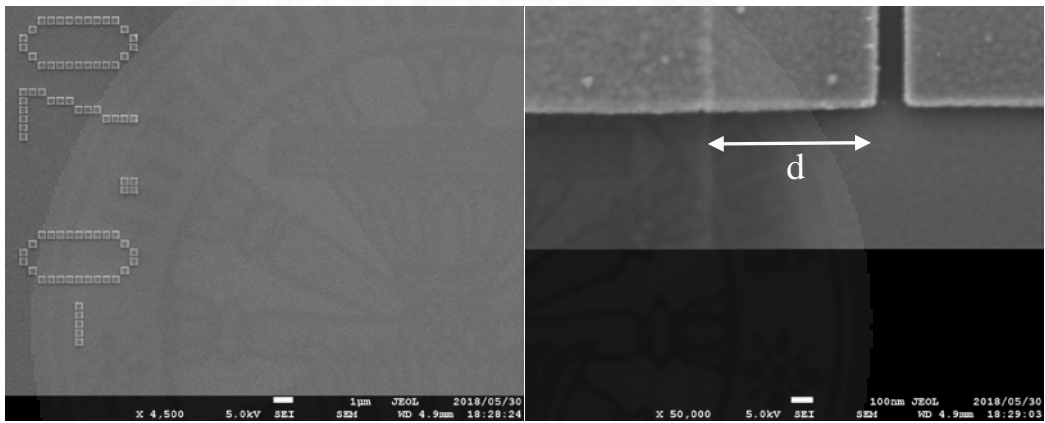
Figure 5.81 SEM of 'C2' specimen.
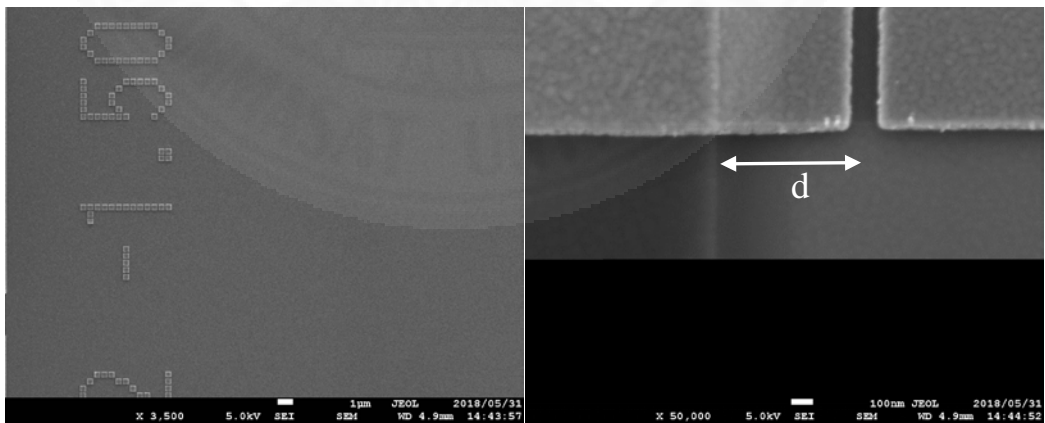
Figure 5.82 SEM of 'D' specimen.
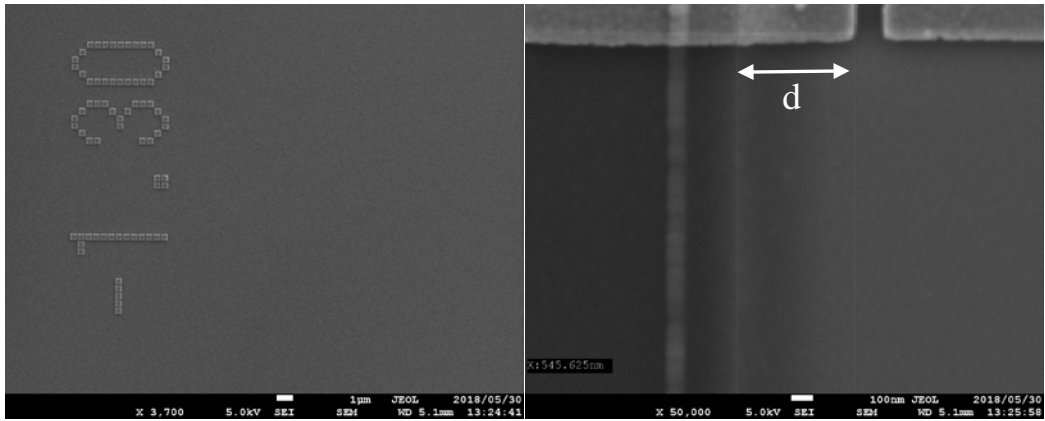
Figure 5.83 SEM of 'E' specimen.
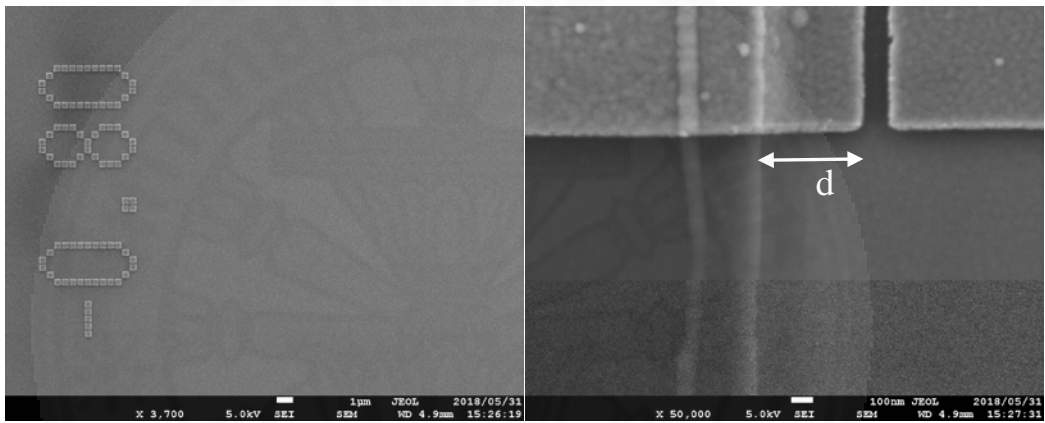
Figure 5.84 SEM of 'F' specimen.
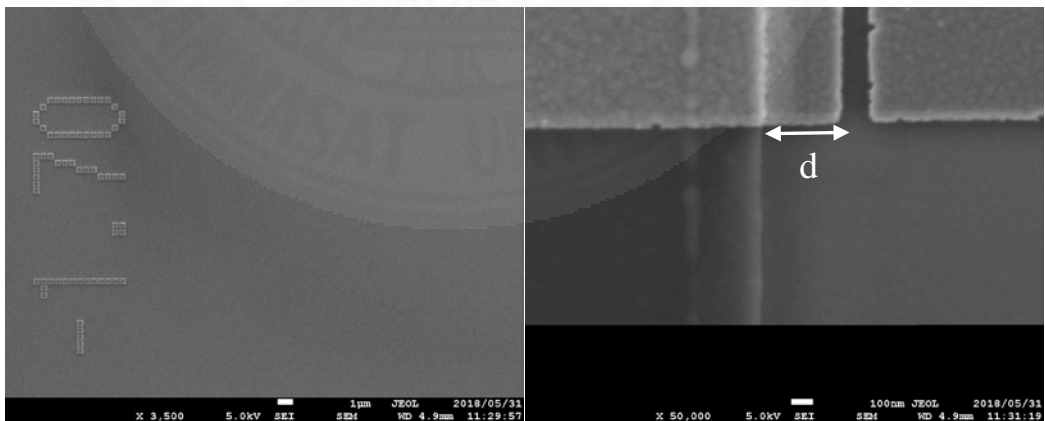
Figure 5.85 SEM of 'G' specimen.
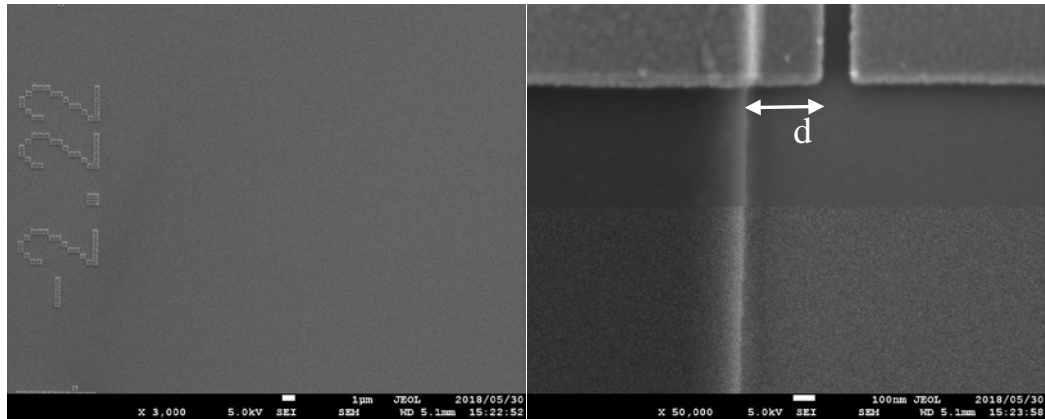
Figure 5.86 SEM of 'H' specimen.
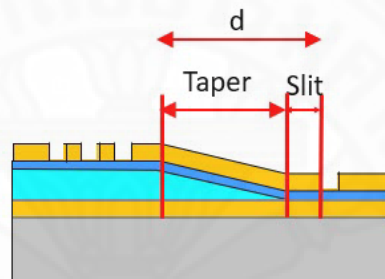
Figure 5.87 The distance between the taper and the slit.

After the lift-off process as shown in figure 5.68-5.75, the microscope pictures show all final 8 specimens after the making is completed and confirm by the SEM observation as shown in figure 5.79-5.86. For one specimen, 3 lines of patterning are fabricated by varying the position of -3.2 μm: 0.02 μm: 1.8 μm that it is made 250 patterns in one line. 3 positions of patterns which are close to the optimized values refer to the simulation results as shown in table 5.6 and figure 5.87 for doing the optical measurement in the last step are selected. Fabrication yield is 1.2%. The optical measurement process and results are shown in the next chapter.

Table 5.6 The optimized position of the slit in our specimens.

Specimen	Angle (deg.)	Distance (d) between taper and slit (μm)	Line	Position
A	10	0.86+0.220=1.08	1	-2.02
		0.856+0.220=1.076	2	-2.06
		0.850+0.220=1.070	3	-2.18
B	15	0.672+0.220=0.892	1	-1.84
		0.670+0.220=0.890	2	-1.88
		0.670+0.220=0.890	3	-1.84
C	20	0.540+0.220=0.760	1	-0.7
		0.540+0.220=0.760	2	-0.7
		0.556+0.220=0.776	3	-0.82
D	25	0.395+0.220=0.615	1	-1.48
		0.390+0.220=0.610	2	-1.5
		0.406+0.220=0.626	3	-1.52
E	30	0.310+0.220=0.530	1	-1.3
		0.325+0.220=0.545	2	-1.3
		0.330+0.220=0.550	3	-1.3
F	35	0.235+0.220=0.455	1	-0.68
		0.246+0.220=0.466	2	-0.8
		0.241+0.220=0.461	3	-0.82
G	40	0.155+0.220=0.375	1	-1.74
		0.138+0.220=0.358	2	-1.72
		0.199+0.220=0.419	3	-1.66
H	50	0.130+0.220=0.350	1	-2.22
		0.130+0.220=0.350	2	-2.22
		0.140+0.220=0.360	3	-2.2

CHAPTER 6
CHARACTERIZATION AND RESULTS

The optical characterization of nano-focusing taper is the last process of our experiment. Before that, 1) the nano-focusing tapers with the light input/output ports (the grating and single hole) was successful fabricated, 2) the nano-focusing tapers with various taper angles was fabricated and to compare its efficiency with the calculation results, finally, the conclusion with analysis will discuss and can select the best specimen to apply for HAMR application.

The figure 6.1 shows the diagram of the optical measurement setup and the realistic optical equipment are shown in figure 6.2-6.3, the details of the function equipment are described below.
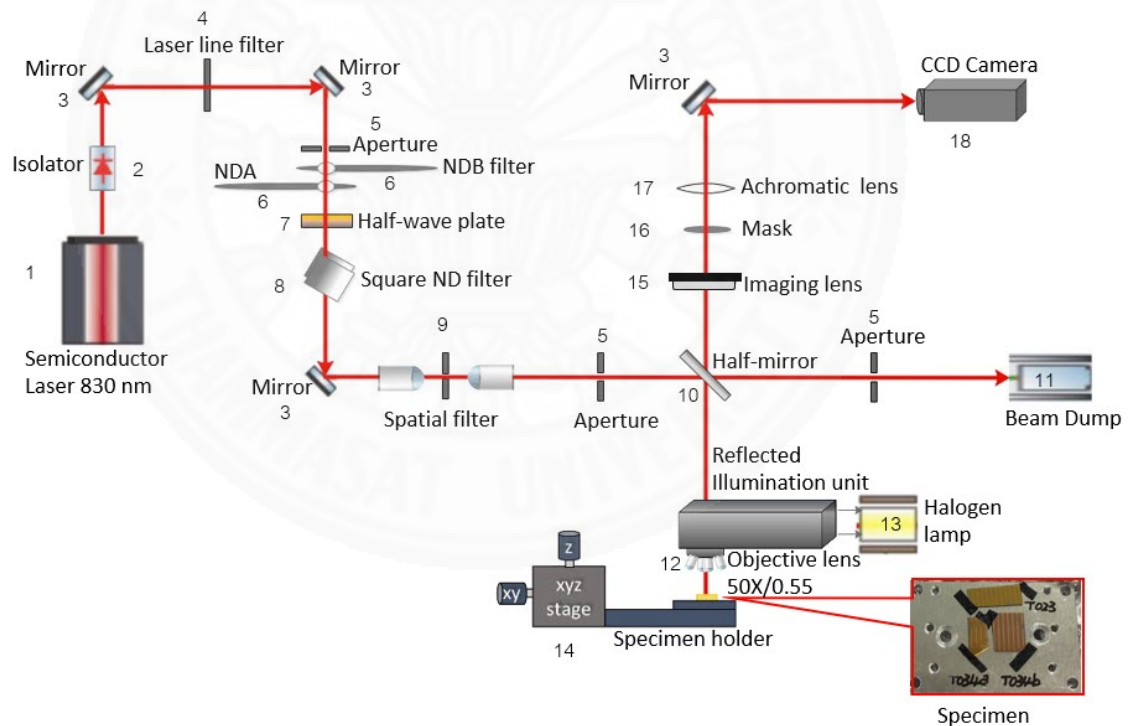
Figure 6.1 The diagram of optical measurement setup
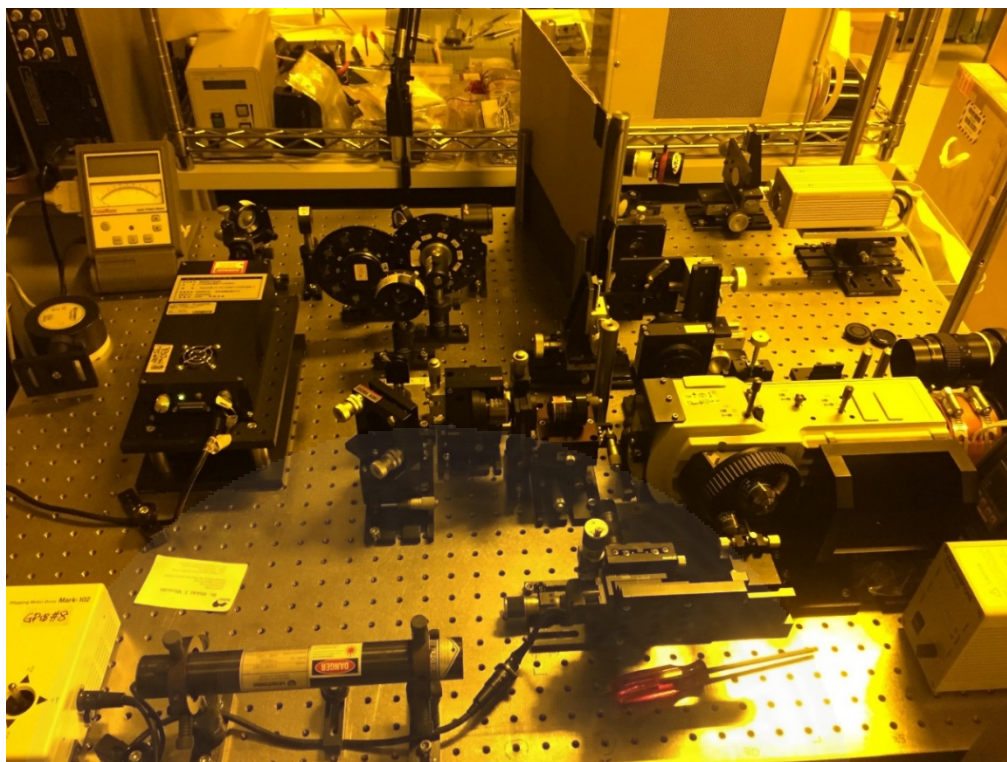
Figure 6.2 The optical measurement setup.
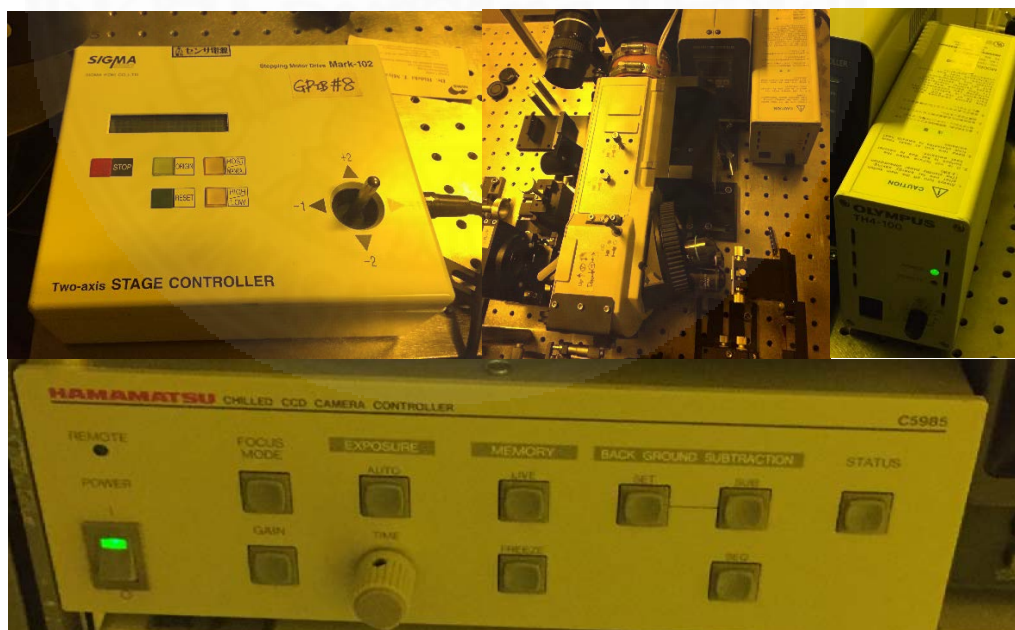
Figure 6.3 (Upper-left) the stepping motor for finding the beam position on grating
(Upper-middle) the objective lens and specimen holder (Upper-right) the white light
source (Bottom) the CCD camera and the exposure time controller.

6.1 The optical setup and functionality

The optical equipment functions are as follows;

1) The light source is the semiconductor Laser at 830 nm-wavelength (En wave FSL-830-75ss), near infrared laser (red light), single mode, vertical polarization, 750 mW.

2) Optical Isolator (diode) (Thorlabs IO-3D-830-VLP) is the high magnetic field device. It protects the reflected light from the specimen and sends it back go back to the light source using the Faraday Effect. If any reflection reverses to the laser light source, it will make an unstable laser source. This problem can be solved by using the optical alignment, but in our case it is very difficult. This can be solved by optical isolator device.

3) Mirror (M) is controlled the light path.

4) Laser Line Filter (Semrock, LL01-830-12.5) use for filtering some noise from the light source, only the narrow sharp peak can be selected.

5) Aperture, it can open widely or narrow for aligning light.

6) Newtrual-density filter, NDA and NDB, for reducing the light intensity. Normally the laser light source is not tunable with the intensity, it can only turn on or turn off and it has only one intensity, for our case, it is 750 mW. For 1 mW is too strong for microscope observation, so, the NDA and NDB can make the tunable intensity, 1% NDB of 1% NDA filtering of the laser source are applied.

7) The half wavelength (Sigma Koki WPQ-8300-ZM), for adjusting the light polarization to TM mode (position is 27.5) and TE mode (position is 72.5). Because the laser source delivered the vertical polarization and it will be slightly changed by the Isolator.

8) The square ND Filter; will use to reduce the light intensity when check the position of spotlight and record data.

9) The combination of lens (Olympus LMPlan IR 10x/0.25), aperture ($\varnothing$ 10 μm), and lens (LMPlan IR 10x/0.25) are the spatial filter as shown in figure 6.4.
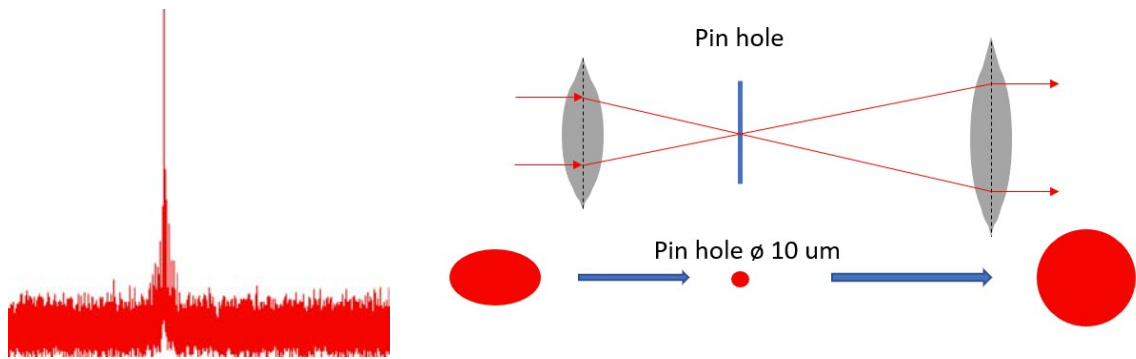
Figure 6.4 (Left) the spectral of laser source (Right) the spatial filter combined with lens, pinhole, and lens.

For semiconductor laser 830 nm, the characteristic consists of two characters. First is the spectral which combines with the main peak and noise. To select only the peak part, the laser line filter no. 4 is used. Second is the spatial, the beam spot shape of the semiconductor laser is not the perfect circular shape and it will cause many problems when incident on the surface of the specimen. For improving, the combination filter as shown in figure 6.4 is applied. After the laser light passes through the special filter, the Gaussian beam spot shape is perfectly circular.

10) Half mirror (45°) for reflecting the light to the objective lens.

11) Beam Dump, the importance device for the light discarding.

12) The objective lens (Olympus LMPlan IR 50x/0.55) is the optical microscope (reflected Illumination unit, Olympus BX-RLA2) using the Halogen lamp. The magnification is 50x/0.55.

13) The halogen lamp (Olympus U-LH100L-3) is the source of the optical microscope no. 12.

14) *XYZ*-state for moving the specimen position in vertical(y) and horizontal(*x*) and focus adjustment (z) by manual and control by stepping motor as shown in figure 6.3 (Upper-left).

15) For CCD camera image as shown in figure 6.5, the structure consists of the objective lens (Olympus LMPlan IR 50x/0.55), Imaging Lens (Olympus U_TLUIR), transparence mask ($\varnothing 100 \sim \varnothing\ 400\ \mu m$, Au/Ti), achromatic lens (Edmund, 45805), and

CCD camera (Hamamatsu, C5985). This structure image magnifies the specimen image twice to the CCD camera. Furthermore, the mask covers the input light which is strongly brighter than the output light. It is easier to observe the output light after cover the input part.

16) Variable aperture mask ($\varnothing100{\sim}\varnothing\ 400\mu m$, Au/Ti) to avoid unnecessary part.

17) Achromatic lens (Edmund, 45805) will magnify the image and send to the CCD camera.

18) Chilled CCD camera (Hamamatsu, C5985) prevents noise and add a cooling system inside.
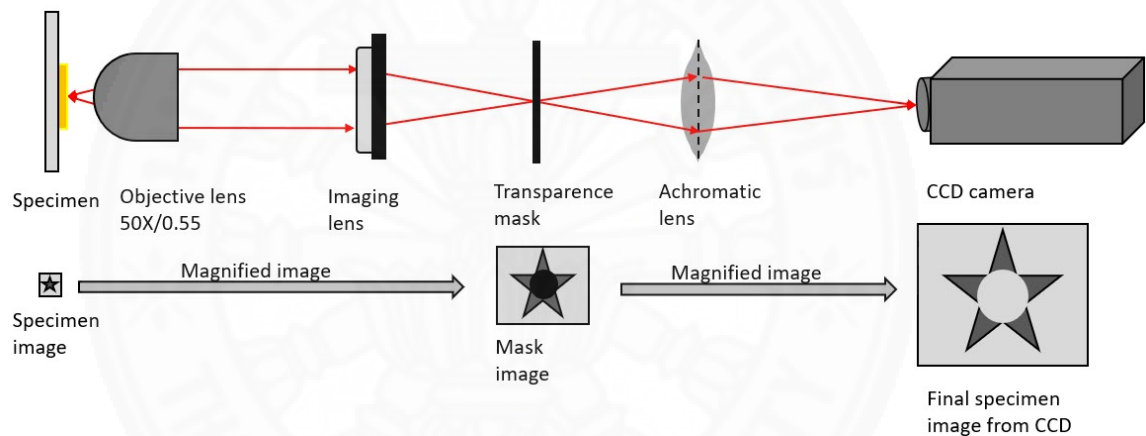
Figure 6.5 CCD camera image

6.2 The alignment of light source

To design the final nano-focusing device, the preliminary measurement was done for forecasting the results such as what is the optimum distance between grating-slit positions? How much the efficiency of device? What is the limitation of the CCD camera detection? How big of the laser spot size? Etc. The details of preliminary measurement is as follows;

6.2.1 The preliminary trial setup (grating-grating)

Firstly, Adjustment of the input beam is necessary, the SPP outside of Au surface is too bright as shown in figure 6.7 and there is no sign of light through the waveguide taper.

Figure 6.6 The pre-test of the realistic T023, T034a, T034b specimen.

G_3um_G_50x_Spot_TM.bmp	G_5um_G_50x_Spot_TM.bmp	G_10um_G_50x_Spot_TM.bmp
G_3um_G_50x_Left_TM.bmp	G_5um_G_50x_Left_TM.bmp	G_10um_G_50x_Left_TM.bmp
G_3um_G_50x_Right_TM.bmp	G_5um_G_50x_Right_TM.bmp	G_10um_G_50x_Right_TM.bmp
G_3um_G_50x_Right_TE.bmp	G_5um_G_50x_Right_TE.bmp	G_10um_G_50x_Right_TE.bmp
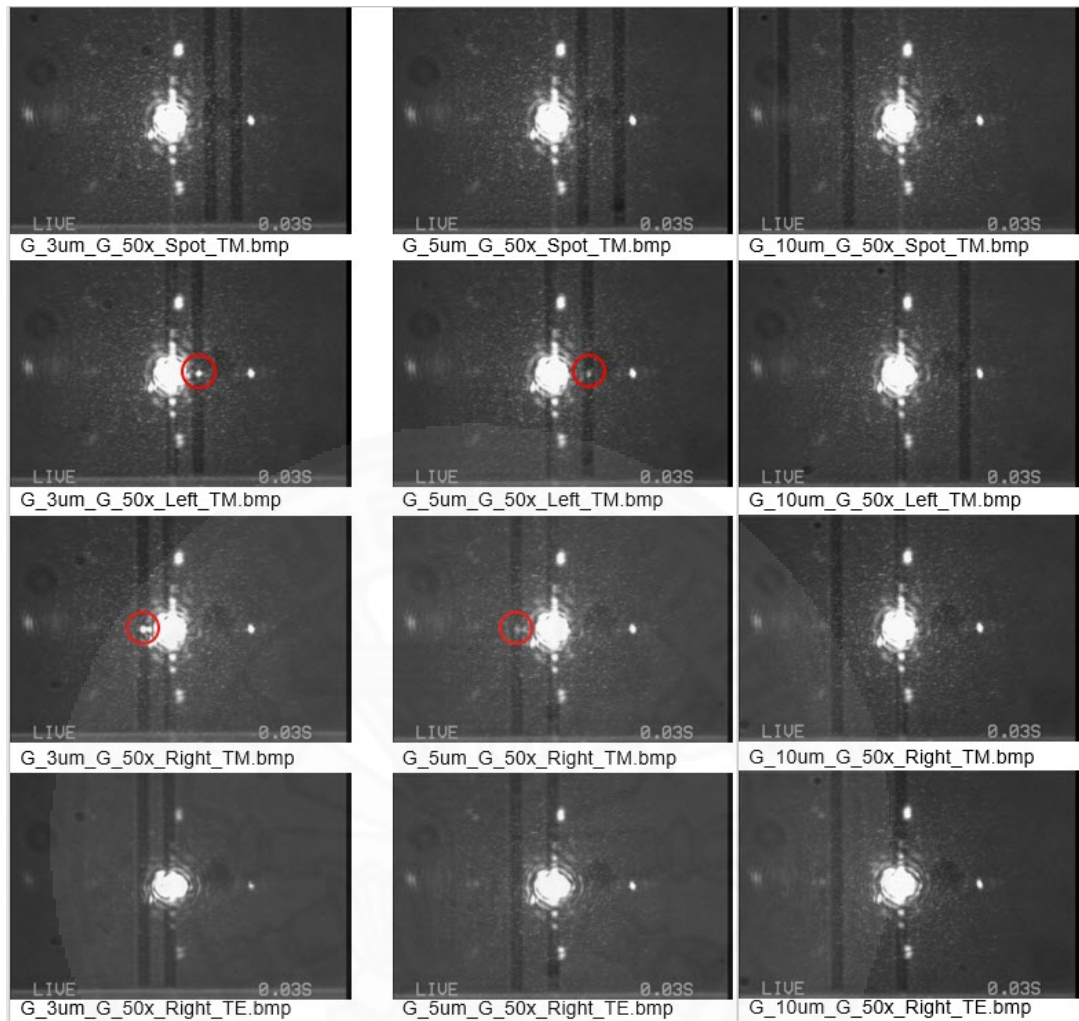
Figure 6.7 The distance between grating-grating 3 μm, 5 μm, and 10 μm of the preliminary test.

6.2.2 The measurement of the first specimen (T020)

To minimize the input beam, the diameter is important, and the measurement of very weak light is practically difficult. The intense reflection of the input grating as shown in the figure 6.8 is too bright and it would be a very serious problem. But finally a small sign of the light through the waveguide taper in position 198.0 is found.

T020_W010_P1980_50x_TM_02.bmp   T020_W010_P1980_50x_TM_01.bmp

T020_W012_P1980_50x_TM_02.bmp   T020_W012_P1980_50x_TM_01.bmp

T020_W014_P1980_50x_TM_02.bmp   T020_W014_P1980_50x_TM_01.bmp

T020_W016_P1980_50x_TM_02.bmp   T020_W016_P1980_50x_TM_01.bmp
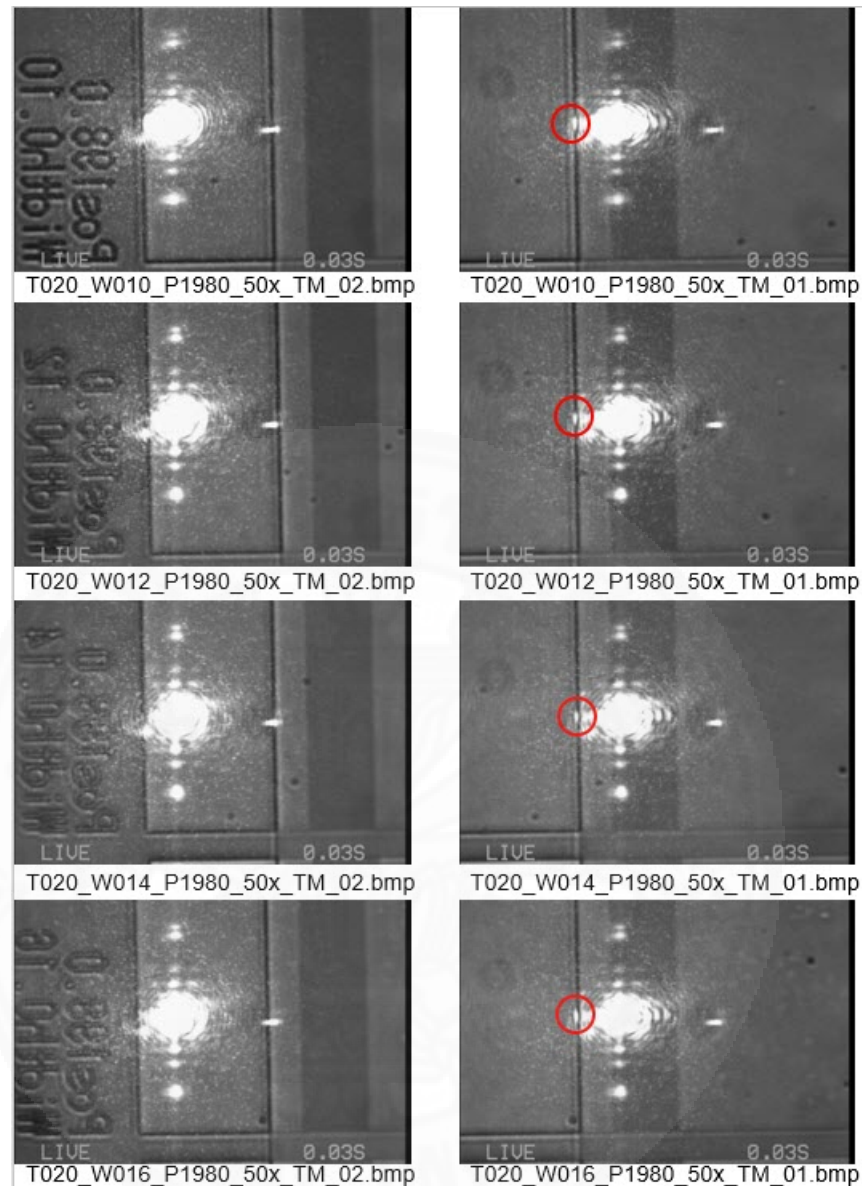
Figure 6.8 The first trial measurement with T020

6.2.3 The measurement of the second specimen (T023)

The reflection at the grating is reduced to about 50% by the Ti outer 20 nm as figure 6.9-6.10. The signal is too weak, although more exposure time of 0.2 s is applied as described in the figure 6.11 so, to extend the SiO2 thickness at the tip part is to add more feasibility to measure the transmission, the optimum thickness will simulate in

the next. There are successfully used the 400-diameter mask to remove the unnecessary reflection spots.
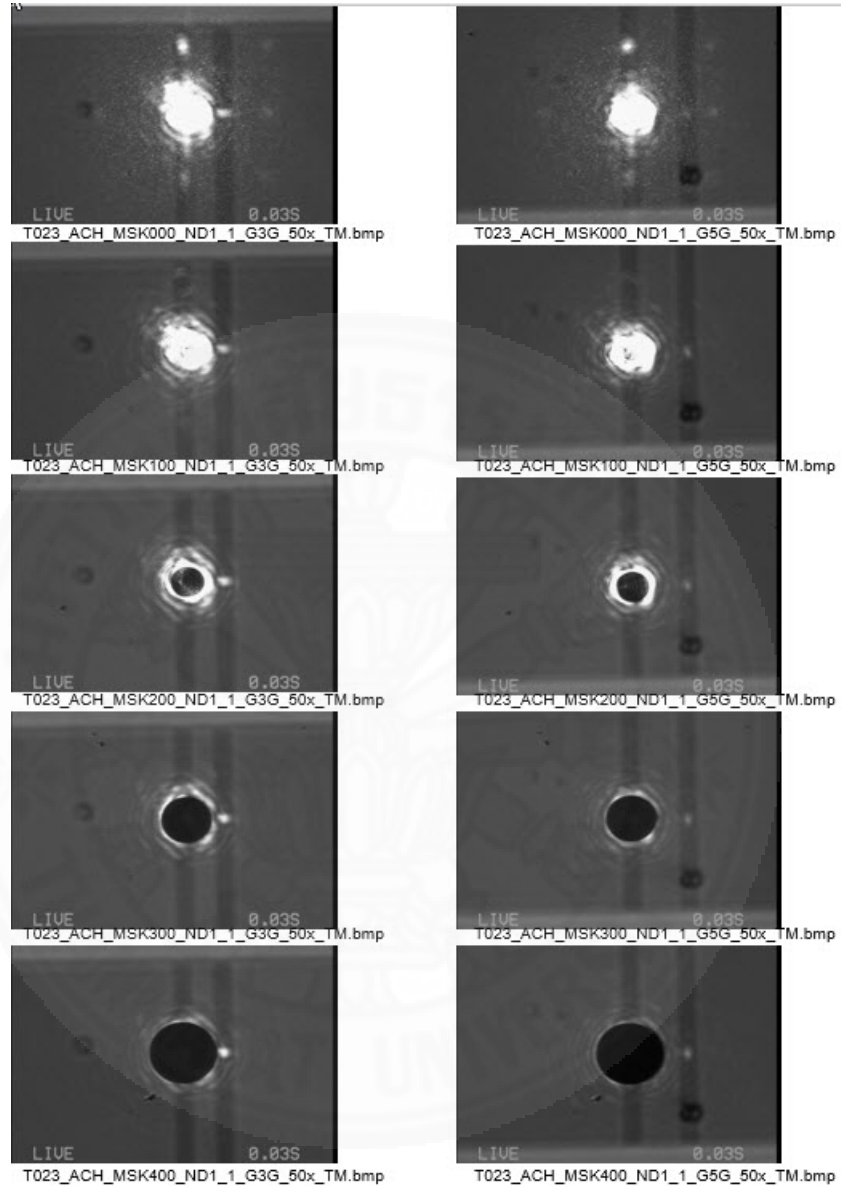
Figure 6.9 T023 grating-grating measurement with mask.
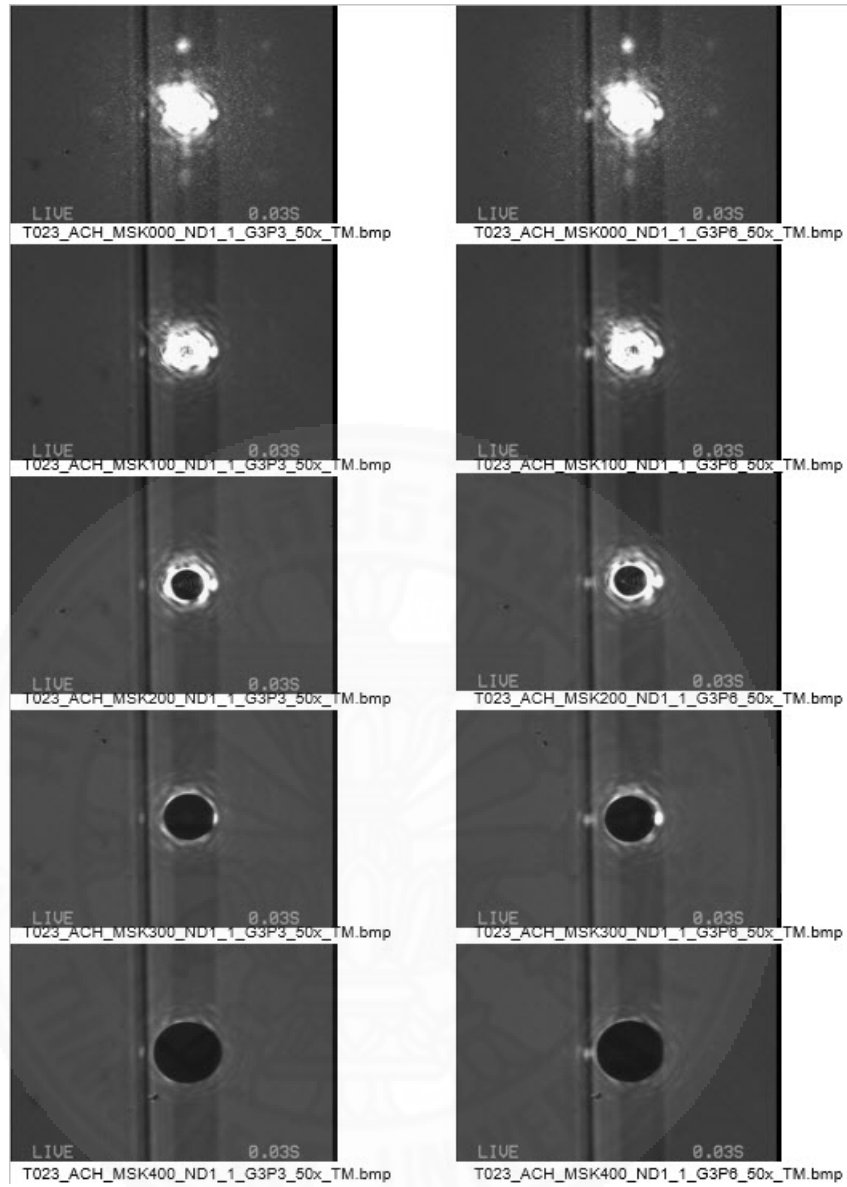
Figure 6.10 T023 grating-slit measurement with mask.
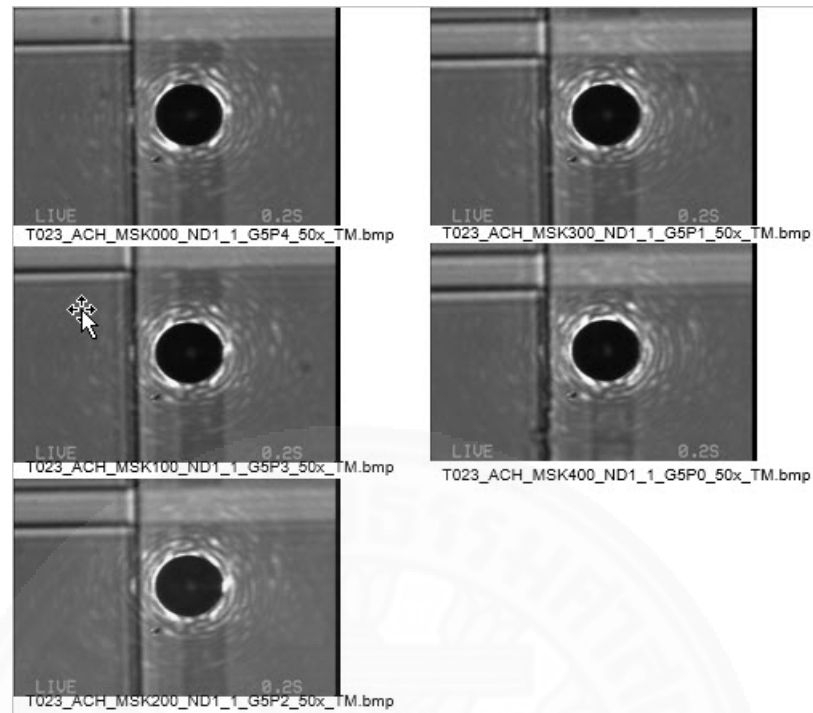
Figure 6.11 T023 measurement applied the longer exposure time to 0.2 s.

6.2.4 The measurement of the third specimen (T034a and T034b)

The transmission as shown in figure 6.12-6.13 is surly observed, but, at the 20 nm-thickness of SiO_2 and grating 4 μm would be the limit. For the grating 3 μm, would be too short due to the incident spot size. So, the grating of 4 μm would be the optimum. The result is very sensitive to the positioning of the spot to the grating. Therefore, the high-precision motorized stage will be used for solving the positioning problem for the final specimen measurement.
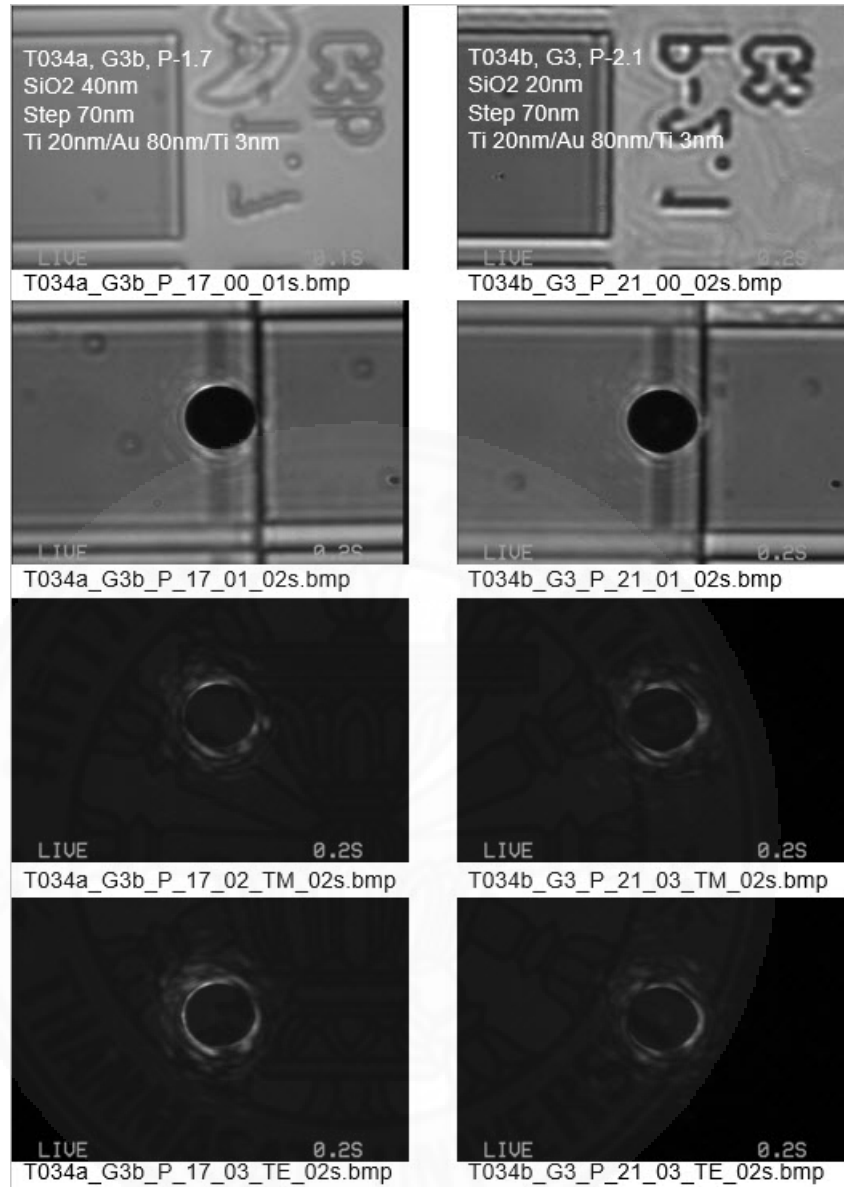
Figure 6.12 T034a-40 nm and T034b-20 nm results when applied TE and TM mode
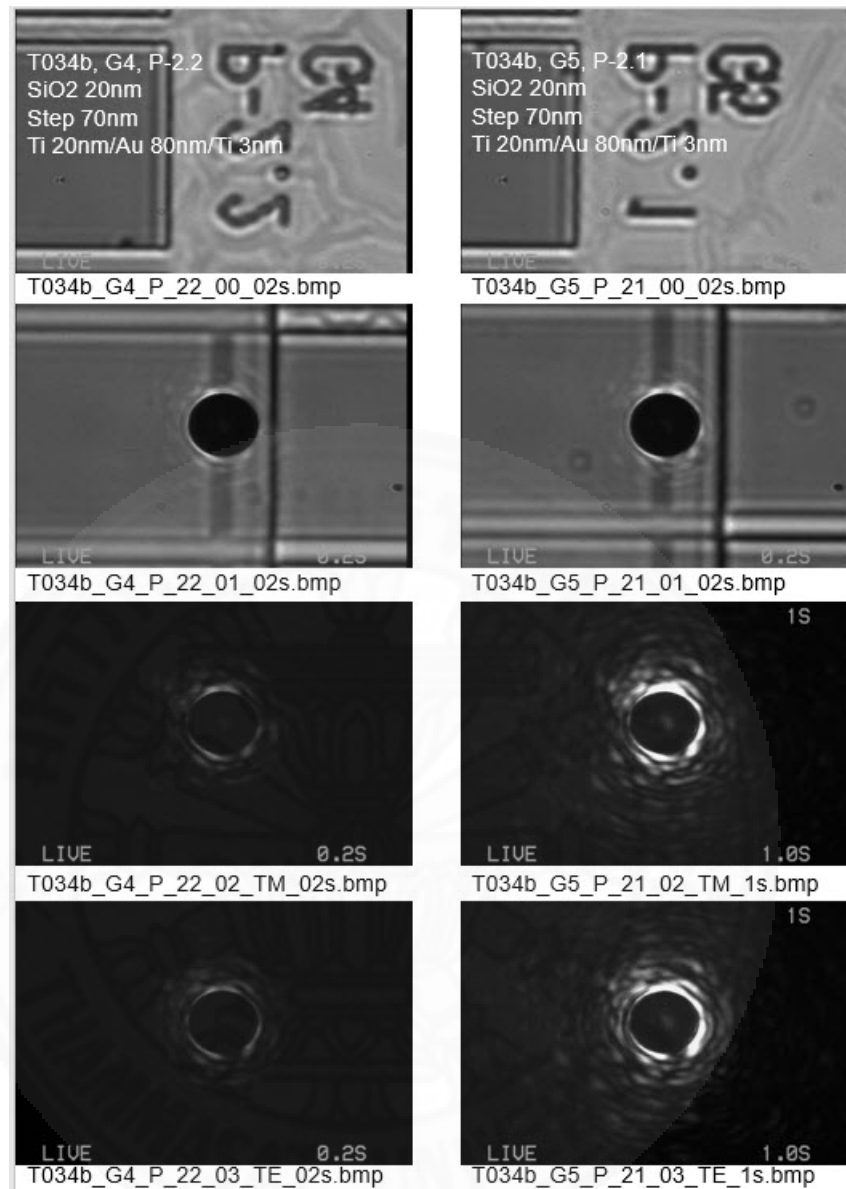
Figure 6.13 T034b results when applied TE and TM mode and exposure time is 1s.

6.3 The measurement procedures

For the optical measurement data, to obtaining the transmission efficiency of the tapers is done by measuring the total power of the input light and the output light by the integration of the position dependent light intensity $I(x, y)$. The way to determine the

power of the input light, the intensity distribution of the reflected spot by an Au mirror was measured. For output light, the intensity distribution of the light from the output slit is measured by the captured image and the output spot was assumed to be a Gaussian distribution with different *x* and *y* widths. Then the data of *I0*, *wx0*, and *wy0* were determined by fitting and do the simple comparison of the input/output power. The procedure to measure, fitting, take data from the image is given in the steps below.

(a) Attaching the specimens to the specimen holders as figure 6.14.

- The same as in the SEM specimen holders.

- Position a specimen around the center of an aluminum specimen holder.

- Align the horizontal and vertical directions as much as possible.

- Fix the specimen with tapes from the top.

- The rotation should be adjusted by the rotation stage, according to the actual CCD image.
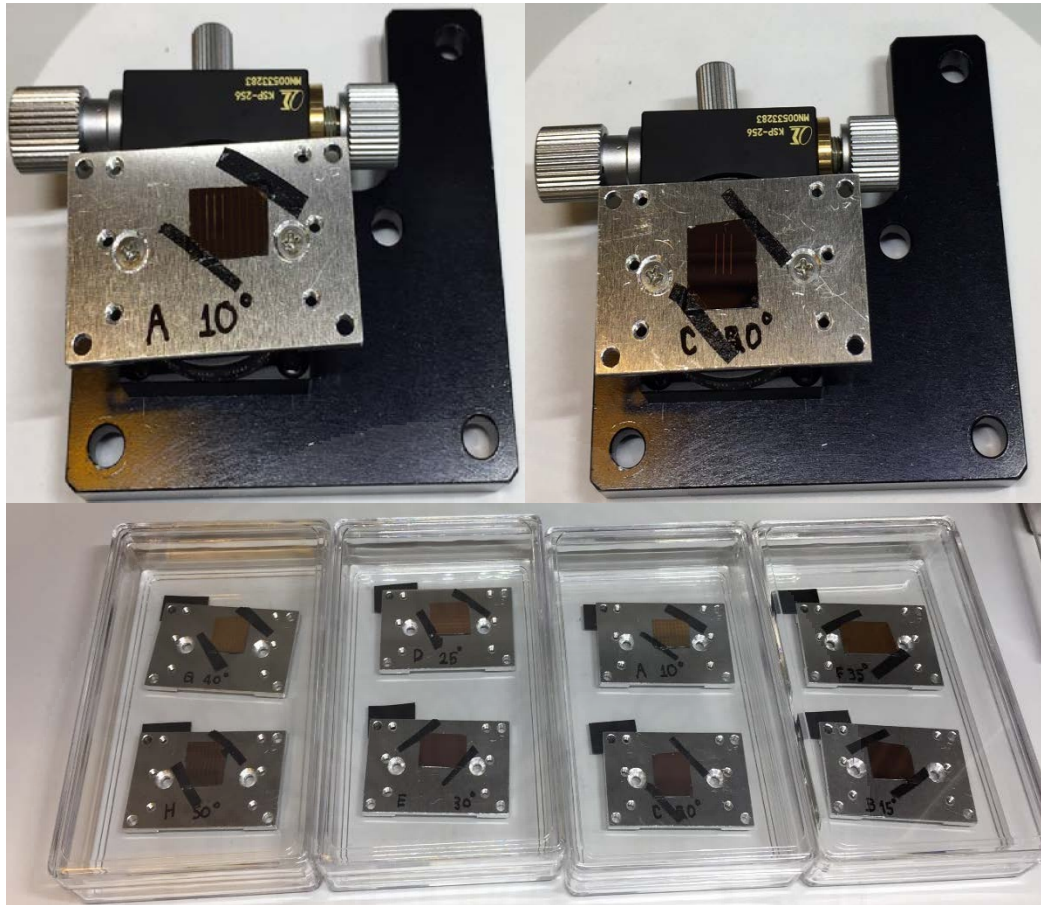
Figure 6.14 Attaching the specimens to the specimen holders

(b) Deciding the order to measure

- At first, decide the order of the measurement.

- Get important results as early as possible.

- Grasp the overall trend as early as possible.

(c) Overall measurement procedure

- First, the exposure time should be determined.

- Move to the initial position from one direction.

- Basically, the white light should be turned off, and capture one image for each motor step.

- At several (initial, middle, and final) positions as shown in figure 6.15, the relation between the grating and the laser spot should be recorded by the white light ON, mask removed, and square ND filters added.
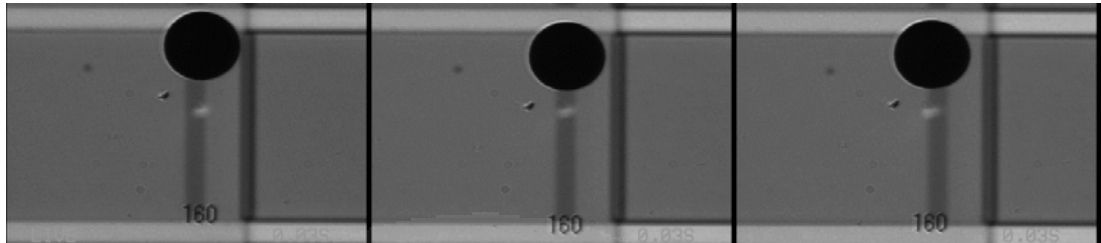
Figure 6.15 (Left) the initial, (Middle) the middle, and (Right) the final position

(d) The first task for each specimen

- Recording the representative images as figure 6.16.

- Purpose: deciding the exposure time and recording a set of TM/TE illumination.

- The exposure time should be optimized for each specimen.

- Position the laser spot at the grating center (can be inaccurate at this moment).

- TM, White light OFF => capture the image => analyze the profile immediately by ImageJ.

- The peak intensity should be as close as possible to 240 counts, as shown in figure 6.17.

- If the intensity is close to 250, it is too strong (saturation).

- If saturation happens, the data were already wrong.

- But if the intensity is too small, the accuracy and resolution is insufficient.

- TE image should also be recorded, for the future comparison between TM and TE.

- To restore the half-wave plate to TM.
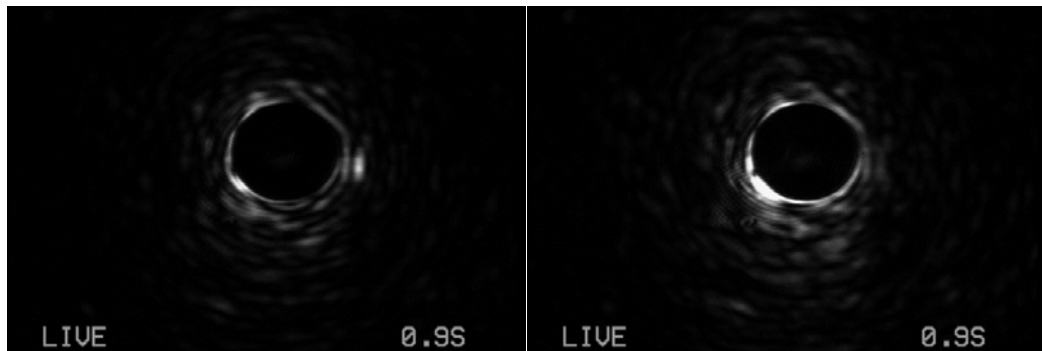
Figure 6.16 (Left) TM mode (Right) TE mode
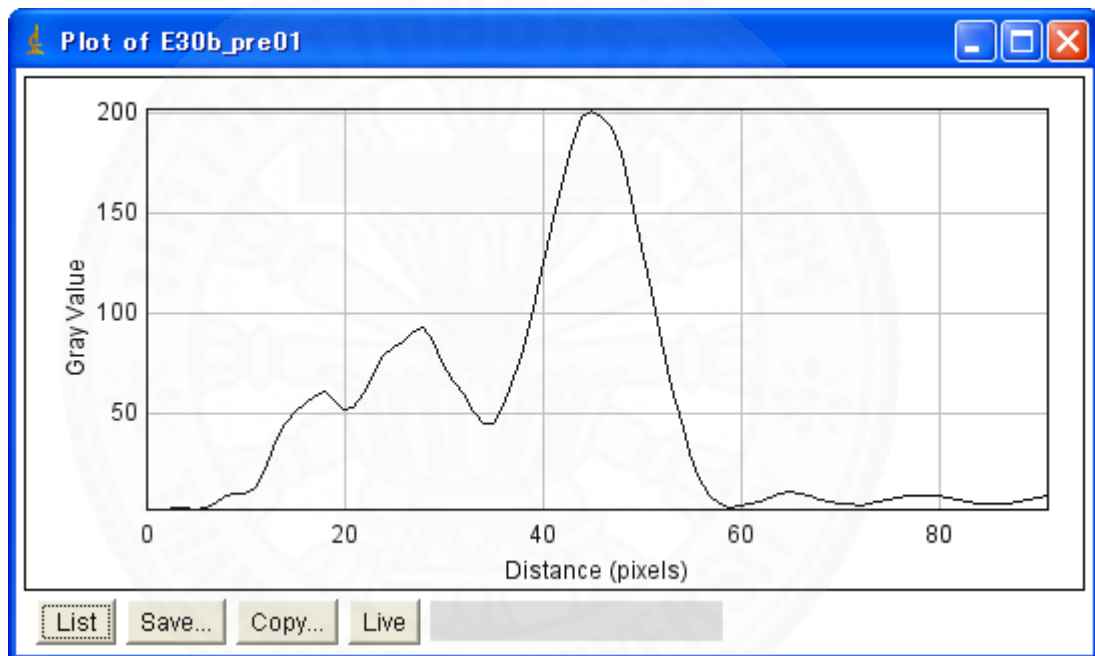
Figure 6.17 The peak intensity output profile using ImageJ which should be as close as possible to 240 counts

(e) Main measurement (only TM)

(e-1) Deciding the scanning steps across the grating

- Try to scan the laser spot across the grating by motor stage,

  and decide how many steps you will record.

- Scanning from the 1/4 to the 3/4 width of the grating (20 steps).

- To recording of a necessary, correct image by systematically capturing
  many images.

(e-2) Recording the grating-laser spot relations at the initial position.

- White light ON, move to the initial position.

- Mask removed, square ND filters inserted, proper exposure time (~0.03 s).

- Reset the position count of the motor stage (optional).

- Capture and save.

(e-3) Recording the output light from the taper for each step (first half)

- Mask inserted, square ND filters removed, exposure time restored, white light
OFF

- For each step, repeat capture and save.

- The file name should include the specimen name, exposure time, and motor
position.

(e-4) Recording the grating-laser spot relations at the middle position.

- White light ON

- Mask removed, square ND filters inserted, proper exposure time (~0.03 s).

- Capture and save.

(e-5) Recording the output light from the taper for each step (final half)

- Mask inserted, square ND filters removed, exposure time restored, white light
OFF

- For each step, repeat capture and save.

- The file name should include the specimen name, exposure time, and motor
position.

(e-6) Recording the grating-laser spot relations at the final position.

- White light ON

- Mask removed, square ND filters inserted, proper exposure time (~0.03 s).

- Capture and save.

6.4 The analysis procedures

(a) Selecting the optimum image

- Think of interpolating the grating-laser spot relations from the initial/middle/final positions.

- ImageJ, horizontal line from the same *x* position => profile (CTRL+K) => save.

- Determine the grating border (*x1*, *x2*) and the spot center (x0) from the profiles as figure 6.18-6.20.

- Plot the spot position relative to the grating [*x0-(x1+x2)/2*] vs motor step as figure 6.21-6.22 and table 6.1.

- It should be linear. If not, something is wrong and may need the measurement again.

- Determine the motor step for which the spot is the closest to the grating center.

Table 6.1 The grating border (*x1, x2*) and the spot center (*x0*) relative to the grating [*x0-(x1+x2)/2*] vs motor step.

step position	x1	x2	x0	x0-(x1+x2)/2
0	34	73	64	10.5
10	37	76	51	-5.5
20	71	110	64	-26.5

Figure 6.18 The profile in step 00

Figure 6.19 The profile in step 10

Figure 6.20 The profile in step 20
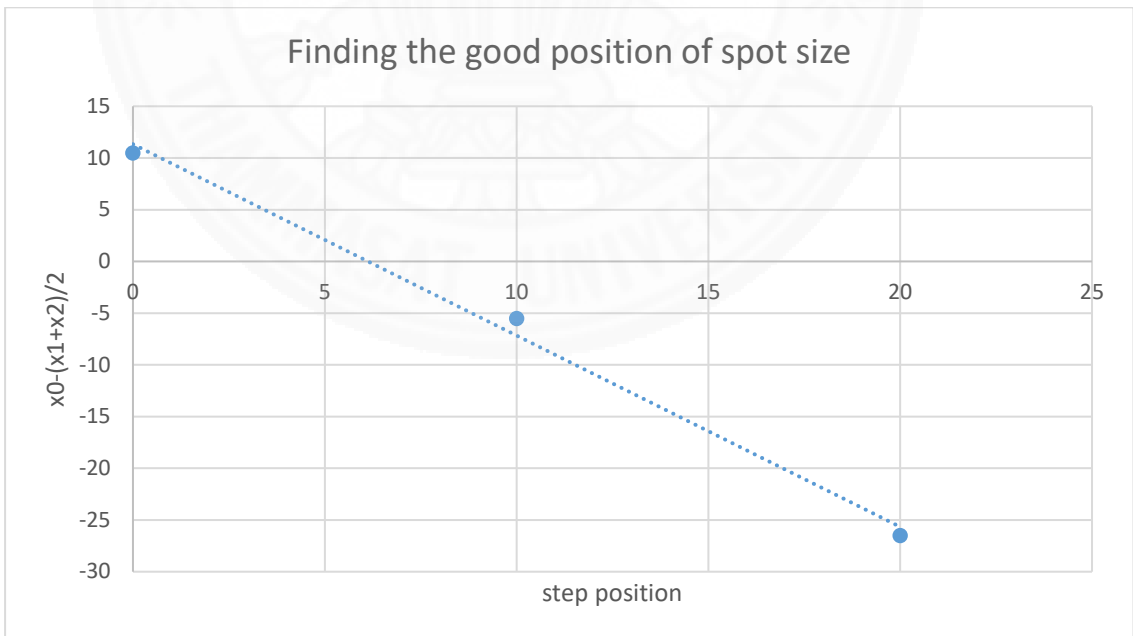
Figure 6.21 The spot position relative to the grating [*x0-(x1+x2)/2*] vs motor step

The magnified axis to determine the middle position of spot
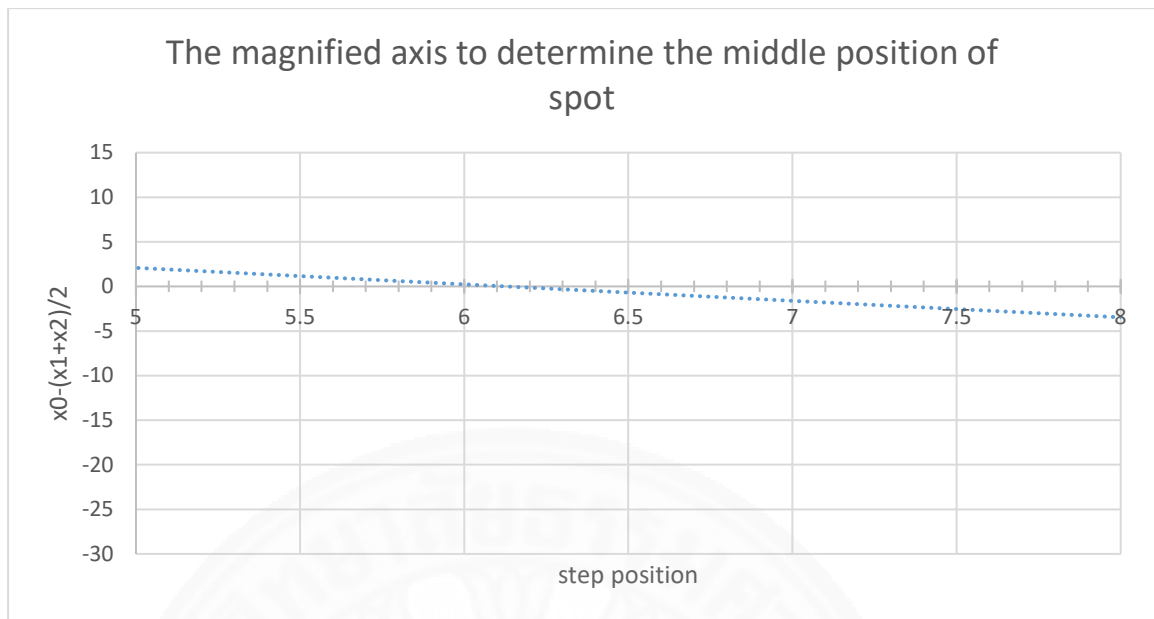
Figure 6.22 The magnification of the axis to determine the exact middle spot position relative to the grating [$x0-(x1+x2)/2$] vs motor step, this case, step no. 6 is the middle spot position.

(b) Measurement of the output light from the taper

- ImageJ, x/y lines at the center of the output spot => profile (CTRL+K) => save as figure 6.23.

- IgorPro, Gaussian fitting of the x/y profiles as figure 6.24-6.25.

- Determine $y0, I0, x0, w0$ of $y=y0+I0*exp(-((x-x0)/w0)^2)$ for both x and y profiles

- $w0$ and $I0$ are important, while $y0$ and $x0$ are not important.

- $wx0$ and $wy0$ [pixels] should be multiplied with 0.05965 μm /pixel to change the unit to [μm].

- $Ix0, Iy0$ should be multiplied with 1/ExpTime to obtain [count/s].

- $Ix0$ and $Iy0$ should be equivalent, in principle, but if not, take their average: $I0=(Ix0+Iy0)/2$.

- $I0*wx0*wy0$ shows the output power for that taper angle as table 6.2.
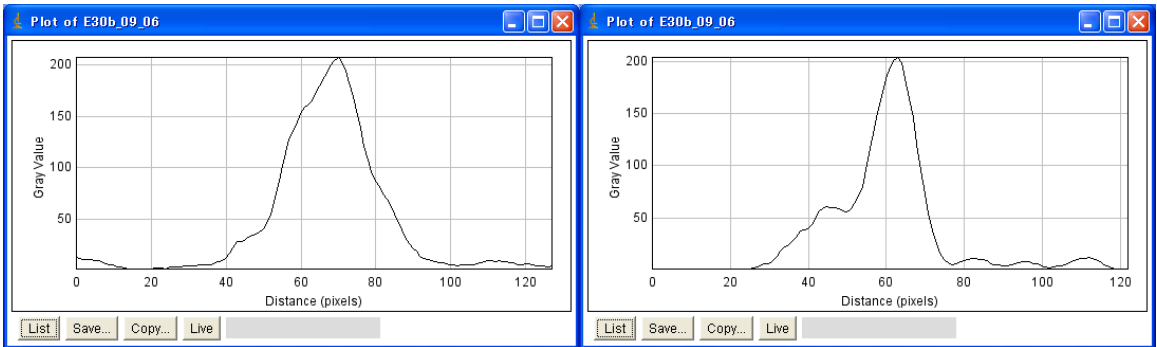
Figure 6.23 (Left) profile of *x* direction (Right) profile of *y* direction
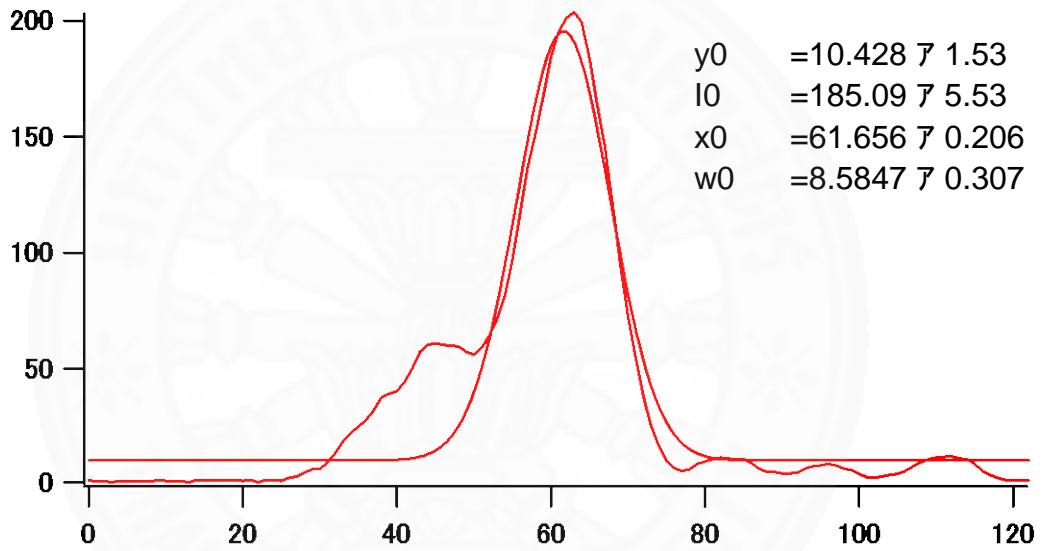
Figure 6.24 Gaussian fitting of the *x* profiles using IgorPro
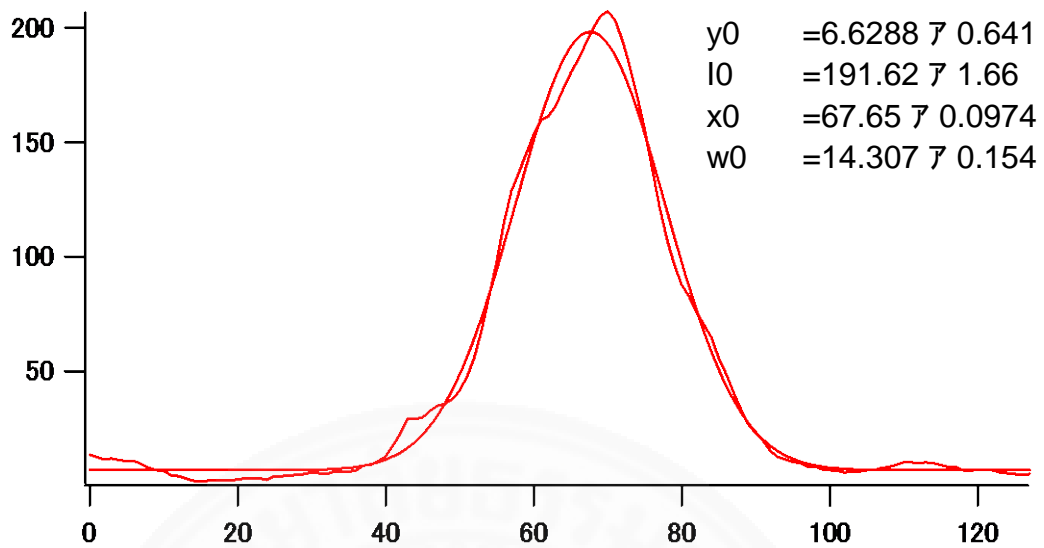
Figure 6.25 Gaussian fitting of the *y* profiles using IgorPro

(c) The compare the taper-angle dependence with the simulation

- Because the incident beam is equivalent to all the data, comparison of the output power straightforwardly means the comparison of the efficiency as shown in table 6.2 and figure 6.26-6.27.

- Input: Intensity distribution of the reflected spot by an Au mirror was measured.

- Au mirror: Reflectance = 98% at 830nm [81].

- The reflected spot was assumed to be a Gaussian distribution.

- Radius: *wi0* = 620 nm.

- Center intensity: *Ii0* = 5.4e+5 counts/s.

- The absolute efficiency can be obtained by taking the input power: *Ii0*wi0^2* = 207,576.

- Actual length in the image: 0.05965 *μm* /pixel.

- Incident power: 610 nW (TM mode), 1280 nW (TE mode).

Table 6.2 The optical measurement results and efficiency.

Nominal angle (deg.)	simple name	Taper angle (deg.)	vertical step (nm)	d	exposure time (s)	step no.	$Ix0=Ix/$ Exposure time	$Iy0=Iy/$ Exposure time	$I0=(Ix0+Iy0)/2$	$wx0 = wx*0.05965$	$wy0 = wy*0.05965$	$I0*wx0*wy0$ (output)	$Ii0*wi0^2$ (input)	eff=output/ input
10	A	10.9	20	1.07	2	9	103.885	102.745	103.315	0.438272	0.943126	42.70486	207576	0.0002057
15	B	14.4	16	0.89	1.6	11	118.3563	118.863	118.6094	0.577812	1.074833	73.6625	207576	0.0003549
20	C1	19.1	23	0.76	2	8	86.28	86.005	86.1425	0.696891	0.609563	36.59326	207576	0.0001763
20	C2	19.1	23	0.76	2	9	109.065	104.075	106.57	0.575903	0.641178	39.35163	207576	0.0001896
25	D	24.9	18	0.61	1.2	9	155.9	158.575	157.2375	0.40704	0.982257	62.86629	207576	0.0003029
30	E	29.1	14	0.55	0.9	6	205.6556	212.911	209.2833	0.512077	0.853413	91.45959	207576	0.0004406
35	F	34.5	26	0.47	1.6	13	138.5563	130.675	134.6156	0.631753	1.028605	87.47649	207576	0.0004214
40	G1	41.3	26	0.37	1.6	6	98.94375	96.4125	97.67813	0.536373	1.49811	78.4888	207576	0.0003781
40	G2	41.3	26	0.42	1.6	13	143.2438	132.906	138.075	0.483254	0.972414	64.8847	207576	0.000313
50	H	49.4	35	0.35	1.6	12	77.01875	72.6563	74.8375	0.436733	0.953804	31.17415	207576	0.0001502
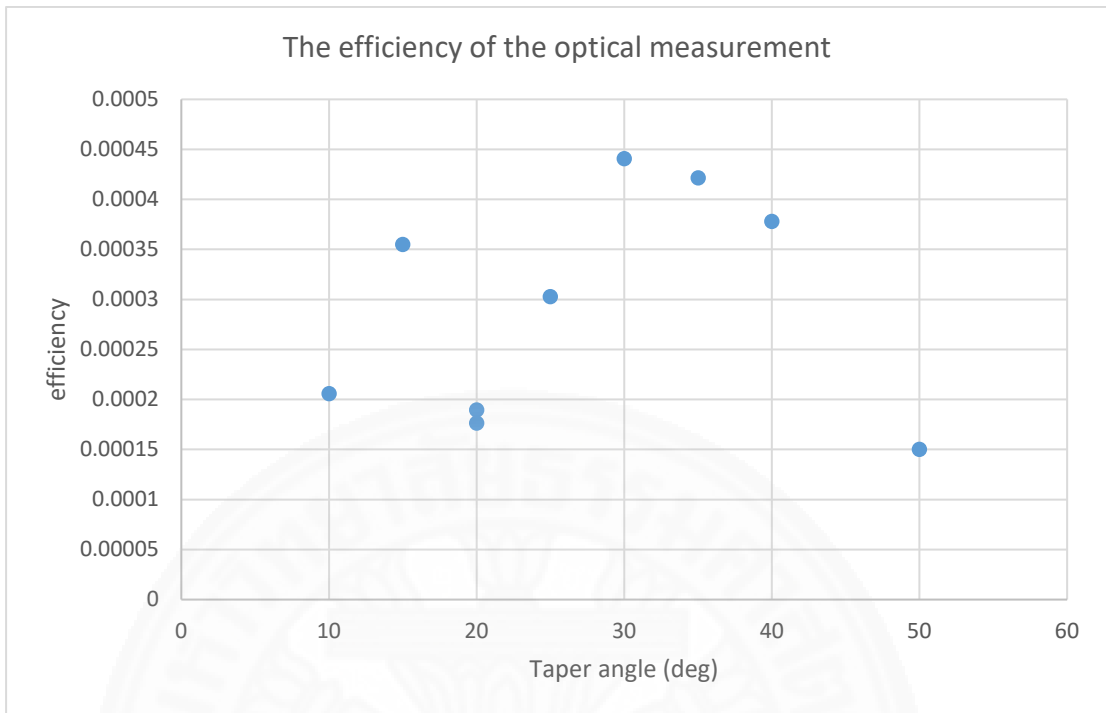
Figure 6.26 The coupling efficiency of the optical measurement
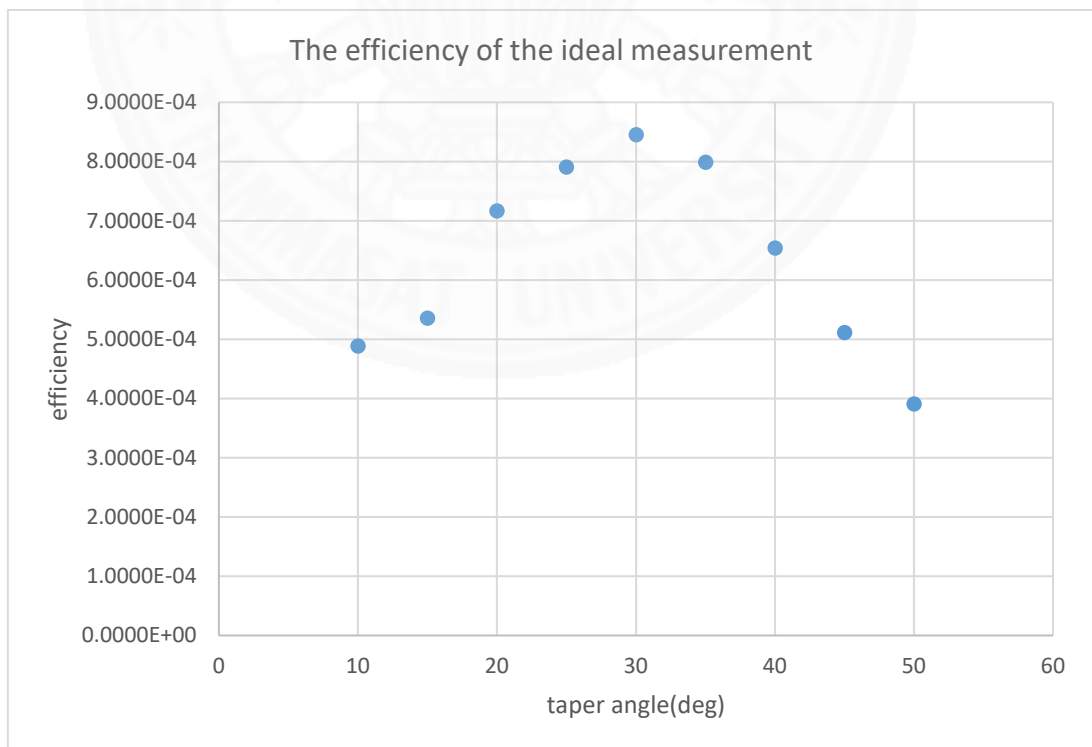
Figure 6.27 The coupling efficiency of the simulation

6.5 The final check with the actual final specimen dimension

As the graph in figure 6.26-6.27, the optical measurement results and simulation results have some differences, but the optimum taper angle is 30 deg. for both cases with the highest efficiency of 0.045%-0.05% and the spot size is 512 nm x 853 nm as shown in table 6.2. There are some factors that might be responsible for the discrepancy between the simulation results and the experiment results are as follows;

- Presence of the vertical steps
- Measurement error of the vertical step
- Discrepancy of the actual taper shape of the ideal linear shape
- Measurement error of the taper-slit distance in the selection of the specimen
- Fabrication error of the grating width
- Fabrication error of the slit width
- Error of the thicknesses of the metal layers
- Error of the Al_2O_3 layer
- Error of the SiO_2 layer
- Presence of the bottom 3-nm-thick Ti at the tip part in the SiO_2 etching process
- Etching depth of the bottom Au in the tip part in the SiO_2 etching process
- Difference in the input Gaussian beam radius (830 nm/620 nm)
- Difference of the 2D and 3D systems

Therefore, the re-simulation by adding the factors above in the simulation is done for finding the discrepancy reasons of the simulation and characterization in the next session.

6.5.1 The actual specimens

The actual specimen's dimension with the vertical step and the presence/absence of the 3-nm-thick Ti at the tip part due to the SiO_2 etching process, will be re-simulated. The simulation parameter setting is shown in table 6.3-6.4 and figure 6.28-6.30. The comparison results between the simulation and experiment results are shown in figure 6.33.

Table 6.3 The actual specimen's dimension.

Target angle	taper angle (deg.)	specimen	d (μm)	vertical step (nm)
10	11.96	A	1.07	20
15	15.36	B	0.89	16
20	18.15	C	0.76	23
25	25.02	D	0.61	18
30	29.78	E	0.545	14
35	35.27	F	0.466	26
40	41.11	G	0.419	26
50	51.77	H	0.35	35

Table 6.4 The parameter setting for the actual specimens.

Structure Layer	thickness (nm)
w_Tiout	20
W_gold upper	80
W_Ti	3
W_Al2O3	40
W_SiO2	200
W_Ti	3
W_gold lower	300
	nm
Number of grating hole	4
Period of grating	520
Width of grating	113
slit width	121
distance between grating and taper	4,000
distance between taper and slit	220

Name	Expression	Value	Description
z0	pi*w0^2/lda	1.455E-6 m	Rayleigh range
w0	620[nm]	6.2E-7 m	Spot radius
w_tip_start	220[nm]	2.2E-7 m	length of start hole in the tip
w_Tiout	20[nm]	2E-8 m	Ti outside width
w_Ti	3[nm]	3E-9 m	Ti inside width
w_t_hole	121[nm]	1.21E-7 m	hole width in the tip
w_sio2R	w_sio2-vl	1.86E-7 m	sio2 remained
w_sio2	200[nm]	2E-7 m	sio2 thickness
w_pml	lda	8.3E-7 m	Thickness of PML domains
w_hole	113[nm]	1.13E-7 m	hole width in body
w_gold_lo...	300[nm]	3E-7 m	lower gold width
w_gold	80[nm]	8E-8 m	gold thickness
w_body_s...	1000[nm]	1E-6 m	body start width
w_al2o3	40[nm]	4E-8 m	sio2Thin layer
w_air_up	2000[nm]	2E-6 m	air width
w_air	1000[nm]	1E-6 m	air thickness
vl	14[nm]	1.4E-8 m	vertical step
theta	0[deg]	0 rad	incident wave angle
Tangle	w_sio2R/h_taperR	0.57231	Tan angle
p_hole	520[nm]	5.2E-7 m	period of hold
n_Ti	3.23-4.0i	3.23-4i	refrectrive index of Ti
n_sio2	1.45	1.45	refrective index of sio2
n_gold	sqrt(Ep_gold)	0.17343-5.2182i	gold properties
n_al2o3	1.76	1.76	refrective index of al2o3
lda	830[nm]	8.3E-7 m	Wavelength
k	2*pi/lda	7.5701E6 1/m	Propagation constant
h_tip	1500[nm]	1.5E-6 m	tip lenght
h_taperR	d-w_tip_start	3.25E-7 m	taper length measured
h_taper	w_sio2R/Tangle	3.25E-7 m	taper length
h_body	w_body_start+3*p_hole+w_hole+before_T	6.673E-6 m	body length
f	c_const/lda	3.612E14 1/s	Frequency
Ep_gold	-27.2-1.81i	-27.2-1.81i	elsilon of gold
E0	1[V/m]	1 V/m	Electric field amplitude
d	545[nm]	5.45E-7 m	distance between taper to slit
cut1	1000[nm]	1E-6 m	cutline 2D at the first position
before_T	4[um]	4E-6 m	distance between grating and taper

Figure 6.28 Parameters of E specimen
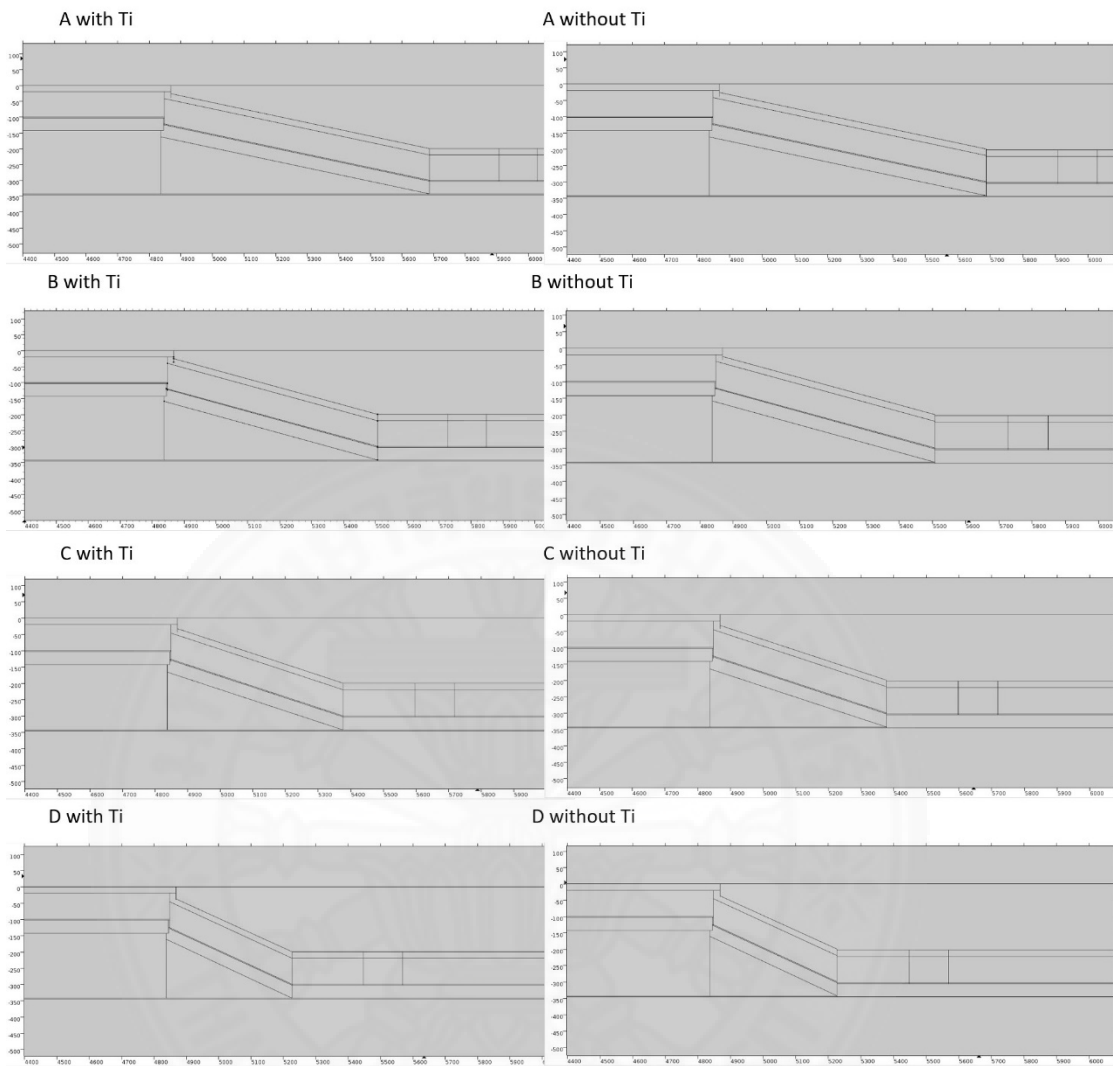
Figure 6.29 A-D specimen with the actual feature; with/without Ti at the tip part.
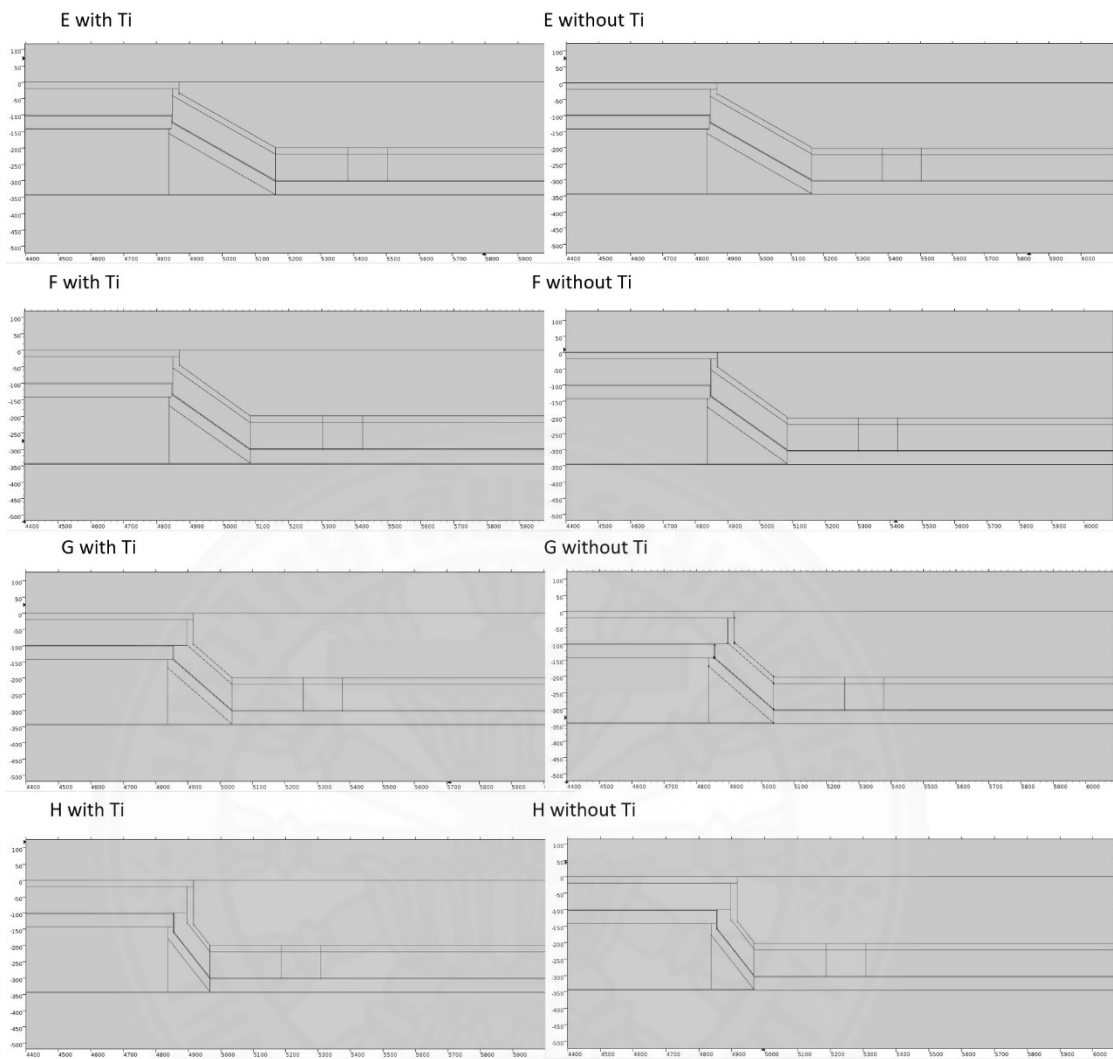
Figure 6.30 E-H specimen with the actual feature; with/without Ti at the tip part.
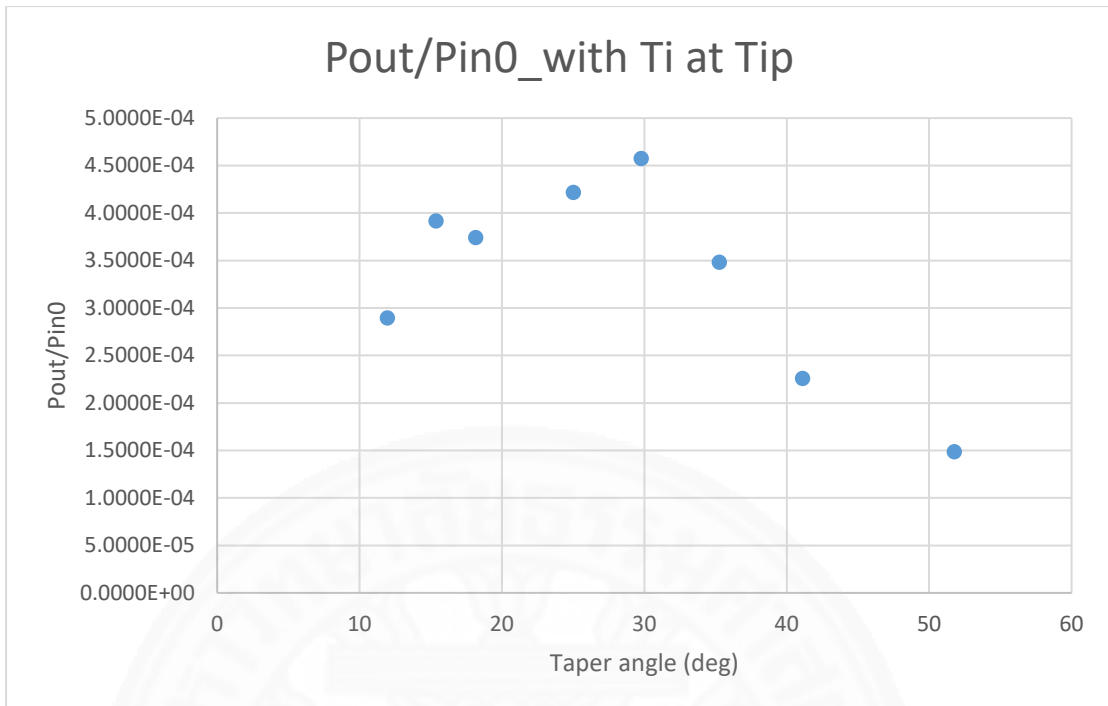
Figure 6.31 The efficiency of A-H specimens with Ti at the tip part.
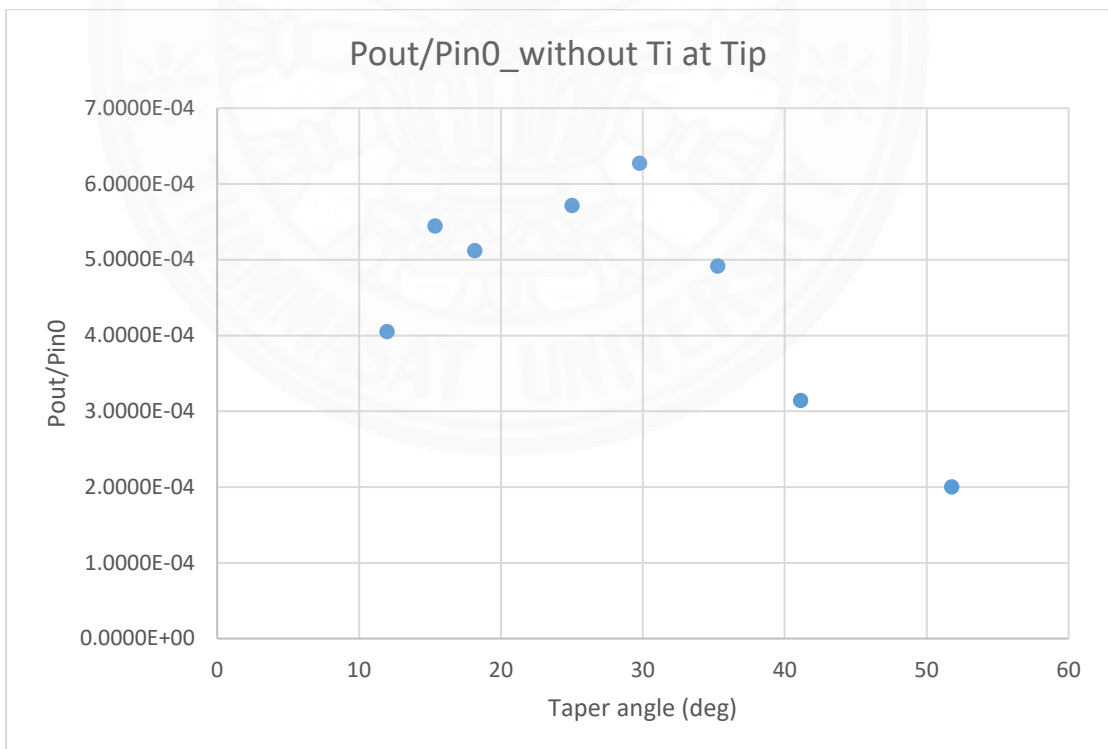
Figure 6.32 The efficiency of A-H specimens without Ti at the tip part.
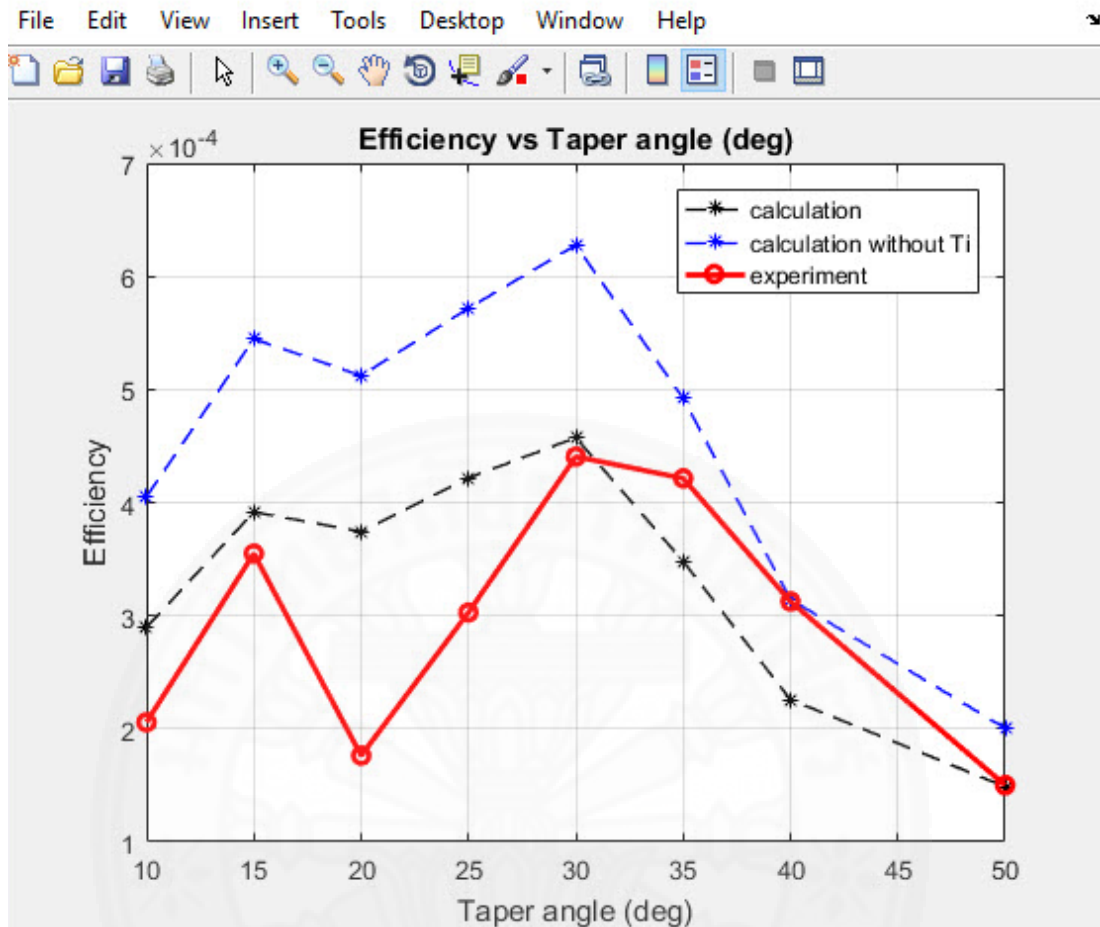
Figure 6.33 The comparison between the calculated results with/without Ti at the tip part and experiment results.

If the vertical step of 15-30 nm is added in the model, the efficiency will drop to about 12%. In addition, if the lower Ti remains at the tip part, the efficiency is reduced to 71-74% as shown in figure 6.31-6.33. The C and D specimens can be explained by this reason. For other specimens, The Ti might be completely removed, and it may get higher efficiency.

6.5.2 The influence of the 3 nm-thickness of Ti

The effect of the 3 nm-thickness of Ti is investigated by parameter setting as shown in figure 6.34-6.35, the results are shown in table 6.5 and figure 6.36-6.38. The very high *Ex* and Power in *y* direction of the model without 3 nm-thickness of Ti are observed. Therefore, in the future work, will apply the new fabrication technique to replace the lift-off process for making the grating and slit patterning so, Ti for adhesion

in lift-off process will no longer be needed which will make the efficiency to improve by 25 times.

Name	Expression	Value	Description
z0	pi*w0^2/lda	2.6075E-6 m	Rayleigh range
w0	lda	8.3E-7 m	Spot radius
w_tip_start	220[nm]	2.2E-7 m	length of start hole in the tip
w_Tiout	20[nm]	2E-8 m	Ti width
w_t_hole	120[nm]	1.2E-7 m	hole width in the tip
w_sio2	200[nm]	2E-7 m	sio2 thickness
w_pml	1000[nm]	1E-6 m	Thickness of PML domains
w_hole	110[nm]	1.1E-7 m	hole width in body
w_gold_lo...	300[nm]	3E-7 m	lower gold width
w_gold	100[nm]	1E-7 m	gold thickness
w_body_s...	1000[nm]	1E-6 m	body start width
w_al2o3	40[nm]	4E-8 m	sio2Thin layer
w_air_up	2000[nm]	2E-6 m	air width
w_air	1000[nm]	1E-6 m	air thickness
theta	0[deg]	0 rad	incident wave angle
p_hole	520[nm]	5.2E-7 m	period of hold
n_Ti	3.23-4.0i	3.23-4i	refrectrive index of Ti
n_sio2	1.45	1.45	refrective index of sio2
n_gold	sqrt(Ep_gold)	0.17343-5.2182i	gold properties
n_al2o3	1.76	1.76	refrective index of al2o3
lda	830[nm]	8.3E-7 m	Wavelength
k	2*pi/lda	7.5701E6 1/m	Propagation constant
h_tip	1500[nm]	1.5E-6 m	tip lenght
h_taper	346[nm]	3.46E-7 m	taper length
h_body	w_body_start+3*p_hole+w_hole+before_T	6.67E-6 m	body length
f	c_const/lda	3.612E14 1/s	Frequency
Ep_gold	-27.2-1.81i	-27.2-1.81i	elsilon of gold
E0	1[V/m]	1 V/m	Electric field amplitude
before_T	4[um]	4E-6 m	distance between grating and taper

Figure 6.34 The parameters setting.
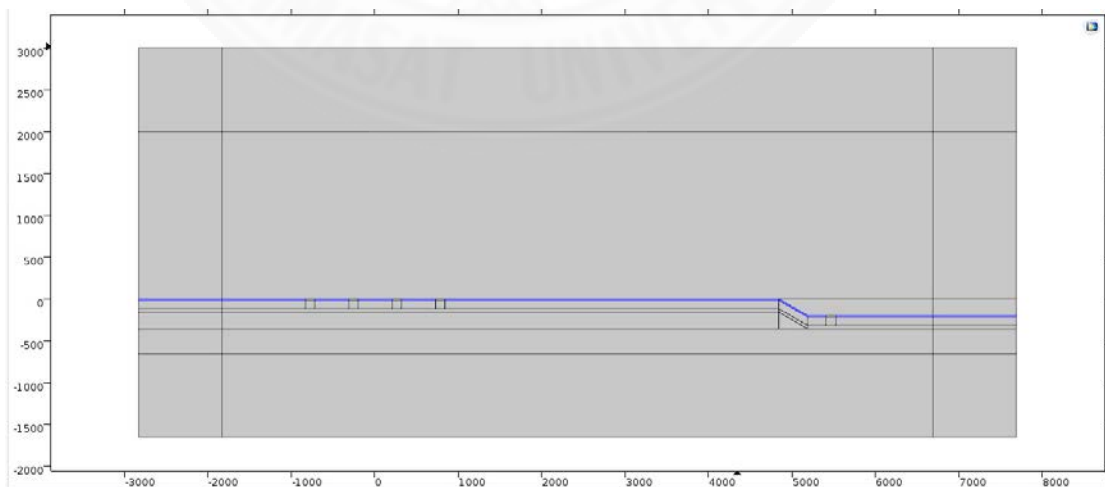
Figure 6.35 The example of Ti setting.

Table 6.5 The influence of the 3 nm-thickness Ti.

Distance between grating and taper	Influence of Ti inside	*w0* (nm)	Pin0	Pout	Pout/Pin0
4	with Ti	830	1.3218E-09	9.6935E-13	7.3336E-04
4	without Ti	830	1.3218E-09	2.5884E-11	1.9582E-02
4	with Ti i	620	1.3218E-09	7.3100E-13	5.5303E-04
4	without Ti	620	1.3218E-09	1.8445E-11	1.3954E-02
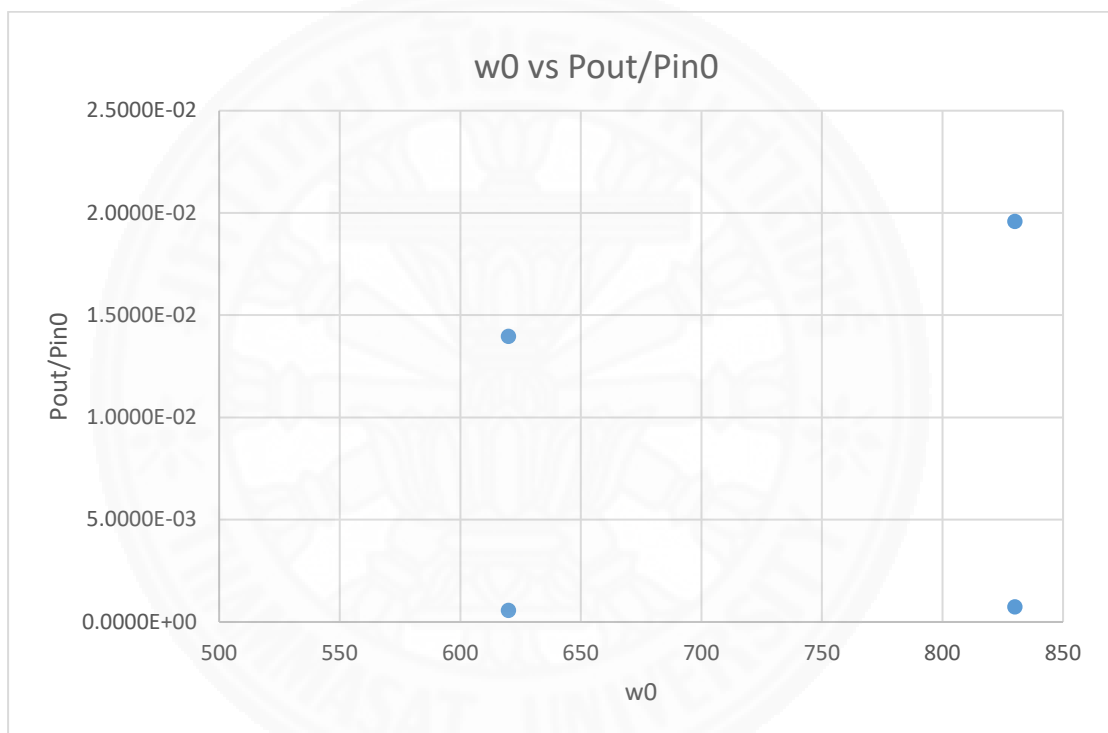
Figure 6.36 The with and without Ti in structure
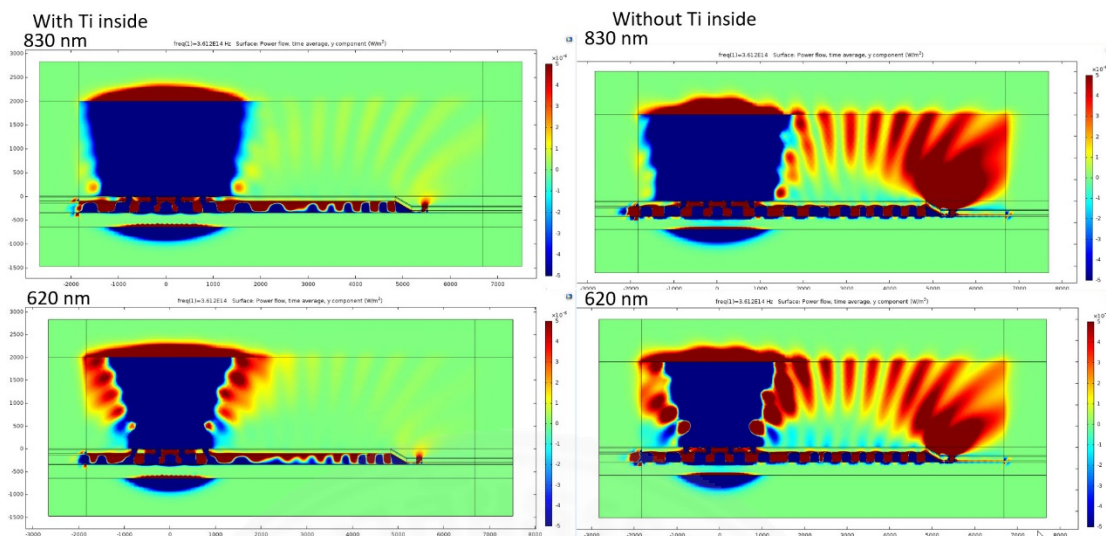
Figure 6.37 The power in *y* direction of with/without 3 nm-thickness of Ti, range -0.1 to 0.1. It is improving the efficiency 25 times.
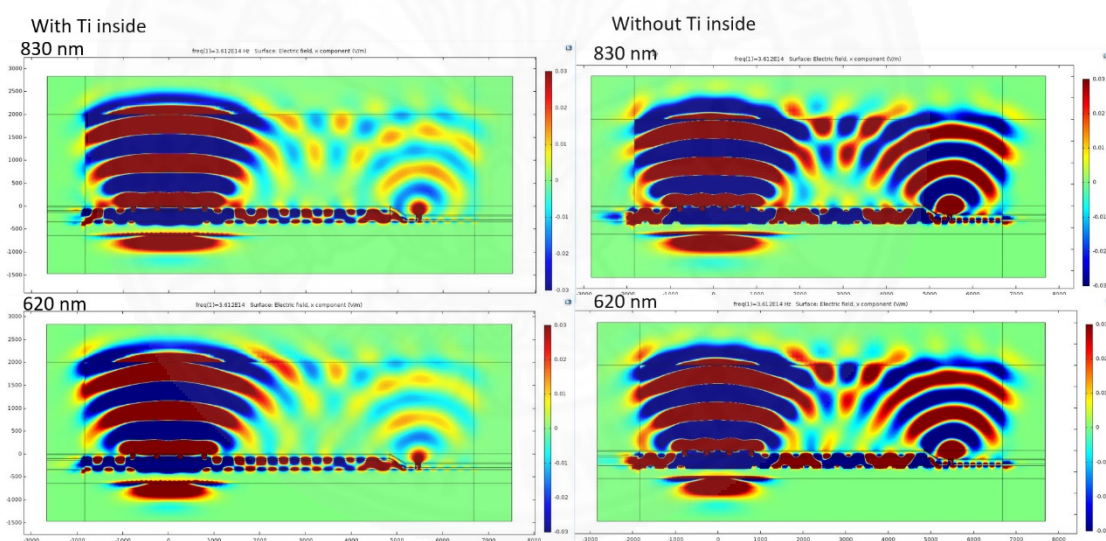
Figure 6.38 The electric field in *x* direction of with/without 3 nm-thickness of Ti, range -0.03 to 0.03.

CHAPTER 7
DISCUSSION AND CONCLUSIONS

In this dissertation, the field enhancement of near field transducer using metamaterial for heat assisted magnetic recording was investigated, thus the NFT based on 3D MIM structure was proposed for confining light on the deep sub-wavelength scale with input and output part made from metamaterial for optical characterization. The fabrication of NFT was also demonstrated which associated with the mass-productive manufacturing using the capability of simple process.

7.1 The conclusion of the structure design simulaiton

The developments of nano-focusing techniques have received wide attention recently. The technique of nano-focusing is to concentrate light into deep sub-wavelength and is one of the major challenges in nano-photonics for many different applications especially for HAMR. One of the promising mechanisms to achieve efficient nano-focusing is the utilization of SPPs propagating along a metal/insulator interface. Different SPP structures to achieve high efficiencies, on-chip nano-focusing have been proposed. One of the proposed SPP structures with the linear-tapering design is on-chip three-dimensional MIM nano-plasmonic photon compressor (3D NPC) by Choo et al. and demonstrated an $Au/SiO_2/Au$ MIM-SPP waveguide with a three-dimensional linear taper. They produced the vertical tapers with angle as large as 15-30 deg. by employing an electron-beam-induced deposition (EBID) technique. However, EBID has an extremely small throughput and is difficult to apply to mass-production. In addition, due to the insufficient deposition resolution of this technique, the minimum waveguide thickness remained at 14 nm.

For feasibility study, the ideal structure of a MIM plasmon waveguide with a linear taper was investigated. The simulation result shows that when the light incident at the bottom of the device, the SPP was produced between the interface of an $Au/SiO_2/Au$ and that SPP pass through the taper angle, it can deliver the light into a nano-scale spot size with the 72% of the coupling efficiency. Then the fabrication based

on a mass-productive process using a standard dry etching technique was succeeded by following the first feasibility study results. The key improvements of our technique are to employ a mixed gas for taper fabrication and the realization of ultra-thin waveguide by the thin film addition following the taper process. By optimizing the compositions of a mixed gas and the etching sequence, the vertical tapers with an angle of 19 deg. was successfully produced, which is very close to the optimum angle given by Choo et al. The optimum $CHF_3:O_2$ flow rate ratio was found to be 60:40. The atomic layer deposition (ALD) technique is applied which can produce thin films of a variety of materials and offer precise thickness with an atomic resolution to produce the ultra-thin dielectric film of Al_2O_3, instead of SiO_2. With this technique the hybrid structure had the minimum waveguide thickness as thin as 5.6 nm. For completing the MIM waveguide and its optical evaluation, lateral patterning in the y direction is necessary as well.

To practical applications, it very difficult to do alignment for the light source to directly incident light to the bottom of the nano-waveguide, the next target is to design the input part and output part using the metamaterial. The fishnet metamaterial was selected and was investigated by using an independence simulation. Then analyzation results are further done compared with Dolling paper. The results are closed to Dolling theory results, so these results can be reliable. Furthermore, for the fabrication and characterization part, both were also succeeded. Although the measurement of metamaterial was not exactly reproduced the results the same as Dolling's paper did, but it can surely see the success of the final specimen with the integrated MIM waveguide and metamaterial structure.

For the final specimens, the metamaterial was combined with the MIM waveguide, the model consists of three parts; light source extraction using metamaterial (input part), intermediate guiding of light and coupling of light into a focusing in the tip part (MIM waveguide), and for the final part, the light is coming out from the slit on the tip part. Due to the device's structure was combine with the MIM waveguide and input part, so that it required the long enough body part. For characterization, the body part of the device must be extended from 0.5 μm to 3.25 μm causing the coupling efficiency was reduced extremely from 72% to 3.65%. However, this output efficiency can be observed in characterization. Lastly, it is found that the optimized taper angle is

not 19 deg. as the feasibility study but it is 30 deg. These new conditions will be considered in the final specimen fabrication and characterization.

7.2 The conclusion of characterization design simulation

The simulation for the characterization, it showed that the propagating length of the first design of 5 nm-Al_2O_3 is too short as only 350 nm. It is insufficient length to do the characterization, so it is extended to 40 nm-Al_2O_3, the propagated length is 1.3 μm. In addition, the lift-off process, the one of fabrication methodology requires Ti for adhesion between Au and SiO_2, thus Ti seriously affected to reduce the efficiency. Another big problem is that the Gaussian beam waist from light source is too large, so that the beam will cover the input and output part, if the distance between the grating and slit is not long enough. As the simulation result, the 4.22 μm-distance is the optimization. However, the increasing distance between grating and taper has reduced the efficiency. Furthermore, the efficiency is sensitive to the upper Au thickness, and the optimum of the upper Au layer thickness is 80 nm. Moreover, the dominance of the SPP propagating on the outer surface was found, the SPP outer was eliminated by adding the 20-nm thickness of Ti which covered the surface structure. Finally, the final specimen of structure which can be observed in the characterization is composed of 300nm-Au/3nm-Ti/200nm- SiO_2/40nm-Al_2O_3/80nm-Au/20nm-Ti. The optimum input structures are the 4 holes of grating, period 520 nm and hole width 110 nm and the optimized taper angle is 30 deg. With all modifications above, the final efficiency is reduced from 3.65% to 0.1%. But these disadvantages will be considered and removed in the future work.

7.3 The conclusion of fabrication and characterization

According to the fabrication, after the exposure of Au, a sudden change in the etching rate was found. The detection of the completion of the SiO_2 etching is to recognize a vertical step smaller than 30 nm. But the vertical step effected to reduce the efficiency around 50%. As the fabrication results, the final specimen in 8 typical taper angles between 10 – 50 deg. are obtained as A to H specimens. The thin unwanted film

is produced within the taper angle, making the reverse sputter and NMP with 10 min-sonification can remove it. Finally, the taper angle was improved with good linearity and controllability. The three good positions of patterns are selected from the whole 250 patterns for doing the characterization. Fabrication yield is about 1.2%.

Characterization part, the dominance of the SPPs propagating on the outer surface was found, this could give an erroneous result. The SPPs of outer surface was eliminated by fabricating the 20-nm thickness of Ti on outer surface and certainly the light come out is SPP through the MIM taper. In the measurement, the incident laser spot was centered to the grating with a precision of 50 nm. As the results, there are some factors that might be responsible for the discrepancy between the simulation results and the experiment results. The re-simulation is calculated by adding some factors in the final model such as the Ti inside is etched, only the bared lower layer of Au is present. The re-simulation results shown that the presence or absence of the vertical step and the 3 nm-thickness of Ti at the tip area are the main factor for the discrepancy between the simulation results and the experiment results. The vertical step effects to reduce the efficiency around 50%. If the lower layer of Ti remains at the tip part, the efficiency is reduced to 71-74%. The C and D specimens can be explained by this reason. For other specimens, the Ti were completely removed, and it may get higher efficiency. In conclusion, the 30 deg. of the taper angle is optimally confirmed, and the efficiency trend is also confirmed by the simulation results. For the characterization, the highest efficiency is 0.045%-0.05% with the 512 nm x 853 nm spot size. The efficiency is dropped from the simulation forecasting because the vertical step appearing in the fabrication process and the Gaussian beam waist reducing to 620 nm.

7.4 The future works

For the future work, the target is to improve the coupling efficiency.

1) For designing, other parameters which relate to the coupling efficiency will be investigated.

2) For simulation, the parameter estimation and sensitivity of an objective function with respect to any parameter in the model should be computed.

3) For the fabrication processes, Ti is very effective in reducing the efficiency, the new fabrication technique should be applied to replace the lift-off process for making the grating and slit patterns so that Ti for adhesion in lift-off process is able to be removed, then the efficiency will be improved by 25 times.

4) For characterization, the distance between the grating and taper should be reduced to 0.72 μm by well-adjusting and well-aligning the beam Gaussian light source, the waist of Gaussian beam radius to 830 nm, and the 5 nm- Al_2O_3 should be applied then the highest efficiency will be increased to be 3.65%.

5) Finally, the new design of the input and output part should be also necessary to improve the coupling efficiency to 72% as closed as the ideal concept design.
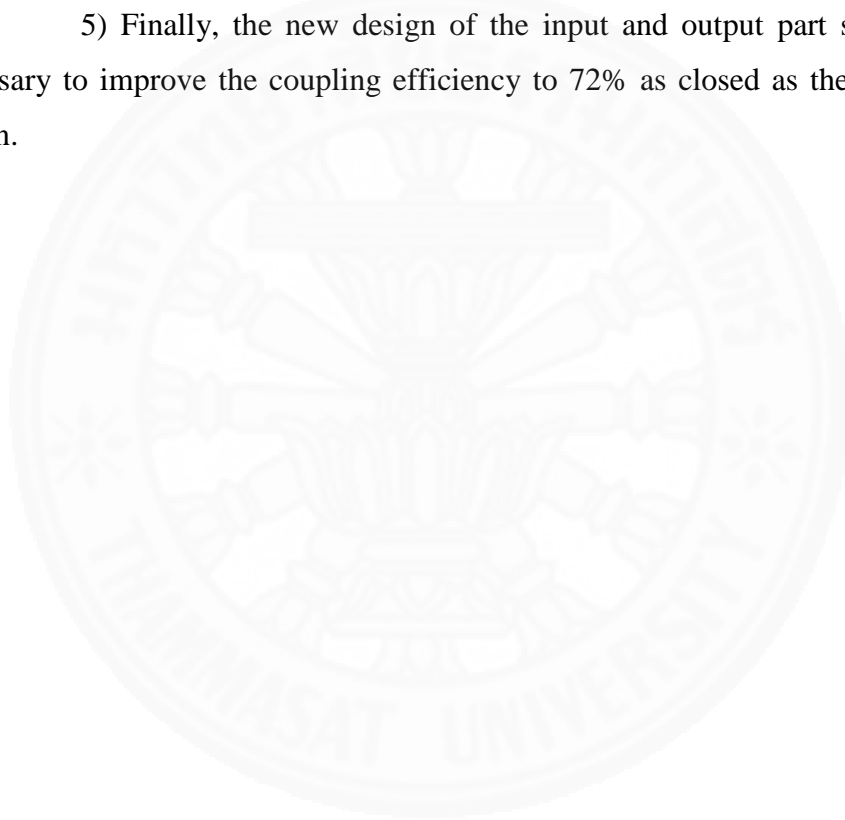
REFERENCES

1. A. Shilov, Hard disk drive with HAMR Technology setz to arrive in 2018, available : http://www.anandtech.com/show/9866/hard-disk-drives-with-hamr-technology-set-to-arrive-in 2018 (2015).

2. A. Shilov, Seagate: Hard disk drives set to stay relevant for 20 years, available : http://www.anandtech.com/show/9858/seagate-hard-disk-drives-set-to-stay-relevant-for-20-years (2015).

3. W. A. Challener and A. V. Itagi, Near-Field Optics for Heat-Assisted Magnetic Recording (Experiment, Theory, and Modeling), Springer Science and Business Media (2009).

4. D. Speliotis, Magnetic recording beyond the first 100 Years, J Magn Magn Mater, 193, 29–35, (1999).

5. A. P. Bean and J. D. Livingston, Superparamagnetism, Jpn J Appl Phys, 30, S120–S129, (1959).

6. T. W. McDaniel, W. A. Challener, K. Sendur, Thermal effect limits in ultrahigh density magnetic recording, IEEE Trans. Magn. 39 (2003) (1972).

7. T. W. McDaniel, Ultimate limits to thermally assisted magnetic recording, J. Phys.: Condens. Matter 17, R315–R332 (2005).

8. Mark H. Kryder, Edward C. Gage, Terry W. McDaniel, William A. Challener, Robert E. Rottmayer, Ganping Ju, Yiao-Tee Hsia, and M. Fatih Erden, Heat Assisted Magnetic Recording, Proceedings of the IEEE 96, (2008).

9. N. Zhou, X. Xu, A. T. Hammack, B. C. Stipe, K. Gao, W. Scholz and E. C. Gage, Plasmonic near-field transducer for heat-assisted magnetic recording, Nanophoton; 3(3): 141–155, (2014).

10. M. Gubbins, Data Storage and HAMR, Seagate Technology, available on : http://www.photonics21.org/download/Annual_Meeting/AnnualMeeting2013/Presentations/HAMRP2130April2013.pdf (2013).

11. L. Lee, X. Jin, K. Gao, A. Itagi, W. A. Challener, Near-field transducers for focusing light, United States Patent, Patent no. US 8,711,662,B2 (2014).

12. M. A. Seigler, W. A. Challener, E. Gage, N. Gokemeijer, G. Ju, B. Lu, K. Pelhos, C. Peng, R. E. Rottmayer, X. Yang, H. Zhou, and T. Rausch, Integrated Heat

Assisted Magnetic Recording Head: Design and Recording Demonstration, IEEE T Magn., 44, No. 1, (2008).

13. S. Bhargava, Heat-Assisted Magnetic Recording: Fundamental Limits to Inverse Electromagnetic Design, PhD. Thesis, University of California at Berkeley (2015).

14. Diffraction Limit Spot, available:

http://www.holoor.co.il/diffractive_optics_products/Images/DiffractionLimitedSpot.png

15. H. Bethe, Theory of diffraction by small holes. Phys Rev., 66:163–82 (1944).

16. H.J. Lezec, A. Degiron, E. Devaux, R.A. Linke, L. Martin-Moreno, F.J. Garcia-Vidal, T.W. Ebbesen, Beaming light from a subwavelength aperture, Science 297:820–2 (2002).

17. E.C. Kinzel, P. Srisungsitthisunti, Y. Li, A. Raman, X. Xu, Extraordinary transmission from high-gain nanoaperture antennas, Appl. Phys. Lett. 96:211116-1–3 (2010).

18. S. Carretero-Palacios, O. Mahboub, F.J. Garcia-Vidal, L. Martin-Moreno, S.G. Rodrigo, C. Genet, T.W. Ebbensen, Mechanisms for extraordinary optical transmission through bull's eye structures, Opt. Exp. 19:10429–42 (2011).

19. W. Srituravanich, L. Pan, Y. Wang, C. Sun, D.B. Bogy, X. Zhang, Flying plasmonic lens in the near field for high-speed nanolithography. Nat. Nanotechnol. 3:733–7 (2008).

20. H. Kim, J. Sohn, M. Lee, B. Lee, S. Suh, E. Cho, Heat-assisted magnetic recording head and method of manufacturing the same. Samsung Elctronics Co., Ltd., US Patent No. 7710686 B2, (2010).

21. K. B. Crozier, A. Sundaramuerthy, G. S. Kino, C. F. Quate, Optical antennas: resonators for local field enhancement. J of Appl Phys, 94:4632–42 (2003).

22. K. Osawa, K. Sekine, M. Saka, N. Nishida, H. Hatano, Optical TAMR head design for placing a heating spot close to a magnetic pole, J Magn Soc Jpn, 33:503–6 (2009).

23. M. Hirata, M. Park, M. Oumi, K. Nakajima, T. Ohkubo, Near-field optical flying head with a triangle aperture. Presented in MORIS Tech Dig, 35–6 (2007).

24.   M. Hirata, S. Tanabe, M. Oumi, M. Park, N. Chiba, L. V. Gonzaga, S. Yu, M. Zhang, Tjiptoharsono F. Light delivery system for heat-assisted magnetic recording. IEEE T Magn., 45:5016–21 (2009).

25.   R.D. Grober, R. J. Schoelkopf, E. D. Prober, Optical antenna: Towardsa unity efficiency near-field optical probe. Appl Phys Lett, 70;1354–6 (1997).

26.   B.J. Kim, J. W. a Flamm, E. S. Ten Have, M. F. Garcia-Parajo, N. F. Van Hulst, J. Brugger, Moulded photoplastic probes for near-field optical applications. J Micros, 202:16–21 (2001).

27.   K. Sendur, W. Challener, Near-field radiation of bow-tie antennas and apertures at optical frequencies. J Micros, 210:279–83 (2003).

28.   W. A. Challener, T. W. McDaniel, C. D. Mihalcea, K. R. Mountfield, K. Pelhos, I. K. Sendur, Light delivery techniques for heat-assisted magnetic recordings. Jpn J Appl Phys, 42:981–8 (2003).

29.   W. A. Challener, E. Gage, A. Itagi, C. Peng, Optical transducers for near field recording. Jpn J Appl Phys, 45:6632–42 (2006).

30.   E. X. Jin, X. Xu, Finite-difference time-domain studies on optical transmission through planar nano-apertures in a metal film. Jpn J Appl Phys, 43:407–17 (2004).

31.   E. X. Jin, X. Xu, Enhanced optical near field from a bowtie aperture. Appl Phys Lett, 88:153110–2 (2006).

32.   E. X. Jin, X. Xu, Plasmonic effects in near-field optical transmission enhancement through a single bowtie-shaped aperture. Appl Phys B; 84:3–9 (2006).

33.   L. Wang, X. Xu, High transmission nanoscale bowtie-shaped aperture probe for near-field optical imaging. Appl Phys Lett, 90:261105-1–3 (2007).

34.   N. Zhou, E. C. Kinzel, X. Xu, Nanoscale ridge aperture as near-field transducer for heat-assisted magnetic recording. Appl Opt, 50: G42–6 (2011).

35.   G. Ju, W. Challener, Y. Peng, M. Seigler, E. Gage, Developments in data storage: materials perspective. John Wiley & Sons, Inc., Chapter 10:193–222 (2011).

36.   W. A. Challener, C. Peng, A. V. Itagi, D. Karns, W. Peng, Y. Peng, X. Yang, X. Zhu, N. J. Gokemeijer, Y-T. Hsia, G. Ju, R. E. Rottmayer, M. A. Seigler, E. C. Gage. Heat-assisted magnetic recording by a near-field transducer with efficient optical energy transfer. Nat Photon, 3:220–4 (2009).

37.   Stipe BC, Strand TC, Poon CC, Balamane H, Boone TD, Katine JA, Li J-L, Rawat V, Nemoto H, Hirotsune A, Hellwig O, Ruiz R, Dobisz E, Kercher DS, Robertson N, Albrecht TR, Terris BD. Magnetic recording at 1.5 Pb m-2 using an integrated plasmonic antenna. Nat Photon, 4:484–8 (2010).

38.   K. Sendur, P. Jones. Effect of fly height and refractive index on the transmission efficiency of near-field optical transducers. Appl Phys Lett, 88:091110-1–3 (2006).

39.   A. Bouhelier, M. R. Beversluis and L. Novotny, Characterization of nano-plasmonic structures by locally excited photoluminescence, Appl. Phys. Lett. 83: 5041 (2003).

40.   E. Petryayeva, U. J. Krull, Localized surface plasmon resonance: Nanostructures, bioassays and biosensing- A review, Elsevier, Analytica Chimica Acta 706: 8-24 (2011).

41.   S. Chawla, Is there any differences between Surface plasmon polariton and surface plasmon resonance, available on:

https://www.researchgate.net/post/Is_there_any_differences_between_Surface_plasmon_polariton_and_surface_plasmon_resonance (2013).

42.   H. W. Lee, G. Papadakis, S. P. Burgos, K. Chander, A. Kriesch, R. Pala, U. Peschel and H. A. Atwater, Nanoscale conducting oxide plasMOStor, published online, Nano Letters, 14 (11), 6463-6468 (2014).

43.   M. Seigler, Introduction to HAMR, Seagate Technology, presentation (2014).

44.   S. A. Maier, Plasmonics: Fundamentals and Applications, Springer (2007).

45.   D. P. O'Connor, Modelling of Nano-Optic Light Delivery Mechanisms

for use in High Density Data Storage, PhD. Thesis, The Queen's University of Belfast (2010).

46.   P. R. West, Ishii S, Naik GV, Emani NK, Shalaev VM, Boltasseva A. Searching for better plasmonic materials. Laser & Photon Rev, 4:795–808 (2010).

47.   D. A. Bobb, G. Zhu, M. Mayy, A. V. Gavrilenko, P. Mead, V. I. Gavrilenko, M. A. Noginow, Engineering of low-loss metal for nano-plasmonic and metamaterials applications. Appl Phys Lett, 95:151102-1–3 (2009).

48.   A. Boltasseva, H. A. Atwater, Low-loss plasmonic metamaterials. Science; 331:290–1 (2011).

49.   G. V. Naik, J. Kim, A. Boltasseva, Oxides and nitrides as alternative plasmonic materials in the optical range. Opt Mater Exp, 1:1090–9 (2011).

50.   G. V. Naik, J. Liu, A. V. Kildishev, V. M. Shalaev, A. Boltasseva, Demonstration of Al:ZnO as a plasmonic component for near-infrared metamaterials. PNAS, 109:8834–8 (2012).

51.   G. V. Naik, V. M. Shalaev, A. Boltasseva, Alternative plasmonic materials: beyond gold and silver. Adv Mater; 25:3264–94 (2013).

52.   Y. Liu, S. Wang, Y. Park, X. Yin, and X. Zhang, Fluorescence enhancement by a two-dimensional dielectric annular Bragg resonant cavity, Opt. Exp. 25029 (2010).

53.   P. Chaturvedi, W.Wu, V. J. Logeeswaran, Z. Yu, M. Saif Islam, S.Y. Wang, R. S. Williams, and N. X. Fang, A Smooth optical superlens, Appl Phys Lett, 96, 043102 (2010).

54.   J. K. Gansel, M. Wegener, S. Burger, and S. Linden, Gold helix photonic metamaterials: A numerical parameter study, Opt. Exp., vol. 18, 1059-1069 (2010).

55.   B. Xu, Y. T. Toh, C. W. Chia, J. Li, J. Zhang, K. Ye, and C. An, Relationship Between Near Field Optical Transducer Laser Absorption and Its Efficiency, IEEE T Magn., 48: 1789-1793 (2012).

56.   L. Wang, Y. Wang, and X. Zhang, Integrated Grating-Nanoslot Probe Tip for Near-Field Subwavelenght Light Confinement and Fluorescent Sensing, IEEE J Sel Top Quant, 20 (3), (2014).

57.   H. Choo, M. Kim, M. Staffaroni, T. J. Seok, J. Bokor, S. Cabrini, P. J. Schuck, M. C. Wu and E. Yablonovitch, Nano-focusing in a metal-insulator-metal gap plasmon waveguide with a three-dimensional linear taper, Nature Photon. 6, 838-844 (2012).

58.   M. Staffaroni, Circuit analysis in metal-optics, theory and applications. PhD Dissertation, University of California at Berkeley, (2011).

59.   T. Brenner, W. Hunziker, M. Smit, M. Bachmann, G. Guekos, and H. Melchior, Vertical InP/InGaAsP tapers for low-loss optical fibre-waveguide coupling, Electron. Lett. 28, 2040-2041 (1992).

60.   S. Ullerich, R. Steingruber, and A. Umbach, Gray-tone lithography and dry etching technique for the fabrication of integrated spot size converters, Microelectron. Eng. 46, 303-306 (1999).

61. B. Jacobs, R. Zengerle, K. Faltin, and W. Weicrshausen, Vertically tapered spot size transformers fabricated by a simple masking technique, Electron. Lett. 31, 794-796 (1995).

62. Z. Yang, N. Fang, A. Wu, J. Chen, M. Zhang, X. Wang, and S. Zou, Fabrication and characterization of integrated three-dimensional linear taper on silicon-on-insulator, Opt. Eng. 48, 303503 (2009).

63. C. Lin, Characterization of the surface plasmon modes in planar metal-insulator-metal waveguides by an attenuated total reflection approach, PhD. Dissertation, Georgia Institute of Technology (2011).

64. N. Angkawisittpan, Novel technique for 3D isotropic metamaterial fabrication. Ph.D. Dissertation, University of Massachusetts Lowell. Lowell, MA, USA (2009).

65. V.G. Veselago, Electrodynamics of substances with simultaneously negative values of ε and μ. Soviet Physics Uspekhi. 10(4): 509-514 (1968).

66. J.B. Pendry, A. J. Holden, W. J. Stewart, and I. Youngs, Extremely low frequency plasmons in metallic mesostructures. Physical Review Letters. 76: 4773-4776 (1996).

67. J.B. Pendry, A. J. Holden, D. J. Robbins, and W. J. Stewart, Magnetism from conductors and enhanced nonlinear phenomena. IEEE T Microw theory, 47(11): 2075-2084 (1999).

68. D. R. Smith, W. J. Padilla, D. C. Vier, S. C. Nemat-Nasser and S. Schultz, Composite medium with simultaneously negative permeability and permittivity. Physical Review Letters. 84(18): 4184-4187 (2000).

69. G. Dolling, Fabrication, and Characterization of Double-Negative Metamaterials for Photonics Design, PhD. Dissertation, University of Karlsruhe (2007).

70. D. Morin, Dispersion, available on:
http://www.people.fas.harvard.edu/~djmorin/waves/dispersion.pdf.

71. G. Dolling, C. Enrich, M. Wegener, C. M. Soukoulis, S. Linden, Simultaneous Negative Phase and Group Velocity of Light in a Metamaterial, Science 312, (2006).

72. J. A. Schuller, E. S. Barnard, W. Cai, Y. C. Jun, J. S. White, and M. L. Brongersma, Plasmonics for extreme light concentration and manipulation, Nature Mater. 9, 193-204 (2010).

73. D. K. Gramotnev and S. I. Bozhevolnyi, Plasmonics beyond the diffraction limit, Nature Photon. 4, 83-91 (2010).

74. M. I. Stockman, Nano-focusing of optical energy in tapered plasmonic waveguides, Phys. Rev. Lett. 93, 137404 (2004).

75. E. Verhagen, A. Polman, and L. (Kobus) Kuipers, Nano-focusing in laterally tapered plasmonic waveguides, Opt. Express 16, 45-57 (2008).

76. D. P. O'Connor, Modelling of Nano-Optic Light Delivery Mechanisms for use in High Density Data Storage, Ph.D thesis, The Queen's University of Belfast, UK (2010).

77. J. A. Dionne, L. A. Sweatlock, and H. A. Atwater, Plasmon slot waveguides: Towards chip-scale propagation with subwavelength-scale localization, Phys. Rev. B 73, 035407 (2006).

78. H. T. Miyazaki and Y. Kurokawa, Squeezing visible light waves into a 3-nm-thick and 55-nm-long plasmon cavity, Phys. Rev. Lett. 96, 097401 (2006).

79. Y. Kurokawa and H. T. Miyazaki, Metal-insulator-metal plasmon nanocavities: Analysis of optical properties, Phys. Rev. B 75, 035411 (2007).

80. S. Vedantam, H. Lee, J. Tang, J. Conway, M. Staffaroni, and E. Yablonovitch, A plasmonic dimple lens for nanoscale focusing of light, Nano Lett. 9, 3447-3452 (2009).

81. P.B. Johnson and R.W. Christy, Optical Constants of the Noble Metals, Physical Review B Volume 6, Number 12, December (1972).

82. COMSOL Multiphysics 4.4 tutorials, Frequency Selective Surface, Complementary Split Ring Resonator; available on: https://www.comsol.jp/model/frequency-selective-surface-periodic-complementary-split-ring-resonator-15711.

83. COMSOL Multiphysics 4.4 tutorials, Fresnel Equations; available on: https://www.comsol.jp/model/fresnel-equations-12407

84. A. Yariv and P.Yeh, Photonics: Optical Electronics in Modern Communication sixth edition, Oxford University Press, New York, Oxford USA. (2007).

85. Penetration, available on: https://en.wikipedia.org/wiki/Penetration_depth.

86. Liff-off, available on: http://nanooptics.uni-graz.at/ol/work/m_ebl.html.

87.   EBeam lithography, available on:

https://www.sheffield.ac.uk/eee/research/ebl/principles.

88.   Dry etching process, available on:

https://www.memsnet.org/mems/processes/etch.html.

89.   E. D. Palik, Handbook of Optical Constants of Solids III, Academic Press, San Diego (1998).

90.   Atomic layer deposition (ALD), available on:

https://www.tue.nl/en/university/departments/applied-physics/research/plasma-

physics-and-radiation-technology/plasma-and-materials-processing-

pmp/facilities/technologies/atomic-layer-deposition-ald/#top.

91.   P.B. Johnson and R.W. Christy, Optical constants of transition metals: Ti, V, Cr, Mn, Fe, Co, Ni, and Pd, Physical Review B Volume 9, 5056, June (1974).
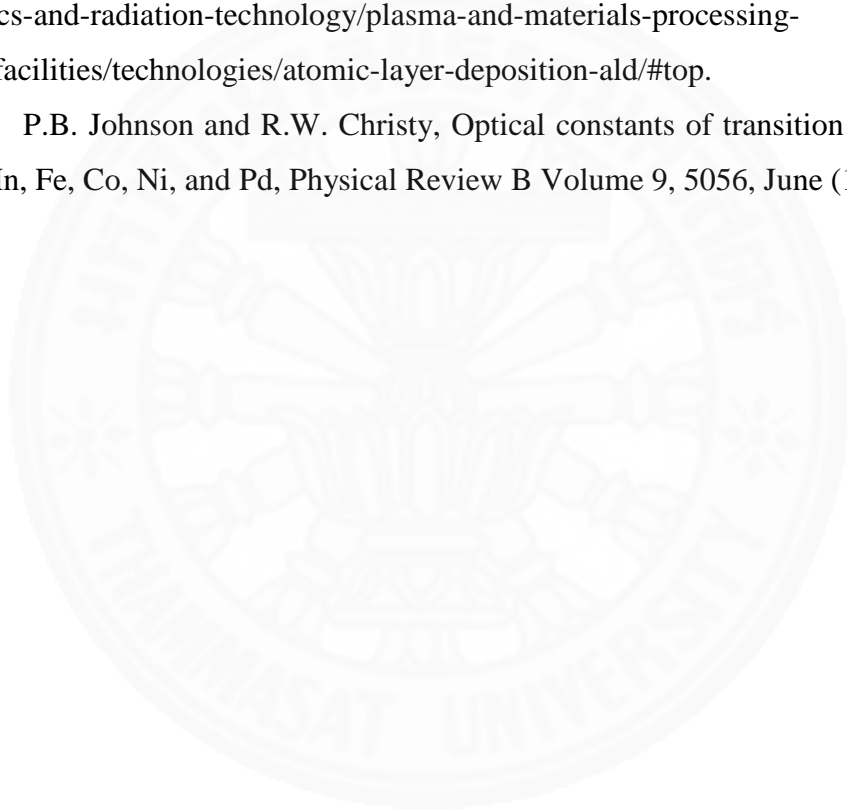
APPENDIX A

The optical constants for noble metal

We followed the Johnson and Christy, 1972 [81] and 1974 [91] results that the frequency effect of the metal properties is in eV unit. But our work is used frequency in Hz and rad/s unit, so we should know the related of these units.

TABLE I. Optical constants for copper, silver, and gold as well as the approximate errors in n and k.

eV	Copper		Silver		Gold		Error	
	n	k	n	k	n	k	Δn	Δk
0.64	1.09	13.43	0.24	14.08	0.92	13.78	±0.18	±0.65
0.77	0.76	11.12	0.15	11.85	0.56	11.21	±0.08	±0.30
0.89	0.60	9.439	0.13	10.10	0.43	9.519	±0.06	±0.17
1.02	0.48	8.245	0.09	8.828	0.35	8.145	±0.04	±0.10
1.14	0.36	7.217	0.04	7.795	0.27	7.150	±0.03	±0.07
1.26	0.32	6.421	0.04	6.992	0.22	6.350	±0.02	±0.05
1.39	0.30	5.768	0.04	6.312	0.17	5.663	±0.02	±0.03
1.51	0.26	5.180	0.04	5.727	0.16	5.083	±0.02	±0.025
1.64	0.24	4.665	0.03	5.242	0.14	4.542	±0.02	±0.015
1.76	0.21	4.205	0.04	4.838	0.13	4.103	±0.02	±0.010
1.88	0.22	3.747	0.05	4.483	0.14	3.697	±0.02	±0.007
2.01	0.30	3.205	0.06	4.152	0.21	3.272	±0.02	±0.007
2.13	0.70	2.704	0.05	3.858	0.29	2.863	±0.02	±0.007
2.26	1.02	2.577	0.06	3.586	0.43	2.455	±0.02	±0.007
2.38	1.18	2.608	0.05	3.324	0.62	2.081	±0.02	±0.007
2.50	1.22	2.564	0.05	3.093	1.04	1.833	±0.02	±0.007
2.63	1.25	2.483	0.05	2.869	1.31	1.849	±0.02	±0.007
2.75	1.24	2.397	0.04	2.657	1.38	1.914	±0.02	±0.007
2.88	1.25	2.305	0.04	2.462	1.45	1.948	±0.02	±0.007
3.00	1.28	2.207	0.05	2.275	1.46	1.958	±0.02	±0.007
3.12	1.32	2.116	0.05	2.070	1.47	1.952	±0.02	±0.007
3.25	1.33	2.045	0.05	1.864	1.46	1.933	±0.02	±0.007
3.37	1.36	1.975	0.07	1.657	1.48	1.895	±0.02	±0.007
3.50	1.37	1.916	0.10	1.419	1.50	1.866	±0.02	±0.007
3.62	1.36	1.864	0.14	1.142	1.48	1.871	±0.02	±0.007
3.74	1.34	1.821	0.17	0.829	1.48	1.883	±0.02	±0.007
3.87	1.38	1.783	0.81	0.392	1.54	1.898	±0.02	±0.007
3.99	1.38	1.729	1.13	0.616	1.53	1.893	±0.02	±0.007
4.12	1.40	1.679	1.34	0.964	1.53	1.889	±0.02	±0.007
4.24	1.42	1.633	1.39	1.161	1.49	1.878	±0.02	±0.007
4.36	1.45	1.633	1.41	1.264	1.47	1.869	±0.02	±0.007
4.49	1.46	1.646	1.41	1.331	1.43	1.847	±0.02	±0.007
4.61	1.45	1.668	1.38	1.372	1.38	1.803	±0.02	±0.007
4.74	1.41	1.691	1.35	1.387	1.35	1.749	±0.02	±0.007
4.86	1.41	1.741	1.33	1.393	1.33	1.688	±0.02	±0.007
4.98	1.37	1.783	1.31	1.389	1.33	1.631	±0.02	±0.007
5.11	1.34	1.799	1.30	1.378	1.32	1.577	±0.02	±0.007
5.23	1.28	1.802	1.28	1.367	1.32	1.536	±0.02	±0.007
5.36	1.23	1.792	1.28	1.357	1.30	1.497	±0.02	±0.007
5.48	1.18	1.768	1.26	1.344	1.31	1.460	±0.02	±0.007
5.60	1.13	1.737	1.25	1.342	1.30	1.427	±0.02	±0.007
5.73	1.08	1.699	1.22	1.336	1.30	1.387	±0.02	±0.007
5.85	1.04	1.651	1.20	1.325	1.30	1.350	±0.02	±0.007
5.98	1.01	1.599	1.18	1.312	1.30	1.304	±0.02	±0.007
6.10	0.99	1.550	1.15	1.296	1.33	1.277	±0.02	±0.007
6.22	0.98	1.493	1.14	1.277	1.33	1.251	±0.02	±0.007
6.35	0.97	1.440	1.12	1.255	1.34	1.226	±0.02	±0.007
6.47	0.95	1.388	1.10	1.232	1.32	1.203	±0.02	±0.007
6.60	0.94	1.337	1.07	1.212	1.28	1.188	±0.02	±0.007

Figure A.1 Optical constant for noble metal [81].

TABLE II. Optical constants for titanium, vanadium, chromium, and manganese.

eV	Titanium		Vanadium		Chromium		Manganese	
	n	k	n	k	n	k	n	k
0.64	3.51	5.19	2.79	7.90	3.71	5.04	3.89	5.95
0.77	3.69	4.70	2.77	6.34	3.66	4.31	3.78	5.41
0.89	3.67	4.37	2.64	5.18	3.69	3.84	3.65	5.02
1.02	3.62	4.15	2.70	4.33	3.67	3.60	3.48	4.74
1.14	3.50	4.02	2.87	3.78	3.58	3.58	3.30	4.53
1.26	3.35	3.97	2.94	3.50	3.41	3.57	3.10	4.35
1.39	3.29	3.96	3.12	3.34	3.30	3.52	2.97	4.18
1.51	3.21	4.01	3.16	3.25	3.20	3.48	2.83	4.03
1.64	3.00	4.01	3.20	3.20	3.08	3.42	2.70	3.91
1.76	2.86	3.96	3.18	3.15	3.05	3.39	2.62	3.78
1.88	2.76	3.84	3.25	3.09	3.09	3.34	2.56	3.65
2.01	2.67	3.72	3.54	3.02	3.17	3.30	2.51	3.54
2.13	2.60	3.58	3.83	3.00	3.22	3.30	2.47	3.43
2.26	2.54	3.43	4.00	3.04	3.18	3.33	2.39	3.33
2.38	2.44	3.30	3.86	3.18	2.94	3.33	2.32	3.23
2.50	2.36	3.19	3.92	3.26	2.75	3.30	2.25	3.14
2.63	2.32	3.10	3.81	3.38	2.51	3.24	2.19	3.06
2.75	2.27	3.04	3.59	3.46	2.33	3.14	2.11	2.98
2.88	2.21	3.01	3.52	3.49	2.19	3.04	2.06	2.90
3.00	2.14	2.98	3.31	3.49	2.08	2.93	2.00	2.82
3.12	2.08	2.95	3.07	3.48	2.00	2.83	1.96	2.74
3.25	1.99	2.93	2.87	3.45	1.92	2.74	1.92	2.67

Figure A.2 Optical constant for Ti [91].

Electron energy [eV] unit
We start from

$$e = hf$$

where e is elementary charge = 1.602176 x 10⁻¹⁹ C, h is Planck constant = 6.626 069 x 10⁻³⁴ Js, and c is speed of light in vacuum = 3 x10⁸ m/s.

$$e = \frac{hc}{\lambda} => \lambda = \frac{hc}{e} = \frac{6.626\,069 \times 10^{-34} \times 3 \times 10^8}{1.602176 \times 10^{-19}}$$
$$\lambda = 1.24 \times 10^{-6} \ [eV]$$

In Johnson and Christy paper, we find the best fitting.
$\omega_p = 8.2801$ [eV]
$$= \frac{8.2801 \times 3 \times 10^8}{1.24 \times 10^{-6}} = 2 \times 10^{15} \ [Hz]$$
$\omega_p = 2 \times 10^{15} \times 2 \times 3.414 = 1.3656 \times 10^{16}$ [rad/s]

$\gamma = 0.0820$ [eV]
$$= \frac{0.0820 \times 3 \times 10^8}{1.24 \times 10^{-6}} = 1.98 \times 10^{13} \ [Hz]$$
$\gamma = 1.98 \times 10^{13} \times 2 \times 3.414 = 1.3519 \times 10^{14}$ [rad/s]

APPENDIX B

MATLAB source code for optical constant curve fitting

```
%TiProperties
clc;
clear;

lda=[1.9375E-06
1.61039E-06
1.39326E-06
1.21569E-06
1.08772E-06
9.84127E-07
8.92086E-07
8.21192E-07
7.56098E-07
7.04545E-07
6.59574E-07
6.16915E-07
5.8216E-07
5.48673E-07
5.21008E-07
4.9600E-07
4.71483E-07
4.50909E-07
4.30556E-07
4.13333E-07
3.97436E-07
3.81538E-07
3.67953E-07
3.54286E-07
3.42541E-07
3.31551E-07
3.20413E-07
3.10777E-07
3.00971E-07
2.92453E-07
2.84404E-07
2.76169E-07
2.6898E-07
2.61603E-07
2.55144E-07
2.48996E-07
2.42661E-07
2.37094E-07
2.31343E-07
2.26277E-07
2.21429E-07
2.16405E-07
2.11966E-07
2.07358E-07
2.03279E-07
1.99357E-07
2.06667E-07
1.91654E-07
1.87879E-07
];
```

```
n=[3.51
3.69
3.67
3.62
3.5
3.35
3.29
3.21
3
2.86
2.76
2.67
2.6
2.54
2.44
2.36
2.32
2.27
2.21
2.14
2.08
1.99
1.9
1.82
1.72
1.61
1.55
1.5
1.45
1.4
1.35
1.3
1.27
1.27
1.26
1.27
1.28
1.3
1.31
1.32
1.32
1.32
1.31
1.31
1.27
1.25
1.22
1.16
1.1
];
k=[5.19
4.7
4.37
4.15
4.02
3.97
3.96
4.01
```

```
4.01
3.96
3.84
3.72
3.58
3.43
3.3
3.19
3.1
3.04
3.01
2.98
2.95
2.93
2.9
2.87
2.82
2.74
2.66
2.57
2.46
2.36
2.26
2.17
2.07
1.99
1.91
1.83
1.77
1.72
1.68
1.66
1.66
1.67
1.68
1.69
1.69
1.68
1.22
1.64
1.62
];
%define 1

Ein= 2;
Wp= 12;
Gam= 3.6;

%Calculation1
E1=(n.^2)-(k.^2);
E2=2.*n.*k;
xx = 2.0E-07:0.3E-07:2.0E-06;
yy = spline(lda,E1,xx)
yz = spline(lda,E2,xx)

figure(1)
plot(lda,E1,'*r')
hold on
```

```
plot(xx,yy,'-r')
legend('real','Spline')
grid on
title('Ti dielectric constant (real)')
xlabel('wavelength (micron)')
ylabel('constant')

figure(2)
plot(lda,E2,'*b')
hold on
plot(xx,yz,'-b')
legend('imag','Spline')
grid on
title('Ti dielectric constant (imaginary)')
xlabel('wavelength (micron)')
ylabel('constant')
```

```
%SiO2 properties
clc;
clear;
lda=[2.96764E-07
3.02188E-07
3.30297E-07
3.34187E-07
3.40407E-07
3.46659E-07
3.61095E-07
3.6506E-07
4.047E-07
4.35883E-07
4.67872E-07
4.86198E-07
5.08634E-07
5.46135E-07
5.77039E-07
5.79142E-07
5.87622E-07
5.89326E-07
6.43922E-07
6.56362E-07
6.67888E-07
7.06593E-07
8.52234E-07
8.94467E-07
1.01407E-06
1.08306E-06
1.12881E-06
1.36237E-06
1.39523E-06
1.46968E-06
1.52971E-06
1.6608E-06
1.68113E-06
1.69341E-06
1.70933E-06
1.81329E-06
1.97032E-06
2.05833E-06
```

```
2.15285E-06
2.43768E-06
];
n=[1.48873
1.48719
1.48053
1.47976
1.47858
1.47746
1.47512
1.47453
1.46961
1.46669
1.46429
1.46313
1.46187
1.46008
1.45885
1.45877
1.45847
1.45841
1.45671
1.45637
1.45608
1.45515
1.45248
1.45185
1.45025
1.444941
1.44888
1.44621
1.44584
1.44497
1.444427
1.44267
1.44241
1.44226
1.44205
1.44069
1.43851
1.43722
1.43576
1.43095
];
x = 2.6E-07:0.3E-07:2.51E-06;
y = spline(lda,n,x)

figure(1)
plot(lda,n,'*r')
hold on
plot(x,y,'-r')
grid on
legend('n','n-fit')
title('SiO2 dielectric constant')
xlabel('wavelength (micron)')
ylabel('refractive index')
```

```
%Al2O3 properties
clc;
clear;
lda=[2.89395E-07
2.96764E-07
3.00039E-07
3.02188E-07
3.13036E-07
3.30042E-07
3.34187E-07
3.46659E-07
3.61095E-07
3.6506E-07
3.6506E-07
3.90687E-07
4.047E-07
4.047E-07
4.35883E-07
4.35883E-07
4.86179E-07
5.46135E-07
5.46135E-07
5.77039E-07
5.79142E-07
5.89382E-07
6.43922E-07
6.43922E-07
6.56362E-07
6.90808E-07
7.06593E-07
8.52234E-07
8.94532E-07
1.01407E-06
1.12881E-06
1.36745E-06
1.3953E-06
1.52973E-06
1.6933E-06
1.7094E-06
1.8134E-06
1.96047E-06
2.15278E-06
2.24964E-06
2.32558E-06
2.43759E-06
3.24437E-06
3.26746E-06
3.30314E-06
3.33065E-06
3.42258E-06
];
n0=[1.81949
1.81595
1.8147
1.81351
1.80906
1.8035
1.80184
```

```
1.79815
1.7945
1.7935
1.79358
1.78826
1.78582
1.78571
1.7811
1.7812
1.77547
1.77067
1.77078
1.76884
1.76871
1.76808
1.76547
1.76538
1.76485
1.76351
1.76303
1.75885
1.75796
1.75547
1.75339
1.74936
1.74888
1.7466
1.74368
1.7434
1.74144
1.73833
1.73444
1.73231
1.73057
1.72783
1.70437
1.70356
1.70231
1.7014
1.69818
];
ne=[1.81021
1.80674
1.8056
1.80437
1.80005
1.7947
1.79293
1.7894
1.78579
1.7849
1.78488
1.7797
1.7773
1.77724
1.77275
1.77279
1.76724
```

```
1.76254
1.76258
1.76069
1.76057
1.75999
1.75739
1.75734
1.75682
1.75549
1.755
1.7509
1.74994
1.74794
1.74549
1.74148
1.74101
1.73874
1.73584
1.73555
1.73362
1.73074
1.7267
1.72455
1.72279
1.72011
1.69688
1.69612
1.69491
1.69397
1.69077
];

x = 2.9E-07:0.3E-07:3.5E-06;
y = csapi(lda,n0,x)
y1 = csapi(lda,ne,x)
figure(1)
plot(lda,n0,'*r')
hold on
plot(lda,ne,'*b')
hold on
plot(x,y,'-r')
hold on
plot(x,y1,'-b')
grid on
legend('n0','ne','n0-fit','ne-fit')
title('Al2O3 dielectric constant')
xlabel('wavelength (micron)')
ylabel('refractive index')
```

```
%Au properties
clear;
clc;
%Define n, k, eV,T
n=[0.92, 0.56, 0.43, 0.35, 0.7, 0.22, 0.17, 0.16, 0.14, 0.13, 0.14];
k=[13.78, 11.21, 9.519, 8.145, 7.150, 6.350, 5.663, 5.083, 4.542,
4.103, 3.697];
```

```matlab
eV=[0.64, 0.77, 0.89, 1.02, 1.14, 1.26, 1.39, 1.51, 1.64, 1.76,
1.88];
lda=1.24e-6./eV;

%Initial value from MATLAB @lsqcurvefit
Ein=6.5681;
Wp=8.6880;
Gam=0.0804;

%Calculation1
E1=(n.^2)-(k.^2);
E2=2.*n.*k;
EWnew=Ein-(Wp^2./((eV.^2)+(i*Gam)*eV)); %Drude model

X=real(EWnew);
Y=imag(EWnew);

%Plot
figure(2);
plot (lda, E1,'*r')
hold on
plot (lda, E2,'*b')
hold on
plot (lda,X,'-r')
hold on
plot (lda,Y,'-b')
legend('real', 'imag','Drude-real','Drude-imag')
grid on
title('Au dielectric constant')
xlabel('wavelength (micron)')
ylabel('constant')
```

BIOGRAPHY

Name	Miss Kruawan Wongpanya
Date of Birth	September 17, 1981
Educational Attainment	2017: Ph.D, Electrical and Computer Engineering, Thammasat University
	2009: A master's degree, Information Engineering. King Mongkut's Institute of Technology Ladkrabang.
	2003: A bachelor's degree, Science (Physic), Naresuan University.
Work Position	-
Scholarship (If any)	Year 2013-2017: Research and Research for Industry Grants (RRI), Thailand Research Fund (TRF) and Seagate (Thailand) Co., Ltd.

Publications

Kruawan Wongpanya, Takeshi Kasaya, Hideki T. Miyazaki, Hirotaka Oosato, Yoshimasa Sugimoto, Wanchai Pijitrojana, "Mass-productive fabrication of a metal-insulator-metal plasmon waveguide with a linear taper for nano-focusing", Appl. Phys. B (2016) 122: 238. doi:10.1007/s00340-016-6515-8.

Work Experiences	Nov. 2011- Sep. 2013: Project Analyst, National Electronics and Computer Technology Center (NECTEC).
	Aug. 2004–Oct. 2011: Research Assistant of Optical and Quantum Communication Laboratory (OQC), NECTEC.